

BỘ KHOA HỌC VÀ CÔNG NGHỆ  
QUỸ PHÁT TRIỂN KHOA HỌC VÀ CÔNG NGHỆ QUỐC GIA

## BÁO CÁO TỔNG HỢP

### KẾT QUẢ THỰC HIỆN ĐỀ TÀI NGHIÊN CỨU CƠ BẢN TRONG KHOA HỌC TỰ NHIÊN

Đề tài:

Nghiên cứu tổng hợp vật liệu zeolite từ tính  $\text{Fe}_3\text{O}_4/\text{NaP}$  có nguồn gốc từ tro trấu không nung và ứng dụng hấp phụ ion ion  $\text{Cu}^{2+}$ ,  $\text{Pb}^{2+}$ ,  $\text{NO}_3^-$  và  $\text{PO}_4^{3-}$  trong nước của ao nuôi tôm

Mã số đề tài: 103.02-2020.64

Chủ nhiệm đề tài: TS. Trần Nguyễn Phương Lan

Thành viên chính: GS. TS. Ju Yi-Hsu

TS. Lương Huỳnh Vũ Thanh

TS. Trần Thị Bích Quyên

Thư ký khoa học: TS. Nguyễn Hoàng Anh

Cần Thơ, tháng 8 năm 2023

BỘ KHOA HỌC VÀ CÔNG NGHỆ  
QUỸ PHÁT TRIỂN KHOA HỌC VÀ CÔNG NGHỆ QUỐC GIA



---

## BÁO CÁO TỔNG HỢP

### KẾT QUẢ THỰC HIỆN ĐỀ TÀI NGHIÊN CỨU CƠ BẢN TRONG KHOA HỌC TỰ NHIÊN

**Tên đề tài: Nghiên cứu tổng hợp vật liệu zeolite từ tính  $\text{Fe}_3\text{O}_4/\text{NaP}$  có nguồn gốc từ tro trấu không nung và ứng dụng hấp phụ ion ion  $\text{Cu}^{2+}$ ,  $\text{Pb}^{2+}$ ,  $\text{NO}_3^-$  và  $\text{PO}_4^{3-}$  trong nước của ao nuôi tôm**

**Mã số đề tài: 103.02-2020.64**

**Chủ nhiệm đề tài: TS. Trần Nguyễn Phương Lan**

**Cần Thơ, tháng 8 năm 2023**



Mã số hồ sơ	
Ngày nhận báo cáo	
(Do Cơ quan điều hành Quyết định)	

## PHẦN I. THÔNG TIN CHUNG

1. Tên đề tài: Nghiên cứu tổng hợp vật liệu zeolite từ tính Fe<sub>3</sub>O<sub>4</sub>/NaP có nguồn gốc từ tro trấu không nung và ứng dụng hấp phụ ion ion Cu<sup>2+</sup>, Pb<sup>2+</sup>, NO<sub>3</sub><sup>-</sup> và PO<sub>4</sub><sup>3-</sup> trong nước của ao nuôi tôm.
2. Mã số: **103.02-2020.64**
3. Danh sách chủ nhiệm, thành viên tham gia thực hiện đề tài

TT	Họ và tên	Đơn vị công tác	Chức danh trong đề tài
1	Trần Nguyễn Phương Lan	Trường Bách Khoa, Đại học Cần Thơ	Chủ nhiệm đề tài
2	Ju Yi-Hsu	Trường Đại học Khoa học và Kỹ thuật Quốc gia Đài Loan	Thành viên nghiên cứu chính
3	Lương Huỳnh Vũ Thanh	Trường Bách Khoa, Đại học Cần Thơ	Thành viên nghiên cứu chính
4	Trần Thị Bích Quyên	Trường Bách Khoa, Đại học Cần Thơ	Thành viên nghiên cứu chính
5	Nguyễn Hoàng Anh	Trường Bách Khoa, Đại học Cần Thơ	Thành viên nghiên cứu chính

4. Tổ chức chủ trì: Đại học Cần Thơ

5. Thời gian thực hiện:

5.1 Theo hợp đồng: 36 tháng, từ (10/2020) đến (10/2023)

5.2 Gia hạn (nếu có): Không có

5.3 Thực hiện thực tế: 36 tháng, từ (10/2020) đến (10/2023)

6. Tổng kinh phí được phê duyệt của đề tài: **568** triệu đồng.

## **PHẦN II. NỘI DUNG VÀ KẾT QUẢ NGHIÊN CỨU**

### **1. Mục tiêu**

Đề xuất nghiên cứu liên quan đến việc tìm ra một loại vật liệu zeolite thân thiện với môi trường có đầy đủ tính năng của một vật liệu hấp phụ nhưng được sản xuất từ nguồn phế phẩm nông nghiệp rất phổ biến ở vùng Đồng bằng sông Cửu Long. Mục đích ban đầu của nghiên cứu này nhằm khẳng định lại khả năng tổng hợp zeolite NaP từ tro trấu không nung bằng phương pháp thủy nhiệt. Các yếu tố ảnh hưởng đến quá trình tổng hợp zeolite NaP như tỷ lệ  $\text{SiO}_2/\text{Al}_2\text{O}_3$ , thời gian phản ứng, nhiệt độ phản ứng và thời gian già hóa cần được nhất quán nghiên cứu. Khả năng kết hợp của zeolite NaP và vật liệu tự tính  $\text{Fe}_3\text{O}_4$  cũng sẽ được nghiên cứu nhằm cải thiện bề mặt hấp phụ của vật liệu zeolite NaP tổng hợp. Ngoài ra, nghiên cứu này sẽ so sánh tiềm năng ứng dụng của zeolite từ tính  $\text{Fe}_3\text{O}_4/\text{NaP}$  và NaP để hấp phụ một số ion  $\text{Cu}^{2+}$ ,  $\text{Pb}^{2+}$ ,  $\text{NO}_3^-$  và  $\text{PO}_4^{3-}$  trong nước giả thải và tiến đến thử nghiệm nước của ao nuôi tôm.

### **2. Nội dung và phạm vi nghiên cứu**

Căn cứ vào mục tiêu nghiên cứu được kỳ vọng, đề xuất đề tài nghiên cứu với chương trình thí nghiệm và phân tích kết quả được chia làm 3 giai đoạn được thực hiện trong 3 năm (36 tháng) như sau:

Giai đoạn 1 (năm thứ nhất): Nội dung nghiên cứu chủ yếu tập trung vào khảo sát các yếu tố ảnh hưởng đến quá trình tổng hợp zeolite NaP từ tro trấu không nung. Sau đó, các tính chất của vật liệu zeolite NaP sẽ được kiểm tra. Kết quả được mong đợi trong giai đoạn

này là tổng hợp được vật liệu NaP có diện tích bề mặt riêng lớn và có độ kết tinh cao. Đây là tiền đề cho quá trình lựa chọn điều kiện tổng hợp tối ưu cho các nghiên cứu tiếp theo.

Giai đoạn 2 (năm thứ hai): Giai đoạn này sẽ tập trung nghiên cứu quá trình tổng hợp vật liệu NaP từ tính. Các thông số ảnh hưởng đến quá trình tổng hợp hạt nano sắt từ  $\text{Fe}_3\text{O}_4$  sẽ được khảo sát như: tỷ lệ phần trăm chất hoạt động bề mặt trong dung dịch, tỷ lệ mol  $\text{FeCl}_3 \cdot 6\text{H}_2\text{O} : \text{NaBH}_4$  và thời gian phản ứng. Các yếu tố ảnh hưởng đến quá trình tạo thành  $\text{Fe}_3\text{O}_4/\text{NaP}$  cũng sẽ được khảo sát. Tính chất của vật liệu từ tính  $\text{Fe}_3\text{O}_4$  và vật liệu zeolite từ tính  $\text{Fe}_3\text{O}_4/\text{NaP}$  sẽ được đánh giá. Kết quả mong đợi trong giai đoạn này là tổng hợp được hạt  $\text{Fe}_3\text{O}_4$  có kích thước tương đối đồng đều và diện tích bề mặt riêng của zeolite  $\text{Fe}_3\text{O}_4/\text{NaP}$  lớn.

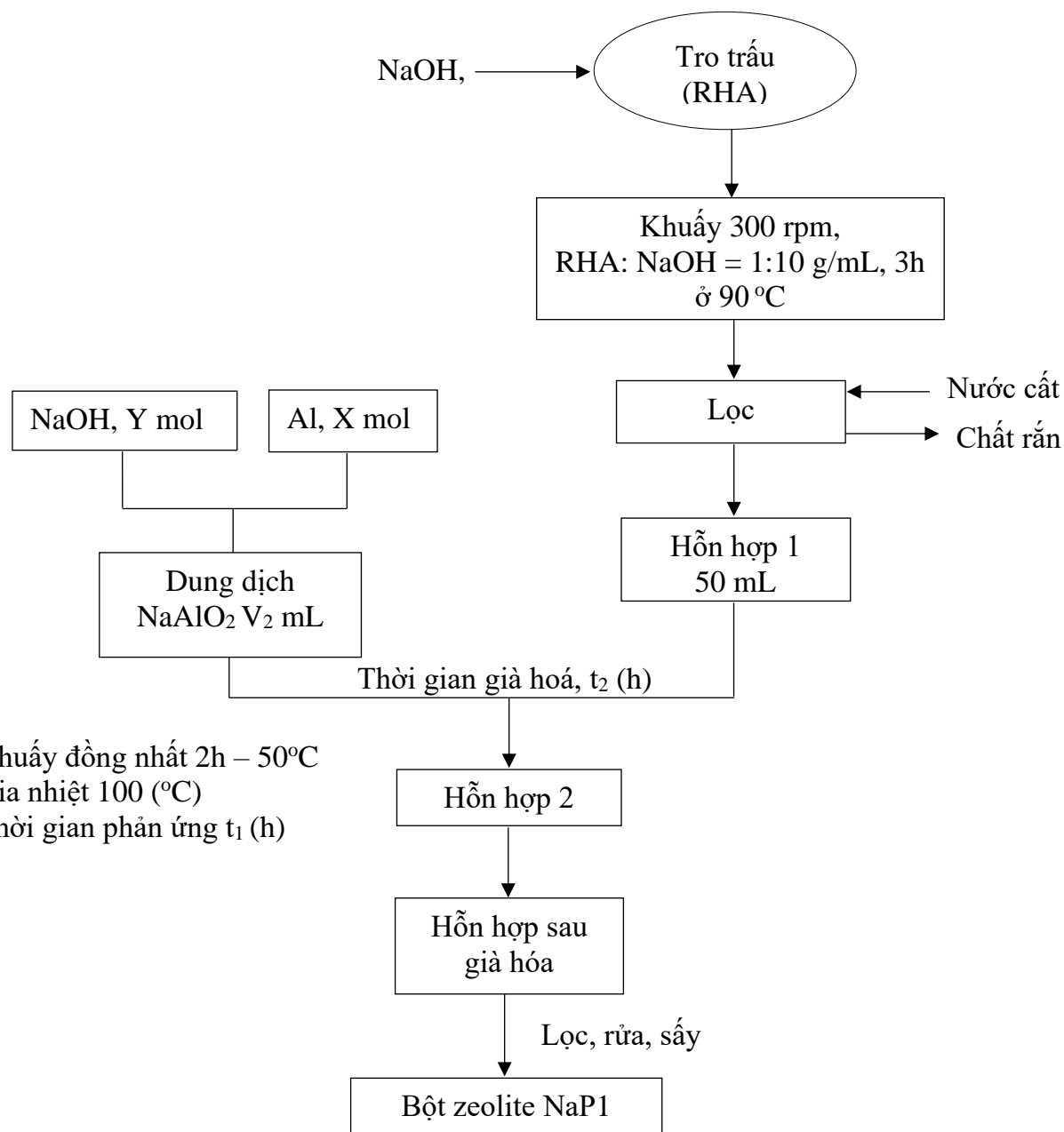
Giai đoạn 3 (năm thứ ba): Giai đoạn cuối sẽ tập trung nghiên cứu và so sánh khả năng hấp phụ một số ion trong nước của ao nuôi tôm như:  $\text{Cu}^{2+}$ ,  $\text{Pb}^{2+}$ ,  $\text{NO}_3^-$  và  $\text{PO}_4^{3-}$  của zeolite NaP và zeolite từ tính NaP/ $\text{Fe}_3\text{O}_4$ . Kết quả kỳ vọng của giai đoạn này là bộ số liệu tối ưu của quá trình hấp phụ ion của 2 vật liệu được tổng hợp, xây dựng các phương trình hấp phụ đẳng nhiệt Langmuir và Freundlich.

### 3. Cách tiếp cận và phương pháp nghiên cứu

(Mô tả chi tiết cách tiếp cận, phương pháp nghiên cứu đã thực hiện để giải quyết vấn đề đặt ra, các bước tiến hành)

Trong giai đoạn 1, các thông số về tính chất hóa của các loại oxit kim loại và cấu trúc tinh thể của silica trong RHA sẽ được xác định. Để thực hiện được những vấn đề này, các công cụ thí nghiệm mong muốn được áp dụng bao gồm các số liệu được thu thập từ phân tích phổ huỳnh quang tia X (X-Ray fluorescence (XRF), và phân tích nhiễu xạ tia X (X-Ray diffraction (XRD)). Các yếu tố ảnh hưởng đến quá trình tổng hợp zeolite NaP như tỷ lệ  $\text{SiO}_2/\text{Al}_2\text{O}_3$ , thời gian phản ứng, nhiệt độ phản ứng và thời gian già hóa sẽ được khảo sát. Kết quả của từng khảo sát sẽ được làm rõ thông qua các công cụ hỗ trợ như kính hiển vi điện tử quét (Scanning electron microscopy (SEM)), XRD, phân tích phổ tia hồng ngoại (Fourier transferred infrared (FTIR)). Ngoài ra, mẫu vật liệu zeolite tối ưu sau khi tổng hợp

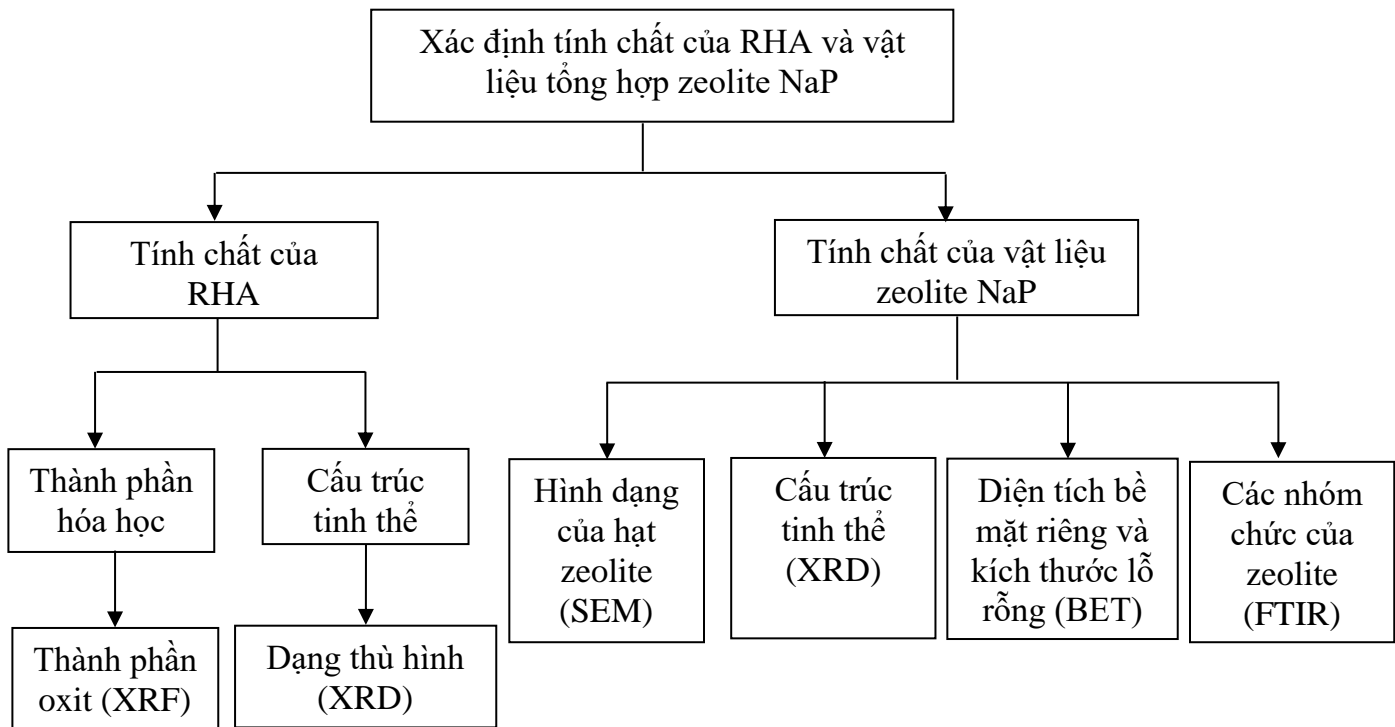
sẽ được xác định diện tích bề mặt riêng và kích thước lỗ rỗng bằng phương pháp Brunauer-Emmett-Teller (BET). Sơ đồ của quá trình tổng hợp zeolite NaP được trình bày ở Hình 5.1. Các yếu tố ảnh hưởng của quá trình tổng hợp zeolite NaP và các phương pháp xác định tính chất của RHA không nung và zeolite NaP được trình bày ở Bảng 5.1 và Hình 5.2



**Hình 5.1 Sơ đồ quy trình tổng hợp zeolite NaP1 từ RHA**

**Bảng 5.1 Thống kê thí nghiệm tổng hợp zeolite NaP từ RHA không nung sẽ được thực hiện trong nghiên cứu**

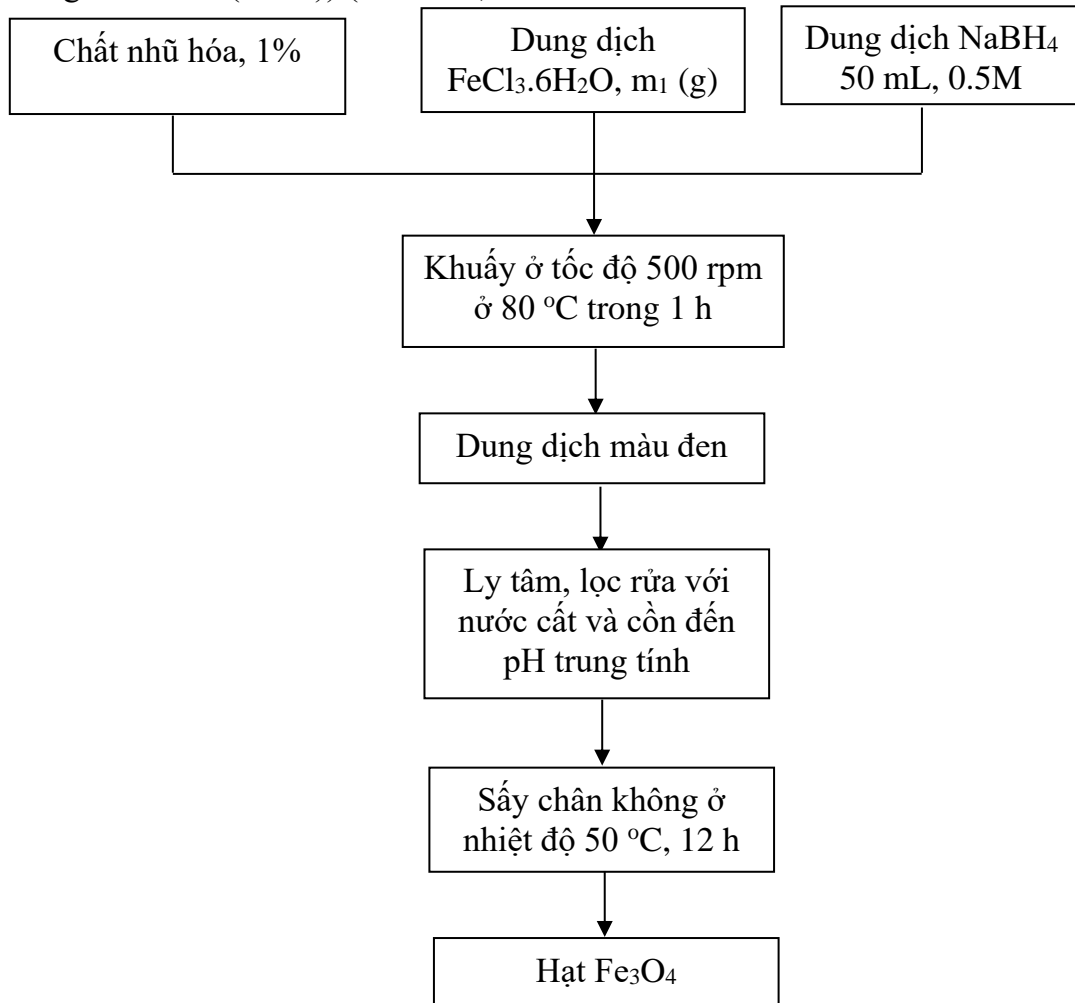
	Các yếu tố ảnh hưởng			
	SiO <sub>2</sub> /Al <sub>2</sub> O <sub>3</sub>	T (°C)	t <sub>1</sub> (h)	t <sub>2</sub> (h)
Các khoảng khảo sát dự kiến	4 - 8	50, 80, 100, 120, 150	2, 4, 6, 8, 10	0, 12, 24, 36



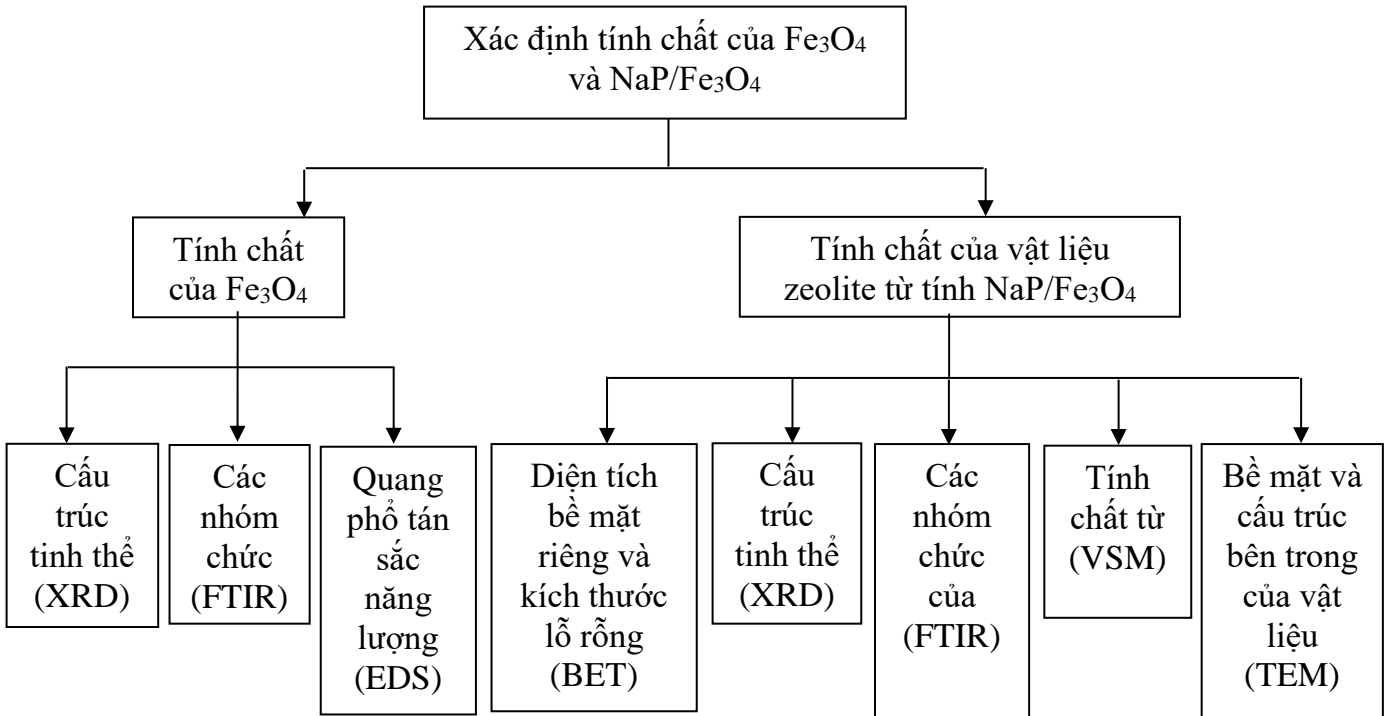
**Hình 5.2 Các phương pháp xác định tính chất của RHA và zeolite NaP1**

Trong giai đoạn 2, nghiên cứu sẽ tập trung khảo sát sự ảnh hưởng của một số chất nhũ hóa như polyvinylpyrrolidone (PVP), cetyltrimethylammonium bromide (CTAB), poly(ethylene oxide) (PEO) và sodium tripolyphosphate (STPP) đến kích thước và hình dạng của Fe<sub>3</sub>O<sub>4</sub> (Hình 5.3). Sau đó, các yếu tố ảnh hưởng đến quá trình phủ NaP lên vật liệu từ tính Fe<sub>3</sub>O<sub>4</sub> cũng được nghiên cứu như thời gian phủ và tỷ lệ của Fe<sub>3</sub>O<sub>4</sub> : NaP. Đánh giá tính chất của Fe<sub>3</sub>O<sub>4</sub> và zeolite từ tính Fe<sub>3</sub>O<sub>4</sub>/NaP sau khi tổng hợp bằng một số phương

pháp phân tích như quang phổ tán sắc năng lượng (Energy Dispersive Spectroscopy (EDS)), phân tích bề mặt và cấu trúc bên trong của vật liệu bằng kính hiển vi điện tử truyền qua (Transmission electron microscopy (TEM)) và tính chất từ bằng máy đo từ (Vibrating sample magnetometer (VSM)) (Hình 5.4).



**Hình 5.3 Quy trình tổng hợp  $\text{Fe}_3\text{O}_4$  sử dụng các loại chất nhũ hóa khác nhau**



**Hình 5.4 Các phương pháp xác định tính chất của Fe<sub>3</sub>O<sub>4</sub> và zeolite từ tính NaP/Fe<sub>3</sub>O<sub>4</sub>**

Giai đoạn 3 sẽ tập trung nghiên cứu về khả năng hấp phụ các ion Cu<sup>2+</sup>, Pb<sup>2+</sup>, NO<sub>3</sub><sup>-</sup> và PO<sub>4</sub><sup>3-</sup> của vật liệu zeolite NaP và Fe<sub>3</sub>O<sub>4</sub>/NaP. Các yếu tố ảnh hưởng đến quá trình hấp phụ như: thời gian hấp phụ, lượng chất hấp phụ, pH của dung dịch và nồng độ của các ion trong nước giả thia và nước ao nuôi tôm sẽ được khảo sát. Dung dịch sau hấp phụ sẽ được phân tích hàm lượng kim loại nặng Cu<sup>2+</sup> và Pb<sup>2+</sup>, bằng máy quang phổ hấp thu nguyên tử (Atomic Absorption Spectrophotometric (AAS)). Nồng độ ion NO<sub>3</sub><sup>-</sup> và PO<sub>4</sub><sup>3-</sup> sẽ được xác định bằng phương pháp quang phổ hấp thụ (UV-vis), lần lượt dựa trên nguyên tắc tạo phức chất có màu với sulfosalicylic acid (TCVN 6180:1996) và ammonium molybdate (TCVN 6202:2008). Dung lượng hấp phụ (q<sub>t</sub>) và hiệu suất hấp phụ (H) tính toán theo các phương trình (1) và (2):

$$\text{Dung lượng hấp phụ (mg/g)} q_t = \frac{(C_0 - C_t) \times V}{m} : (1)$$

$$\text{Hiệu suất hấp phụ (%)}: H = \frac{(C_0 - C_t)}{C_0} \times 100 : (2)$$

Trong đó: C<sub>0</sub> và C<sub>t</sub> (mg/L) lần lượt là nồng độ của các ion trước và sau quá trình hấp phụ. V (mL) là thể tích của dung dịch và m (mg) là khối lượng của NaP hoặc Fe<sub>3</sub>O<sub>4</sub>/NaP.

Ngoài ra, các phương trình hấp phụ đẳng nhiệt Langmuir (3) và Freundlich (4) cũng sẽ được thực hiện trong giai đoạn này.

$$\text{Langmuir: } \frac{1}{q_e} = \frac{1}{q_m K_L C_e} + \frac{1}{q_m} \quad (3)$$

$$\text{Freundlich: } \ln q_e = \ln K_F + \frac{1}{n} \ln C_e \quad (4)$$

Trong đó:  $q_e$  (mg/g) và  $q_m$  (mg/g) lần lượt là dung lượng hấp phụ tại thời điểm cân bằng và dung lượng hấp phụ cực đại,  $C_e$  (mg/L) là nồng độ chất bị hấp phụ lúc cân bằng,

#### 4. Kết quả nghiên cứu

(Mô tả các kết quả nghiên cứu đạt được. Đánh giá về các kết quả nghiên cứu bao gồm tính mới, giá trị khoa học, giá trị thực tiễn và khả năng ứng dụng kết quả nghiên cứu)

Đề tài được đề xuất đóng góp vào việc nghiên cứu tổng hợp các vật liệu hấp phụ từ phụ phẩm RHA, có khả năng hấp phụ hiệu quả các ion ô nhiễm trong môi trường nước. Ngoài ra, đề tài được đề xuất cũng đóng góp các án phẩm có chất lượng cao trong lĩnh vực hấp phụ.

##### (1) Xuất bản bốn bài báo khoa học đăng trên tạp chí quốc tế có trong danh mục của ISI (SCI) với tiêu đề như sau:

- (i) Facile synthesis of zeolite NaX using rice husk ash without pretreatment (Journal of the Taiwan Institute of Chemical Engineers – SCIE).
- (ii) Facile synthesis of superparamagnetic thiamine/Fe<sub>3</sub>O<sub>4</sub> with enhanced adsorptivity toward divalent copper ions (Chemosphere – SCIE).
- (iii) Studies on the performance of functionalized Fe<sub>3</sub>O<sub>4</sub> as phosphate adsorbent and assessment to its environmental compatibility (Journal of the Taiwan Institute of Chemical Engineers – SCIE).
- (iv) Evaluation of the potential removal of phosphate using rice husk ash-derived zeolite NaP1 (Journal of Chemical Technology & Biotechnology – SCIE).

##### (2) Xuất bản hai bài báo khoa học đăng trên tạp chí trong nước:

(i) Xử lý methylene blue bằng zeolite NaX với silica có nguồn gốc từ tro trấu (Tạp chí Khoa học và Công nghệ Việt Nam).

(ii) Tổng hợp vật liệu composite NaX/Fe<sub>3</sub>O<sub>4</sub> và đánh giá khả năng hấp phụ nitrate (Tạp chí Khoa học và Công nghệ Đại học Thái Nguyên).

**(3) Công bố một báo cáo tại hội thảo quốc tế.**

### **PHẦN III. KẾT QUẢ CÔNG BỐ VÀ ĐÀO TẠO**

#### **1. Kết quả công bố**

STT	Công trình khoa học	ISSN/ ISBN	Tình trạng (Đã in/chấp nhận đăng)
1	<b>Công trình công bố quốc tế trên tạp chí thuộc danh mục ISI</b>		
1.1	Phuong Lan Tran-Nguyen, Kim-Phung Ly, Luong Huynh Vu Thanh, Artik Elisa Angkawijaya, Shella Permatasari Santoso, Nguyen-Phuong-Dung Tran, Meng-Lin Tsai, Yi-Hsu Ju, “Facile synthesis of zeolite NaX using rice husk ash without pretreatment”, Journal of the Taiwan Institute of Chemical Engineers, vol. 123, pp. 338-345, 2021, SCIE. <a href="https://doi.org/10.1016/j.jtice.2021.05.009">https://doi.org/10.1016/j.jtice.2021.05.009</a>	1876-1070	Đã in
1.2	Phuong Lan Tran-Nguyen, Artik Elisa Angkawijaya, Quoc Nam Ha, Yen Nhi Tran Chuong, Alchris Woo Go, Vania Bundjaja, Chintya Gunarto, Shella Permatasari Santoso, Yi-Hsu Ju, “Facile synthesis of superparamagnetic thiamine/Fe <sub>3</sub> O <sub>4</sub> with enhanced adsorptivity toward	0045-6535	Đã in

	divalent copper ions”, Chemosphere, vol. 291, 132759, 2021, SCIE.  <a href="https://doi.org/10.1016/j.chemosphere.2021.132759">https://doi.org/10.1016/j.chemosphere.2021.132759</a>		
1.3	Artik Elisa Angkawijaya, Yen Nhi Tran-Chuong, Quoc Nam Ha, Phuong Lan Tran-Nguyen, Shella Permatasari Santoso, Vania Bundjaja, Alchris Woo Go, Hsien-Yi Hsu, Yi-Hsu Ju, “Studies on the performance of functionalized Fe <sub>3</sub> O <sub>4</sub> as phosphate adsorbent and assessment to its environmental compatibility”, Journal of the Taiwan Institute of Chemical Engineers, vol. 131, 104162, 2022, SCIE.  <a href="https://doi.org/10.1016/j.jtice.2021.104162">https://doi.org/10.1016/j.jtice.2021.104162</a>	1876-1070	Đã in
1.4	Phuong Lan Tran-Nguyen, Kim-Phung Ly, Thanh-Ty Nguyen, Shella Permatasari Santoso, Nguyen-Phuong-Dung Tran, Artik Elisa Angkawijaya, Maria Yuliana, Minh-Nhut Nguyen, Tuan Thi-Tran-Anh, “Evaluation of the potential removal of phosphate using rice husk ash-derived zeolite NaP1”, vol. 98, no. 6, pp. 1465-1477, 2023, SCIE.  <a href="https://doi.org/10.1002/jctb.7365">https://doi.org/10.1002/jctb.7365</a>	0268-2575	Đã in
2	Công trình công bố quốc tế trên tạp chí không thuộc ISI		
3	Công trình công bố trên tạp chí khoa học chuyên ngành trong nước		

3.1	Trần Nguyễn Phương Lan, Lý Kim Phụng, Lương Huỳnh Vũ Thanh, Nguyễn Hồng Nam, Trần Thị Bích Quyên, Lê Phan Hưng, “Xử lý methylene blue bằng zeolite NaX với silica có nguồn gốc từ tro trâu”, Tạp chí Khoa học và Công nghệ Việt Nam 64(6), trang 14-18, 2022. <a href="https://doi.org/10.31276/VJST.64(6).14-18">https://doi.org/10.31276/VJST.64(6).14-18</a>	1859-4794	Đã in
3.2	Trần Nguyễn Phương Lan, Lý Kim Phụng, Nguyễn Thanh Tỷ, Nguyễn Minh Nhựt, Trần Thị Bích Quyên, Dương Thị Mỹ Tuyên, Đoàn Văn Hồng Thiện, “Tổng hợp vật liệu composite NaX/Fe <sub>3</sub> O <sub>4</sub> và đánh giá khả năng hấp phụ nitrate”, Tạp chí Khoa học và Công nghệ Đại học Thái Nguyên 228(02), trang 166-174, 2023. <a href="https://doi.org/10.34238/tnu-jst.7145">https://doi.org/10.34238/tnu-jst.7145</a>	1859-2171	Đã in
3.3	Luong Huynh Vu Thanh, Dao Lam Gia Hao, Phan Thi Diem Trang, Pham Minh Tien, Tran Thi Bich Quyen, Dang Huynh Giao, Tran Nguyen Phuong Lan. Green and facile synthesis of Fe <sub>3</sub> O <sub>4</sub> nanoparticles using the <i>Citrus aurantifolia</i> fruit juice associated with NaBH <sub>4</sub> and its adsorption of Cr(VI) in aqueous solution. Vietnam Journal of Catalysis and Adsorption, 10 (4), trang 90-100, 2021. <a href="https://doi.org/10.51316/jca.2021.074">https://doi.org/10.51316/jca.2021.074</a>	0866-7411	Đã in
3.4	Tran Nguyen Phuong Lan, Nguyen Thanh Ty, Ly Kim Phung, Hong Nam Nguyen, Cao Thi Xuan	0866-7411	Được chấp nhận

	Vy, Huynh Quoc Khanh, Tran Thi Bich Quyen. Removal of ion Cu <sup>2+</sup> and Pb <sup>2+</sup> using zeolite NaP1 with the silica source utilized from rice husk ash Vietnam Journal of Catalysis and Adsorption.		
4	Báo cáo khoa học đăng ký yêu hội nghị quốc tế		
4.1	Phuong Lan Tran-Nguyen, Kim-Phung Ly, Xuan Vy Cao-Thi, Minh-Tien Pham, Duc-Duy Le, Tran Thi Minh Thu, Nguyen Thi Nhu Y, The removal of phosphate using NaP/Chitosan composite, International Conference on Environmental Engineering and Renewable Energy (ICENVERE-23), Taipei, Taiwan, June 23 <sup>rd</sup> – 24 <sup>th</sup> , 2023.		Đã in

### **Tổng hợp kết quả công bố ISI:**

- Số bài báo ISI đề tài đăng ký: 02
- Số bài báo ISI đề tài đã được công bố/chấp nhận công bố: 04

### **Ghi chú:**

- Gửi kèm toàn văn các công bố trên tạp chí, hội nghị; sách chuyên khảo.
- Cột công trình khoa học:
  - o Liệt kê các bài báo đăng trên tạp chí theo thứ tự <*tên tác giả, tên công trình, tên tạp chí/nhà xuất bản, số phát hành, năm phát hành, trang đăng công trình, mã công trình đăng tạp chí/sách chuyên khảo (DOI), loại tạp chí ISI (SCI/SCIE)*>
  - o Liệt kê các bài báo đăng tại hội nghị theo thứ tự <*tên tác giả, tên công trình, tên hội nghị, địa điểm tổ chức, năm phát hành, trang đăng công trình*>

## **2. Kết quả đào tạo**

STT	Họ và tên	Thời gian tham gia đề tài (số tháng)	Công trình công bố
Học viên cao học			
1	Phạm Minh Tiên	12	Phuong Lan Tran-Nguyen, Kim-Phung Ly, Xuan Vy Cao-Thi, Minh-Tien Pham, Duc-Duy Le, Tran Thi Minh Thu, Nguyen Thi Nhu Y, The removal of phosphate using NaP/Chitosan composite, International Conference on Environmental Engineering and Renewable Energy (ICENVERE-23), Taipei, Taiwan, June 23 <sup>rd</sup> – 24 <sup>th</sup> , 2023.

**Ghi chú:**

- Gửi kèm bản photo trang bìa luận án/luận văn và bằng hoặc giấy chứng nhận nghiên cứu sinh/thạc sỹ nếu học viên đã bảo vệ thành công luận án/luận văn;
- Cột công trình công bố ghi như mục III.1.

#### **PHẦN IV. TÌNH HÌNH SỬ DỤNG KINH PHÍ**

*(Chi tiết sử dụng kinh phí theo phụ lục 1)*

STT	Nội dung chi	Kinh phí được duyệt (triệu đồng)	Kinh phí thực hiện (triệu đồng)	Ghi chú
A	Chi phí trực tiếp	539.6	539.6	
1	Nhân công lao động khoa học	539.454	539.454	
2	Nguyên, nhiên vật liệu			

3	Thiết bị, dụng cụ			
4	Đi lại, công tác phí			
5	Dịch vụ thuê ngoài			
6	Chi phí trực tiếp khác	0.1455	0.1455	
<b>B</b>	<i>Chi phí gián tiếp</i>	28.4	28.4	
1	Chi phí quản lý của tổ chức chủ trì	28.4	28.4	
	<b>Tổng số:</b>	568	568	

## PHẦN V. KIẾN NGHỊ

(Về phát triển các kết quả nghiên cứu của đề tài; về quản lý, tổ chức thực hiện ở các cấp)

Cần Thơ, ngày 28 tháng 08 năm 2023

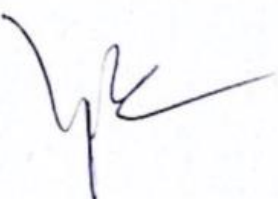
**Tổ chức chủ trì đề tài**

(Thủ trưởng đơn vị ký tên, đóng dấu)

**Chủ nhiệm đề tài**

(Họ tên, chữ ký)



  
Tran Nguyen Phuong Lan

BỘ KHOA HỌC VÀ CÔNG NGHỆ  
QUỸ PHÁT TRIỂN KHOA HỌC VÀ CÔNG NGHỆ QUỐC GIA



---

**PHỤ LỤC**  
**BÁO CÁO TỔNG HỢP**

**KẾT QUẢ THỰC HIỆN ĐỀ TÀI NGHIÊN CỨU CƠ BẢN  
TRONG KHOA HỌC TỰ NHIÊN**

Tên đề tài: Nghiên cứu tổng hợp vật liệu zeolite từ tính  $\text{Fe}_3\text{O}_4/\text{NaP}$  có nguồn gốc từ tro trấu không nung và ứng dụng hấp phụ ion ion  $\text{Cu}^{2+}$ ,  $\text{Pb}^{2+}$ ,  $\text{NO}_3^-$  và  $\text{PO}_4^{3-}$  trong nước của ao nuôi tôm

Mã số đề tài: 103.02-2020.64

Chủ nhiệm đề tài: TS. Trần Nguyễn Phương Lan

Thành viên chính: GS. TS. Ju Yi-Hsu

TS. Lương Huỳnh Vũ Thanh

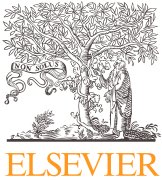
TS. Trần Thị Bích Quyên

Thư ký khoa học: TS. Nguyễn Hoàng Anh

## DANH MỤC BÀI BÁO KHOA HỌC

STT	Công trình khoa học	ISSN/ ISBN	Tình trạng
1	Công trình công bố quốc tế trên tạp chí thuộc danh mục ISI		
1.1	Phuong Lan Tran-Nguyen, Kim-Phung Ly, Luong Huynh Vu Thanh, Artik Elisa Angkawijaya, Shella Permatasari Santoso, Nguyen-Phuong-Dung Tran, Meng-Lin Tsai, Yi-Hsu Ju, “Facile synthesis of zeolite NaX using rice husk ash without pretreatment”, Journal of the Taiwan Institute of Chemical Engineers, vol. 123, pp. 338-345, 2021, SCIE.	1876-1070	Đã in
1.2	Phuong Lan Tran-Nguyen, Artik Elisa Angkawijaya, Quoc Nam Ha, Yen Nhi Tran Chuong, Alchris Woo Go, Vania Bundjaja, Chintya Gunarto, Shella Permatasari Santoso, Yi-Hsu Ju, “Facile synthesis of superparamagnetic thiamine/Fe <sub>3</sub> O <sub>4</sub> with enhanced adsorptivity toward divalent copper ions”, Chemosphere, vol. 291, 132759, 2021, SCIE.	0045-6535	Đã in
1.3	Artik Elisa Angkawijaya, Yen Nhi Tran-Chuong, Quoc Nam Ha, Phuong Lan Tran-Nguyen, Shella Permatasari Santoso, Vania Bundjaja, Alchris Woo Go, Hsien-Yi Hsue, Yi-Hsu Ju, “Studies on the performance of functionalized Fe <sub>3</sub> O <sub>4</sub> as phosphate adsorbent and assessment to its environmental compatibility”, Journal of the Taiwan Institute of Chemical Engineers, vol. 131, 104162, 2022, SCIE.	1876-1070	Đã in
1.4	Phuong Lan Tran-Nguyen, Kim-Phung Ly, Thanh-Ty Nguyen, Shella Permatasari Santoso, Nguyen-Phuong-Dung Tran, Artik	0268-2575	Đã in

	Elisa Angkawijaya, Maria Yuliana, Minh-Nhut Nguyen, Tuan Thi-Tran-Anh, “Evaluation of the potential removal of phosphate using rice husk ash-derived zeolite NaP1”, vol. 98, no. 6, pp. 1465-1477, 2023, SCIE.		
2	Công trình công bố quốc tế trên tạp chí không thuộc danh mục ISI		
3	Công trình công bố trên tạp chí khoa học chuyên ngành trong nước		
3.1	Trần Nguyễn Phương Lan, Lý Kim Phụng, Lương Huỳnh Vũ Thanh, Nguyễn Hồng Nam, Trần Thị Bích Quyên, Lê Phan Hưng, “Xử lý methylene blue bằng zeolite NaX với silica có nguồn gốc từ tro trấu”, Tạp chí Khoa học và Công nghệ Việt Nam 64(6), trang 14-18, 2022.	1859-4794	Đã in
3.2	Trần Nguyễn Phương Lan, Lý Kim Phụng, Nguyễn Thanh Tỷ, Nguyễn Minh Nhựt, Trần Thị Bích Quyên, Dương Thị Mỹ Tuyên, Đoàn Văn Hồng Thiện, “Tổng hợp vật liệu composite NaX/Fe <sub>3</sub> O <sub>4</sub> và đánh giá khả năng hấp phụ nitrate”, Tạp chí Khoa học và Công nghệ Đại học Thái Nguyên 228(02), trang 166-174, 2023.	1859-2171	Đã in
4	Báo cáo khoa học đăng ký yếu hội nghị quốc tế		
4.1	Phuong Lan Tran-Nguyen, Kim-Phung Ly, Xuan Vy Cao-Thi, Minh-Tien Pham, Duc-Duy Le, Tran Thi Minh Thu, Nguyen Thi Nhu Y, The removal of phosphate using NaP/Chitosan composite, International Conference on Environmental Engineering and Renewable Energy (ICENVERE-23), Taipei, Taiwan, June 23 <sup>rd</sup> – 24 <sup>th</sup> , 2023.		Đã in



## Facile synthesis of zeolite NaX using rice husk ash without pretreatment



Phuong Lan Tran-Nguyen<sup>a,\*</sup>, Kim-Phung Ly<sup>b</sup>, Luong Huynh Vu Thanh<sup>b</sup>, Artik Elisa Angkawijaya<sup>c</sup>, Shella Permatasari Santoso<sup>d</sup>, Nguyen-Phuong-Dung Tran<sup>e</sup>, Meng-Lin Tsai<sup>e</sup>, Yi-Hsu Ju<sup>c,f</sup>

<sup>a</sup> Department of Mechanical Engineering, Can Tho University, Campus II, 3/2 street, Can Tho city 900100, Vietnam

<sup>b</sup> Department of Chemical Engineering, Can Tho University, Campus II, 3/2 street, Can Tho city 900100, Vietnam

<sup>c</sup> Graduate Institute of Applied Science and Technology, National Taiwan University of Science and Technology, #43, Sec. 4, Keelung Rd., Taipei 10607, Taiwan

<sup>d</sup> Department of Chemical Engineering, Widya Mandala Surabaya Catholic University, Kalijudan 37, Surabaya 60133, Indonesia

<sup>e</sup> Department of Materials Science and Engineering, National Taiwan University of Science and Technology, #43, Sec. 4, Keelung Rd., Taipei 10607, Taiwan

<sup>f</sup> Department of Chemical Engineering, National Taiwan University of Science and Technology, 43 Keelung Rd. Sec. 4, Taipei 10607, Taiwan

### ARTICLE INFO

#### Article History:

Received 19 February 2021

Revised 29 April 2021

Accepted 9 May 2021

Available online 25 May 2021

#### Keywords:

Rice husk ash

Zeolite NaX

Aging time

Energy and time saving integrated process

### ABSTRACT

Rice husk ash (RHA) is an abundant agricultural waste in Mekong Delta, Vietnam. The utilization of RHA for zeolites production has been widely studied by pretreating RHA before reaction. In this study, zeolite NaX was synthesized directly using RHA without any pretreatment. Key parameters including molar ratios of SiO<sub>2</sub> to Al<sub>2</sub>O<sub>3</sub> and Na<sub>2</sub>O to Al<sub>2</sub>O<sub>3</sub>, reaction time, and aging time were investigated. The results showed that the optimal conditions for the synthesis of zeolite NaX are: molar ratio of SiO<sub>2</sub>/Al<sub>2</sub>O<sub>3</sub> = 4, molar ratio of Na<sub>2</sub>O/Al<sub>2</sub>O<sub>3</sub> = 10, reaction time = 4 h, and without aging. Zeolite NaX with a specific surface area of 388 m<sup>2</sup>/g and a pore diameter of 12.37 Å was obtained, which were comparable to the published data. The method developed in this work is an energy and time saving, integrated, and environmental friendly process. It has the potential to be applied for synthesizing other types of zeolite.

© 2021 Taiwan Institute of Chemical Engineers. Published by Elsevier B.V. All rights reserved.

## 1. Introduction

Zeolites are inorganic materials with regular microporous structure which have been widely developed and used in many applications [1,2]. The structure of zeolite consists of the network of tetrahedral [SiO<sub>4</sub>]<sup>4-</sup> and [AlO<sub>4</sub>]<sup>5-</sup> [1]. These tetrahedrons are linked through oxygen-spherical bonds to form an open structure with empty holes [2]. Many types of zeolite such as zeolite X, A, P1, Y or ZSM-5 have been successfully synthesized from commercial silica sources or wastes with high silica content [1,3–6]. Zeolite X which belongs to the faujasite (FAU) family with large pore size (about 8 Å) [1] possessed special properties in the adsorption of heavy metals, gas or organic wastes [1,7–8]. Zeolite X has been synthesized using silica sources such as kaolin [2], bauxite [1], diatomite [9], bagasse fly ash [10], coal fly ash [11], and RHA [4,12].

RHA, an agricultural waste, can cause serious environmental pollution [13]. Mekong Delta is the major agricultural center of Vietnam which produces tens of million ton of rice annually [14]. Rice husks are often used as fuel, partially replacing coal and gas [13]. A small portion of RHA, the residue of burning rice husk, is used as organic fertilizer, light concrete, or activated carbon [15]. However,

the amount of rice husk is huge and the main treatment is usually burning or landfilling [13]. These treatment methods cause greenhouse gas emissions, air pollution, and consume large areas for landfilling [13]. Meanwhile, RHA is well-known as a rich source of silica (about 90%) [16] and is an excellent source for the synthesis of zeolite, silica and cordierite [4,17,18]. Zeolite synthesis from RHA [11,13] opens a new route in alleviating environmental pollution caused by RHA.

In previous studies for producing zeolite NaX, RHA required calcination or chemical pretreatment before reaction [4,12,19]. Meanwhile, the processes involved were complicate, energy and time consuming and low economic efficiency [4,5,12,20]. There were some reports on the synthesis of zeolite NaX using untreated RHA but the reaction time required was quite long [21,22]. In addition, previous studies have not given the full evaluation on the important factors that affected the synthesis of zeolite NaX from the RHA without calcination. In this study, the effects molar ratios of SiO<sub>2</sub>/Al<sub>2</sub>O<sub>3</sub> and Na<sub>2</sub>O/Al<sub>2</sub>O<sub>3</sub>, reaction time and aging time on the final zeolite product were carefully investigated under mild conditions and shorter reaction time. The mechanism of the formation of NaX was also proposed. RHA and zeolite products were characterized by X-ray diffraction (XRD), field emission scanning electron microscopy (FESEM), dynamic light scattering (DLS), Brunauer - Emmett - Teller (BET), and X-ray fluorescence (XRF).

\* Corresponding author.

E-mail address: [tnplan@ctu.edu.vn](mailto:tnplan@ctu.edu.vn) (P.L. Tran-Nguyen).

## 2. Experimental

### 2.1. Raw materials

RHA was collected from Nam Tien Joint Stock Company, Tra Noc Industrial Park, Can Tho City, Vietnam. The collected ash was directly used for the zeolite synthesis. Other chemicals such as sodium hydroxide pellets and aluminum powder (purity 99%, Union Chemical Industry Company Ltd.) were obtained from commercial sources.

### 2.2. Synthesis of zeolite NaX

The synthesis procedure of zeolite NaX, based on previous studies with some modifications, is depicted in Fig. 1 [2,22]. RHA and NaOH solution (5 M) were placed in a round bottom flask and stirred at 300 rpm and 90°C for 3 h with a certain solid/liquid ratio [23]. A refluxed condenser was applied during the reaction. After the reaction, the products were collected and filtered to separate the aqueous fraction, mainly sodium silicate, from the solid fraction. NaAlO<sub>2</sub> solution was prepared by dissolving aluminum powder in NaOH solution according to the required molar ratio. Then, the prepared NaAlO<sub>2</sub> solution was gradually added to the aqueous fraction at 50°C and vigorously stirred for 2 h. After obtaining a homogeneous gel mixture, the mixture was heated to 90°C and kept for certain time T<sub>1</sub> (h). Then, the supernatant was aged at T<sub>2</sub> (h). The precipitate was then collected by filtration, centrifuged and dried at 100°C until constant weight to obtain the zeolite NaX powder. Each data was the results of triplicate experiments.

### 2.3. Characterization

The zeolite NaX products were characterized by using XRD, BET, FE-SEM, DLS and XRF while the composition of RHA was analyzed by using XRF and TGA. XRD was performed on a D8 Advance instrument (Bruker), with an X-ray diffractometer using CuK radiation ( $\lambda = 1.54056 \text{ \AA}$ ) scanned at 7.0000 degree/min, an applied current of 30 mA and an accelerating voltage of 40 kV. FE-SEM measurement was taken with a Hitachi S-4800 scanning electron microscope. DLS from SZ-100 (Horiba) was used to determine the size distribution profile of NaX. The analysis of major and trace elements in RHA and the synthesized NaX was processed by using XRF (S8 TIGER Series 2, Bruker). TGA was also performed by using a thermogravimetric analyzer (Pyris Diamond TG-DTA, PerkinElmer Instrument, USA). BET was applied for determining the specific surface area and the pore diameter of the synthesized NaX. The sample was dried for 16 h at 105°C before being analyzed with a Nova 2000 (Quantachrome Instruments, USA).

## 3. Results and discussion

XRD was used to determine the polymorphism of SiO<sub>2</sub> in the untreated RHA [5]. Fig. 2a shows that only a broad peak of SiO<sub>2</sub> appeared at  $2\theta = 22^\circ$ , indicating amorphous form of silica [5]. The amorphous SiO<sub>2</sub> dominated in the untreated RHA, so it was a potential material for zeolite synthesis [15]. Moreover, XRF result showed that silica accounts for > 95% of the RHA (Table 1). The total weight loss from room temperature to 800°C was about 1.5% (Fig. 2b). Very

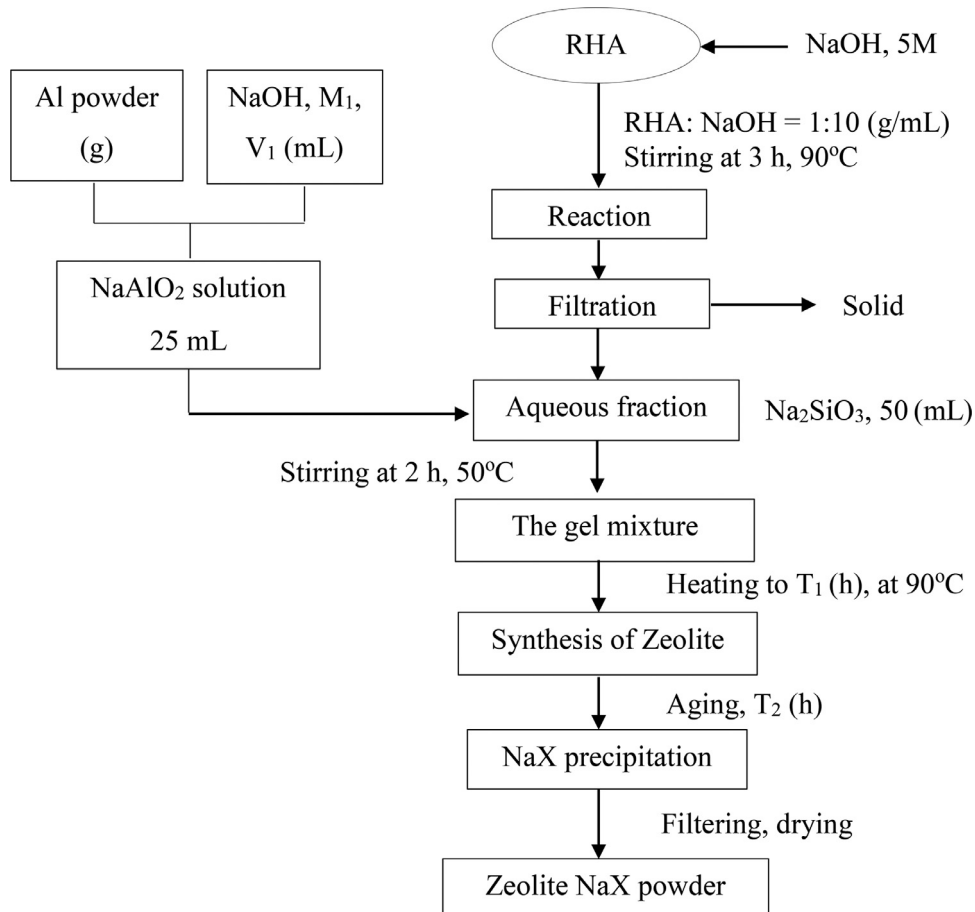


**Fig. 1.** Flowchart of zeolite NaX synthesis process.

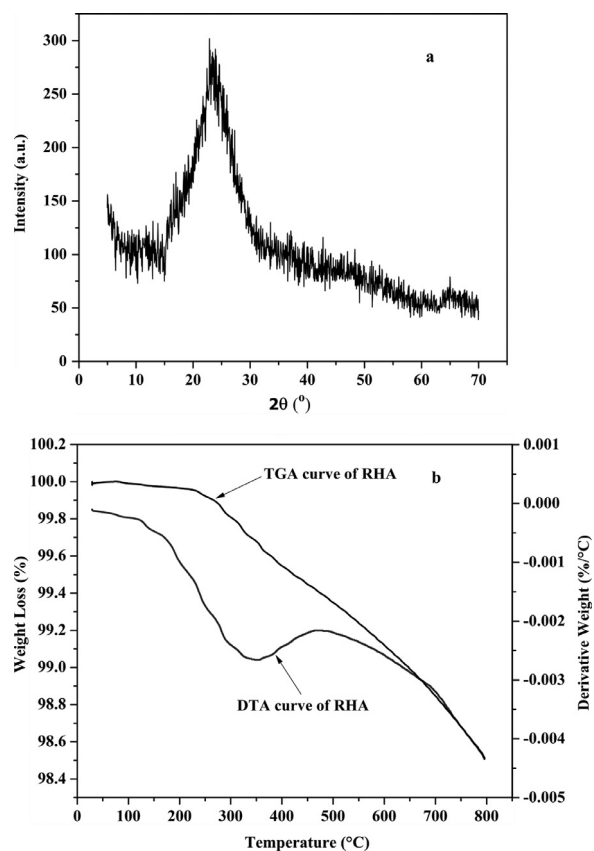


**Fig. 2.** XRD pattern of silica from RHA and thermogravimetric curve of RHA.

**Table 1**  
Chemical composition of RHA used in this study.

Elements	Content (%)
SiO <sub>2</sub>	96.11
K <sub>2</sub> O	1.47
Al <sub>2</sub> O <sub>3</sub>	1.16
CaO	0.48
P <sub>2</sub> O <sub>5</sub>	0.2
MnO	0.19
Fe <sub>2</sub> O <sub>3</sub>	0.15
Na <sub>2</sub> O	0.11
SO <sub>3</sub>	0.03
Sb <sub>2</sub> O <sub>3</sub>	0.03
CdO	0.02
SnO <sub>2</sub>	0.02
ZnO	0.02
BaO	0.01
SrO	0.01
Ta <sub>2</sub> O <sub>5</sub>	0.01

little weight loss between 100 and 200°C was observed due to the removal of adsorbed water on the surface of particles. Some organic matter may be retained in RHA [24]. From 200 to 600°C, a more rapid weight loss was observed owing to decomposition of organic matter which was also reported by Fernandes et al. [25].

It was reported that 90°C is the suitable reaction temperature for zeolite X synthesis [2,12,26–29], so 90°C was used in this study. To better understand the formation of zeolite X [30,31], a reaction mechanism was proposed in Fig. 3. The mechanism could be described as follows: the precursor sources are firstly dissolved to form silica and alumina tetrahedra. The two tetrahedra are combined to form gel aluminosilicate, followed by formation of secondary structures such as sodalite cages and double six member-rings (D6R) in the presence of OH<sup>-</sup>. The secondary structures then combine to create crystal

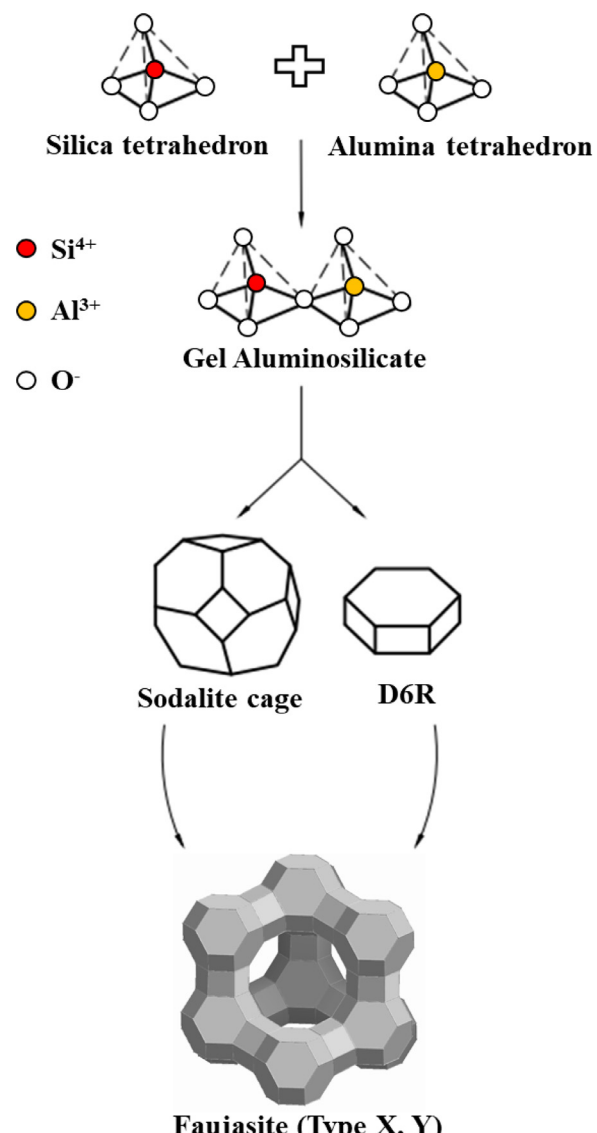


**Fig. 3.** The proposed mechanism of zeolite NaX formation.

seeds, which enter the growth phase influenced by reaction time and temperature. Finally, the complete crystals of zeolite X are found.

### 3.1. Effect of SiO<sub>2</sub>/Al<sub>2</sub>O<sub>3</sub>

Zeolites were synthesized at SiO<sub>2</sub>/Al<sub>2</sub>O<sub>3</sub> molar ratios from 2.0 to 4.5 with the other reaction conditions fixed (Fig. 4). The main peaks in XRD patterns of the synthesized zeolite were compared with the standard peaks of NaA, NaX and NAP1 (JCPDS card No. 38-0237, JCPDS card No. 43-0142 and JCPDS card No. 39-0219, respectively). In Fig. 4a, a single phase zeolite NaA was formed at SiO<sub>2</sub>/Al<sub>2</sub>O<sub>3</sub> = 2.0. When this ratio was increased to 2.5 (Fig. 4b), all peaks of zeolite NaA decreased and peaks of zeolite NaX appeared with low intensity. Al-Jubouri et al. successfully synthesized pure zeolite NaA at SiO<sub>2</sub>/Al<sub>2</sub>O<sub>3</sub> between 1.0 and 2.0 and obtained formation of zeolite X at a ratio > 2.0 [32]. In fact, as this ratio was increased from 3.0 to 4.0 (Fig. 4c–4h), a significant increase of zeolite NaX peaks intensity and decrease peaks intensity of zeolite NaA, which completely disappeared at a ratio of 4.0.

At ratios of 3.0 and 3.125, alternating formation of zeolite NaA and NaX was observed. More zeolite NaA was formed at a ratio of 3.0 while the main peak of zeolite NaX was found at a ratio of 3.125 with the coexistence of zeolite NaA. This result agrees with those reported in

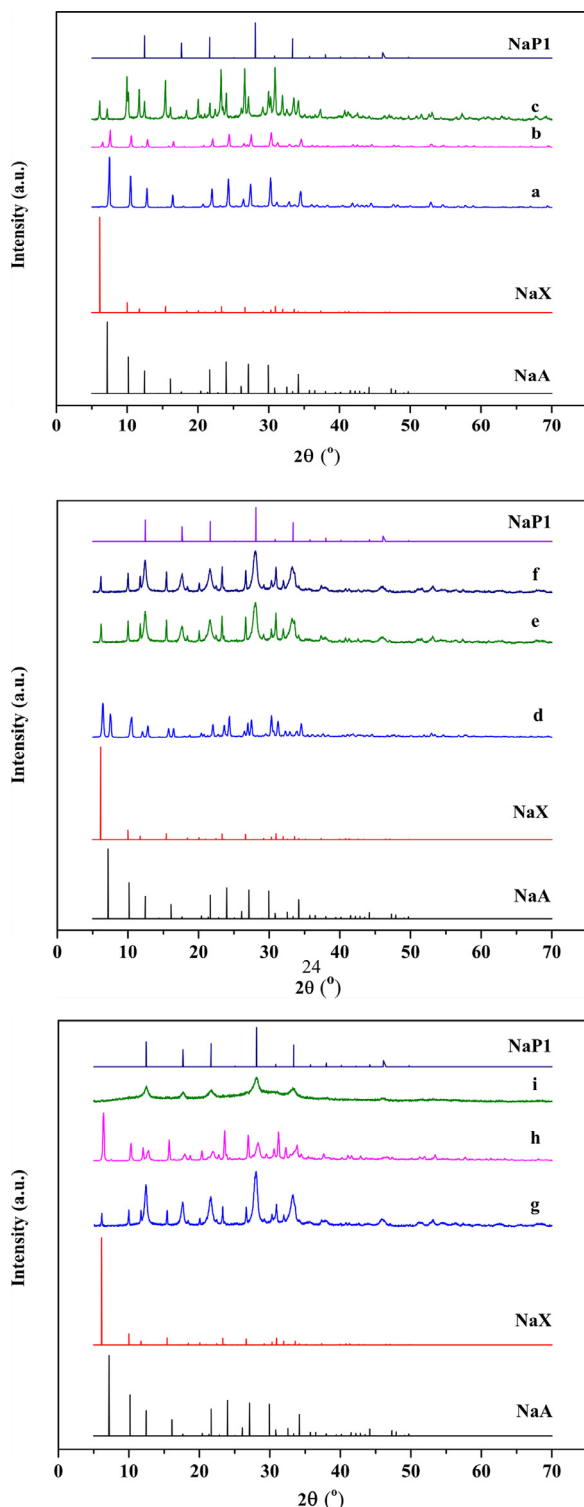


**Fig. 4.** XRD patterns at different molar ratios of  $\text{SiO}_2/\text{Al}_2\text{O}_3$  and the standard of zeolite NaA, NaX and NaP1. (a) 2.0, (b) 2.5, (c) 3.0, (d) 3.125, (e) 3.25, (f) 3.5, (g) 3.75, (h) 4.0, and (i) 4.5.

literature when the ratio used was above 2.5 [28,33,34]. An increase of this ratio resulted in a decrease of NaA and the appearance of NaX [28]. Between the ratio of 3.25 - 4.0, the peak of NaA almost completely disappeared because the significant decrease in the solubility of  $\text{Si}^{4+}$  ions as  $\text{Al}^{3+}$  ion concentration was increased. The low concentrations of  $\text{Si}^{4+}$  ions favored the formation of structure such as double four member-ring (D4R); thus, zeolite A usually appeared at low  $\text{SiO}_2/\text{Al}_2\text{O}_3$

ratio [4,28]. It was reported that  $\text{SiO}_2/\text{Al}_2\text{O}_3$  ratio for the synthesis of zeolite NaA should be  $< 3.0$  [32,35]. Alternating peaks of zeolite NaX and NaP1 were observed at a ratio of 3.25 and NaX with high intensity can be found at ratio  $> 3.5$ . Besides the predominant formation of zeolite NaX, the sample still contained a little zeolite NaP1. Similar results of NaX at a ratio of 4.0 using different feedstock were reported [3,36]. The tendency to form zeolite NaP1 when increasing this ratio was also mentioned previously [29,37]. At a ratio of 4.3, NaX was the dominant zeolite [37]. At ratio between 3.0 and 4.8, the products contained NaA, NaX and NaP1 [38].

As  $\text{SiO}_2/\text{Al}_2\text{O}_3$  ratio was increased to 4.5 (Fig. 4i), zeolite NaP1 peaks started to appear. Similar trend was reported by Hildebrandt et al. (2014) [39]. The formation of NaP1 was more significant when changing this molar ratio and a decrease of Al used favored the formation of zeolite NaP1 [36,40]. The control of the  $\text{SiO}_2/\text{Al}_2\text{O}_3$  molar ratio was crucial to achieve single-phase zeolite NaX. A ratio of 4.0 was chosen to achieve NaX zeolite crystallized with high intensity.

### 3.2. Effect of $\text{Na}_2\text{O}/\text{Al}_2\text{O}_3$

Previous studies reported different results in the synthesis of zeolite X when changing  $\text{Na}_2\text{O}/\text{Al}_2\text{O}_3$  ratio [33,41,42]. In this study,  $\text{Na}_2\text{O}/\text{Al}_2\text{O}_3$  ratios from 2.0 to 12 were investigated (Fig. 5). At a ratio of 2.0, only amorphous phase was found. When this ratio was increased to 8.0, the peaks of zeolite NaX and NaP1 appeared with NaX as the dominant phase. To eliminate zeolite NaP1,  $\text{Na}_2\text{O}/\text{Al}_2\text{O}_3$  ratio was increased to 10.0. At a ratio of 10.0, the peaks of zeolite NaX and NaP1 appeared with NaX as the dominant phase. To eliminate zeolite NaP1,  $\text{Na}_2\text{O}/\text{Al}_2\text{O}_3$  ratio was increased to 12.0. At a ratio of 12.0, the peaks of zeolite NaX and NaP1 disappeared and only NaA was found.

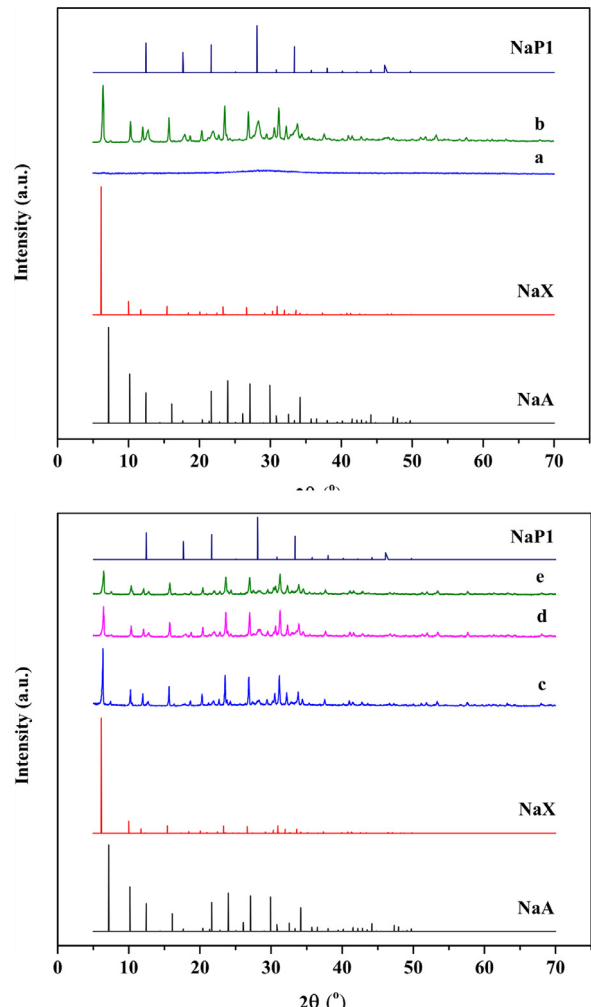


**Fig. 5.** XRD patterns at different molar ratios of  $\text{Na}_2\text{O}/\text{Al}_2\text{O}_3$  and the standard of zeolite NaA, NaX and NaP1. (a) 2.0, (b) 8.0, (c) 10.0, (d) 11.0, and (e) 12.0.

$\text{Al}_2\text{O}_3 = 12.0$  was applied based on previous studies which reported that an increase of alkalinity of the reaction mixture inhibited zeolite NaP1 formation [3,34,43]. However, more alkaline added resulted in a decrease of peaks intensity of zeolite NaX (Fig. 5e). An increase of NaOH would decrease NaX owing to poor stability of zeolite in high alkaline solution [42]. Fig. 5d shows similar crystallization to that of  $\text{Na}_2\text{O}/\text{Al}_2\text{O}_3 = 12$  and the peaks of zeolite NaX were weaker than that of  $\text{Na}_2\text{O}/\text{Al}_2\text{O}_3 = 8.0$ . The characteristic peaks of zeolite NaX indicated high crystallinity at a ratio of 10.0 (Fig. 5c). Crystallize zeolite NaX only existed with high intensity when optimal alkalinity of the reaction mixture was employed [44].

$\text{OH}^-$  group was the stimulator in forming primary structures and helped forming the bonds between the  $\text{SiO}_4$  and  $\text{AlO}_4^-$  tetrahedra. If alkalinity of the mixture was low, the  $\text{OH}^-$  group was not enough to form bonds of tetrahedra. When the alkaline concentration reached the required level, tetrahedral bonds were easily formed to facilitate the crystallization of zeolite X. At too high alkalinity, the tetrahedra would be partially dissolved, resulting in a decrease of the crystallinity [45]. At  $\text{Na}_2\text{O}/\text{Al}_2\text{O}_3 = 10.0$ , the product was of high crystallinity intensity with almost no interference.

### 3.3. Effect of reaction time

Fig. 6 shows the effect of reaction time on the synthesis of zeolite NaX. At 2 h, the characteristic peaks of zeolite NaX appeared with low intensity. The optimal reaction time with high crystallinity was between 3 and 6 h [28]. In this study, a reaction time of 4 h was employed to obtain NaX with high crystallinity (Fig. 6b).

A decrease in characteristic peaks intensity of zeolite NaX and the formation of zeolite NaP1 with low intensity were observed at 6 h. At prolonged reaction time, the peak intensity of the desired products started to decrease [46]. Only zeolite NaX crystallized well at a specific reaction time [9,47]. At 8 h, the result was not much different from that of 6 h. However, when the reaction time was increased from 4 h to 6 h, crystallization intensity rapidly increased and formed relatively uniform crystals [48]. This trend was also mentioned before [28,49].

Fig. 7 indicates that the crystals were not uniformly formed and some non-crystallized aluminosilicate gel regions existed at 2 h. At 4 h, the crystals formed complete structure with almost no visible amorphous region. The morphology of NaX crystals in this work was similar to those of Garcia et al. (2016) and Zhang et al. (2019) [36,50]. Zeolite X had higher crystallinity at 4 h than that at longer time in other studies using RHA [4,12]. Microwave assistance and ultrasonic treatment could be used to speed up dissolution of precursors, help formation of bonds, and promote rapid growth of crystals [27,51].

The effect of aging time on the nucleation and crystallization of zeolite crystal was reported before [34,52], and investigated in this study. Fig. 8 shows that aging time from 0 to 24 h had no effect. This can be explained because the prolonged aging time would support the formation of GIS family zeolites like zeolite P instead of zeolite A and X. Similar results were reported by Ghasemi and Younesi (2012) and Thuadaj and Nuntiya (2012) [19,53].

In this work, the alkalinity of solution was investigated because it also affected on the nucleation and crystallization of zeolite crystals. In stead of using microwave and ultrasound assistance to help shortening nucleation and reaction time of zeolite [27,51], this study employed the increase of solution alkalinity to improve the reaction rate. The morphology of samples obtained at aging time of 0 h and 6 h was examined (Fig. 8). No significant difference between 0 h and 6 h was observed; thus, aging was unnecessary in this work.

### 3.4. Comparison of the current method with published methods

Many different feedstocks were used for zeolite synthesis such as commercial/natural mineral sources, wastes from industrial and agricultural production such as diatomite, fly ash and RHA. Generally,

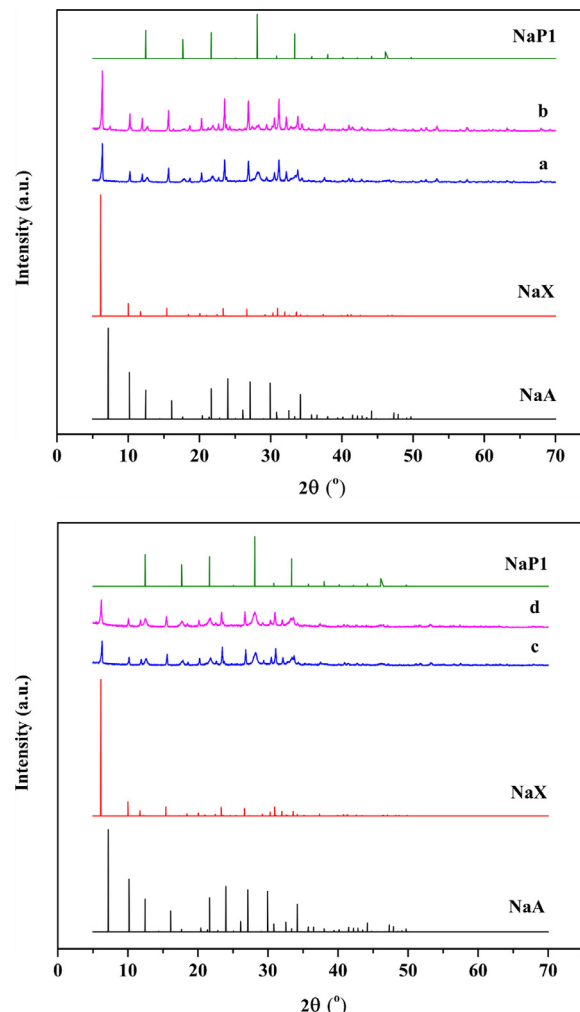
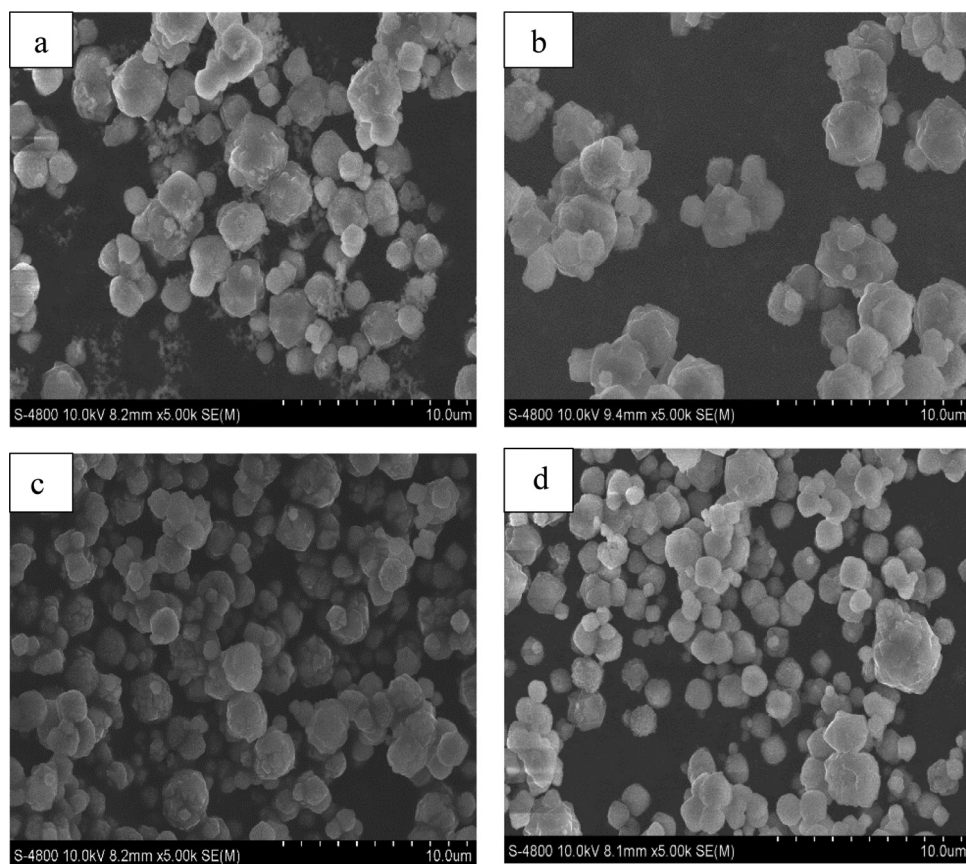


Fig. 6 . XRD patterns at different reaction time and the standard of zeolite NaA, NaX and NaP1. (a) 2 h, (b) 4 h, (c) 6 h, and (d) 8 h.

when using waste and natural mineral precursors, most required pre-treatment like fusing at high temperatures or extracting silica which needs long time before subjecting to zeolite synthesis. Thuadaj et al. (2012) prepared zeolite X from fly ash and amorphous silica RHA by fusion at 550°C [53] while Muriithi et al. (2020) used fly ash as the precursor with a reaction time of 9 h [11]. Wang et al. (2018) carried out the synthesis in 24 h to extract  $\text{Na}_2\text{SiO}_3$  from RHA [20]. Ghasemi and Younesi pretreated (2012) RHA with HCl, then calcinated at 700°C for 6 h before proceeded to the synthesis of zeolite X [19]. The surface area ( $\text{m}^2/\text{g}$ ) and pore diameter (Å) of their synthesized NaX was 89.96 and 92, respectively compared to a surface area of 388.4 and a pore volume of 12.37 of this study. In terms of reaction time, this study required is much shorter (4 h) than the 48 h required in their study [19]. The research of Katsuki et al. (2009) used a procedure similar to this study, and obtained NaX zeolite with a surface area of 553  $\text{m}^2/\text{g}$  at a longer reaction time of 6 h. However, rice husk had to be burned in nitrogen gas at 600–1000°C before used as the raw material for the synthesis [22]. Although Zhang et al. (2013) synthesized NaX using commercial silica source and a specific surface area of 526  $\text{m}^2/\text{g}$  was obtained; however, the reaction time needed was 15 h [26], which was much longer than that of this work (4 h).

This study could directly synthesize zeolite X using RHA without calcination and the optimal conditions were  $\text{SiO}_2/\text{Al}_2\text{O}_3$  molar ratio of 4.0,  $\text{Na}_2\text{O}/\text{Al}_2\text{O}_3$  molar ratio of 10.0, reaction time of 4 h and without aging. The ratio of  $\text{SiO}_2/\text{Al}_2\text{O}_3$  of 4 was comparable with that from other publications; nevertheless, the  $\text{Na}_2\text{O}/\text{Al}_2\text{O}_3$  molar ratio of 10



**Fig. 7.** FESEM images of the NaX at different reaction time. (a) 2 h, (b) 4 h, (c) 6 h, and (d) 8 h.

was much higher than that of other studies. The higher molar ratio of  $\text{Na}_2\text{O}/\text{Al}_2\text{O}_3$  would help the formation of high purity and crystallinity NaX as mentioned. Although this study used agricultural by-product as the feedstock, the specific surface area of the synthesized NaX was quite high ( $388 \text{ m}^2/\text{g}$ ). Additionally, DLS result showed that the average particles size of the synthesized NaX was 484.1 nm.

The total reaction time, including extraction of silica, stirring to obtain homogenous mixture and synthesis of zeolite, was estimated to be about 10 h while calcination or fusion was not required, thus the process was carried out at mild conditions. Therefore, this work could provide an integrated and promising process to obtain valuable materials with low energy consumption and low cost. The low pore diameter of the synthesized NaX (12.37 Å) was due to the use of RHA

without calcination. This precursor source may contain organic matters which partially blocked the pores of the products, resulting in lower specific surface area and pore diameter of NaX than those of some studies, as shown in Table 2.

In general, this study was performed to evaluate the impact of factors affecting the formation of zeolite NaX from RHA without pretreatment. The final product was the highly crystallized zeolite NaX with a relatively large surface area compared to similar studies using other waste sources. Materials with a large surface area have been mentioned in previous studies with good adsorption capacity of  $\text{CO}_2$ , or dyes [9,13,54,55]. Our preliminary results on the adsorption of methylene blue by zeolite NaX showed that the removal capacity of the dye can be more than 80% (data not shown). In addition, the

**Table 2**  
Comparison of zeolite synthesized in this study with those in other studies.

Raw materials	Reaction conditions				Surface area ( $\text{m}^2/\text{g}$ )	Pore diameter (Å)	References
	Ratio of $\text{SiO}_2/\text{Al}_2\text{O}_3$	Ratio of $\text{Na}_2\text{O}/\text{Al}_2\text{O}_3$	Reaction time (h)	Aging time (h)			
$\text{SiO}_2$ commercial	3.5	3.5	15	-	526	-	[26]
Diatomite	-	-	5	0.5	53	-	[9]
Fly ash and amorphous silica <sup>a</sup> (Fused 550°C – 1 h)	3.71	-	24	18 <sup>b</sup>	232.73	-	[53]
Coal fly ash (Fused 550°C – 1.5 h with NaOH)	3.63	4.9	9	0	257	122	[11]
RHA (extracted $\text{Na}_2\text{SiO}_3$ by NaOH in 70°C and 24 h)	4.0	5.5	24	0	644	18.8	[20]
RHA (pretreated HCl and calcined at 700°C in 6 h)	4.0	-	48	0	89.96	92	[19]
Rice husk (carbonized at 600–1000°C for 1 h and extracted $\text{Na}_2\text{SiO}_3$ by NaOH 2N at 90° C)	1.9	-	6	0	553	-	[22]
RHA (without calcined)	4.0	10.0	4	0	388.41	12.37	This study

<sup>a</sup> silica was extracted from RHA

<sup>b</sup> aging before reaction

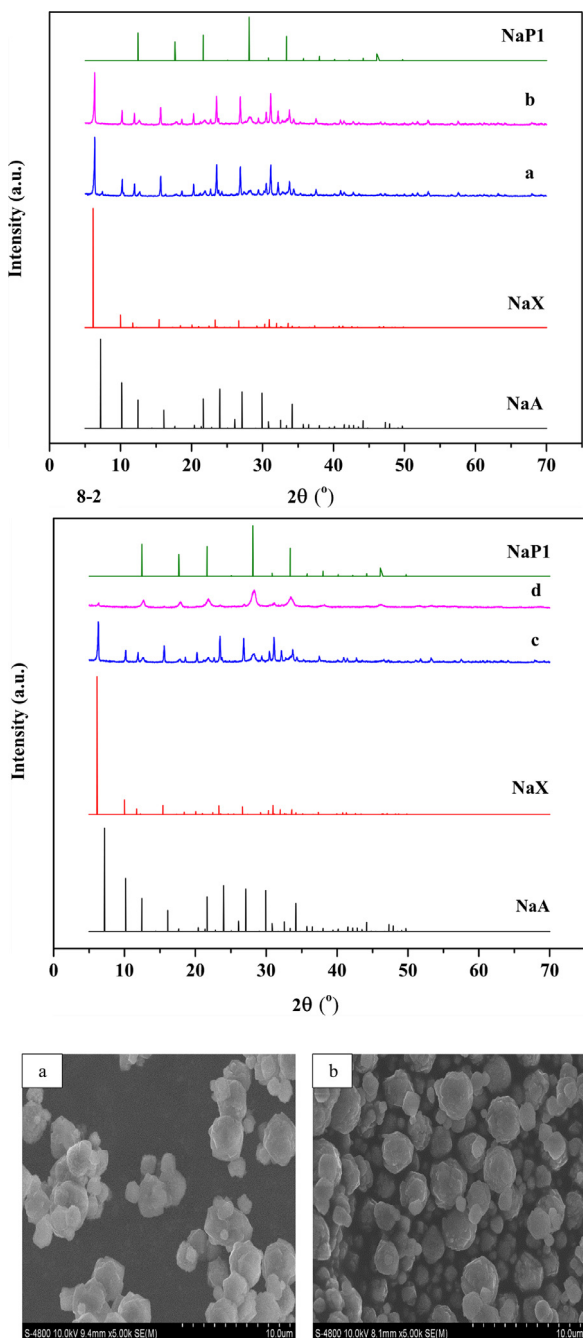


**Fig. 8.** XRD patterns at different aging time and the standard of zeolite NaA, NaX and NaP1. (a) 0 h, (b) 6 h, (c) 12 h, and (d) 24 h. FESEM images of NaX at different aging time. (a) 0 h, and (b) 6 h.

combination of materials synthesized from waste with other materials to create composite materials with outstanding properties at low cost is also a remarkable trend [8,56–58]. Furthermore, the synthetic method in this work can also be used for synthesizing other types of zeolites such as zeolite NaA and NaP1.

#### 4. Conclusions

In this study, zeolite NaX was successfully synthesized by directly using RHA without any pretreatment. The synthesis process was simple, environmental friendly, time-saving and energy-saving.

Moreover, the optimal condition of zeolite NaX synthesis such as reaction time of 4 h, reaction temperature of 90 °C, SiO<sub>2</sub>/Al<sub>2</sub>O<sub>3</sub> molar ratio of 4, Na<sub>2</sub>O/Al<sub>2</sub>O<sub>3</sub> molar ratio of 10 and without aging were comparable to other works which employed RHA as the feedstock. The obtained NaX with a specific surface area of 388 m<sup>2</sup>/g suggests its potential application in environmental remedy.

#### Declaration of Competing Interest

The authors declare no known competing financial interests or personal relationships that could have appeared to influence the work reported in this paper.

#### CRediT authorship contribution statement

**Phuong Lan Tran-Nguyen:** Conceptualization, Methodology, Investigation, Resources, Writing – original draft. **Kim-Phung Ly:** Conceptualization, Methodology, Writing – original draft. **Luong Huynh Vu Thanh:** Writing – review & editing. **Artik Elisa Angkawijaya:** Writing – review & editing. **Shella Permatasari Santoso:** Writing – review & editing. **Nguyen-Phuong-Dung Tran:** Writing – review & editing. **Meng-Lin Tsai:** Writing – review & editing.

#### Acknowledgment

This research was funded by Vietnam National Foundation for Science and Technology Development (NAFOSTED) under Grant Number [103.02-2020.64](#).

#### References

- [1] Qiang Z, Shen X, Guo M, Cheng F, Zhang M. A simple hydrothermal synthesis of zeolite X from bauxite tailings for highly efficient adsorbing CO<sub>2</sub> at room temperature. *Microporous Mesoporous Mater* 2019;287:77–84.
- [2] Ma Y, Yan C, Alshameri A, Qiu X, Zhou C. Synthesis and characterization of 13X zeolite from low-grade natural kaolin. *Adv Powder Technol* 2014;25:495–9.
- [3] Novembre D, Di Sabatino B, Gimeno D, Pace C. Synthesis and characterization of Na-X, Na-A and Na-P zeolites and hydroxysodalite from metakaolinite. *Clay Miner* 2011;46:339–54.
- [4] Santasnachok C, Kurniawan W, Hinode H. The use of synthesized zeolites from power plant rice husk ash obtained from Thailand as adsorbent for cadmium contamination removal from zinc mining. *J Environ Chem Eng* 2015;3:2115–26.
- [5] Mohamed R, Mkhald I, Barakat M. Rice husk ash as a renewable source for the production of zeolite NaY and its characterization. *Arab J Chem* 2015;8:48–53.
- [6] Jesudoss SK, Vijaya JJ, Kaviyarasu K, Kennedy LJ, Ramalingam RJ, Al-Lohedane HA. Anti-cancer activity of hierarchical ZSM-5 zeolites synthesized from rice-based waste materials. *RSC Adv* 2018;8:481–90.
- [7] Arslan A, Veli S. Zeolite 13X for adsorption of ammonium ions from aqueous solutions and hen slaughterhouse wastewaters. *J Taiwan Inst Chem Eng* 2012;43:393–8.
- [8] Sivalingam S, Sen S. Efficient removal of textile dye using nanosized fly ash derived zeolite-x: Kinetics and process optimization study. *J Taiwan Inst Chem Eng* 2019;96:305–14.
- [9] Yao G, Lei J, Zhang X, Sun Z, Zheng S. One-step hydrothermal synthesis of zeolite X powder from natural low-grade diatomite. *Materials* 2018;11:1–14.
- [10] Purnomo CW, Salim C, Hinode H. Synthesis of pure Na-X and Na-A zeolite from bagasse fly ash. *Microporous Mesoporous Mater* 2012;162:6–13.
- [11] Muriithi GN, Petrik LF, Doucet FJ. Synthesis, characterisation and CO<sub>2</sub> adsorption potential of NaA and NaX zeolites and hydrotalcite obtained from the same coal fly ash. *J CO<sub>2</sub> Util* 2020;36:220–30.
- [12] Wang Y, Jia H, Chen P, Fang X, Du T. Synthesis of La and Ce modified X zeolite from rice husk ash for carbon dioxide capture. *J Mater Res Technol* 2020;9. doi: [10.1016/j.jmrt.2020.02.061](https://doi.org/10.1016/j.jmrt.2020.02.061).
- [13] Ng EP, Awala H, Tan KH, Adam F, Retoux R, Mintova S. EMT-type zeolite nanocrystals synthesized from rice husk. *Microporous Mesoporous Mater* 2015;204:204–9.
- [14] Clauss K, Ottinger M, Leinenkugel P, Kuenzer C. Estimating rice production in the Mekong Delta, Vietnam, utilizing time series of Sentinel-1 SAR data. *Int J Appl Earth Obs Geoinf* 2018;73:574–85.
- [15] Azat S, Korobeynyk A, Moustakas K, Inglezakis V. Sustainable production of pure silica from rice husk waste in Kazakhstan. *J Clean Prod* 2019;217:352–9.
- [16] Costa JAS, Paranhos CM. Systematic evaluation of amorphous silica production from rice husk ashes. *J Clean Prod* 2018;192:688–97.

- [17] Kaviyarasu K, Manikandan E, Kennedy J, Jayachandran M, Maaza M. Rice husks as a sustainable source of high quality nanostructured silica for high performance Li-ion battery reutilization by sol-gel method – a review. *Adv Mater Lett* 2016;7: 684–96.
- [18] Sembiring S, Simanjuntak W, Situmeang R, Riyanto A, Sebayang K. Preparation of refractory cordierite using amorphous rice husk silica for thermal insulation purposes. *Ceram Int* 2016;42:8431–7.
- [19] Ghasemi Z, Younesi H. Preparation of free-template nanometer-sized Na-A and-X zeolites from rice husk ash. *Waste Biomass Valorization* 2012;3:61–74.
- [20] Wang Y, Du T, Jia H, Qiu Z, Song Y. Synthesis, characterization and CO<sub>2</sub> adsorption of NaA, NaX and NaZSM-5 from rice husk ash. *Solid State Sci* 2018;86:24–33.
- [21] Kurniawan W, Hinode H. Lean condition procedure for utilization of silica from rice husk as zeolite precursor. *Indonesian J Comput, Eng Des* 2020;2:111–21.
- [22] Katsuki H, Komarneni S. Synthesis of Na-A and/or Na-X zeolite/porous carbon composites from carbonized rice husk. *J Solid State Chem* 2009;182:1749–53.
- [23] Shelke VR, Bhagade SS, Mandavgane SA. Mesoporous silica from rice husk ash. *Bull Chem React Eng Catal* 2010;5:63–7.
- [24] Thiedeitz M, Schmidt W, Harder M, Krankel T. Performance of rice husk ash as supplementary cementitious material after production in the field and in the lab. *Materials* 2020;13:4319.
- [25] Fernandes Jj, Calheiros D, Kieling AG, Moraes CAM, Rocha TLAC, Brehm FA, Modolo RCE. Characterization of rice husk ash produced using different biomass combustion techniques for energy. *Fuel* 2016;165:351–9.
- [26] Zhang X, Tang D, Zhang M, Yang R. Synthesis of NaX zeolite: Influence of crystallization time, temperature and batch molar ratio SiO<sub>2</sub>/Al<sub>2</sub>O<sub>3</sub> on the particulate properties of zeolite crystals. *Powder Technol* 2013;235:322–8.
- [27] Ansari M, Aroujalian A, Raisi A, Dabir B, Fathizadeh M. Preparation and characterization of nano-NaX zeolite by microwave assisted hydrothermal method. *Adv Powder Technol* 2014;25:722–7.
- [28] Yang T, Han C, Liu H, Yang L, Liu D, Tang J, Luo Y. Synthesis of Na-X zeolite from low aluminum coal fly ash: characterization and high efficient As (V) removal. *Adv Powder Technol* 2019;30:199–206.
- [29] Nazir LSM, Yeong YF, Sabdin S. Formation of pure NaX zeolite: effect of ageing and hydrothermal synthesis parameters. *IOP Conf Ser: Mater Sci Eng* 2018;458:012002.
- [30] Murayama N, Tanabe M, Yamamoto H, Shibata J. Reaction, mechanism and application of various zeolite syntheses from coal fly ash. *Mater Trans* 2003;44:2475–80.
- [31] Masoudian SK, Sadighi S, Abbasi A. Synthesis and characterization of high aluminum zeolite X from technical grade materials. *Bull Chem React Eng* 2013;8:54–60.
- [32] Al-Jubouri SM, Sabbar HA, Lafta HA, Waisi BI. Effect of synthesis parameters on the formation 4A zeolite crystals: characterization analysis and heavy metals uptake performance study for water treatment. *Desalin Water Treat* 2019;165:290–300.
- [33] Garshabi V, Jahangiri M, Anbia M. Equilibrium CO<sub>2</sub> adsorption on zeolite 13X prepared from natural clays. *Appl Surf Sci* 2017;393:225–33.
- [34] Abdullahi T, Harun Z, Othman MHD. A review on sustainable synthesis of zeolite from kaolinite resources via hydrothermal process. *Adv Powder Technol* 2017;28:1827–40.
- [35] Ayele L, Pérez-Pariente J, Chebude Y, Díaz I. Conventional versus alkali fusion synthesis of zeolite A from low grade kaolin. *Appl Clay Sci* 2016;32:485–90.
- [36] García A, López CM, García LV, Casanova J, Goldwasser M. Improvements in the synthesis of zeolites with low Si/Al ratio from Venezuelan sodium silicate for an environmentally friendly process. *Ing e Investig* 2016;36:62–9.
- [37] Zhou C, Alshameri A, Yan C, Qiu X, Wang H, Ma Y. Characteristics and evaluation of synthetic 13X zeolite from Yunnan's natural halloysite. *J Porous Mater* 2013;20:587–94.
- [38] Wang C, Zhou J, Wang Y, Yang M, Li Y, Meng C. Synthesis of zeolite X from low-grade bauxite. *J Chem Technol Biotechnol* 2013;88:1350–7.
- [39] Hildebrando EA, Andrade CGB, Rocha Junior CAFD, Angélica RS, Valenzuela-Díaz FR, Neves RdDF. Synthesis and characterization of zeolite NaP using kaolin waste as a source of silicon and aluminum. *Mater Res* 2014;17:174–9.
- [40] Ali IO, El-Sheikh SM, Salama TM, Bakr MF, Fodial MH. Controllable synthesis of NaP zeolite and its application in calcium adsorption. *Sci China Mater* 2015;58:621–33.
- [41] Juengsuwanthanon K, Winnefeld F, Chindaprasirt P, Pimraksa K. Correlation between initial SiO<sub>2</sub>/Al<sub>2</sub>O<sub>3</sub>, Na<sub>2</sub>O/Al<sub>2</sub>O<sub>3</sub>, Na<sub>2</sub>O/SiO<sub>2</sub> and H<sub>2</sub>O/Na<sub>2</sub>O ratios on phase and microstructure of reaction products of metakaolin-rice husk ash geopolymer. *Constr Build Mater* 2019;226:406–17.
- [42] Nazir LSM, Yeong YF, Chew TL. Controlled growth of Faujasite Zeolite with NaX topology by manipulating solution aging and Na<sub>2</sub>O/Al<sub>2</sub>O<sub>3</sub> ratios. *Colloid Surf A-Physicochem Eng Asp* 2020;600:124803.
- [43] Qiu X, Liu Y, Li D, Yan C. Preparation of NaP zeolite block from fly ash-based geopolymer via in situ hydrothermal method. *J Porous Mater* 2015;22:291–9.
- [44] Chaves TF, Pastore HO, Cardoso D. A simple synthesis procedure to prepare nanosized faujasite crystals. *Microporous Mesoporous Mater* 2012;161:67–75.
- [45] Ngoc DT, Pham TH, Nguyen KDH. Synthesis, characterization and application of nanozeolite NaX from Vietnamese kaolin. *Adv Nat Sci: Nanosci Nanotechnol* 2013;4:1–12.
- [46] Sivalingam S, Sen S. Swift sono-hydrothermal synthesis of pure NaX nanocrystals with improved sorption capacity from industrial resources. *Appl Surf Sci* 2019;463:190–6.
- [47] Johnson E, Asik J, Arshad S. The effect of crystallization time and temperature on hydrothermal synthesis of zeolite Nax from Bongawan kaolin. *FEIIC Int J Eng Technol* 2016;13:33–9.
- [48] Ferdov S. Conventional synthesis of layer-like zeolites with faujasite (FAU) structure and their pathway of crystallization. *Microporous Mesoporous Mater* 2020;303:110263.
- [49] Grand J, Awala H, Mintova S. Mechanism of zeolites crystal growth: new findings and open questions. *Cryst Eng Comm* 2016;18:650–64.
- [50] Zhang S, Cui M, Chen J, Ding Z, Wang X, Mu Y, Meng C. Modification of synthetic zeolite X by thiourea and its adsorption for Cd (II). *Mater Lett* 2019;236:233–5.
- [51] Ng TYS, Chew TL, Yeong YF, Jawad ZA, Ho CD. Zeolite RHO synthesis accelerated by ultrasonic irradiation treatment. *Sci Rep* 2019;9:1–11.
- [52] Liu L, Du T, Li G, Yang F, Che S. Using one waste to tackle another: Preparation of a CO<sub>2</sub> capture material zeolite X from laterite residue and bauxite. *J Hazard Mater* 2014;278:551–8.
- [53] Thuadaij P, Nuntiya A. Preparation and characterization of faujasite using fly ash and amorphous silica from rice husk ash. *Procedia Eng* 2012;32:1026–32.
- [54] Hor KY, Chee JMC, Chong MN, Jin B, Saint C, Poh PE, Aryal R. Evaluation of physicochemical methods in enhancing the adsorption performance of natural zeolite as low-cost adsorbent of methylene blue dye from wastewater. *J Clean Prod* 2016;1–13.
- [55] Krachuamram S, Chanapattharapol KC, Kamonsuttipajit N. Synthesis and characterization of NaX-type zeolites prepared by different silica and alumina sources and their CO<sub>2</sub> adsorption properties. *Microporous Mesoporous Mater* 2020;310.
- [56] Dehghani MH, Dehghan A, Alidadi H, Dolatabadi M, Mehrabpour M, Converti A. Removal of methylene blue dye from aqueous solutions by a new chitosan/zeolite composite from shrimp waste. *Kinetic Equil Study* 2017; 34:1699–707.
- [57] Abasian P, Radmansourib M, Jouybaric MH, Ghasemid MV, Mohammadi A, Irafin M, et al. Incorporation of magnetic NaX zeolite/DOX into the PLA/chitosan nanofibers for sustained release of doxorubicin against carcinoma cells death in vitro. *Int J Biol Macromol* 2019;121:398–406.
- [58] Cao J, Wang P, Shen J, Sun Q. Core-shell Fe<sub>3</sub>O<sub>4</sub>@zeolite NaA as an Adsorbent for Cu<sup>2+</sup>. *Materials* 2020;13:5047.



# Facile synthesis of superparamagnetic thiamine/Fe<sub>3</sub>O<sub>4</sub> with enhanced adsorptivity toward divalent copper ions

Phuong Lan Tran-Nguyen <sup>a, \*\*, 1</sup>, Artik Elisa Angkawijaya <sup>b, \*, 1</sup>, Quoc Nam Ha <sup>c</sup>, Yen Nhi Tran-Chuong <sup>c</sup>, Alchris Woo Go <sup>b</sup>, Vania Bundjaja <sup>c</sup>, Chintya Gunarto <sup>c,d</sup>, Shella Permatasari Santoso <sup>d,c</sup>, Yi-Hsu Ju <sup>c,b,e</sup>

<sup>a</sup> Department of Mechanical Engineering, Can Tho University, 3/2 Street, Can Tho City, Viet Nam

<sup>b</sup> Graduate Institute of Applied Science, National Taiwan University of Science and Technology, #43, Sec. 4, Keelung Rd., Taipei, 10607, Taiwan

<sup>c</sup> Department of Chemical Engineering, National Taiwan University of Science and Technology, #43, Sec. 4, Keelung Rd., Taipei, 10607, Taiwan

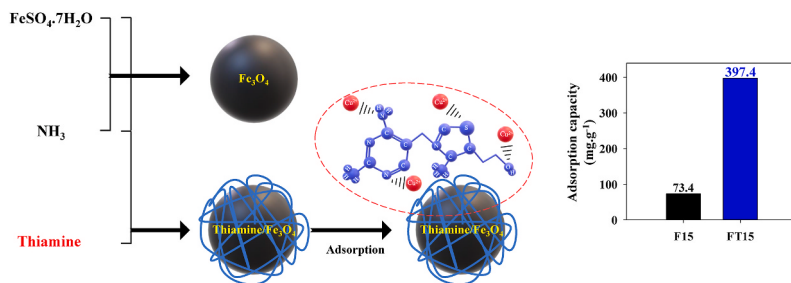
<sup>d</sup> Department of Chemical Engineering, Widya Mandala Surabaya Catholic University, Kalijudan 37, Surabaya, 60114, Indonesia

<sup>e</sup> Taiwan Building Technology Center, National Taiwan University of Science and Technology, #43, Sec. 4, Keelung Rd., Taipei, 10607, Taiwan

## HIGHLIGHTS

- Thiamine/Fe<sub>3</sub>O<sub>4</sub> (FT) adsorbent synthesized via one step chemical oxidation method.
- The N- and S-groups in thiamine enhanced FT adsorption capacity for Cu removal.
- FT has 5.69 times higher adsorption capacity than unmodified Fe<sub>3</sub>O<sub>4</sub>.
- After repeated usage, the FT capacity remained 1.95 times higher than fresh Fe<sub>3</sub>O<sub>4</sub>.
- The magnetic properties of FT facilitate adsorbent recovery from the wastewater.

## GRAPHICAL ABSTRACT



## ARTICLE INFO

Handling Editor: Junfeng Niu

### Keywords:

Magnetite  
Fe<sub>3</sub>O<sub>4</sub>  
Thiamine  
Heavy metals  
Superparamagnetic adsorbent

## ABSTRACT

The development of environmentally friendly adsorbents has been extensively carried out to overcome the detrimental effects of heavy metal accumulation, which has persistently become a global ecological problem. In pursuit of generating eco-friendly adsorbents, a green method for synthesizing thiamine functionalized-Fe<sub>3</sub>O<sub>4</sub> (FT) was developed in this study. A one-step chemical oxidation and functionalization technique was used to prepare FT using the ammonia-containing solvent. A molar ratio of ammonia:Fe:thiamine of 15:1:1 was shown to produce FT15 with high yield, adsorptivity, and purity. XRD, XPS, FTIR, SEM, and SQUID characterization of FT15 revealed the formation of superparamagnetic thiamine functionalized Fe<sub>3</sub>O<sub>4</sub> in their particles. This superparamagneticity facilitates the easy recovery of FT15 particles from the waste-containing solution by using an external magnetic force. The batch adsorption of Cu(II) onto FT15 showed the best fit with the Sips adsorption isotherm model with a maximum adsorption capacity of 426.076 mg g<sup>-1</sup>, which is 5.69-fold higher capacity than the control unmodified Fe<sub>3</sub>O<sub>4</sub> (F15). After five adsorption-desorption cycles, the FT15 can maintain up to 1.95-

\* Corresponding author.

\*\* Corresponding author.

E-mail addresses: [tnplan@ctu.edu.vn](mailto:tnplan@ctu.edu.vn) (P.L. Tran-Nguyen), [artikelisa@mail.ntust.edu.tw](mailto:artikelisa@mail.ntust.edu.tw), [artikelisa@yahoo.com](mailto:artikelisa@yahoo.com) (A.E. Angkawijaya).

<sup>1</sup> These authors contribute equally.

fold higher capacity than the freshly synthesized F15. Observation on the physicochemical properties of the post-adsorption materials showed the contribution of an amine group, pyrimidine ring, and the thiazolium group of thiamine in boosting its adsorption capacity. This study provides important findings to advance the adsorptivity of magnetic adsorbents with promising recoverability from aqueous solution by employing naturally available and environmentally friendly compounds such as thiamine.

## 1. Introduction

Heavy metals such as copper (Cu), chromium (Cr), and zinc (Zn) are known to be essential to human health yet detrimental when they occur in excess (Olivares and Uauy, 1996; Anderson, 1997; Barceloux, 1999). Despite its carcinogenic and organ irritating effect, Cu still is widely used in many industrial processes which effluents may eventually release and contaminate the environment (Aydin et al., 2008; Parida et al., 2012; Briffa et al., 2020; Kinuthia et al., 2020; Obasi and Akudinobi, 2020). To cope with this problem, the World Health Organization (WHO), the United State Environmental Protection Administration (USEPA), and other governmental bodies had set a permissible limit of Cu availability in drinking water, up to  $2 \text{ mg L}^{-1}$  (Al-Saydeh et al., 2017), which eventually promote the development of Cu removal techniques, such as metal complexation, ion exchange, liquid-liquid extraction, co-precipitation, bio-sorption, and adsorption (Le et al., 2010; Bhaumik et al., 2011; Shan et al., 2015). Among them, adsorption is the widely used approach due to its eco-friendly nature, facile operation, and high efficiency (De Gisi et al., 2016; Burakov et al., 2018; Arora, 2019; Rashid et al., 2021). In line with the growing implementation of the adsorption technique, it is necessary to generate an adsorbent with improved adsorption capacity.

$\text{Fe}_3\text{O}_4$  nanoparticles (NPs) are superparamagnetic material that exhibits a strong saturation magnetization. This material had been widely used in the biomedical application for targeted drug delivery and immunoassays (Hu et al., 2006; Nasongkla et al., 2006), carrier for enzyme immobilization for different uses (Jordan et al., 2011; Zhu et al., 2014), and industrial application for catalytic degradation, groundwater remediation, and hazardous waste treatment (Le et al., 2010; Bhaumik et al., 2011). Owing to its magnetic properties,  $\text{Fe}_3\text{O}_4$  is considered an unparalleled adsorbent in terms of feasibility to recover its post-adsorption particle from wastewater. Several synthesis routes of  $\text{Fe}_3\text{O}_4$  NPs through chemical oxidation (Chaki et al., 2015), solid-state reaction (Iljinis et al., 2005), sol-gel (Tang et al., 2004), co-precipitation (Do Kim et al., 2007), hydrothermal processes (Khollam et al., 2002), and ultrasonic method (Lu et al., 2006) have been reported previously. However, it has been widely acknowledged that the  $\text{Fe}_3\text{O}_4$  surface is prone to oxidation upon contact with the atmosphere, which eventually may cause particle aggregation and lead to the reduction of their magnetism and dispersibility in water (Kalia et al., 2014). To cope with this problem, several magnetite composites had been developed, where polymer (Liu et al., 2008), noble metals (Sun et al., 2012), metal oxides (Rajabi et al., 2016), or vitamins (Azizi and Heydari, 2014; Shaterian and Molaei, 2019) were used as the compositing compounds. Beside improving its water dispersibility, the  $\text{Fe}_3\text{O}_4$  composites postulated to possess improved adsorption performance (Liu et al., 2008; Boyer et al., 2010; Mahdavian and Mirrahimi, 2010; Sun et al., 2012; Kalia et al., 2014; Rajabi et al., 2016). For instance, a study by Mahdavian et al. reported the synthesis of magnetic nano adsorbent (MNPs-COOH) via graft polymerization of 3-aminopropyl triethoxysilane, acryloyl chloride, and acrylic acid. The MNPs-COOH reportedly can form complex with heavy metals via its COOH groups and has an adsorption capacity of  $30 \text{ mg g}^{-1}$  and  $40 \text{ mg g}^{-1}$  for Cu(II) ions and Pb(II) removal, respectively (Mahdavian and Mirrahimi, 2010). Another study by Pang et al. reported an amino functionalization of  $\text{Fe}_3\text{O}_4$  by addition of polyethylenimine. The synthesized functional magnetite was found can efficiently adsorb Cu(II) and Zn(II) and Cd(II), with a capacity of 157.8, 138.8 and  $105.2 \text{ mg g}^{-1}$ , respectively (Pang et al.,

2011). More recently, amino acids and vitamins had been more frequently used as the compositing compound for  $\text{Fe}_3\text{O}_4$  owing to their ability to provide additional adsorption sites on magnetite surface and may improve their reusability (Liu et al., 2008; Pang et al., 2011; Azizi and Heydari, 2014; Shaterian and Molaei, 2019).

In this study, thiamine (vitamin B1) was used as the compositing and functionalizing agent during  $\text{Fe}_3\text{O}_4$  synthesis. Thiamine possesses various functional groups in its structure, such as covalent bonded-carboxylate groups, amine groups, hydroxyl, and sulfate groups. These functional groups allow the interaction of thiamine with adsorbate molecules via redox reaction (Shaterian and Molaei, 2019), hydrogen bonding (Samal et al., 2000; Jiang et al., 2018), chemical complexation, electrostatic attraction, and Van der Waals forces (Sud et al., 2008; Pang et al., 2011). In addition, a single-step synthesis and thiamine functionalization of  $\text{Fe}_3\text{O}_4$  was developed. The effect of precursor ratio on the product yield, characteristic, and adsorption performance of the synthesized materials were discussed in this work. The isotherm adsorption model, adsorbent reusability, and the post-adsorption/desorption characterization were provided to elucidate the adsorption mechanism of Cu(II) by thiamine-functionalized  $\text{Fe}_3\text{O}_4$  (FT).

## 2. Materials and methods

### 2.1. Materials

The chemicals were used without further purification, and the solutions were freshly made using deionized (DI)-water from the NANO Ultrapure water system with a resistance of  $18.3 \text{ M}\Omega \text{ cm}^{-1}$ . Iron (II) sulfate heptahydrate ( $\text{FeSO}_4 \cdot 7\text{H}_2\text{O}$ , New Jersey, USA), copper (II) chloride dihydrate ( $\text{CuCl}_2 \cdot 2\text{H}_2\text{O}$ , Belgium, Germany) were manufactured by Acros Organics. Thiamine hydrochloride ( $\text{C}_{12}\text{H}_{18}\text{Cl}_2\text{N}_4\text{OS}$ ) was purchased from Sigma, St. Louis, MO. Hydrochloric acid (HCl, Hampton, NH) and sodium hydroxide (NaOH, Loughborough, UK) were the product of Fisher Scientific. Ammonia ( $\text{NH}_3$ ) was manufactured by Showa, Japan.

### 2.2. Preparation and modification of $\text{Fe}_3\text{O}_4$ nanoparticles

The thiamine modified- $\text{Fe}_3\text{O}_4$  (FT) were synthesized through one-step chemical oxidation. Briefly, 12 mM of thiamine aqueous solution was added into 12 mM of  $\text{FeSO}_4 \cdot 7\text{H}_2\text{O}$  aqueous solution. Then  $\text{NH}_3$  solution was added at varied molar ratios of  $\text{NH}_3$ : Fe: thiamine (Table 1). The mixture was allowed to react for 1 h at  $90^\circ\text{C}$  and 500 rpm mixing. During the reaction, the color of the mixture changed from brownish yellow to black. The black powder was then separated using a magnet, washed with DI water until constant pH, and dried under vacuum ( $40^\circ\text{C}$ , 760 mmHg) for 24 h. As a control, unmodified  $\text{Fe}_3\text{O}_4$  (F) was prepared at the same condition in the absence of thiamine.

### 2.3. Characterization

The crystal structures of F and FT were examined by using an X-ray Diffractometer Bruker D2 Phaser with  $\text{Cu-K}\alpha$  radiation ( $\lambda = 1.54184 \text{ \AA}$ ) at 30 kV and 10 mA. Thermogravimetric analysis (TGA) was performed using a TA instruments/TGA 550, operated at a temperature range of 30–700 °C with a heating rate of  $10^\circ\text{C min}^{-1}$  under  $\text{N}_2$  flow.

The following physicochemical analysis was done for FT15 due to its

**Table 1**

Parameters used for the synthesis of Fs and FTs.

Sample name	Molar ratios			pH <sup>a</sup>	Yield <sub>Fe</sub> (%) <sup>b</sup>	Yield <sub>Fe + thiamine</sub> (%) <sup>c</sup>
	NH <sub>3</sub>	Fe	Thiamine			
Thiamine-functionalized Fe <sub>3</sub> O <sub>4</sub> (FT)						
FT10	10	1	1	9.33	24.40 ± 0.36	11.02 ± 0.16
FT15	15	1	1	9.56	30.00 ± 0.09	13.56 ± 0.04
FT20	20	1	1	9.94	30.90 ± 0.33	13.96 ± 0.15
FT30	30	1	1	10.03	31.83 ± 1.26	14.38 ± 0.57
FT50	50	1	1	10.29	31.26 ± 0.63	14.13 ± 0.28
Control: unmodified Fe <sub>3</sub> O <sub>4</sub> (F)						
F10	10	1	0	9.70	20.26 ± 0.60	
F15	15	1	0	9.90	25.66 ± 1.56	
F20	20	1	0	10.18	26.14 ± 0.78	
F30	30	1	0	10.25	27.79 ± 0.45	
F50	50	1	0	10.19	24.88 ± 1.02	

<sup>a</sup> pH of solution at the end of the reaction.<sup>b</sup> The amount of product formed per amount of FeSO<sub>4</sub>·7H<sub>2</sub>O reactant used, calculated as Yield<sub>Fe</sub> =  $\frac{m_{product}}{m_{FeSO_4 \cdot 7H_2O}} \times 100\%$ .<sup>c</sup> The amount of product formed per amount of FeSO<sub>4</sub>·7H<sub>2</sub>O and thiamine reactants used, calculated as Yield<sub>Fe + thiamine</sub> =  $\frac{m_{product}}{m_{FeSO_4 \cdot 7H_2O} + m_{thiamine}} \times 100\%$ .

superior Cu(II) removal efficiency compared to the other FTs. Detailed analysis was also conducted on F15 as a control. More discussion regarding the selection of optimum synthesis parameters is described in Section 3.1. The Fourier transform infrared (FTIR) spectra were recorded using a Shimadzu Tracer-100 FTIR spectrophotometer with KBr pellets as the background. The morphology of prepared materials was examined by a high-resolution field-emission scanning electron microscope (SEM, JEOL JMS-6500 F) at an accelerating voltage of 15.0 kV. The magnetic property was determined by super-conducting quantum interference technique (MPMS3 SQUID) at 303 K. Chemical states of F15 and FT15 were determined using X-ray photoelectron spectroscopy (XPS, VG ESCALAB 250) with Al K $\alpha$  (1486.6 eV) source and 15–400 mm X-ray spot size, operated at 3 kV and 1 mA. The nitrogen (N<sub>2</sub>) adsorption-desorption isotherm was carried out at 77 K using a BELSORP-max analyzer. The samples were degassed using Belprep-vacII for 7 h at 353 K before the analysis. The specific surface area ( $A_s$ ) was calculated from the adsorption branch using the Brunauer–Emmett–Teller (BET) model. The surface charges and hydrodynamic diameter ( $D_h$ ) of F15 and FT15 were determined using a zeta potential analyzer (ZetaPALS, Brookhaven 90 Plus); each sample was prepared at a concentration of 1 mg mL<sup>-1</sup> in DI water prior for the analysis.

The pH point of zero charge (pH<sub>PZC</sub>) measurement was done according to a procedure described by Angkawijaya et al. (2020). In brief, a series of test solutions were prepared by adding 1 mg of sample into 1 mL of 0.1 M KNO<sub>3</sub> solution. The pH was adjusted from 2 to 10 using 0.1 M HCl solution or 0.1 M NaOH solution. The mixtures were then placed in an incubator at 30 °C under constant shaking (200 rpm). After 24 h, the final pH of the solutions was measured by a pH meter (Denver Instrument UB-10).

#### 2.4. Adsorption experiment

##### 2.4.1. Effect of pH

2.5 mg of F15 or FT15 was added into a series of 10 mL Cu(II) solutions at an initial concentration (C<sub>0</sub>) of 100 mg L<sup>-1</sup>. The Cu(II) solution

was prepared by dissolving CuCl<sub>2</sub>·2H<sub>2</sub>O in DI water. The pH of the solution was adjusted from 2 to 6 by adding 0.1 M HCl or NaOH. The mixture was then incubated at 30 °C and 200 rpm shaking. After 24 h, the adsorbent particles were separated from the solution using a magnet. The heavy metal ions content in the residual solutions were analyzed using an inductively coupled plasma-optical emission spectrometry (ICP-OES; Thermo iCAP 7000).

##### 2.4.2. Adsorption isotherm

The adsorption isotherm study was conducted with C<sub>0</sub> from 10 to 1000 mg L<sup>-1</sup> and an initial pH of ~5.0. Into the Cu(II) solution, 2.5 mg of either F15 or FT15 was added. The mixture was then incubated for 24 h at 30 °C and 200 rpm shaking. The residual concentration of Cu(II) was determined by ICP-OES. The adsorption capacity was then calculated according to Eq. (1):

$$Q_e = \frac{(C_0 - C_e)}{m} \times V \quad (1)$$

where Q<sub>e</sub> (mg g<sup>-1</sup>) is the equilibrium adsorption capacity, C<sub>0</sub> and C<sub>e</sub> (mg L<sup>-1</sup>) represent the initial and final concentrations of heavy metal ions, respectively, V (L) is the total volume of the solution, and m (g) is the mass of adsorbent.

The adsorption isotherm plots were constructed from the Q<sub>e</sub> vs C<sub>e</sub> data points and were fitted against five adsorption isotherm models (Langmuir, Freundlich, Temkin, Redlich-Peterson, and Sips). The adsorption data plotting and fitting were done using SigmaPlot 12.5 computer software.

##### 2.4.3. Adsorbent reusability

Adsorbent regeneration was carried out by immersing the post-adsorption FT15 particles (Cu@FT15) in a 1.5 M HCl solution. The particles were shaken in the solution overnight at 30 °C, followed by 3 times DI water washing and drying under vacuum (40 °C, 760 mmHg, 24 h). Subsequently, the amount of desorbed Cu(II) was measured using ICP-OES, and the desorption efficiency (%D) was calculated according to Eq. (2).

$$\%D = \frac{m_d}{m_t} \times 100\% \quad (2)$$

where m<sub>d</sub> (mg) is the amount of desorbed Cu(II) and m<sub>t</sub> (mg) is the total amount of Cu(II) in Cu@FT15. The adsorption efficiency (%) was calculated according to Eq. (3).

$$\% \text{Adsorption efficiency} = \frac{Q_n}{Q_e} \times 100\% \quad (3)$$

where Q<sub>n</sub> (mg g<sup>-1</sup>) is the adsorption capacity in the n<sup>th</sup> cycle, with n is the order of adsorption-desorption cycles.

## 3. Results and discussion

### 3.1. Effect of reactant molar ratio on the purity, yield, and adsorptivity potential of the synthesized materials

The crystallinity pattern was used to confirm the formation of Fe<sub>3</sub>O<sub>4</sub> and other Fe-oxidized species. Fig. 1a and b show the XRD patterns of FTs and Fs prepared at various molar ratios of NH<sub>3</sub>: Fe: thiamine. It can be observed that all synthesized samples (FT10–FT50) and their controls (F10–F50) have a certain degree of similarity to the typical XRD pattern of Fe<sub>3</sub>O<sub>4</sub> (COD 9009768) (Morel et al., 2008; Shaghholani et al., 2015). Specifically, the main peaks at 2θ of 30.3, 35.7, 43.4, 53.8, 57.3, and 62.9° which attributed to (200), (311), (400), (422), (511), and (440) planes of cubic inverse spinel Fe<sub>3</sub>O<sub>4</sub>. Additional peaks at 2θ of 20.9, 30.6, and 49.5° can be observed in F10, F20, F30, and F50 samples. The matching of the samples' XRD with the database also indicates the formation of other Fe-oxidized species, i.e., iron (III) oxide (Fe<sub>2</sub>O<sub>3</sub>) and iron

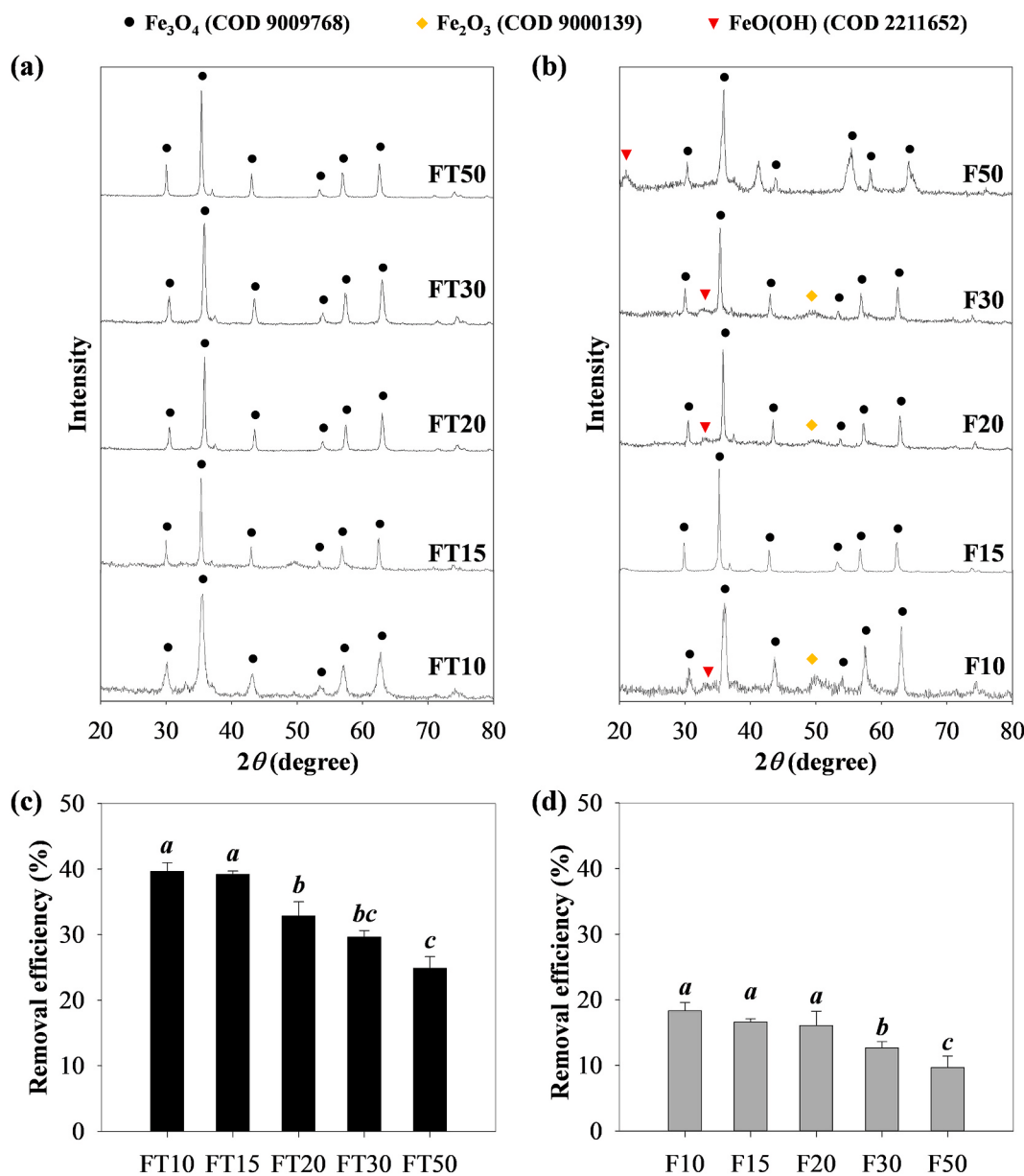
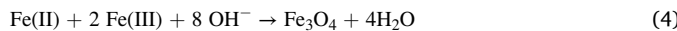


**Fig. 1.** XRD patterns of (a) thiamine-functionalized  $\text{Fe}_3\text{O}_4$  (FTs) and (b) unmodified  $\text{Fe}_3\text{O}_4$  (Fs) as controls. (c, d) The  $\text{Cu}(\text{II})$  removal efficiency of (c) FTs and (d) Fs. Different lowercase letters above the graph bars denote significant differences among different molar ratios of substrates (ANOVA and Tukey's test,  $p < 0.05$ ).

(III) oxide-hydroxide ( $\text{FeO(OH)}$ ). These species are the side products which might be generated during the formation of  $\text{Fe}_3\text{O}_4$ , as described in following reaction sequence in Eqs. (4)–(6) (Kiyama, 1974; Tamura et al., 1979; Alibeigi and Vaezi, 2008; Jiang et al., 2011; Fan et al., 2018).



Interestingly, no side products were detected in F15 samples; suggesting that a proper addition of  $\text{NH}_3$  (as the alkaline compound) may produce an appropriate ratio of  $\text{Fe}(\text{II})$  and  $\text{Fe}(\text{III})$  in the system, thus hinder the generation of  $\text{Fe}_2\text{O}_3$  and  $\text{FeO(OH)}$  (Alibeigi and Vaezi, 2008; Jiang et al., 2011). It is also worth mentioning that the addition of thiamine to the system (FT10–FT50) may inhibit the formation of  $\text{Fe}(\text{III})$  oxides, which is confirmed from the absence of the  $\text{Fe}_2\text{O}_3$  and  $\text{FeO(OH)}$  peaks in the recorded XRD patterns of FTs. This phenomenon can be

attributed to the metal chelating ability of thiamine, which may suppress the formation of  $\text{Fe}(\text{III})$  oxides (Cramer et al., 1981; Flora et al., 1986; Bencini and Borghi, 1987) and promote the generation of intermediate  $\text{Fe}(\text{II})$  and  $\text{Fe}(\text{III})$  hydroxide that readily transformed to  $\text{Fe}_3\text{O}_4$  (Pankratov and Anuchina, 2019). These results suggest that the optimum addition of  $\text{NH}_3$  and thiamine is necessary for synthesizing high purity  $\text{Fe}_3\text{O}_4$ , and suppressing  $\text{Fe}_2\text{O}_3$  and  $\text{FeO(OH)}$  formation.

Besides crystallinity, the optimum molar ratio of  $\text{NH}_3$ :  $\text{Fe}$ : thiamine for producing  $\text{Fe}_3\text{O}_4$ -based adsorbent was evaluated based on the product yield and their  $\text{Cu}(\text{II})$  removal efficiency. As presented in Table 1, the  $\text{Yield}_{\text{Fe}}$  of both FTs and Fs increased from 24.40% to 30.00% and 20.26%–25.66%, respectively, when the ratio of  $\text{NH}_3$  in the system was increased from 10 to 15. However, no significant difference was observed when a higher amount of  $\text{NH}_3$  was used. The amount of  $\text{NH}_3$  used in the formation of FTs and Fs was also shown to affect their  $\text{Cu}(\text{II})$  removal efficiency (Fig. 1c and d). Overall, the FTs showed higher  $\text{Cu}(\text{II})$  removal ability (ranging between 24.90 and 39.70%) compared to the Fs (with removal efficiency ranging between 9.67 and 18.35%). In Fig. 1c,

it can be observed that FT10 and FT15 possess the comparably high Cu (II) removal ability, that is 39.68% and 39.19%, while the FTs prepared at higher NH<sub>3</sub> amount (FT20, FT30, and FT50) showed lower potency. Similar trend can be observed for their respective control, where the F10, F15, and F20 demonstrated substantially higher Cu(II) removal efficiency compared to F30 and F50. It is also worth mentioning that the removal efficiency proportionally decreased with the reduced %mass of thiamine in the adsorbent. As shown in Figure S1, comparisons of the TGA curves of the control and the thiamine functionalized materials suggest that the substantially bigger mass loss in FTs are due to the presence of the thiamine in the sample (Chakravarty et al., 2010; Golubeva and Pavlova, 2014; Mallakpour and Sadaty, 2016). The TGA data reveals that FT10 and FT15 possess considerably high thiamine content of 20.81% and 22.29%, respectively, while the FT20, FT30, and

FT50 contain ~14.60%, 13.83%, and 11.51% weight of thiamine. The reduced thiamine content in FT20, FT30, and FT50 might be due to the occurrence of excess OH<sup>-</sup>, which inhibits the incorporation of thiamine to the Fe<sub>3</sub>O<sub>4</sub> core. These results imply that a molar ratio of NH<sub>3</sub>: Fe: thiamine 15:1:1 was the best condition for synthesizing FT with high yield, purity, and Cu(II) removal ability; thus, more detailed characterization and adsorption study were done for FT15 (and F15 as control).

### 3.2. Characterization of FT15

As presented in Fig. 2a and b, there are two deconvoluted peaks in the Fe 2p spectra of FT15 (711.5 eV and 725.4 eV) and F15 (711.2 eV and 725.5 eV). These peaks are assigned to Fe 2p<sub>1/2</sub> and Fe 2p<sub>3/2</sub>, which is in good accordance with the XPS spectra of magnetite (Fe<sub>3</sub>O<sub>4</sub>) (Saha

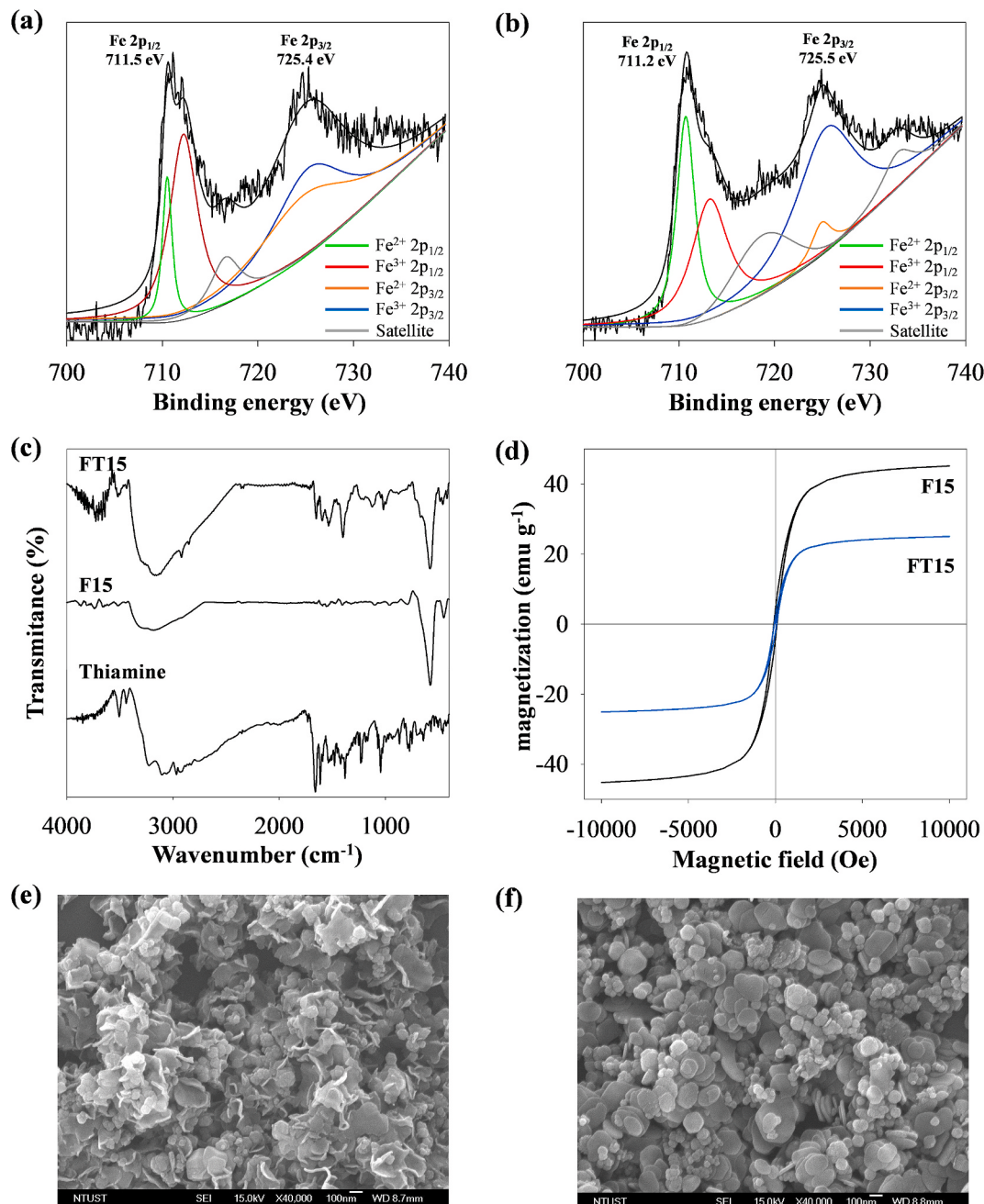


**Fig. 2.** Characterization of FT15. The XPS spectra of (a) FT15 and (b) F15. F15 data was provided as a control. (c) FTIR spectra of FT15, F15 and thiamine spectra were provided as a control. (d) Magnetization hysteresis loop of FT15 (blue plot) and control F15 (black plot). SEM images of (e) FT15 and (f) F15 as control. (For interpretation of the references to color in this figure legend, the reader is referred to the Web version of this article.)

et al., 2013; Travlou et al., 2013). Calculation of the Fe(II) to Fe(III) ratio resulted in the value of  $\sim 0.5$  (specifically, 0.54 for FT15 and 0.51 for F15), which further confirmed the formation of  $\text{Fe}_3\text{O}_4$  (Yamashita and Hayes, 2008). Fig. 2c shows the FTIR spectra of FT15 along with F15 as control and thiamine for reference. The peak corresponds to the vibration of Fe–O (Sui et al., 2015; Ahmad et al., 2020) can be observed at  $582 \text{ cm}^{-1}$  and  $575 \text{ cm}^{-1}$  for FT15 and F15, respectively; this peak also confirms the occurrence of  $\text{Fe}_3\text{O}_4$  in both samples. The N,S-functionalization of  $\text{Fe}_3\text{O}_4$  through the addition of thiamine was also confirmed from the appearance of thiamine characteristic peaks (Kolawole and Adeyemo, 1995; Jiang et al., 2014; Masoud et al., 2017): (1) at  $1652 \text{ cm}^{-1}$  and  $1597 \text{ cm}^{-1}$ , which attributed to the  $\text{NH}_2$  bending and  $\text{C}=\text{N}$  stretching; (2) the  $\text{C}=\text{C}$ ,  $\text{C}=\text{N}$  stretching of pyrimidine ring at  $1442$  and  $1539 \text{ cm}^{-1}$ ; (3) the  $\text{C}=\text{C}$ ,  $\text{C}=\text{N}$  stretching of thiazole ring at  $1367$  and  $1399 \text{ cm}^{-1}$ ; (4) the C–O stretching of the primary alcohol group at  $1043 \text{ cm}^{-1}$ ; and (5) the C–S stretching of thiazole group at  $760 \text{ cm}^{-1}$  in FT15 chromatogram. These results suggest the presence of both  $\text{Fe}_3\text{O}_4$  and thiamine-functional groups in FT15.

The magnetic properties of F15 and FT15 were evaluated by the magnetization vs. magnetic field ( $M - H$ ) variations curve, as shown in Fig. 2d. The magnetic hysteresis loop of both prepared-adsorbents mimics the typical S-shaped curves that passing through the origin with the presence of the remnant magnetization ( $M_r$ ) and coercivity field ( $H_c$ ) close to zero after the removal of external applied magnetic field. These suggest that both FT15 and F15 were superparamagnetic (Chomchoey et al., 2010) and indicate the properties of single-domain grains with the relatively stable magnetization (Muxworthy and Williams, 2006). FT15 and F15 exhibited the saturation magnetization ( $M_s$ )

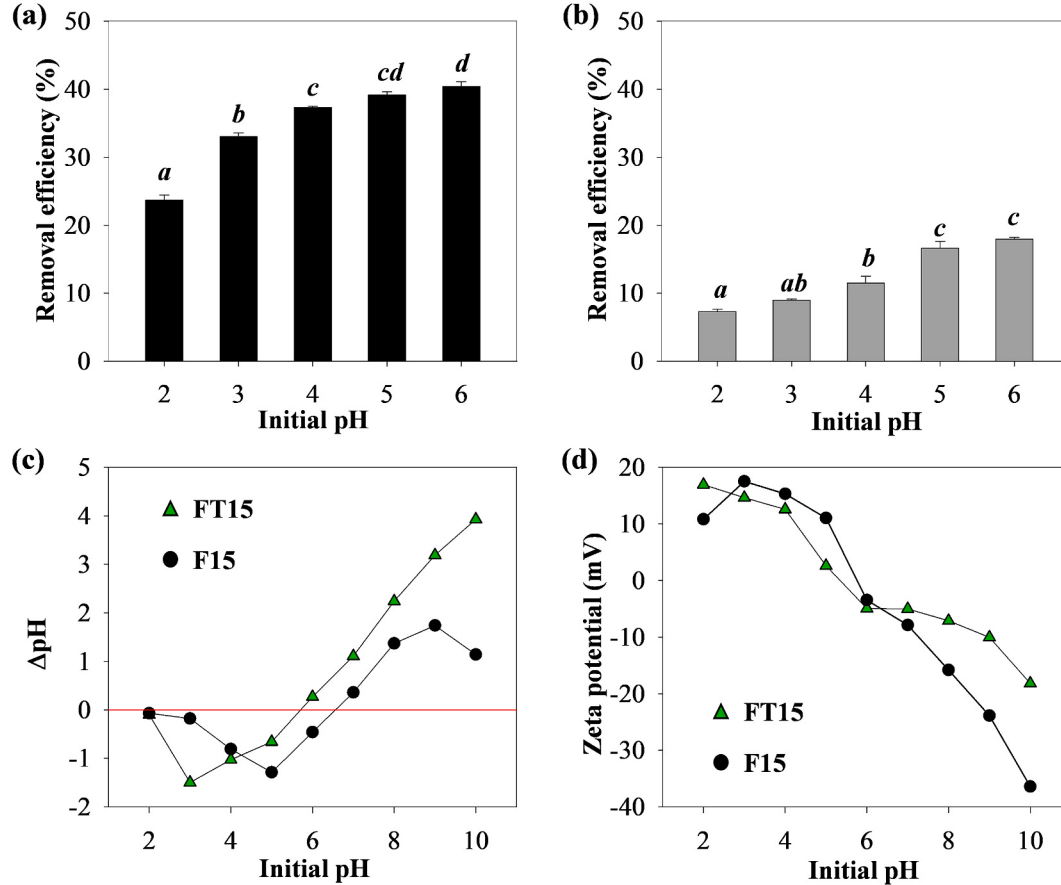
of  $25.06$  and  $45.21 \text{ emu g}^{-1}$ , respectively. The decrease of  $M_s$  after thiamine modification is attributed to the capping effect of the non-magnetic thiamine (Azizi and Heydari, 2014). Disregard of the reduced  $M_s$ , these values is postulated to be sufficient for magnetic recovery from the solution (Zhang et al., 2017).

Fig. 2e and f show the SEM micrograph of FT15 and F15, respectively. The SEM of FT15 reveals the combination of foliaceous and spherical-shaped particles, which is commonly observed in the SEM imaging of thiamine thus confirm the occurrence of thiamine within FT15 sample. On the other hand, a typical sub-spherical irregular particle similar to micrograph of  $\text{Fe}_3\text{O}_4$  (Ma et al., 2012) can be found in SEM images of both FT15 and F15. Based on the hydrodynamic size and the surface area of the FT15 ( $D_h = 552.0 \text{ nm}$  and  $a_s = 35.78 \text{ m}^2 \text{ g}^{-1}$ ) and F15 ( $D_h = 414.8 \text{ nm}$  and  $a_s = 25.25 \text{ m}^2 \text{ g}^{-1}$ ), it showed that thiamine functionalization caused an enlargement in the adsorbent particle size and provided bigger contact site for adsorbate removal. These characterizations results confirm the successful formation of superparamagnetic thiamine-functionalized  $\text{Fe}_3\text{O}_4$  with sufficient saturated magnetization to facilitate its recovery from the wastewater.

### 3.3. Study on the adsorption performance

#### 3.3.1. Effect of pH on the removal of Cu(II) by FT15 and F15

The pH of the solution exerts a profound influence on the removal of heavy metals in an aqueous solution due to the dynamic distribution of heavy metals species and ionic state of functional groups of the adsorbents at different pH (Pang et al., 2011). The influence of pH on the removal efficiency of Cu(II) is presented in Fig. 3a and b. The increase of



**Fig. 3.** Effect of pH on the Cu(II) removal efficiency of (a) FT15 and (b) F15 adsorbent. Different lowercase letters above the graph bars denote significant differences among different initial pH (ANOVA and Tukey's test,  $p < 0.05$ ). (c) The pH point of zero charge ( $\text{pH}_{\text{PZC}}$ ) and (d) zeta potential measurement of FT15 (green triangle symbols) at different initial pH. F15 data (black circle symbols) was provided as a control. (For interpretation of the references to color in this figure legend, the reader is referred to the Web version of this article.)

pH from 2 to 6 has a positive effect on the adsorption of Cu(II) by FT15 and F15, as implied by the surge increase of removal efficiency from 23.69% to 40.41% for FT15, and from 9.67% to 18.35% in control F15. This phenomenon might be caused by the availability of excess proton ( $H^+$ ) at pH < 5 that may block the active sites on the adsorbent surface ( $-NH_3^+$  and  $-OH$ ), thus reduce their affinity toward Cu(II) (Wang et al., 2011; Sharma et al., 2018). The lower Cu(II) removal efficiency at low pH might also be attributed to the occurrence of an equally positive charge between the adsorbent surface and Cu(II); as confirmed by its  $pH_{PZC}$  and zeta potential value (Fig. 3c and d).

The highest Cu(II) removal efficiency by FT15 and F15 occurred at pH 5.0 or 6.0; where these adsorbents have a negative surface charge at these pHs, as indicated from its negative zeta potential (Fig. 3d). The occurrence of negatively charged adsorbent and positively charged Cu(II) leads to electrostatic attraction, which promotes the removal efficiency of FT15 and F15. The FT15 and F15 were more negatively charged with zeta potential values of  $-5.02\text{ mV}$  and  $-7.87\text{ mV}$ , respectively, at pH 7, where these values reduced further to  $-18.18\text{ mV}$

and  $-36.44\text{ mV}$  at pH 10. While these negative surface charges may attract the positive-charged adsorbate, the likelihood may not be valid for the heavy metal-containing wastewater system since Cu(II) ion tends to form Cu(II) hydroxide precipitate at pH > 6, thus making it inaccessible for adsorbent uptake (Shen et al., 2012; Ahmad et al., 2020). Based on the high Cu(II) removal efficiency of FT15 and F15 at this particular pH and the unnecessary of pH adjustment (initial pH of Cu(II) solution), pH 5 was chosen as the best condition for the removal of Cu(II).

### 3.3.2. Adsorption isotherm

Fig. 4 shows the isotherm data ( $Q_e$  vs  $C_e$ ) of F15 and FT15 at  $30^\circ\text{C}$ . The adsorption curves of F15 and FT15 system can be classified as the typical L-type curve with subclass 2 according to the classification by Giles et al. The L-type curves were widely observed for the adsorption of ions in aqueous solutions and is typically found in the adsorption process driven by van der Waals forces; meanwhile, subclass 2 indicates no intermolecular interaction between the solutes (Giles et al., 1960; Piccin

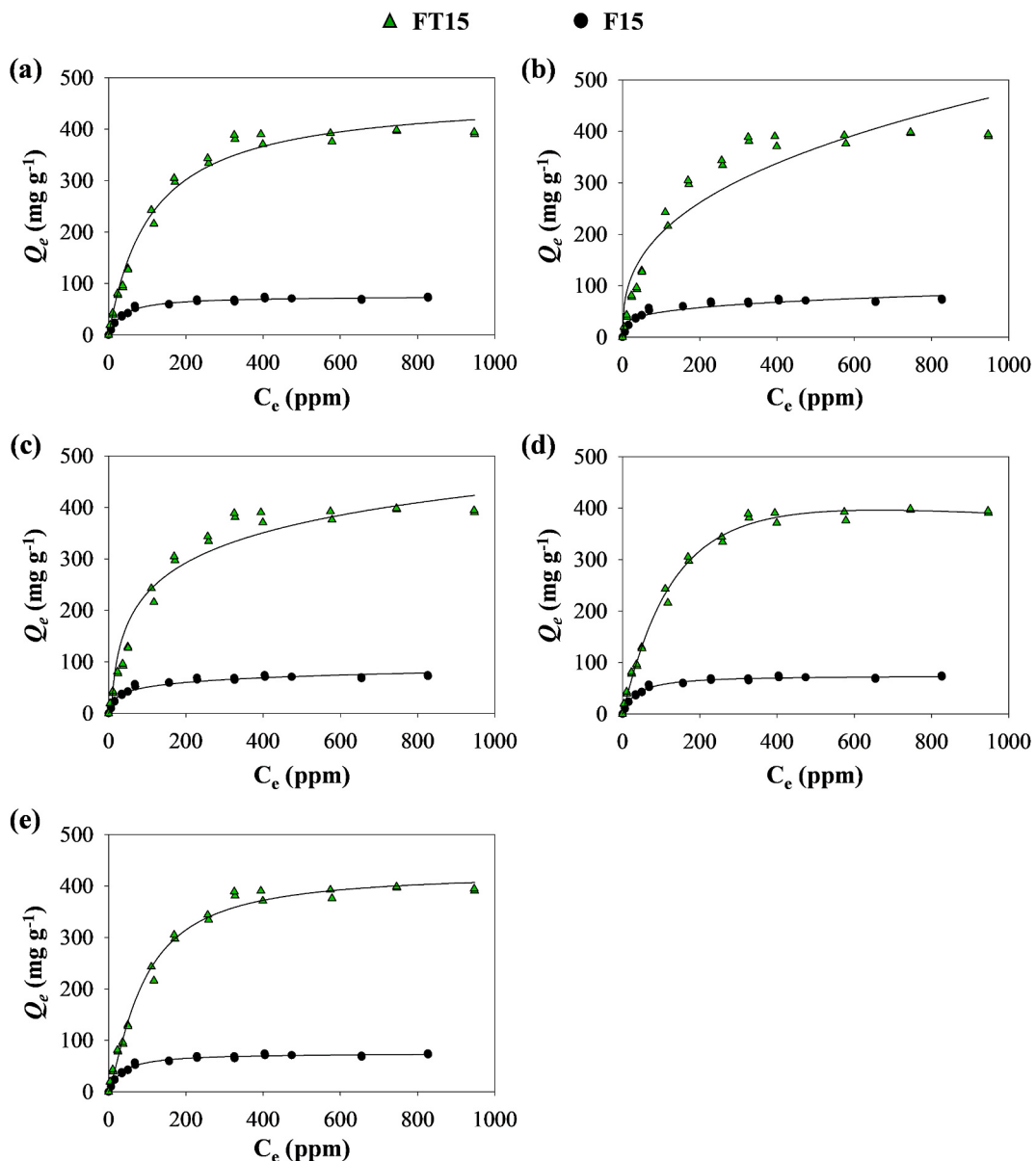


**Fig. 4.** Adsorption isotherm of Cu(II) onto FT15 (green triangle symbols). The solid lines represent the fits of (a) Langmuir, (b) Freundlich, (c) Temkin, (d) Redlich-Peterson, and (e) Sips isotherm models; F15 data (black circle symbols) was provided as control. (For interpretation of the references to color in this figure legend, the reader is referred to the Web version of this article.)

et al., 2017). A long plateau can also be observed in the experimental data of both adsorbents, which signify the saturation of the adsorbent monolayer (Giles et al., 1960).

The adsorption data were fitted with several isotherm models (Langmuir, Freundlich, Temkin, Redlich-Peterson, and Sips), and the fitting results were presented as the solid lines in Fig. 4, while the determined constants were summarized in Table 2. The two-parameter Langmuir and Freundlich models usually are employed to specify the adsorption behavior of the system. According to the model fitting, the Langmuir model gave better fits (with  $R^2 \sim 0.99$ ) for Cu(II) adsorption compared to the Freundlich models (with  $R^2 \sim 0.91$ ). This implies that the adsorption of Cu(II) onto F15 and FT15 are monolayer adsorption, the adsorption onto the surface of the adsorbent is uniform, and no interaction was found among the Cu(II) molecules (Langmuir, 1916). The dimensionless separation factor ( $R_L$ ), which was developed by Weber and Chakravorti, is another essential characteristic of the Langmuir model (Weber and Chakravorti, 1974). The  $R_L$  values of both F15 and FT15 fall within the range of 0–1 (specifically between 0.0391 and 0.9289), indicating the favorable adsorption of Cu(II) onto the investigated adsorbents. The favorability for the adsorption system also can be evaluated from the  $n_F$  value of the Freundlich model, which should have values ranging from 1 to 10 (Al-Ghouti and Da'ana, 2020). As listed in Table 2, the  $n_F$  of F15 and FT15 were found to be 4.117 and 2.704, respectively; indicating the favorability of the adsorption system. The Temkin model also gave a poor fitting to the adsorption data with an  $R^2$

**Table 2**  
The experimental maximum capacity ( $Q_{exp}$ ) and calculated isotherm parameters for Cu(II) adsorption onto FT15.

	FT15			F15 <sup>a</sup>		
$Q_{exp}$ (mg g <sup>-1</sup> )	397.400			73.400		
<b>Langmuir<sup>b</sup></b>						
$Q_L$ (mg g <sup>-1</sup> )	467.038	±	11.156	75.769	±	0.971
$K_L$ (L g <sup>-1</sup> )	0.009	±	0.001	0.029	±	0.002
$R^2$	0.986			0.988		
<b>Freundlich<sup>c</sup></b>						
$K_F$ (L g <sup>-1</sup> )	36.881	±	7.875	15.837	±	2.194
$\frac{1}{n_F}$	2.704	±	0.257	4.117	±	0.407
$R^2$	0.907			0.901		
<b>Temkin<sup>d</sup></b>						
$B$ (J mol <sup>-1</sup> )	84.197	±	4.320	13.072	±	0.617
$A_T$ (L g <sup>-1</sup> )	0.161	±	0.171	0.051	±	0.207
$R^2$	0.944			0.962		
<b>Redlich-Peterson<sup>e</sup></b>						
$K_{RP}$ (L g <sup>-1</sup> )	3.056	±	0.159	2.078	±	0.198
$\beta$	1.242	±	0.040	1.016	±	0.026
$a_{RP}$ (L mg <sup>-1</sup> )	0.001	±	0.000	0.025	±	0.006
$R^2$	0.995			0.989		
<b>Sips<sup>f</sup></b>						
$Q_s$ (mg g <sup>-1</sup> )	426.076	±	10.810	74.909	±	1.568
$s_p$	1.290	±	0.083	1.050	±	0.079
$a_s$ (mg L <sup>-1</sup> )	0.003	±	0.001	0.025	±	0.006
$R^2$	0.991			0.989		

The parameters were obtained by non-linear fitting with the following equations.

<sup>a</sup> F15 data was provided as control.

$$b \quad Q_e = \frac{Q_L \cdot K_L \cdot C_e}{1 + K_L \cdot C_e}; R_L = \frac{1}{1 + K_L \cdot C_0} \quad (\text{Langmuir, 1916}).$$

$$c \quad Q_e = K_F \cdot C_e^{n_F} \quad (\text{Freundlich, 1907}).$$

$$d \quad Q_e = B \cdot \ln(A_T \cdot C_e) \quad (\text{Temkin, 1940}).$$

$$e \quad Q_e = \frac{K_{RP} \cdot C_e}{1 + a_{RP} \cdot C_e^\beta} \quad (\text{Redlich and Peterson, 1959}).$$

$$f \quad Q_e = \frac{Q_s \cdot a_s \cdot C_e^{s_p}}{1 + a_s \cdot C_e^{s_p}} \quad (\text{Sips, 1948}).$$

0.962 for F15 and 0.944 for FT15 with the value of parameter  $B$  and  $A_T$  of Temkin model lies between 13.072 and 84.197 J mol<sup>-1</sup> and 0.051–0.161 L mg<sup>-1</sup>, respectively.

The isotherm models with three-parameter (i.e., Redlich-Peterson and Sips model) were also studied to validate the two-parameter models. The Redlich-Peterson and Sips models feature the adsorption mechanism of both Langmuir and Freundlich models, and they can be applied for either homogenous or heterogeneous systems (Hill, 1910; Al-Ghouti and Da'ana, 2020). Both Redlich-Peterson and Sips models showed a high correlation coefficient ( $R^2$  ranging from 0.989 to 0.995) to the experimental data. However, the Redlich-Peterson fitting overestimates the experimental value before the plateau region and underestimates after it reaches saturation (Fig. 4d). In addition, it can be observed that the calculated  $Q_{RP} = (K_{RP}/a_{RP})$  yielded a much higher value compared to the  $Q_{exp}$ . On the other hand, the  $Q_s$  from Sips fitting produced a closer maximum capacity value compared to the one obtained from the experimental data. These imply that the Sips model would best describe the adsorption isotherm. The homogeneity of the adsorption system can be predicted based on the Sips isotherm exponent ( $s_p$ ) value of F15 and FT15. These  $s_p$  values are nearly 1, which confirmed that both adsorbents possess homogeneous adsorption sites, and the Sips model would reduce to Langmuir rather than Freundlich model. A comprehensive comparison of several functionalized Fe<sub>3</sub>O<sub>4</sub> and Fe<sub>3</sub>O<sub>4</sub> composites as the adsorbent for Cu(II) removal is presented in Table S1 (Ahmad et al., 2020; Kalantari et al., 2014; Pang et al., 2011; Ren et al., 2012; Roy and Bhattacharya, 2012; Sui et al., 2015; Wang et al., 2017; Yi et al., 2018; Zhao et al., 2016). It is worth mentioning that the FT15 has superior adsorption capacity than the other reported adsorbent. Compared to F15, the adsorption capacity of FT15 is 5.69-fold higher, indicating the synergistic effect of thiamine on Cu removal. To gain insight into the mechanism of Cu removal by FT15, characterizations by means of XRD and FTIR analysis were done on the post-adsorption materials (Cu@FT15).

### 3.4. Post adsorption study

#### 3.4.1. Characterization of the spent adsorbent

Fig. 5a and b show the XRD and IR spectra of Cu(II)-containing FT15 (Cu@FT15). Compared to the one before adsorption, there are appearances of new peaks, particularly at 20 of 27.5, 29.1, 31.7, 32.5, 47.8, 58.3, and 59.3° which can be assigned to the crystal plane of CuO (COD 9016057) and CuS (COD 9009584). The IR spectra of the Cu@FT15 displayed a significant shift and disappearance of O–H and N–H stretching peaks. Four corresponding peaks were initially found in FT15, at 3513, 3433, 3293, and 3158 cm<sup>-1</sup>, and upon Cu(II) adsorption, only 1 peak at 3420 cm<sup>-1</sup> was found in the IR spectra of Cu@FT15. Several peak shifts also can be observed in the C=C, C=N stretching of pyrimidine ring (to 1467 and 1521 cm<sup>-1</sup>) and C=C, C=N stretching of thiazole ring (merged to 1352 cm<sup>-1</sup>) upon Cu(II) adsorption. In addition, the C–S stretching peaks, which initially occurred at 760 cm<sup>-1</sup>, also disappeared in the IR spectra of Cu@FT15. Several new bands attributed to the Cu–O and Cu–S bonds (Riyaz et al., 2016; Ho et al., 2017) can also be observed at 802 cm<sup>-1</sup> and 618 cm<sup>-1</sup>. These results suggest the involvement of the amine group, pyrimidine ring, and the thiazolium group of thiamine in FT15 during the Cu(II) adsorption.

Based on the characterization of post-adsorption FT15, the possible adsorption mechanism of Cu(II) onto the FT15 system is illustrated in Figure S2. The XRD and FTIR results showed the occurrence of Cu-oxide, Cu-sulfite species, along with the involvement of thiamine-functional groups (such as amine, hydroxyl, N,S-thiazolium ring, and N,S-pyrimidine ring) during the adsorption process. This suggests that the complexation between Cu(II) and functional groups of thiamine is the main cause of the Cu adsorption onto FT15.

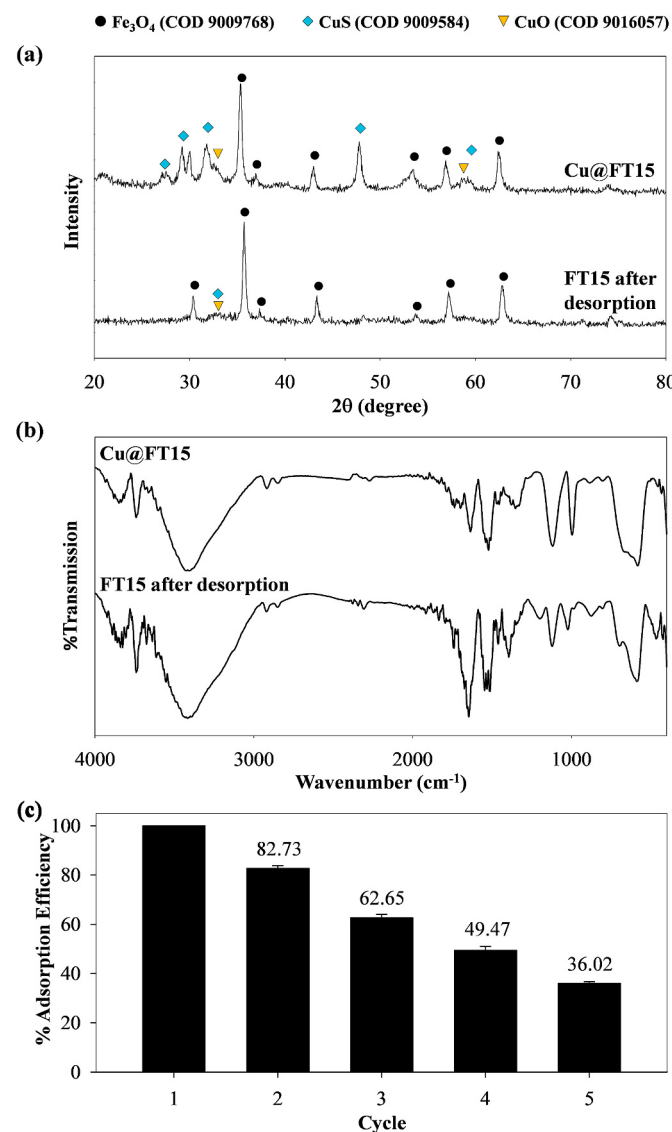


**Fig. 5.** (a) XRD patterns and (b) FTIR spectra of Cu@FT15 and FT15 after 1 time adsorption (upper panel) and desorption (lower panel). (c) Reusability of FT15 for Cu(II) removal after 5 adsorption-desorption cycles.

#### 3.4.2. Reusability study

Approximately 90% of Cu(II) can be desorbed and recovered from each adsorption-desorption cycle. As shown in Fig. 5c, the adsorption efficiency of the regenerated-FT15 decreased to 82.73% in the second cycle, and only ~36.02% efficiency remained after the fifth cycle. The reduction in its efficiency might be caused by the accumulation of undesorbed Cu(II) on the active sites of FT15. Characterization of the FT15 after desorption was done to elucidate its decreased adsorption efficiency. A small amount of Cu(II) compounds can be observed in both XRD (Fig. 5a, lower panel, 20 ~32°) and FTIR (Fig. 5b, lower panel, wavenumber 806 cm⁻¹) spectra of FT15 after desorption.

Further observation on the FTIR data of FT15 after desorption also showed the shifting and disappearance of several functional groups, particularly the NH<sub>2</sub> bending, C=N stretching of both pyrimidine and thiazolium rings, and the C-S stretching of thiazole group. These results confirm the incomplete elution and the loss of active sites on the adsorbent. Despite the substantial reduction of removal efficiency upon 5 adsorption-desorption cycles, the FT15 adsorption capacity is shown to be ~1.95-fold higher than the control unmodified Fe<sub>3</sub>O<sub>4</sub> (F15).

#### 4. Conclusion

The successful synthesis of thiamine modified-Fe<sub>3</sub>O<sub>4</sub> (FT) via one-step chemical oxidation and functionalization process was demonstrated in this work. The molar ratio of NH<sub>3</sub> to Fe to thiamine significantly affected the physicochemical properties and adsorption ability of the FTs. The FT synthesized at molar ratio (NH<sub>3</sub>:Fe:thiamine) of 15:1:1 showed a 5.69-fold higher adsorption capacity for Cu(II) removal than the unmodified Fe<sub>3</sub>O<sub>4</sub>. The occurrence of amine, pyrimidine, and thiazole groups in thiamine structure contributed to the enhanced adsorption capacity of the FT15. Based on the free active sites, the FT15 adsorbent exhibited close to 50% adsorption efficiency after 4 adsorption-desorption cycles. The enhanced adsorption capacity and reusability highlighted the potential application of FT15 as an adsorbent for wastewater treatment.

#### Declaration of competing interest

The authors declare that they have no known competing financial interests or personal relationships that could have appeared to influence the work reported in this paper.

#### Acknowledgements

This research was funded by Vietnam National Foundation for Science and Technology Development (NAFOSTED) under Grant Number 103.02-2020.64 to P.L. Tran-Nguyen. A.E. Angkawijaya is supported by the Taiwan Ministry of Science and Technology (MOST 109-2221-E-011-058 and MOST 110-2221-E-011-018) and National Taiwan University of Science and Technology (101H451403). S.P. Santoso is supported by the Widya Mandala Surabaya Catholic University (344a/WM01.5/N/2021).

#### Appendix A. Supplementary data

Supplementary data to this article can be found online at <https://doi.org/10.1016/j.chemosphere.2021.132759>.

#### Author contribution

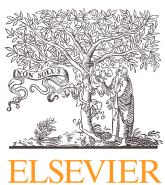
P.L.T.-N. and A.E.A. Conceptualization; Data curation; Funding acquisition; Investigation; Writing - review & editing. Q.N.H. Formal analysis; Investigation; Methodology; Visualization; Writing - original draft. Y.N.T.-C. Formal analysis; Investigation; Methodology. A.W.G. Supervision; Project administration; Resources; Writing - review & editing. V.B. and C.G. Formal analysis; Investigation. S.P.S. Supervision; Writing - review & editing. Y.-H.J. Supervision; Resources; Writing - review & editing.

#### References

- Ahmad, M., Wang, J., Xu, J., Zhang, Q., Zhang, B., 2020. Magnetic tubular carbon nanofibers as efficient Cu (II) ion adsorbent from wastewater. *J. Clean. Prod.* 252, 119825.
- Al-Ghouti, M.A., Da'ana, D.A., 2020. Guidelines for the use and interpretation of adsorption isotherm models: a review. *J. Hazard Mater.* 393, 122383.
- Al-Sayeh, S.A., El-Naas, M.H., Zaidi, S.J., 2017. Copper removal from industrial wastewater: a comprehensive review. *J. Ind. Eng. Chem.* 56, 35–44.
- Alibeigi, S., Vaezi, M.R., 2008. Phase transformation of iron oxide nanoparticles by varying the molar ratio of Fe<sup>2+</sup>:Fe<sup>3+</sup>. *Chem. Eng. Technol.* 31, 1591–1596.
- Anderson, R.A., 1997. Chromium as an essential nutrient for humans. *Regul. Toxicol. Pharmacol.* 26, S35–S41.
- Angkawijaya, A.E., Santoso, S.P., Bundjaja, V., Soetaredjo, F.E., Gunarto, C., Ayucitra, A., Ju, Y.-H., Go, A.W., Ismadji, S., 2020. Studies on the performance of bentonite and its composite as phosphate adsorbent and phosphate supplementation for plant. *J. Hazard Mater.* 399, 123130.
- Arora, R., 2019. Adsorption of heavy metals—A review. *Mater. Today: Proceedings* 18, 4745–4750.
- Aydin, H., Bulut, Y., Yerlikaya, C., 2008. Removal of copper (II) from aqueous solution by adsorption onto low-cost adsorbents. *J. Environ. Manag.* 87, 37–45.

- Azizi, K., Heydari, A., 2014. Vitamin B1 supported on silica-encapsulated  $\gamma$ -Fe<sub>2</sub>O<sub>3</sub> nanoparticles: design, characterization and application as a greener biocatalyst for highly efficient acylation. *RSC Adv.* 4, 8812–8816.
- Barceloux, D.G., 1999. Copper. *J. Toxicol. Clin. Toxicol.* 37, 217–230.
- Bencini, A., Borghi, E., 1987. Complexes of vitamin B1 with transition metal ions. Crystal and molecular structure of Zn(thiamine)Cl<sub>3</sub>·0.4H<sub>2</sub>O. *Inorg. Chim. Acta* 135, 85–91.
- Bhaumik, M., Maity, A., Srinivasu, V., Onyango, M.S., 2011. Enhanced removal of Cr (VI) from aqueous solution using polypyrrole/Fe<sub>3</sub>O<sub>4</sub> magnetic nanocomposite. *J. Hazard Mater.* 190, 381–390.
- Boyer, C., Whittaker, M.R., Bulmus, V., Liu, J., Davis, T.P., 2010. The design and utility of polymer-stabilized iron-oxide nanoparticles for nanomedicine applications. *NPG Asia Mater.* 2, 23–30.
- Briffa, J., Sinagra, E., Blundell, R., 2020. Heavy metal pollution in the environment and their toxicological effects on humans. *Heliyon* 6, e04691.
- Burakov, A.E., Galunin, E.V., Burakova, I.V., Kucherova, A.E., Agarwal, S., Tkachev, A.G., Gupta, V.K., 2018. Adsorption of heavy metals on conventional and nanostructured materials for wastewater treatment purposes: a review. *Ecotoxicol. Environ. Saf.* 148, 702–712.
- Chaki, S., Malek, T.J., Chaudhary, M., Tailor, J., Deshpande, M., 2015. Magnetite Fe<sub>3</sub>O<sub>4</sub> nanoparticles synthesis by wet chemical reduction and their characterization. *Adv. Nat. Sci. Nanosci. Nanotechnol.* 6, 035009.
- Chakravarty, P., Berendt, R.T., Munson, E.J., Young Jr., V.G., Govindarajan, R., Suryanarayanan, R., 2010. Insights into the dehydration behavior of thiamine hydrochloride (vitamin B1) hydrates: Part II. *J. Pharmaceut. Sci.* 99, 1882–1895.
- Chomchoe, N., Bhongsuwan, D., Bhongsuwan, T., 2010. Magnetic properties of magnetite nanoparticles synthesized by oxidative alkaline hydrolysis of iron powder. *Agriculture and Natural Resources* 44, 963–971.
- Cramer, R.E., Maynard, R.B., Ibers, J.A., 1981. A metal ion complex of vitamin B1: the preparation and structure of Cd(thiamine)Cl<sub>3</sub>·0.6H<sub>2</sub>O. *J. Am. Chem. Soc.* 103, 76–81.
- De Gisi, S., Lofrano, G., Grassi, M., Notarnicola, M., 2016. Characteristics and adsorption capacities of low-cost sorbents for wastewater treatment: a review. *Sustainable Materials and Technologies* 9, 10–40.
- Do Kim, K., Kim, S.S., Choa, Y.-H., Kim, H.T., 2007. Formation and surface modification of Fe<sub>3</sub>–O<sub>4</sub> nanoparticles by co-precipitation and sol-gel method. *J. Ind. Eng. Chem.* 13, 1137–1141.
- Fan, J., Zhao, Z., Ding, Z., Liu, J., 2018. Synthesis of different crystallographic FeOOH catalysts for peroxymonosulfate activation towards organic matter degradation. *RSC Adv.* 8, 7269–7279.
- Flora, S.J., Singh, S., Tandon, S.K., 1986. Chelation in metal intoxication XVIII: combined effects of thiamine and calcium disodium versenate on lead toxicity. *Life Sci.* 38, 67–71.
- Freundlich, H., 1907. Über die adsorption in lösungen. *Z. Phys. Chem.* 57, 385–470.
- Giles, C.H., MacEwan, T.H., Nakhwa, S.N., Smith, D., 1960. 786. Studies in adsorption. Part XI. A system of classification of solution adsorption isotherms, and its use in diagnosis of adsorption mechanisms and in measurement of specific surface areas of solids. *J. Chem. Soc.* 3973–3993.
- Golubeva, O.Y., Pavlova, S.V., 2014. Adsorption of thiamine hydrochloride (vitamin B1) by synthetic layered silicates with a montmorillonite structure. *Glass Phys. Chem.* 40, 375–379.
- Hill, A.V., 1910. The possible effects of the aggregation of the molecules of haemoglobin on its dissociation curves. *J. Physiol.* 40, 4–7.
- Ho, W.C.J., Tay, Q., Qi, H., Huang, Z., Li, J., Chen, Z., 2017. Photocatalytic and adsorption performances of faceted cuprous oxide (Cu<sub>2</sub>O) particles for the removal of methyl orange (MO) from aqueous media. *Molecules* 22, 677.
- Hu, F., Wei, L., Zhou, Z., Ran, Y., Li, Z., Gao, M., 2006. Preparation of biocompatible magnetite nanocrystals for in vivo magnetic resonance detection of cancer. *Adv. Mater.* 18, 2553–2556.
- Ilijinas, A., Brucas, R., Stankus, V., Dudonis, J., 2005. Synthesis of Fe<sub>3</sub>O<sub>4</sub> thin films by solid state reactions. *Mater. Sci. Eng. C* 25, 590–594.
- Jiang, F., Ye, H., Li, H., Sun, K., Yin, J., Zhu, H., 2018. Metal complexes of folic acid for lithium ion storage. *Chem. Commun.* 54, 4971–4974.
- Jiang, L., Li, M., Li, C., Sun, H., Xu, L., Jin, B., Liu, Y., 2014. Terahertz spectra of L-ascorbic acid and thiamine hydrochloride studied by terahertz spectroscopy and density functional theory. *J. Infrared, Millim. Terahertz Waves* 35, 871–880.
- Jiang, W., Lai, K.-L., Hu, H., Zeng, X.-B., Lan, F., Liu, K.-X., Wu, Y., Gu, Z.-W., 2011. The effect of [Fe3+]/[Fe2+] molar ratio and iron salts concentration on the properties of superparamagnetic iron oxide nanoparticles in the water/ethanol/toluene system. *J. Nanoparticle Res.* 13, 5135.
- Jordan, J., Kumar, C.S., Theegala, C., 2011. Preparation and characterization of cellulase-bound magnetite nanoparticles. *J. Mol. Catal. B Enzym.* 68, 139–146.
- Kalantari, K., Ahmad, M.B., Masoumi, H.R.F., Shamel, K., Basri, M., Khandanlou, R., 2014. Rapid adsorption of heavy metals by Fe<sub>3</sub>O<sub>4</sub>/talc nanocomposite and optimization study using response surface methodology. *Int. J. Mol. Sci.* 15, 12913–12927.
- Kalia, S., Kango, S., Kumar, A., Haldorai, Y., Kumari, B., Kumar, R., 2014. Magnetic polymer nanocomposites for environmental and biomedical applications. *Colloid Polym. Sci.* 292, 2025–2052.
- Khollam, Y., Dhage, S., Potdar, H., Deshpande, S., Bakare, P., Kulkarni, S., Date, S., 2002. Microwave hydrothermal preparation of submicron-sized spherical magnetite (Fe<sub>3</sub>O<sub>4</sub>) powders. *Mater. Lett.* 56, 571–577.
- Kinuthia, G.K., Ngure, V., Beti, D., Lugalia, R., Wangila, A., Kamau, L., 2020. Levels of heavy metals in wastewater and soil samples from open drainage channels in Nairobi, Kenya: community health implication. *Sci. Rep.* 10, 8434.
- Kiyama, M., 1974. Conditions for the formation of Fe<sub>3</sub>O<sub>4</sub> by the air oxidation of Fe(OH)<sub>2</sub> suspensions. *Bull. Chem. Soc. Jpn.* 47, 1646–1650.
- Kolawole, G.A., Adeyemo, A.O., 1995. Iron (III) complexes of vitamin B1 and those of bromo, iodo, perchlorato, and thiocyanato analogues. *Synth. React. Inorg. Met. Org. Chem.* 25, 1597–1619.
- Langmuir, I., 1916. The constitution and fundamental properties of solids and liquids. Part I. Solids. *J. Am. Chem. Soc.* 38, 2221–2295.
- Le, T.T.H., Nguyen, X.H., Hai, N.T.L., Phu, N.D., Hai, N.H., 2010. Arsenic removal by Fe<sub>3</sub>O<sub>4</sub> Nanoparticles and microorganisms. *Science and Technology Journal of Agriculture and Rural Development*.
- Liu, J.-F., Zhao, Z.-S., Jiang, G.-B., 2008. Coating Fe<sub>3</sub>O<sub>4</sub> magnetic nanoparticles with humic acid for high efficient removal of heavy metals in water. *Environ. Sci. Technol.* 42, 6949–6954.
- Lu, X., Mao, H., Chao, D., Zhang, W., Wei, Y., 2006. Ultrasonic synthesis of polyaniiline nanotubes containing Fe<sub>3</sub>O<sub>4</sub> nanoparticles. *J. Solid State Chem.* 179, 2609–2615.
- Ma, P., Luo, Q., Chen, J., Gan, Y., Du, J., Ding, S., Xi, Z., Yang, X.J.I.j.o.n., 2012. Intraperitoneal injection of magnetic Fe3O4-nanoparticle induces hepatic and renal tissue injury via oxidative stress in mice, 7, 4809.
- Mahdavian, A.R., Mirrahimi, M.A.-S., 2010. Efficient separation of heavy metal cations by anchoring polyacrylic acid on superparamagnetic magnetite nanoparticles through surface modification. *Chem. Eng. J.* 159, 264–271.
- Mallakpour, S., Sadaty, M.A., 2016. Thiamine hydrochloride (vitamin B1) as modifier agent for TiO<sub>2</sub> nanoparticles and the optical, mechanical, and thermal properties of poly (vinyl chloride) composite films. *RSC Adv.* 6, 92596–92604.
- Masoud, M.S., Ghareeb, D.A., Ahmed, S.S., 2017. Synthesis, characterization, spectral, thermal analysis and computational studies of thiamine complexes. *J. Mol. Struct.* 1137, 634–648.
- Morel, A.-L., Nikitenko, S.I., Gionnet, K., Wattiaux, A., Lai-Kee-Him, J., Labrugere, C., Chevalier, B., Deleris, G., Petibois, C., Brisson, A., 2008. Sonochemical approach to the synthesis of Fe<sub>3</sub>O<sub>4</sub>@SiO<sub>2</sub> core–shell nanoparticles with tunable properties. *ACS Nano* 2, 847–856.
- Muxworthy, A.R., Williams, W., 2006. Critical single-domain/multidomain grain sizes in noninteracting and interacting elongated magnetite particles: implications for magnetosomes. *J. Geophys. Res.: Solid Earth* 111.
- Nasongkla, N., Bey, E., Ren, J., Ai, H., Khemtong, C., Guthi, J.S., Chin, S.-F., Sherry, A.D., Boothman, D.A., Gao, J., 2006. Multifunctional polymeric micelles as cancer-targeted, MRI-ultrasensitive drug delivery systems. *Nano Lett.* 6, 2427–2430.
- Obasi, P.N., Akudinobi, B.B., 2020. Potential health risk and levels of heavy metals in water resources of lead-zinc mining communities of Abakaliki, southeast Nigeria. *Appl. Water Sci.* 10, 184.
- Olivares, M., Uauy, R., 1996. Copper as an essential nutrient. *Am. J. Clin. Nutr.* 63, 791s–796s.
- Pang, Y., Zeng, G., Tang, L., Zhang, Y., Liu, Y., Lei, X., Li, Z., Zhang, J., Xie, G., 2011. PEI-grafted magnetic porous powder for highly effective adsorption of heavy metal ions. *Desalination* 281, 278–284.
- Pankratov, D.A., Anuchina, M.M., 2019. Nature-inspired synthesis of magnetic non-stoichiometric Fe3O4 nanoparticles by oxidative in situ method in a humic medium. *Mater. Chem. Phys.* 231, 216–224.
- Parida, K., Mishra, K.G., Dash, S.K., 2012. Adsorption of copper (II) on NH<sub>2</sub>-MCM-41 and its application for epoxidation of styrene. *Ind. Eng. Chem. Res.* 51, 2235–2246.
- Piccin, J.S., Cadaval, T.R.S.A., de Pinto, L.A., Dotto, G.L., 2017. Adsorption isotherms in liquid Phase: experimental, modeling, and interpretations. In: Bonilla-Petriciolet, A., Mendoza-Castillo, D.I., Reynel-Ávila, H.E. (Eds.), *Adsorption Processes for Water Treatment and Purification*. Springer International Publishing, Cham, pp. 19–51.
- Rajabi, S.K., Sohrabnezhad, S., Ghafourian, S., 2016. Fabrication of Fe<sub>3</sub>O<sub>4</sub>@CuO core-shell from MOF based materials and its antibacterial activity. *J. Solid State Chem.* 244, 160–163.
- Rashid, R., Shafiq, I., Akhter, P., Iqbal, M.J., Hussain, M., 2021. A state-of-the-art review on wastewater treatment techniques: the effectiveness of adsorption method. *Environ. Sci. Pollut. Control Ser.* 28, 9050–9066.
- Redlich, O., Peterson, D.L., 1959. A useful adsorption isotherm. *J. Phys. Chem.* 63, 1024–1024.
- Ren, J., Bopape, M.F., Setshedi, K., Kitinya, J.O., Onyango, M.S., 2012. Sorption of Pb (II) and Cu (II) by Low-Cost magnetic eggshells-Fe<sub>3</sub>O<sub>4</sub> powder. *Chem. Ind. Chem. Eng. Q.* 18, 221–231.
- Riyaz, S., Parveen, A., Azam, A., 2016. Microstructural and optical properties of CuS nanoparticles prepared by sol–gel route. *Perspectives in Science* 8, 632–635.
- Roy, A., Bhattacharya, J., 2012. Removal of Cu (II), Zn (II) and Pb (II) from water using microwave-assisted synthesized maghemite nanotubes. *Chem. Eng. J.* 211, 493–500.
- Saha, A.K., Sharma, P., Sohn, H.-B., Ghosh, S., Das, R.K., Hebard, A.F., Zeng, H., Balagand, C., Walter, G.A., Moudgil, B.M., 2013. Fe doped CdTeS magnetic quantum dots for bioimaging. *J. Mater. Chem. B* 1, 6312–6320.
- Samal, S., Das, R., Dey, R., Acharya, S., 2000. Chelating resins VI: chelating resins of formaldehyde condensed phenolic Schiff bases derived from 4, 4'-diaminodiphenyl ether with hydroxybenzaldehydes—synthesis, characterization, and metal ion adsorption studies. *J. Appl. Polym. Sci.* 77, 967–981.
- Shaghholani, H., Ghoreishi, S.M., Mousazadeh, M., 2015. Improvement of interaction between PVA and chitosan via magnetite nanoparticles for drug delivery application. *Int. J. Biol. Macromol.* 78, 130–136.
- Shan, C., Ma, Z., Tong, M., Ni, J., 2015. Removal of Hg (II) by poly (1-vinylimidazole)-grafted Fe<sub>3</sub>O<sub>4</sub>@SiO<sub>2</sub> magnetic nanoparticles. *Water Res.* 69, 252–260.
- Sharma, P., Singh, A.K., Shahi, V.K., 2018. Selective adsorption of Pb (II) from aqueous medium by cross-linked chitosan-functionalized graphene oxide adsorbent. *ACS Sustain. Chem. Eng.* 7, 1427–1436.
- Shaterian, H.R., Molaei, P., 2019. Fe<sub>3</sub>O<sub>4</sub>@vitamin B1 as a sustainable superparamagnetic heterogeneous nanocatalyst promoting green synthesis of trisubstituted 1, 3-thiazole derivatives. *Appl. Organomet. Chem.* 33, e4964.

- Shen, H., Pan, S., Zhang, Y., Huang, X., Gong, H., 2012. A new insight on the adsorption mechanism of amino-functionalized nano- $\text{Fe}_3\text{O}_4$  magnetic polymers in Cu (II), Cr (VI) co-existing water system. *Chem. Eng. J.* 183, 180–191.
- Sips, R., 1948. On the structure of a catalyst surface. *J. Chem. Phys.* 16, 490–495.
- Sud, D., Mahajan, G., Kaur, M., 2008. Agricultural waste material as potential adsorbent for sequestering heavy metal ions from aqueous solutions—A review. *Bioresour. Technol.* 99, 6017–6027.
- Sui, N., Wang, L., Wu, X., Li, X., Sui, J., Xiao, H., Liu, M., Wan, J., William, W.Y., 2015. Polyethylenimine modified magnetic graphene oxide nanocomposites for  $\text{Cu}^{2+}$  removal. *RSC Adv.* 5, 746–752.
- Sun, Y., Tian, Y., He, M., Zhao, Q., Chen, C., Hu, C., Liu, Y., 2012. Controlled synthesis of  $\text{Fe}_3\text{O}_4/\text{Ag}$  core-shell composite nanoparticles with high electrical conductivity. *J. Electron. Mater.* 41, 519–523.
- Tamaura, Y., Chyo, G.S., Katsura, T., 1979. The  $\text{Fe}_3\text{O}_4$ -formation by the ‘Ferrite Process’: oxidation of the reactive  $\text{Fe(OH)}_2$  suspension induced by sucrose. *Water Res.* 13, 21–31.
- Tang, N., Zhong, W., Jiang, H., Wu, X., Liu, W., Du, Y., 2004. Nanostructured magnetite ( $\text{Fe}_3\text{O}_4$ ) thin films prepared by sol-gel method. *J. Magn. Magn. Mater.* 282, 92–95.
- Temkin, M., 1940. Kinetics of ammonia synthesis on promoted iron catalysts. *Acta physiochim. URSS* 12, 327–356.
- Travlou, N.A., Kyzas, G.Z., Lazaridis, N.K., Deliyanni, E.A., 2013. Functionalization of graphite oxide with magnetic chitosan for the preparation of a nanocomposite dye adsorbent. *Langmuir* 29, 1657–1668.
- Wang, F., Zhang, L., Wang, Y., Liu, X., Rohani, S., Lu, J., 2017.  $\text{Fe}_3\text{O}_4@\text{SiO}_2@\text{CS-TETA}$  functionalized graphene oxide for the adsorption of methylene blue (MB) and Cu (II). *Appl. Surf. Sci.* 420, 970–981.
- Wang, X., Liang, X., Wang, Y., Wang, X., Liu, M., Yin, D., Xia, S., Zhao, J., Zhang, Y., 2011. Adsorption of Copper (II) onto activated carbons from sewage sludge by microwave-induced phosphoric acid and zinc chloride activation. *Desalination* 278, 231–237.
- Weber, T.W., Chakravorti, R.K., 1974. Pore and solid diffusion models for fixed-bed adsorbers. *AIChE J* 20, 228–238.
- Yamashita, T., Hayes, P., 2008. Analysis of XPS spectra of  $\text{Fe}^{2+}$  and  $\text{Fe}^{3+}$  ions in oxide materials. *Appl. Surf. Sci.* 254, 2441–2449.
- Yi, X., He, J., Guo, Y., Han, Z., Yang, M., Jin, J., Gu, J., Ou, M., Xu, X., 2018. Encapsulating  $\text{Fe}_3\text{O}_4$  into calcium alginate coated chitosan hydrochloride hydrogel beads for removal of Cu (II) and U (VI) from aqueous solutions. *Ecotoxicol. Environ. Saf.* 147, 699–707.
- Zhang, J., Han, J., Wang, M., Guo, R., 2017.  $\text{Fe}_3\text{O}_4/\text{PANI}/\text{MnO}_2$  core-shell hybrids as advanced adsorbents for heavy metal ions. *J. Mater. Chem.* 5, 4058–4066.
- Zhao, J., Liu, J., Li, N., Wang, W., Nan, J., Zhao, Z., Cui, F., 2016. Highly efficient removal of bivalent heavy metals from aqueous systems by magnetic porous  $\text{Fe}_3\text{O}_4-\text{MnO}_2$ : adsorption behavior and process study. *Chem. Eng. J.* 304, 737–746.
- Zhu, Y.-T., Ren, X.-Y., Liu, Y.-M., Wei, Y., Qing, L.-S., Liao, X., 2014. Covalent immobilization of porcine pancreatic lipase on carboxyl-activated magnetic nanoparticles: characterization and application for enzymatic inhibition assays. *Mater. Sci. Eng. C* 38, 278–285.



## Studies on the performance of functionalized $\text{Fe}_3\text{O}_4$ as phosphate adsorbent and assessment to its environmental compatibility

Artik Elisa Angkawijaya<sup>a,\*</sup>, Yen Nhi Tran-Chuong<sup>b,†</sup>, Quoc Nam Ha<sup>b,‡</sup>, Phuong Lan Tran-Nguyen<sup>c</sup>, Shella Permatasari Santoso<sup>d,b</sup>, Vania Bundjaja<sup>b</sup>, Alchris Woo Go<sup>a</sup>, Hsien-Yi Hsu<sup>e,f</sup>, Yi-Hsu Ju<sup>a,b,g</sup>

<sup>a</sup> Graduate Institute of Applied Science, National Taiwan University of Science and Technology, #43, Sec. 4, Keelung Rd., Taipei, Taiwan

<sup>b</sup> Department of Chemical Engineering, National Taiwan University of Science and Technology, #43, Sec. 4, Keelung Rd., Taipei, Taiwan

<sup>c</sup> Department of Mechanical Engineering, Can Tho University, 3/2 Street, Can Tho City, Vietnam

<sup>d</sup> Department of Chemical Engineering, Widya Mandala Surabaya Catholic University, Kalijudan 37, Surabaya, Indonesia

<sup>e</sup> School of Energy and Environment & Department of Materials Science and Engineering, City University of Hong Kong, Kowloon Tong, Hong Kong, China

<sup>f</sup> Shenzhen Research Institute of City University of Hong Kong, Shenzhen, China

<sup>g</sup> Taiwan Building Technology Center, National Taiwan University of Science and Technology, #43, Sec. 4, Keelung Rd., Taipei, Taiwan



### ARTICLE INFO

#### Article History:

Received 14 September 2021

Revised 9 November 2021

Accepted 22 November 2021

Available online 12 December 2021

#### Keywords:

eutrophication  
phosphate removal  
thiamine  
magnetic iron oxide  
adsorption  
plant growth

### ABSTRACT

**Background:** The pressing demand to increase agricultural productivity amid the rapidly growing population has exponentially boosted fertilizers usage. Phosphate (Pi) runoff from fertilizers induces eutrophication in water sources and severely affects its surrounding ecosystems. To cope with Pi accumulation problem, this study reported the synthesis of an environmentally friendly magnetic adsorbent, namely  $\text{Fe}_3\text{O}_4$ /thiamine (thF).

**Method:** A one-step chemical oxidation and functionalization technique for thF synthesis was developed. X-ray diffraction (XRD), X-ray photoelectron spectroscopy (XPS), Fourier-transform infrared spectroscopy (FTIR), nitrogen ( $\text{N}_2$ ) sorption, and superconducting quantum interference device (SQUID) analysis were conducted to ensure the formation of  $\text{Fe}_3\text{O}_4$ , confirm the successful incorporation of thiamine, and gain insight into the factors influencing the adsorptivity of thF-363.

**Significant Findings:** The thF synthesized at 363 K (thF-363) produces an adsorbent with the highest Pi removal efficiency compared to other synthesis conditions. The thF-363 showed up to 1.51-fold higher adsorption capacity than the unmodified  $\text{Fe}_3\text{O}_4$ . The large surface area and occurrence of thiamine functional groups are the contributing factors in enhancing its adsorption capacity for Pi removal. The thF-363 did not adversely affect the growth of the model plant, *Arabidopsis thaliana*; demonstrating its suitability as an environmentally friendly adsorbents for Pi removal from eutrophicated water with the feasibility of magnetic separation from an aqueous system.

© 2021 Taiwan Institute of Chemical Engineers. Published by Elsevier B.V. All rights reserved.

### 1. Introduction

Phosphorus in phosphate (Pi) form is essential for every organism, including humans, animals, and plants. Appropriate Pi intake is majorly related to bone–teeth health and overall growth for animals and humans [1]. Similarly, Pi availability is also affiliated to plant vigor, where Pi deficiency had been acknowledged to affect root growth. The prolonged starvation eventually can be detrimental to the sustainability of agriculture [2,3]. Due to its indispensable nature,

most global Pi consumption is allocated for the production of fertilizers and animal feed supplements [4,5]. Pi-fertilizers are regularly applied on agricultural soil to maintain adequate-high levels of Pi to satisfy the plant demand for growth and development. However, only less than half of the administered Pi is absorbed by crops while the remainder is leached to the environment through soil and often end-up in water [6,7]. Accumulation of Pi in the water body had been acknowledged as the primary cause of eutrophication which sets off a series of detrimental effects in the aquatic ecosystem; from the algal bloom to the generation of hypoxic or anoxic ‘dead zone’ which affect the availability of oxygen in water [8]. To alleviate this issue, various methods such as chemical precipitation, biological treatment, anion exchange, electro-coagulation, acid-thermal treatment, and adsorption have been developed to efficiently remove

\* Corresponding Author: Artik Elisa Angkawijaya, Graduate Institute of Applied Science, National Taiwan University of Science and Technology

E-mail addresses: [artikelisa@mail.ntust.edu.tw](mailto:artikelisa@mail.ntust.edu.tw), [artikelisa@yahoo.com](mailto:artikelisa@yahoo.com)  
(A.E. Angkawijaya).

† These authors contribute equally.

excess Pi from water resources [9–16]. Among them, adsorption is one of the most used methods in managing Pi concentration in water, owing to its inexpensive and straightforward operation.

Several composite adsorbents prepared from a combination of inorganic and organic compounds had been widely used for Pi removal application. For instance, MgO/biochar possessed Pi adsorption capacity up to 122 mg/g [17], the adsorption capacity of montmorillonite-iron crosslinked alginate, and its zirconium modified alginate can reach 48.78 mg/g and 67.72 mg/g, respectively [18,19]. While various adsorbents with excellent adsorption capacity for Pi removal had been developed, separation of the post-adsorption adsorbent from the water is the main issue that leads to the impracticality of those adsorbents. Filtration and/or centrifugation procedure are commonly performed to recover the adsorbent from treated water. In this work, an adsorbent with magnetic-separability property was developed, with  $\text{Fe}_3\text{O}_4$  as the core material. Superparamagnetic  $\text{Fe}_3\text{O}_4$  possesses remarkable magnetic properties that allow its practical separation post-adsorption using an external magnetic field [20–22]. Besides their superparamagnetic and adsorbing properties, the low toxicity, durability, biocompatibility, low cost, and chemical stability of  $\text{Fe}_3\text{O}_4$  made them the promising adsorbent for water treatment [23–26].

In this study, a composite material consisting of  $\text{Fe}_3\text{O}_4$  and thiamine was developed to generate magnetic adsorbent with enhanced adsorption capacity. Thiamine, also known as Vitamin B1, is a water-soluble vitamin beneficial for plants and animals due to its antioxidant activity. It may also function as a cofactor for various metabolic activities [27,28]. In plants, thiamine is distributed in leaves, seeds, flowers, and roots; and is known to play a role to protect plant from abiotic and biotic stresses [29,30]. Thiamine molecule consists of a pyrimidine ring (4-amino-2-methyl-5-pyrimidyl) which is connected to a thiazole ring (4-methyl-5- $\beta$ -hydroxyethylthiazolium) through a methylene bridge [31]. The occurrence of these N-functional groups in thiamine, which tends to be positively charged, is expected to promote the adsorption capacity toward anionic Pi ions [32–34]. In addition, through the beneficial effect of thiamine for plant stress adaptation, the post-adsorption thiamine-functionalized  $\text{Fe}_3\text{O}_4$  (thF) can be a potential Pi-supplement to support plant growth. This study also investigated the effect of synthesis temperature on the product yield and its Pi-removal performance. Several physicochemical characterizations were carried out to elucidate the properties of thF, including crystallinity pattern, surface chemistry, surface functional groups, porosity, and magnetic behavior. The physicochemical properties of thF were compared to that of unmodified  $\text{Fe}_3\text{O}_4$  (F) to confirm the successful incorporation of thiamine. Adsorption isotherm of Pi by thF and F at different temperatures was conducted to study their adsorption behavior and mechanism. The environmental compatibility of these adsorbents was also assessed.

## 2. Materials and methods

### 2.1. Materials

All chemicals used were of analytical grade and were used without any pretreatment. Iron(II) sulfate heptahydrate ( $\text{FeSO}_4 \cdot 7\text{H}_2\text{O}$ , purity >99.5%) and hydrochloric acid (HCl, purity 37%) were purchased from Acros Organics, New Jersey, USA. Ammonia ( $\text{NH}_3$ , purity 28–30%) and potassium dihydrogen phosphate ( $\text{KH}_2\text{PO}_4$ , purity ≥99.5%) were manufactured by Showa, Tokyo, Japan. Thiamine hydrochloride ( $\text{C}_{12}\text{H}_{17}\text{ClN}_4\text{OS.HCl}$ , purity ≥99%) was a product of Sigma, St.Louis, MO, Germany. Sodium hydroxide ( $\text{NaOH}$ , purity >97%) was obtained from Fisher Scientific, Loughborough, UK. The solutions used for the experiments were freshly prepared before use by dissolving a certain amount of chemicals in deionized (DI) water with 18.3 MΩ·cm.

### 2.2. Synthesis of magnetite-based adsorbent

For thF synthesis, 0.2024 g of thiamine and 0.1668 g of  $\text{FeSO}_4 \cdot 7\text{H}_2\text{O}$  (Fe salt) were dissolved in 20 mL of DI water. The solution was left to react for 1 h under constant mixing at 300 rpm at certain temperatures, as listed in Table 1. Subsequently, ammonia was added (molar ratio of  $\text{NH}_4\text{OH}$ , Fe salt, and thiamine 10:1:1). The mixture was then left to react for another hour. The precipitate generated from the reaction was magnetically separated from the supernatant with an external magnetic force. The pH of the supernatants was determined by Denver Instrument UltraBasic pH Benchtop Meters UB-10 and was presented as the solution pH at the end of the reaction (Table 1). On the other hand, the solid product was washed at least 3 times with DI water and ethanol and dried at 313 K under vacuum for 24 h. The unmodified  $\text{Fe}_3\text{O}_4$  was prepared using a similar procedure, without the addition of thiamine, and used as a control.

### 2.3. Characterization

Thermogravimetric analysis (TGA) was performed using a TA instruments/TGA 550, operated at a temperature range of 303–973K with a heating rate of 10 K/min under  $\text{N}_2$  flow. The crystal pattern of the prepared magnetite nanoparticles (thFs and Fs) was analyzed by a Bruker D2 Phaser X-ray diffractometer (XRD) using Cu-K $\alpha$  radiation operating at 30 kV and 10 mA. Fourier-transform infrared spectroscopy (FTIR) analysis was performed on a Shimadzu IRTtracer-100. The oxidation states of Fe element in the samples were determined using an X-ray photoelectron spectroscopy (XPS, Thermo Fischer Scientific, VG ESCALAB 250). The magnetic properties were measured by a superconducting quantum interference device (SQUID, MPMS 3) at 300 K. Surface area and pore properties were determined by  $\text{N}_2$  adsorption-desorption isotherm procedure using a BEL Belsorp Max

**Table 1**  
Synthesis temperature used and its influence on yield and Pi removal ability of the synthesized materials. Data are means ± SD from three replicates.

Sample name	Temp (K)	pH*	Yield <sub>Fe</sub> ** (%)	Yield <sub>Fe+thiamine</sub> *** (%)	% Removal
thF-303	303	9.24	31.00 ± 1.39 <sup>ac</sup>	14.00 ± 0.64	17.09 ± 1.76
thF-333	333	9.14	30.04 ± 0.55 <sup>ab</sup>	13.57 ± 0.25	34.37 ± 0.88
thF-363	363	9.11	33.93 ± 1.02 <sup>a</sup>	15.01 ± 0.46	48.33 ± 1.06
F-303	303	9.98	29.44 ± 0.55 <sup>bc</sup>		3.92 ± 0.49
F-333	333	9.92	27.16 ± 0.51 <sup>bd</sup>		5.82 ± 0.46
F-363	363	9.83	25.72 ± 0.30 <sup>d</sup>		7.67 ± 0.18

\* pH of solution at the end of the reaction.

\*\* The amount of product formed per amount of  $\text{FeSO}_4 \cdot 7\text{H}_2\text{O}$  reactant used, calculated as Yield<sub>Fe</sub> =  $\frac{m_{\text{product}}}{m_{\text{FeSO}_4 \cdot 7\text{H}_2\text{O}}} \times 100\%$ .

\*\*\* The amount of product formed per amount of  $\text{FeSO}_4 \cdot 7\text{H}_2\text{O}$  and thiamine reactants used, calculated as Yield<sub>Fe+thiamine</sub> =  $\frac{m_{\text{product}}}{m_{\text{FeSO}_4 \cdot 7\text{H}_2\text{O}} + m_{\text{thiamine}}} \times 100\%$ .

analyzer. Prior to the sorption experimentation, the samples were degassed at 393 K for 4 h. The N<sub>2</sub> adsorption-desorption data ( $V_a$  vs  $\frac{p}{p_0}$ ) were then fitted with Brunauer–Emmett–Teller (BET) model, with mathematical expression shown in [equation \(1\)](#).

$$\frac{p}{V_a(p_0 - p)} = \frac{1}{V_m c} + \frac{c - 1}{V_m c} \left( \frac{p}{p_0} \right) \quad (1)$$

where  $V_m$  (cm<sup>3</sup>(STP)/g) and  $V_a$  (cm<sup>3</sup>(STP)/g) are the gas volume at the monolayer coverage and the total gas volume adsorbed at the standard state (T= 273.15 K and P= 101.3 kPa), c is the BET constant and  $\frac{p}{p_0}$  (kPa) is the relative pressure. The obtained  $V_m$  value was then utilized to calculate the BET surface area ( $a_{s,BET}$ , cm<sup>2</sup>/g) by the following [equation \(2\)](#).

$$a_{s,BET} = \frac{V_m N A_{cs}}{22414} \quad (2)$$

where N is the Avogadro's number ( $6.023 \times 10^{23}$  mol<sup>-1</sup>),  $A_{cs}$  (cm<sup>2</sup>) is adsorbate cross-sectional area ( $16.2 \times 10^{20}$ ), 22414 cm<sup>3</sup>(STP)/mol is the molar volume of gas at STP. The total pore volume ( $V_p$ , cm<sup>3</sup>/g) and the mean pore diameter ( $d_p$ , nm) was determined by [equations \(3\)](#) and [\(4\)](#), respectively.

$$V_p = \frac{V M}{22414 \times \rho_a} \quad (3)$$

$$d_p = \frac{4 \times V_p}{a_{s,BET}} \times 1000 \quad (4)$$

where V(cm<sup>3</sup>(STP)/g) is amount N<sub>2</sub> adsorbed at last adsorption point,  $\rho_a$  is the density of adsorptive (0.808 g/cm<sup>3</sup>), and M is the nitrogen molecular weight (28.0134 g/mol).

The point of zero charge (pH<sub>PZC</sub>) determination was done according to the reported procedure [\[35\]](#). In brief, 10 mg of adsorbent was added into a series of 10 mL KNO<sub>3</sub> 0.1 M solution with initial pH between 2 to 10. The initial pH of these KNO<sub>3</sub> solutions was adjusted by HCl 0.1 M or NaOH 0.1 M. Subsequently, the mixture solution was placed on a shaking incubator (200 rpm) at 303 K. After 36 h incubation, the supernatants were collected and were used for final pH determination. The ΔpH was calculated by subtracting the value of the final pH from the initial pH. The pH<sub>PZC</sub> of each particle is the pH where ΔpH equal to 0.

#### 2.4. Adsorption Study

A 10,000 mg/L Pi stock solution was prepared by dissolving 10 g of KH<sub>2</sub>PO<sub>4</sub> in 1 L of DI water. The diluted Pi solution was then prepared from the stock solution and was used for the adsorption experiment. The residual concentration of Pi solution post-adsorption was measured by a colorimetric procedure using a UV-Vis spectrophotometer Shimadzu UV 2600. The Pi solution was filtered using a 0.22 μm PVDF syringe filter membrane prior to the colorimetric measurement. To these filtered solutions, ammonium molybdate-based reagent was added to produce a blue-colored solution which absorbance was measured at 880 nm wavelength [\[36\]](#).

##### 2.4.1. Screening of Pi adsorption potential

Adsorbent (10 mg) was added into 10 mL Pi solutions at an initial concentration of 100 mg/L, the adsorption process lasted for 24 h under constant shaking at 200 rpm, and a temperature of 303 K. After 24 h, the adsorbent was magnetically separated from the supernatant, and the concentration of Pi that remained in the supernatant was measured.

##### 2.4.2. Effect of pH on Pi adsorption

The effect of pH on Pi removal was investigated between pH range of 2 to 10. NaOH (0.1 M) or HCl (0.1 M) was used to adjust the initial pH of the Pi solution ( $C_0 = 100$  mg/L). Into the 10 mL Pi solution,

10 mg adsorbent was added, and the mixtures was then placed in a shaking incubator at 200 rpm and 303 K. After 24 h, the supernatant was separated, and the amount of residual Pi that remained in the supernatant was measured.

#### 2.4.3. Adsorption isotherm

The adsorption of Pi by the samples was conducted at pH 3 and 4 for F-363 and thF-363 samples, respectively. A series of 10 mL Pi solutions at a varied concentration (50 to 10,000 mg/L) were prepared in scintillation vials, then 10 mg of the sample was added. These vials were then placed in a shaking incubator, which operated at 200 rpm under a controlled temperature of 303, 318, or 333K. After 24h, residual Pi in the supernatant was measured.

#### 2.4.4. Data processing

The percent removal of Pi (% Removal) and the equilibrium amount of Pi adsorbed per unit mass of adsorbent ( $Q_e$ ) were calculated based on the [equations \(5\)](#) and [\(6\)](#), respectively.

$$\% \text{Removal} = \frac{(C_0 - C_e)}{C_0} \times 100\% \quad (5)$$

$$Q_e = \frac{(C_0 - C_e)}{m} \times V \quad (6)$$

where  $C_0$  (mg/L) and  $C_e$  (mg/L) are the initial and equilibrium concentration of Pi, V (L) is the volume of the solution, and m (g) is the mass of adsorbents.

The adsorption data were plotted as  $Q_e$  vs  $C_e$  and were fitted against the Langmuir and Freundlich model, which is mathematically expressed as [equations \(7\)](#) and [\(8\)](#), respectively. These two models are used to respectively describe the monolayer and multilayer adsorption process that might occur during the adsorbate-adsorbent interaction [\[37\]](#).

$$Q_e = \frac{Q_L K_L C_e}{1 + K_L C_e} \quad (7)$$

$$Q_e = K_F C_e^{\frac{1}{n_F}} \quad (8)$$

where  $Q_L$  (mg/g) is the Langmuir maximum adsorption capacity,  $K_L$  (L/mg) is the Langmuir adsorption equilibrium constant,  $K_F$  (mg/g)(L/mg)<sup>1/n</sup> is Freundlich isotherm constant related to adsorption capacity, and  $n_F$  is a dimensionless constant related to the favorability of adsorption. Furthermore, the suitability of adsorbents for Pi adsorption was evaluated from the value of the constant separation factor ( $R_L$ ) obtained from the following [equation \(9\)](#).

$$R_L = \frac{1}{1 + K_L C_0} \quad (9)$$

Besides the model mentioned above, the Sips three-parameters model was employed for the data fitting purpose. This model is a modified form of the Freundlich equation, which follows the continuous increase of capacity as an increase of concentration but has a finite limit at the sufficiently high concentration [\[38\]](#). The mathematical expression of the Sips model is given in [equation \(10\)](#).

$$Q_e = \frac{Q_S K_S C_e^{n_S}}{1 + K_S C_e^{n_S}} \quad (10)$$

where  $Q_S$  is the Sips maximum adsorption capacity (mg/g),  $K_S$  is the Sips equilibrium constant related to the adsorption affinity (L/mg), and  $n_S$  is the Sips model exponent that expresses the heterogeneity of the adsorbent. Sips model reduces to Langmuir model as the  $n_S= 1$  and reduces to Freundlich when either  $C_e$  or  $K_S \rightarrow 0$ . These isotherm models were fitted with the experimental data gathered to evaluate the adsorption mechanisms to better understand how adsorbates interact with adsorbents. The linear regression (LR), nonlinear regression (NLR), and orthogonal distance regression (ODR) analyses

[39, 40] were performed by minimizing the sum of the squares of the residuals/error (SSE, equation 11) while the model coefficients were iteratively modified. The LR and NLR analyses were carried out using Microsoft Excel equipped with Solver data analysis tool pack with the regression results assessed through the resulting coefficient of determination ( $R^2$ , equation 12), adjusted R-squared ( $R_{adj}^2$ , equation 13), while the ODR analysis was conducted with the Origin2019 software.

$$SSE = \sum_{i=1}^n (Q_e - \widehat{Q}_e)^2 \quad (11)$$

$$R^2 = 1 - \frac{\sum_{i=1}^n (Q_e - \widehat{Q}_e)^2}{\sum_{i=1}^n (Q_e - \overline{Q}_e)^2} \quad (12)$$

$$R_{adj}^2 = 1 - \frac{(1 - R^2)(n - 1)}{n - k - 1} \quad (13)$$

where  $\widehat{Q}_e$  is the fitted value of equilibrium amount of Pi adsorbed per unit mass of adsorbent (mg/g),  $\overline{Q}_e$  is the average mean value of the equilibrium amount of Pi adsorbed per unit mass of adsorbent (mg/g),  $n$  is the number of experimental data points, and  $k$  is the number of parameters in the model, including the equilibrium concentrations predicted.

The thermodynamic parameters, i.e. the change in Gibbs free energy ( $\Delta G^\circ$ ), enthalpy ( $\Delta H$ ), and entropy ( $\Delta S$ ), were based on the equations (14) to (17) [41].

$$\Delta G^\circ = -RT \ln K_d \quad (14)$$

$$\Delta G^\circ = \Delta H - T\Delta S \quad (15)$$

$$\ln K_d = -\frac{\Delta H}{RT} + \frac{\Delta S}{R} \quad (16)$$

$$K_d = 55.51 \times K_L \times 1000 \times MW_{adsorbate} \quad (17)$$

where  $K_d$  is the thermodynamic equilibrium constants dimensionless of the adsorption process [42].  $R$  is the gas constant (8.314 J/mol.K) while  $T$  is the absolute temperature (K). By plotting  $\ln K_d$  versus  $1/T$ , the change in  $\Delta H$ ,  $\Delta S$ , and  $\Delta G^\circ$  can be obtained.

## 2.5. Arabidopsis thaliana growth media supplementation

To assess the environmental compatibility of the F-363 and thF-363, the freshly synthesized materials were administered to the plant growth media [43]. *A. thaliana* Col-0 ecotype was used as the model plant. The half-strength Murashige and Skoog (MS) basal medium supplemented with 1% (w/v) sucrose, 0.8% (w/v) agar media was prepared according to previous publications [3, 44–46]. For the F-363 or thF-363 treatment group, 0.1 wt.% of respective materials were added into the basal media. The *A. thaliana* seeds were germinated and grown under continuous light condition at 295 K. After 14 days of vertical growth, the aerial fresh weight and primary root length of the seedlings were measured. Three independent biological experiments with 8 seedlings per replicate were performed for control, F-363, and thF-363-treated samples. Statistical analysis was conducted using the GraphPad Prism 8.0 software, and significant differences between different growth media compositions were examined by one-way analysis of variance (ANOVA) with Tukey's posthoc test.

## 3. Results and Discussion

This study employed three synthesis temperatures (303, 333, and 363 K) for thFs and Fs preparation. To ensure that the suitability of these conditions, firstly, the thiamine thermal stability was tested. As

shown in Figure S1, a negligible amount of % mass loss (~0.19%) of thiamine was observed upon 2 h isothermal heating at 363 K (the highest temperature used for the synthesis), which implies that the thiamine remained stable and did not undergo thermal degradation during the synthesis process.

The formation of thFs appears to depend on temperature, as implied from the increase in yield as the reaction temperature was increased (Table 1). The increase of synthesis temperature from 303 K to 333 K resulted in the decrease of thF Yield<sub>Fe</sub> from 31.00% to 30.04%. However, the Yield<sub>Fe</sub> was increased from 30.04% to 33.93% as the synthesis temperature increased from 333 K to 363 K. The increase in synthesis temperature shows a favorable effect on the formation of thF, which could be attributed to the high energy supply at higher temperature, thus facilitating the formation of thF. The supply of energy was reported to affect the nucleation rate in the formation of metal-organic complexes [47, 48], which could also be the case in the formation of thF involving the interaction between thiamine and Fe<sub>3</sub>O<sub>4</sub>. Meanwhile, the higher thF-303 Yield<sub>Fe</sub> (compared to Yield<sub>Fe</sub> of thF-333) was attributed to the generation of side product FeO(OH); as shown by the occurrence of two additional XRD peaks at  $2\theta$  of 20.81° and 40.21° (Figure S2a), which were attributed to the reported (220) and (420) crystal plane of FeO(OH) (JCPDS No. 01-077-0247) [49, 50]. Interestingly, no contaminant peaks were observed in thF-333 and thF-363 samples (Figures S2b and 1a).

Besides yield, the synthesis temperature was shown to positively affect the Pi removal efficiency of the resultant thFs, and the highest % Pi removal was achieved upon the usage of thF-363 as the adsorbent. This enhanced adsorption potential might be attributed to the higher composition of thiamine in thF prepared at 363K than the one synthesized at 333K. The TGA plots (Figure S2d and e) confirmed that the thF-363 contained approximately 15.16% thiamine, while only ~6.94% of the thF-333 consisted of thiamine. The higher thiamine content in thF-363 provides more adsorption sites for better Pi removal. The proposed interaction between the thF-363 and Pi is described in subsection 3.3. Based on the above-mentioned results, thF-363 has better Pi removal efficiency and higher Yield<sub>Fe</sub> than thF-303 and thF-333; thus, detailed characterization and Pi adsorption studies were carried out for thF-363 and F-363 (as the control).

### 3.1. Characterization of thF-363

Figure 1a shows the crystal pattern of F-363 and thF-363; both samples had seven distinct diffraction peaks at similar  $2\theta$  angles, and these XRD patterns match well with the XRD pattern of Fe<sub>3</sub>O<sub>4</sub> reference (JCPDS 19-0629), indicating the successful formation of Fe<sub>3</sub>O<sub>4</sub> particles. The crystallinity of thF-363 was 57.8%, which is significantly lesser than the F-363 (81.2%). This reduced crystallinity can be attributed to the incorporation of thiamine on the magnetite core. The formation of Fe oxide was also confirmed by the occurrence of Fe-O functional group at ~576 cm<sup>-1</sup> and ~573 cm<sup>-1</sup> in the thF-363 and F-363 FTIR spectra (Figure 1b). Beside the Fe peak, thiamine fingerprint spectra, specifically the N-H group (3314 cm<sup>-1</sup>), C-H aliphatic group (2922 cm<sup>-1</sup>), aromatic amine C-N group (1652 cm<sup>-1</sup>), C=C group (1524 cm<sup>-1</sup>), C-S group (1325 cm<sup>-1</sup>), and C-O group (1037 cm<sup>-1</sup>) can be observed in the FTIR spectra of thF-363 which verify the formation of thiamine-functionalized Fe<sub>3</sub>O<sub>4</sub>. XPS analysis was performed to investigate the elemental state of Fe ions in thF-363 and F-363. As shown in Figure 1c, three peaks of iron (Fe 2p) with binding energies at 710.8, 712.3, and 724.8 eV, respectively attributed to Fe<sup>3+</sup> 2p<sub>3/2</sub>, Fe<sup>2+</sup> 2p<sub>3/2</sub> and Fe 2p<sub>1/2</sub>, can be observed in the XPS patterns of F-363 [51, 52]. Similarly, the thF-363 samples also showed three Fe 2p-related XPS spectra with the binding energy of 710.7, 712.6, and 724.7 eV (Figure 1d). Based on the stoichiometric, the Fe<sup>2+</sup>:Fe<sup>3+</sup> ratio of thF-363 and F-363 is shown to be 0.34:0.66 and 0.37:0.63, respectively. These ratios are comparable to the previously reported Fe<sub>3</sub>O<sub>4</sub>

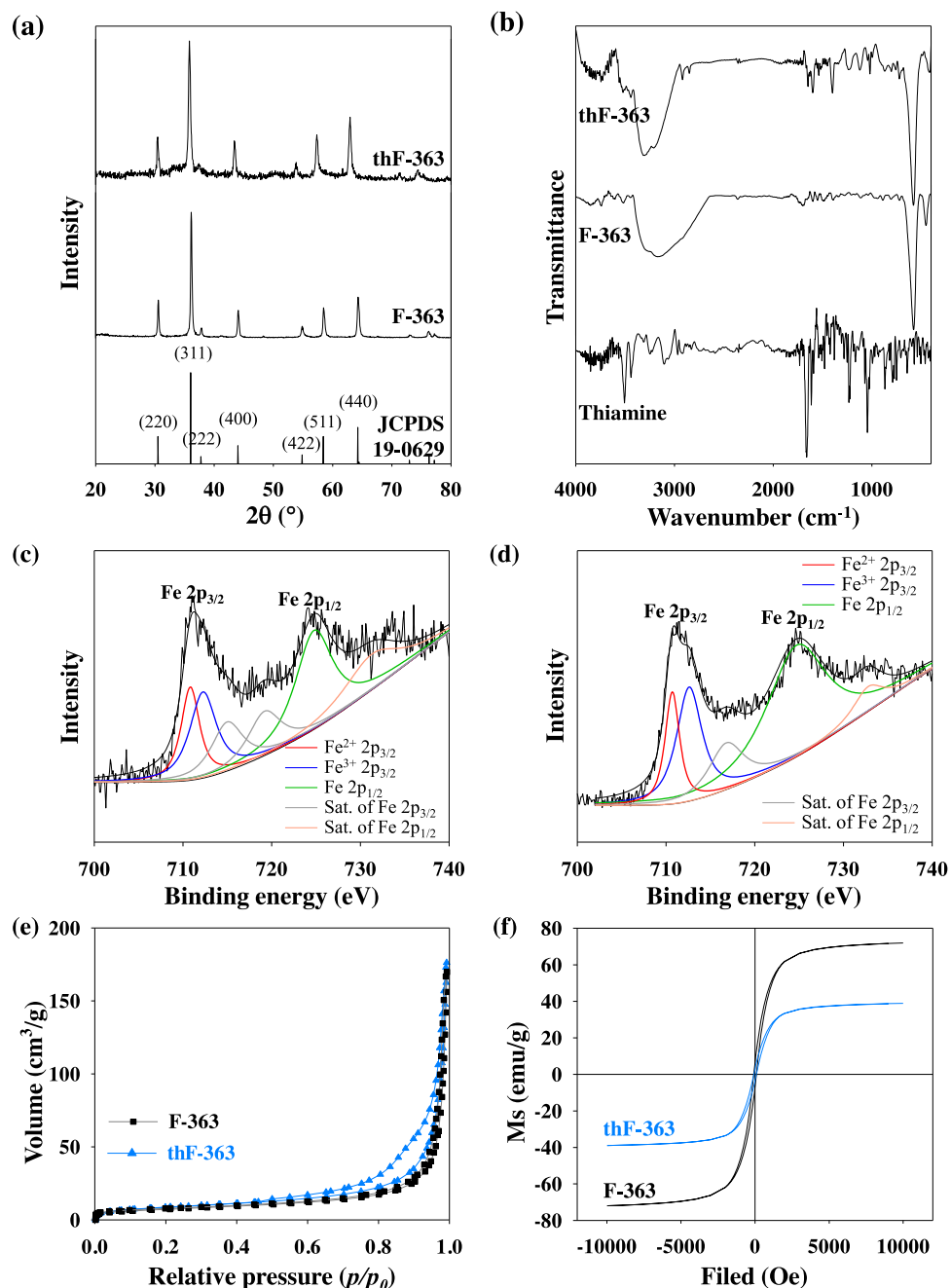


**Figure 1.** (a) Powder XRD pattern and (b) FTIR spectra of the thiamine-functionalized  $\text{Fe}_3\text{O}_4$  synthesized at 363 K (thF-363) and control; unmodified  $\text{Fe}_3\text{O}_4$  synthesized at 363 K (F-363). (c,d) The XPS spectra of (c) F-363 and (d) thF-363. (e) The  $\text{N}_2$  adsorption-desorption isotherms curves and (f) hysteresis curves showing the magnetic properties of F-363 (black) and thF-363 (blue).

data [52], suggesting that the iron oxide in thF-363 and F-363 are in  $\text{Fe}_3\text{O}_4$  form.

The  $\text{N}_2$  adsorption-desorption isotherms of thF-363 and F-363 are shown in Figure 1e. According to IUPAC classification [53], the isotherm peak of both samples exhibited the type IV isotherms curve with H3-types hysteresis loop, which is commonly observed for mesoporous materials. Upon fitting by BET model, the  $d_p$  of thF-363 and F-363 is 32.913 nm and 36.976 nm, respectively, which is within the range of mesoporous material (2 to 50 nm). In addition, the thF-363 particles have an  $a_{s,BET}$  of 32.999  $\text{m}^2/\text{g}$  that is greater than that of the control (27.490  $\text{m}^2/\text{g}$ ). Figure 1f displays the magnetic hysteresis curves of thF-363 and F-363 measured at 300 K. The saturation magnetization values ( $M_s$ ) of thF-363 and F-363 is 84.67 and 91.71 emu/g. Lower  $M_s$  value of thF-363 might be due to the addition of thiamine

which is non-magnetic. Despite the smaller  $M_s$  value, thF-363 (and F-363) fell into the classification of superparamagnetic material. Disregard of the reduced  $M_s$ , these values are postulated to be sufficient for magnetic recovery from solution [54].

### 3.2. Effect of initial pH on Pi adsorption

The influence of initial pH on the Pi removal by thF-363 and F-363 adsorbent was presented in Figures 2a and 2b. Optimum Pi removal by using thF-363 can be achieved when the initial pH of the adsorbate was set at pH 4. On the other hand, the efficiency of Pi removal by F-363 decreased upon increasing pH, and the optimum removal can be obtained between pH 2–3. The pH for Pi adsorption is essentially concentrated at low pH for both samples, which can be

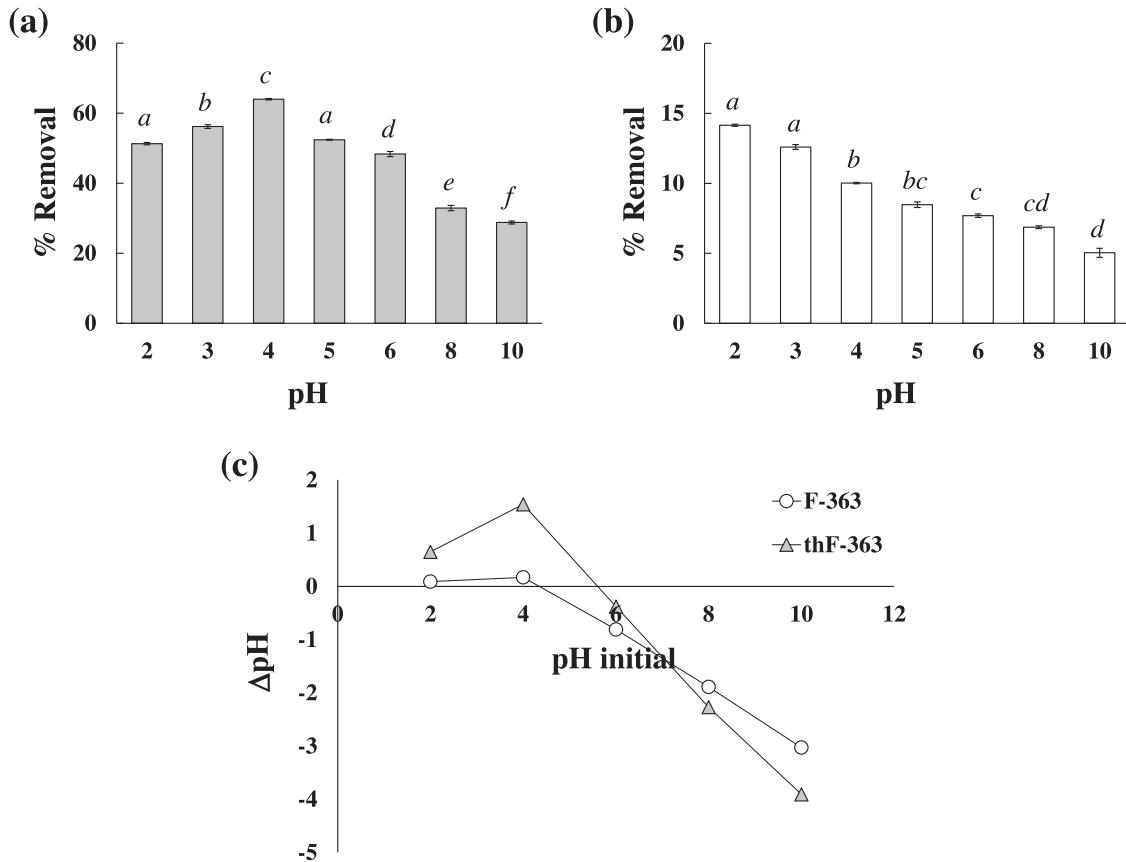


**Figure 2.** Effect of solution pH on Pi adsorption onto (a) thF-363 and (b) F-363. (c) The pH of point of zero charge of thF-363 and F-363. Data are means  $\pm$  SD from three replicates. Different lowercase letters above the graph bars denote significant differences among different pH (ANOVA and Tukey's test,  $p < 0.05$ ).

explained by observing the  $pH_{PZC}$  of thF-363 and F-363 adsorbent. As shown in Figure 2c, the  $pH_{PZC}$  value for thF-363 and F-363 is 5.6 and 4.4, respectively. The  $pH_{PZC}$  value indicates the surface charge tendency of the adsorbent; positive surface charge occurs at pH solution  $< pH_{PZC}$ , while negative surface charge occurs at pH solution  $> pH_{PZC}$  [55].

The interaction of Pi and thF-363 at acidic and basic pH is illustrated in Figure 3. At acidic pH (i.e., pH solution  $< pH_{PZC}$ ), thF-363 particles are positively charged while Pi dominantly presents as

negatively charged species ( $H_2PO_4^-$ ) [56]. The opposite charges between the adsorbent and adsorbate generate electrostatic attraction, which promotes the adsorption of Pi onto the adsorbent surface. At basic pH (i.e., pH solution  $> pH_{PZC}$ ), thF-363 tends to be negatively charged; and, Pi dominantly occurs as negatively charged species of  $HPO_4^{2-}$  [56]. The same charges between thF-363 and Pi lead to repulsion force, which demotes the adsorption of Pi. A similar effect of surface charge on the adsorption performance of adsorbent has also been reported in other works [46,57,58]. For example, Jiang et al. [57]

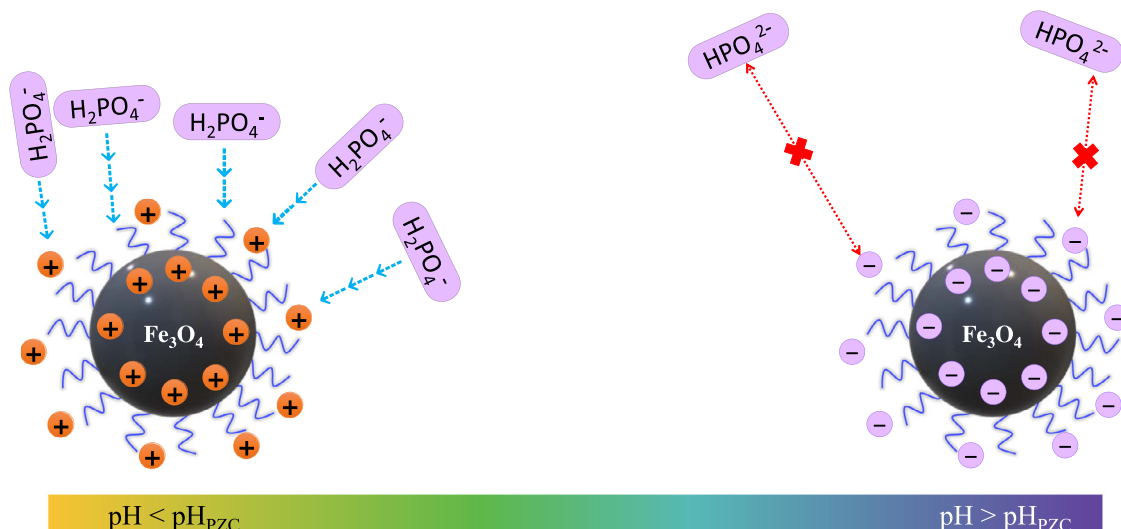


**Figure 3.** Illustration on the effect of pH, adsorbent surface charge, and adsorbate species distribution on the thF-363 and Pi interaction.

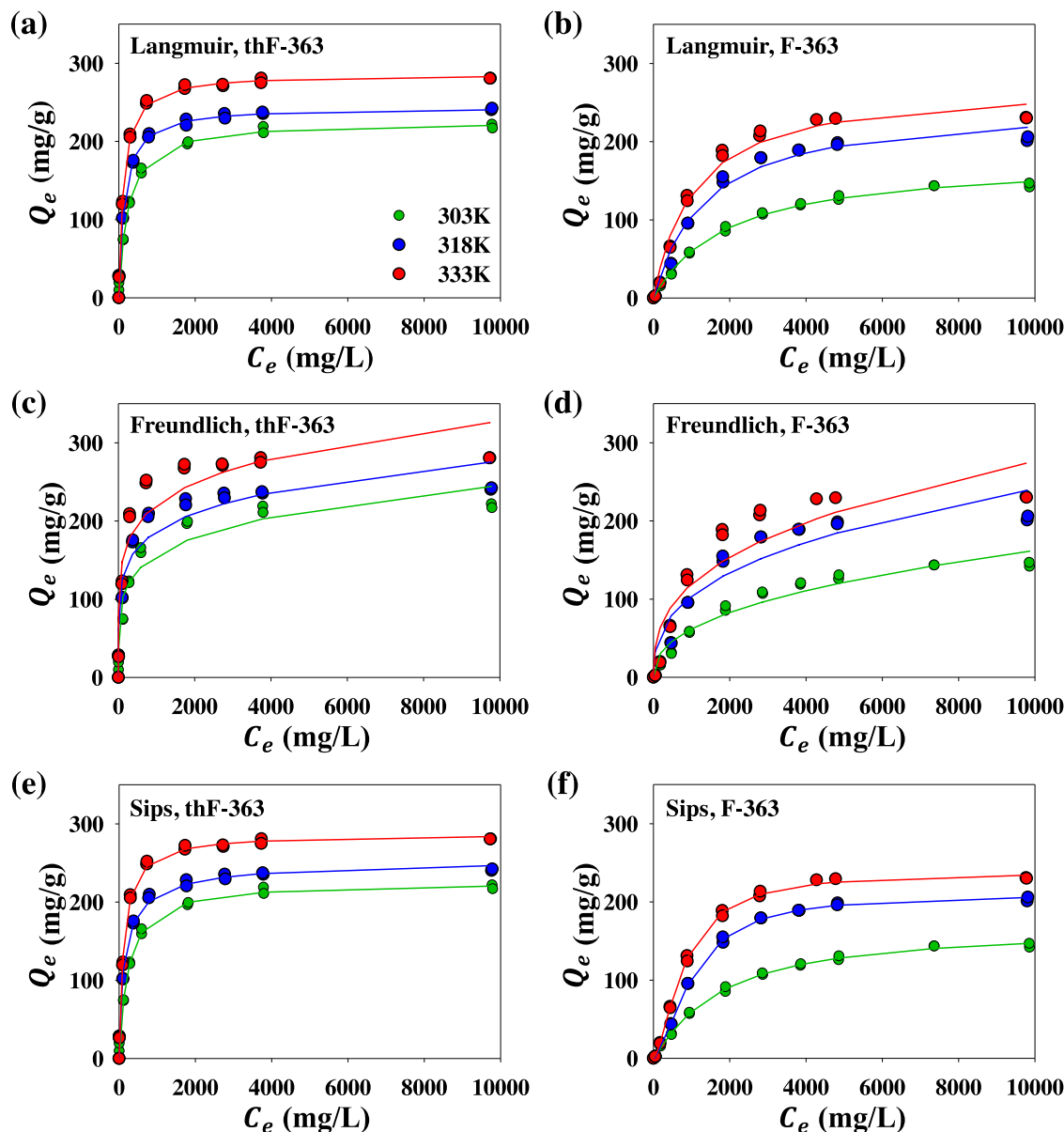


**Figure 4.** Isotherm data of Pi adsorption on (a,c,e) thF-363 and (b,d,f) F-363 at three different adsorption temperatures (303 K, green; 318 K, blue; and 333 K, red symbols). The experiments were done in triplicate. The lines represent the (a, b) Langmuir, (c, d) Freundlich, and (e,f) Sips data fitting.

reported that the  $\text{Fe}_3\text{O}_4$  particles were negatively charged at pH 7, which led to the electrostatic adsorption between the particles and positively charged anthocyanin. In addition, the occurrence of excess hydroxyl ions also may act as competing molecules and occupy the adsorption site of Pi anions on the adsorbent [59].

### 3.3. Adsorption isotherm of Pi onto thF-363 magnetic adsorbent

The adsorption isotherm plays a crucial role in determining the maximum adsorption capacity and estimating the adsorption mechanism of adsorbents. The isotherm study of Pi on thF-363 and F-363 was conducted at adsorption temperatures of 303, 318, and 333 K (Figure 4). At any given temperature, the system containing thF-363 displayed typical H-adsorption curves, which suggests that the adsorption was driven by the electrostatic forces due to different charges of adsorbate and adsorbent. While for F-363 adsorbent, the system shows an L-type curve which commonly occurs in the adsorption of ions in aqueous solutions and the adsorption process is driven

by van der Waals forces [60]. Overall, the adsorption process with an adsorbent plateau at high adsorbate concentration follows the sub-class classification number 2, demonstrating the absence of the inter-molecular forces between the adsorbed-adsorbate molecules and the adsorbate molecules in bulk solution [61]. Both thF-363 and F-363 tend to exhibit endothermic adsorption behavior, where the equilibrium adsorption capacity ( $Q_e$ ) increases with temperature.

Three isotherm models, Langmuir, Freundlich, and Sips, were used to evaluate the adsorption behavior of Pi onto magnetite sorbent thF-363 and F-363; the calculated parameters of NLR fitting the isotherm models are listed in Table 2. The NLR fitting method was chosen as the best regression method since it gave the smallest SSE value and the closest fitting to the experimental data compared to LR and ODR methods (Tables S1, S2, and Figures S3, S4). The Sips model showed the best fitting with the experimental data of both thF-363 ( $R_{adj}^2 = 0.988\text{-}0.994$ ) and F-363 ( $R_{adj}^2 = 0.997\text{-}0.999$ ). The goodness of fitting also is displayed on the value of calculated  $Q_s$  from the Sips model, which showed the closest resemblance to the  $Q_{exp}$ . The Sips

**Table 2**

Adsorption isotherm parameters of Pi adsorption on either thF-363 or F-363 obtained from nonlinear regression fitting using Langmuir, Freundlich, and Sips models.

Model	Parameter (Unit)	thF-363			F-363		
		303 K	318 K	333 K	303 K	318 K	333 K
<b>Langmuir</b>	$Q_{exp}$ (mg/g)	221.993	242.281	280.954	146.977	206.093	230.923
	$Q_l$ (mg/g)	226.051	243.906	286.376	177.699	248.289	275.639
	$K_L$ (L/mg)	0.0042	0.0072	0.0086	0.0005	0.0007	0.0009
	$R_L$	0.02-0.83	0.01-0.74	0.01-0.70	0.17-0.98	0.13-0.97	0.1-0.96
	$R^2$	0.994	0.987	0.994	0.997	0.982	0.983
	$R_{adj}^2$	0.993	0.986	0.994	0.997	0.980	0.981
<b>Freundlich</b>	$K_F$ (mg/g)(L/mg) <sup>-n</sup>	39.190	57.528	67.881	3.519	8.388	9.833
	$n_F$	5.017	5.866	5.854	2.404	2.743	2.752
	$R^2$	0.938	0.923	0.886	0.951	0.894	0.875
	$R_{adj}^2$	0.933	0.918	0.879	0.948	0.887	0.868
	SSE	559.782	1443.821	911.814	139.427	1811.293	2575.329
<b>Sips</b>	$K_S$ (mg/g)	225.837	257.013	287.680	168.019	209.278	238.421
	$K_S$ (L/g)	0.004	0.025	0.010	0.0003	0.00001	0.00002
	$n_S$	1.005	0.748	0.967	1.108	1.695	1.594
	$R^2$	0.994	0.989	0.994	0.998	0.999	0.999
	$R_{adj}^2$	0.993	0.988	0.994	0.997	0.999	0.999
	SSE	559.683	1211.164	905.877	101.864	70.988	156.020

model also can be used to confirm the satisfactory of the Langmuir or Freundlich fitting. Based on the fitting results, the  $n_S$  value of all the adsorption systems is close to 1, indicating their better approach to the Langmuir model. Furthermore, the  $K_S$  of the Sips model does not show zero value, which confirms the Langmuir approach [35,62].

In agreement with the Sips fitting result, the Langmuir model showed better fitting with the experimental data for both adsorbents, while the fitting with Freundlich model tends to deviate strongly from the experimental data. Based on the Langmuir isotherm, the maximum adsorption capacity of Pi increased from 226.051 to 286.376 mg/g for thF-363 and 177.699 to 275.639 mg/g for F-363 at the increasing adsorption temperature. Proportionally, the equilibrium constant  $K_L$  value also increased at higher temperature. On the other hand, the favorability of adsorbent towards Pi was evaluated by the value of the separation factor constant ( $R_L$ ) which can be obtained from Langmuir model. The value of  $R_L$  of all adsorption experiments showed the value between 0 and 1, indicating that the synthesized adsorbents were all suitable for the Pi adsorption [63]. Disregards of the data fitting, the  $n_F$  values of both samples fallen within the 2-10 range which indicate the adsorption is favorable [63]. It is also worth mentioning that the thF-363 showed substantially higher adsorption capacity compared to F-363; up to 1.51-fold higher capacity for adsorption at 303K.

The mechanism of Pi adsorption on F-363 and thF-363 is illustrated in Figure 5. The adsorption of Pi on F-363 was driven by the electrostatic attraction between the anionic species of Pi and positively charged F-363, which is a typical phenomenon observed in the adsorption of anionic Pi onto iron oxides-based sorbents [64,65]. Distinctively, the enhanced adsorption capacity in thF-363 adsorbent may be attributed to the presence of thiamine, which provides additional amino ( $-NH_2$ ) binding sites. The high Pi adsorption on the  $-NH_2$  functionalized adsorbents has been reported in several works [66-68], wherein the anionic Pi establishes electrostatic attraction with the protonated species of the  $-NH_2$  functional group.

Pi removal through adsorption method had been previously studied using various magnetite-based adsorbents [66,68-71]. A comparison of the maximum Pi adsorption capacities onto thF-363, F-363, and other magnetite composite adsorbents is presented in Table 3. The capacity of thF-363 for Pi adsorption is significantly higher than other reported magnetite adsorbents, which show the superiority of thF-363 adsorbent.

### 3.4. Adsorption thermodynamic

Thermodynamic parameters can be used to estimate the characteristics of Pi adsorption onto the adsorbent surface. Figure 6 shows the adsorption thermodynamic of the adsorbents. The negative  $\Delta G^\circ$

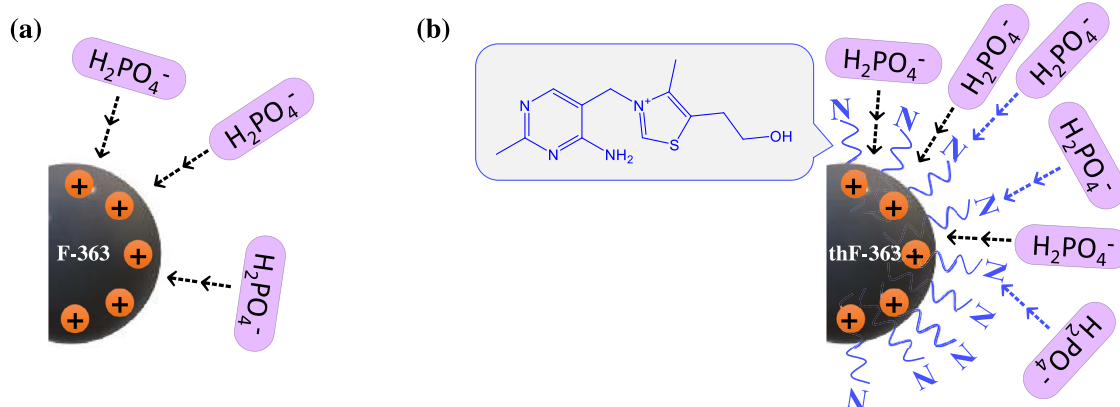


Figure 5. Possible mechanism of Pi adsorption on (a) F-363 and (b) thF-363.

**Table 3**

Comparison of Pi adsorption capacities and optimum adsorption condition of thF-363, F-363, and previously reported magnetite-based adsorbents.

Adsorbent	Conditions	$Q_{max}$ (mg/g)	References
thF-363	pH 4, 333 K	287.7	This study
F-363	pH 3, 333 K	238.4	This study
Fe <sub>3</sub> O <sub>4</sub> /ZrO <sub>2</sub> /chitosan	pH 3, 298 K	26.5	[68]
Fe <sub>3</sub> O <sub>4</sub> @LDH composites	pH 3	26.5–36.9	[69]
Fe <sub>3</sub> O <sub>4</sub> @alkali-treated calcium-silicate	pH 8, 298 K	128	[70]
Chitosan/Al <sub>2</sub> O <sub>3</sub> /Fe <sub>3</sub> O <sub>4</sub> nanofiber	pH 3, 303 K	130.9	[66]
Rectorite/Fe <sub>3</sub> O <sub>4</sub> -CTAB	pH 5, 303 K	174.5	[71]

value at all given temperatures demonstrate the thermodynamically favorable and spontaneous adsorption of Pi onto the thF-363 and F-363 surface. Specifically -26.22, -28.47, and -30.72 kJ/mol for the  $\Delta G^\circ$  of thF-363 at 303, 318, and 333 K, and  $\Delta G$  -20.83, -22.67, and -24.52 kJ/mol for F-363 at 303, 318, and 333 K. The  $\Delta H$  for each temperature increase was evaluated to observe the heat transfer direction in the adsorption system. Positive  $\Delta H$  values obtained in the Pi–thF-363 system was 27.66 kJ/mol, 10.24 kJ/mol and 19.23 kJ/mol when the adsorption temperature was increased from 303 to 318K, 318 to 333 K, and 303 to 333 K, respectively. The same positive values of  $\Delta H$  were calculated from the system containing F-363 as well ( $\Delta H$  = 18.84 kJ/mol for 303 → 318 K, 13.89 kJ/mol for 318 → 333 K, and 16.44 kJ/mol for 303 → 333 K).

303 → 333 K). These positive  $\Delta H$  values indicate that the adsorption process happens endothermically and favors high temperature [58,72], as confirmed by the maximum adsorption capacity increase when the temperature increases from 303 to 333 K (Table 2).

The  $\Delta S$  value for each temperature increase was also calculated. A positive value of  $\Delta S$  was found at each temperature increase. For instance, the  $\Delta S = 0.178 \text{ kJ/mol}\cdot\text{K}$  and  $0.150 \text{ kJ/mol}\cdot\text{K}$  when the adsorption temperature in Pi–thF-363 system increased from 303 to 318K and 303 to 333K, respectively. In the system containing F-363, the  $\Delta S_{303 \rightarrow 318}$  was 0.131 kJ/mol·K and  $\Delta S_{303 \rightarrow 333}$  is 0.123 kJ/mol·K. The positive  $\Delta S$  values indicate the increase in the disorder of ions in the adsorbate-adsorbent interface along with the increase in temperature [63,73].

### 3.5. Environmental compatibility assessment of thF-363 on plant growth

The usage of non-environmentally friendly adsorbents for contaminant removal from wastewater may evoke ecological risk toward soils, plants, and their surrounding ecosystem. To evaluate the environmental compatibility of thF-363, this work focused on its effect on the overall growth of *A. thaliana* seedlings upon supplementation to plant growth media. The evaluation was based on phenotypical observation of the seedling aerial and root development. Figure 7a

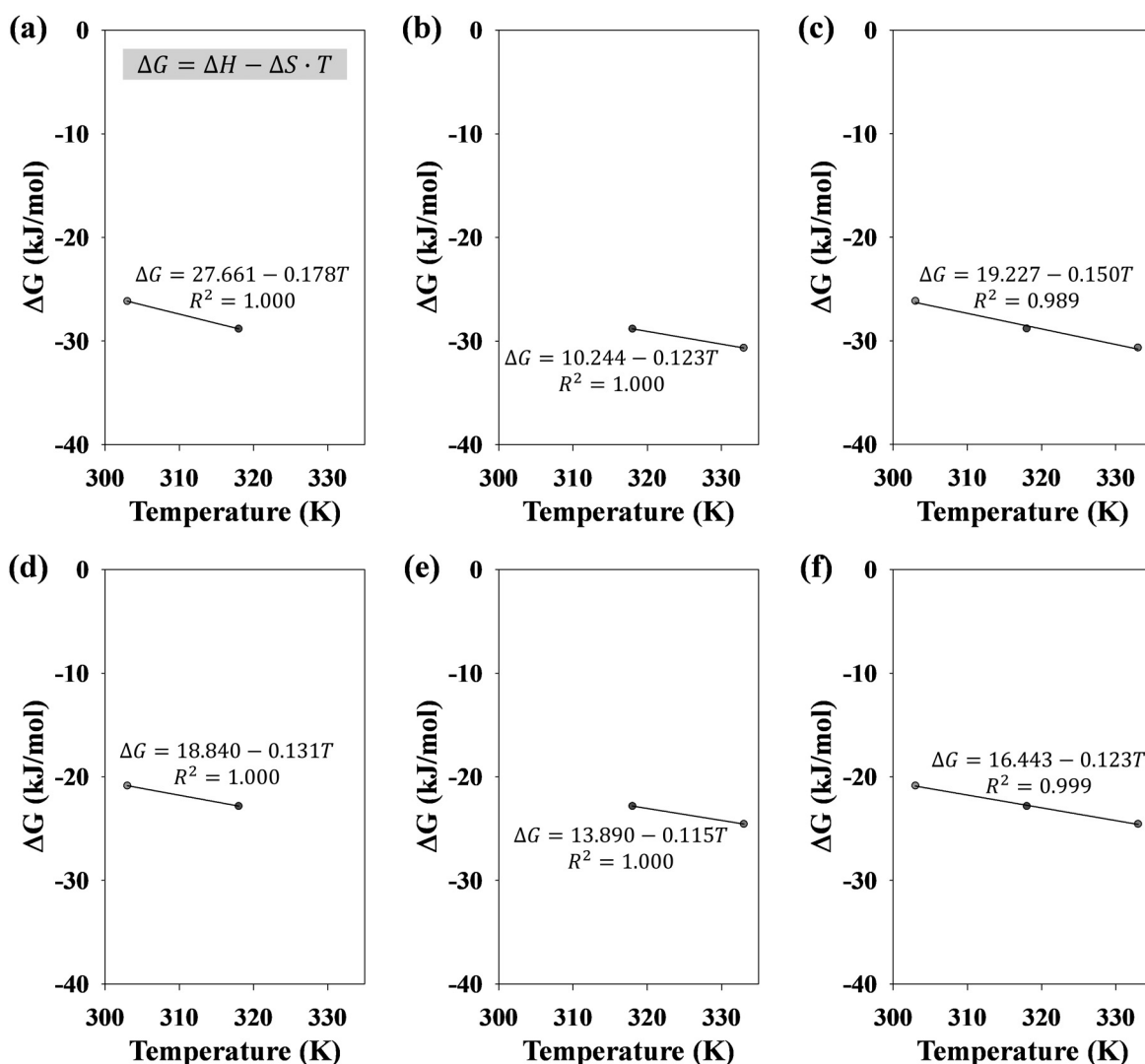
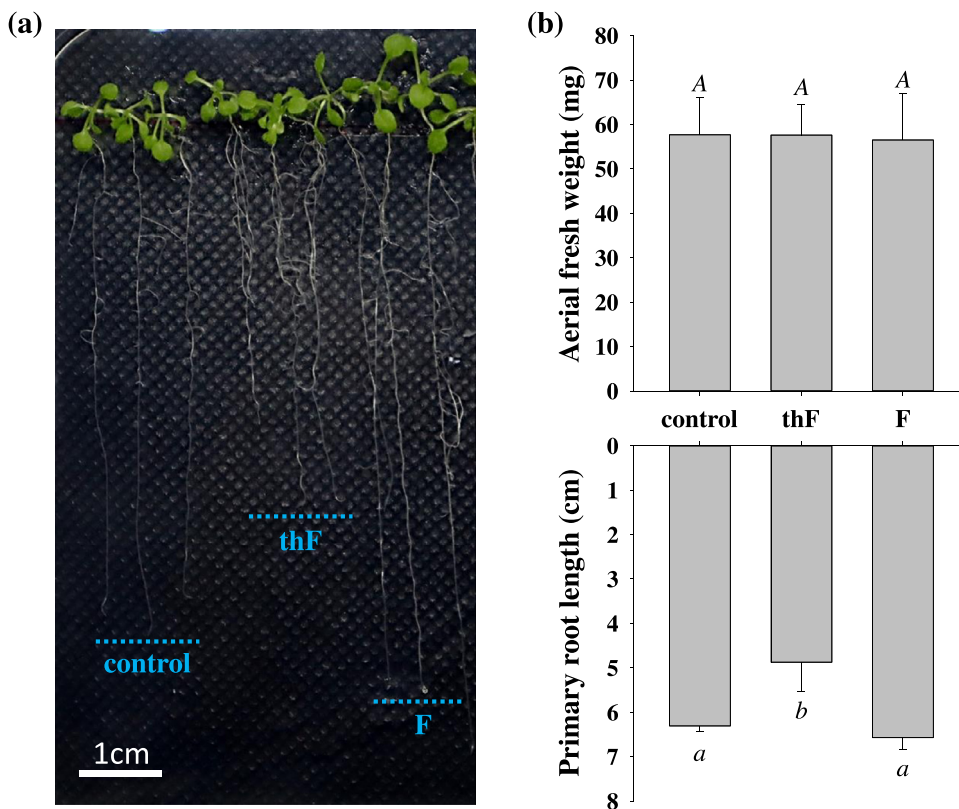


Figure 6. Adsorption thermodynamics for the removal of Pi by (a-c) thF-363 and (d-f) F-363.



**Figure 7.** Growth observation of *Arabidopsis thaliana* seedlings grown on supplemented media. (a) Image of 14-day-old seedlings. (b) Aerial fresh weight (upper panel) and primary root length (lower panel) of the seedlings. Data are means  $\pm$  SD from three replicates, with 8 seedlings observed per replicate. Different letters above and below the graph bars denote significant differences among different growth media (ANOVA and Tukey's test,  $p < 0.05$ ).

shows the representative 14-day-old seedlings grown on basal (control), thF-363 supplemented (thF), and F-363 supplemented (F) media. The measured aerial fresh weight and primary root length of the seedlings are presented in Figure 7b. No observable difference can be seen between the aerial fresh weight of seedlings grown on the thF, F, and control. However, the thF-363 supplementation slightly affects the primary root growth of the seedlings (Figure 7b, lower panel). This phenomenon might be due to the high adsorption capacity of freshly synthesized thF-363, which reduces nutrient availability in the media, thus inhibiting root growth. Nevertheless, both modified and unmodified  $\text{Fe}_3\text{O}_4$  caused minimal to no adverse effects on phenotypical growth of seedlings' root and aerial tissues, which suggest their non-phytotoxic properties.

#### 4. Conclusion

An environmentally friendly adsorbent with high adsorption capacity toward phosphate ions (Pi), namely thiamine-functionalized  $\text{Fe}_3\text{O}_4$  (thF), was successfully synthesized through *in-situ* reaction by combining  $\text{NH}_4\text{OH}$ :Fe:thiamine at a molar ratio of 10:1:1 and a temperature of 363 K. Detailed characterization through XRD, XPS, FTIR, SQUID, and  $\text{N}_2$  adsorption-desorption isotherm confirmed the formation of  $\text{Fe}_3\text{O}_4$ , the incorporation of thiamine, and gave insight on the other physicochemical properties of the thF-363. The thiamine functionalization was shown to substantially increase the adsorption capacity for Pi removal up to 1.51-fold (at 303 K) compared to the unmodified  $\text{Fe}_3\text{O}_4$ . The improved adsorption capacity is attributed to the synergistic effect of the surface charge, area, and the occurrence of the thiamine functional group in thF-363. The adsorption process fitted well with the Langmuir and Sips isotherm model, with a maximum adsorption capacity of 287.680 mg/g at 333 K. The Pi adsorption to the adsorbents followed endothermic and spontaneous

mechanisms. Both modified and unmodified  $\text{Fe}_3\text{O}_4$  showed a non-toxic effect on plant growth, confirming their environmentally-friendly nature.

#### Author Contribution

A.E.A. Conceptualization; Data curation; Funding acquisition; Investigation; Writing. Y.N.T.-C. Formal analysis; Investigation; Methodology; Visualization; Writing. Q.N.H. Formal analysis; Investigation; Methodology. P.L.T.-N. Funding acquisition; Supervision; Project administration. S.P.S., and A.W.G. Supervision; Project administration; Resources. V.B. Formal analysis. H.-Y. H and Y.-H.J. Supervision; Resources.

#### Declaration of Competing Interest

The authors declare that the research was conducted without any commercial or financial relationships that could be construed as a potential conflict of interest.

#### Acknowledgments

This research was funded by Vietnam National Foundation for Science and Technology Development (NAFOSTED) under Grant Number 103.02-2020.64 to P.L. Tran-Nguyen. A. E. Angkawijaya is supported by the Ministry of Science and Technology (MOST 109-2221-E-011-058 and MOST 110-2221-E-011-018) and the National Taiwan University of Science and Technology (101H451403). S.P. Santoso is supported by Widya Mandala Surabaya Catholic University through an Internal Research Grant.

## Supplementary materials

Supplementary material associated with this article can be found in the online version at doi:[10.1016/j.jtice.2021.104162](https://doi.org/10.1016/j.jtice.2021.104162).

## References

- [1] Jordan RM, Myers VS, Yoho B, Spurrell FA. Effect of Calcium and Phosphorus Levels on Growth, Reproduction and Bone Development of Ponies. *J Anim Sci* 1975;40(1):78–85.
- [2] Chaudhary MI, Adu-Gyamfi JJ, Saneoka H, Nguyen NT, Suwa R, Kanai S, et al. The effect of phosphorus deficiency on nutrient uptake, nitrogen fixation and photosynthetic rate in mungbean, mungbean and soybean. *Acta Physiologae Plantarum* 2008;30(4):537–44.
- [3] Angkawijaya AE, Nguyen VC, Nakamura Y. Enhanced root growth in phosphate-starved Arabidopsis by stimulating de novo phospholipid biosynthesis through the overexpression of *LYSOPHOSPHATIDIC ACID ACYLTRANSFERASE 2 (LPAT2)*. *Plant, Cell & Environment* 2017;40(9):1807–18.
- [4] Wang GC. 4 - Nonmetallurgical slags editor. In: Wang GC, editor. *The Utilization of Slag in Civil Infrastructure Construction*. Woodhead Publishing; 2016. p. 63–85.
- [5] USGS. Phosphate rock editor. In: Summaries MC, editor. *Phosphate Rock Statistics and Information*. U.S Geological Survey; 2021<https://pubs.usgs.gov/periodicals/mcs2021/mcs2021-phosphate.pdf>.
- [6] Alewell C, Ringeval B, Ballabio C, DA Robinson, Panagos P, Borrelli P. Global phosphorus shortage will be aggravated by soil erosion. *Nature Communications* 2020;11(1):4546.
- [7] Hua K, Zhu B. Phosphorus loss through surface runoff and leaching in response to the long-term application of different organic amendments on sloping croplands. *J Soils Sed* 2020;20(9):3459–71.
- [8] Diaz RJ, Rosenberg R. Spreading Dead Zones and Consequences for Marine Ecosystems. *Science* 2008;321(5891):926–9.
- [9] Huang H, Liu J, Zhang P, Zhang D, Gao F. Investigation on the simultaneous removal of fluoride, ammonia nitrogen and phosphate from semiconductor wastewater using chemical precipitation. *Chem Eng J* 2017;307:696–706.
- [10] Bui TH, Hong SP, Kim C, Yoon J. Performance analysis of hydrated Zr (IV) oxide nanoparticle-impregnated anion exchange resin for selective phosphate removal. *Journal of Colloid and Interface Science* 2021;586:741–7.
- [11] Bui TH, Hong SP, Yoon J. Development of nanoscale zirconium molybdate embedded anion exchange resin for selective removal of phosphate. *Water research* 2018;134:22–31.
- [12] Bektaş N, Akbulut H, Inan H, Dimoglu A. Removal of phosphate from aqueous solutions by electro-coagulation. *J Hazard Mater* 2004;106(2–3):101–5.
- [13] Hashim KS, Al Khaddar R, Jasim N, Shaw A, Phipps D, Kot P, et al. Electrocoagulation as a green technology for phosphate removal from River water. *Separation and Purification Technology* 2019;210:135–44.
- [14] Lin J-Y, Kim M, Li D, Kim H, Huang C-p. The removal of phosphate by thermally treated red mud from water: The effect of surface chemistry on phosphate immobilization. *Chemosphere* 2020;247:125867.
- [15] dos Reis GS, Thue PS, Cazacliu BG, Lima EC, Sampaio CH, Quattrone M, et al. Effect of concrete carbonation on phosphate removal through adsorption process and its potential application as fertilizer. *Journal of Cleaner Production* 2020;256:120416.
- [16] Tanada S, Kabayama M, Kawasaki N, Sakiyama T, Nakamura T, Araki M, et al. Removal of phosphate by aluminum oxide hydroxide. *Journal of colloid and interface science* 2003;257(1):135–40.
- [17] Zhu D, Chen Y, Yang H, Wang S, Wang X, Zhang S, et al. Synthesis and characterization of magnesium oxide nanoparticle-containing biochar composites for efficient phosphorus removal from aqueous solution. *Chemosphere* 2020;247:125847.
- [18] Das TK, Scott Q, Bezbarua AN. Montmorillonite-iron crosslinked alginate beads for aqueous phosphate removal. *Chemosphere* 2021;281:130837.
- [19] Abdellaoui Y, Abou Oualid H, Hsini A, El Ibrahimy B, Laabd M, El Ouardi M, et al. Synthesis of zirconium-modified Merlinoite from fly ash for enhanced removal of phosphate in aqueous medium: Experimental studies supported by Monte Carlo/SA simulations. *Chem Eng J* 2021;404:126600.
- [20] Yoon S-Y, Lee C-G, Park J-A, Kim J-H, Kim S-B, Lee S-H, et al. Kinetic, equilibrium and thermodynamic studies for phosphate adsorption to magnetic iron oxide nanoparticles. *Chem Eng J* 2014;236:341–7.
- [21] Wang S, Bian S, Liu J, Li J, Xu S, Liang Z. Highly adsorptive pristine and magnetic biochars prepared from crayfish shell for removal of Cu(II) and Pb(II). *Journal of the Taiwan Institute of Chemical Engineers* 2021;127:175–85.
- [22] Zhang Z, Yang G, Wu J, He J-S, Zhang Y-Z, Tian D, et al. Enhanced properties of magnetic ultralight pear sponge assisted by Fenton-like reaction for oil-water separation. *Journal of the Taiwan Institute of Chemical Engineers* 2021;126:332–40.
- [23] Fatima H, Lee D-W, Yun HJ, Kim K-S. Shape-controlled synthesis of magnetic Fe<sub>3</sub>O<sub>4</sub> nanoparticles with different iron precursors and capping agents. *RSC advances* 2018;8(41):22917–23.
- [24] Lu W, Shen Y, Xie A, Zhang W. Green synthesis and characterization of superparamagnetic Fe<sub>3</sub>O<sub>4</sub> nanoparticles. *J Magn Magn Mater* 2010;322(13):1828–33.
- [25] Veloso SR, Ferreira PM, Martins JA, Coutinho PJ, Castanheira E. Magnetogels: Prospects and main challenges in biomedical applications. *Pharmaceutics* 2018;10(3):145.
- [26] Wu W, Jiang C, Roy VA. Recent progress in magnetic iron oxide–semiconductor composite nanomaterials as promising photocatalysts. *Nanoscale* 2015;7(1):38–58.
- [27] Pourcel L, Moulin M, Fitzpatrick TB. Examining strategies to facilitate vitamin B1 biofortification of plants by genetic engineering. *Frontiers in plant science* 2013;4:160.
- [28] Tunc-Ozdemir M, Miller G, Song L, Kim J, Sodek A, Koussevitzky S, et al. Thiamin confers enhanced tolerance to oxidative stress in *Arabidopsis*. *Plant physiology* 2009;151(1):421–32.
- [29] Asensi-Fabado MA, Munné-Bosch S. Vitamins in plants: occurrence, biosynthesis and antioxidant function. *Trends in plant science* 2010;15(10):582–92.
- [30] Yusof ZNB. Thiamine and its role in protection against stress in plants (enhancement in thiamine content for nutritional quality improvement). *Nutritional Quality Improvement in Plants*. Springer; 2019. p. 177–86.
- [31] Tomlinson RV, Kuhlman DP, Torrence PF, Tieckelmann H. Precursors of the pyrimidine and thiazole rings of thiamine. *Biochimica et Biophysica Acta (BBA) - General Subjects* 1967;148(1):1–10.
- [32] Naeimi H, Ansari Z. Effective preparation of amine-functionalized nano magnetite as a precursor of novel solid acid catalyst for one-pot synthesis of xanthenes under solvent-free conditions. *Journal of the Taiwan Institute of Chemical Engineers* 2018;85:265–72.
- [33] Lin Y-F, Chen H-W, Chen Y-C, Chiou C-S. Application of magnetite modified with polyacrylamide to adsorb phosphate in aqueous solution. *Journal of the Taiwan Institute of Chemical Engineers* 2013;44(1):45–51.
- [34] Yin Z, Zhu L, Mo F, Li S, Hu D, Chu R, et al. Preparation of biochar grafted with amino-riched dendrimer by carbonization, magnetization and functional modification for enhanced copper removal. *Journal of the Taiwan Institute of Chemical Engineers* 2021;121:349–59.
- [35] Santoso SP, Bundjaja V, Angkawijaya AE, Gunarto C, Go AW, Yuliana M, et al. One-step synthesis of nitrogen-grafted copper-gallic acid for enhanced methylene blue removal. *Scientific reports* 2021;11(1):12021.
- [36] Lowry OH, Lopez JA. The determination of inorganic phosphate in the presence of labile phosphate esters. *The Journal of biological chemistry* 1946;162:421–8.
- [37] Shahryari Z, Goharrizi AS, Azadi M. Experimental study of methylene blue adsorption from aqueous solutions onto carbon nano tubes. *International Journal of Water Resources and Environmental Engineering* 2010;2147483647(2):016–28.
- [38] Saruchi Kumar V. Adsorption kinetics and isotherms for the removal of rhodamine B dye and Pb<sup>2+</sup> ions from aqueous solutions by a hybrid ion-exchanger. *Arab J Chem* 2019;12(3):316–29.
- [39] El-Khaiary MI. Least-squares regression of adsorption equilibrium data: Comparing the options. *J Hazard Mater* 2008;158(1):73–87.
- [40] Cantrell CA. Technical Note: Review of methods for linear least-squares fitting of data and application to atmospheric chemistry problems. *Atmos Chem Phys* 2008;8(17):5477–87.
- [41] Lima EC, Gomes AA, Tran HN. Comparison of the nonlinear and linear forms of the van't Hoff equation for calculation of adsorption thermodynamic parameters ( $\Delta S^\circ$  and  $\Delta H^\circ$ ). *J Mol Liq* 2020;311:113315.
- [42] Lima EC, Hosseini-Bandegharaei A, Moreno-Piraján JC, Anastopoulos I. A critical review of the estimation of the thermodynamic parameters on adsorption equilibria. Wrong use of equilibrium constant in the Van't Hooff equation for calculation of thermodynamic parameters of adsorption. *J Mol Liq* 2019;273:425–34.
- [43] Santoso SP, Angkawijaya AE, Yuliana M, Bundjaja V, Soetaredjo FE, Ismadji S, et al. Saponin-intercalated organoclays for adsorptive removal of  $\beta$ -carotene: Equilibrium, reusability, and phytotoxicity assessment. *Journal of the Taiwan Institute of Chemical Engineers* 2020;117:198–208.
- [44] Estelle MA, Somerville C. Auxin-resistant mutants of *Arabidopsis thaliana* with an altered morphology. *Mol Gen Genet* 1987;206:200–6.
- [45] Nakamura Y, Awai K, Masuda T, Yoshioka Y, Takamiya K-i, Ohta H. A Novel Phosphatidylcholine-hydrolyzing Phospholipase C Induced by Phosphate Starvation in *Arabidopsis*. *J Biol Chem* 2005;280:7469–76.
- [46] Angkawijaya AE, Santoso SP, Bundjaja V, Soetaredjo FE, Gunarto C, Ayucitra A, et al. Studies on the performance of bentonite and its composite as phosphate adsorbent and phosphate supplementation for plant. *J Hazard Mater* 2020;399:123130.
- [47] Bunzen H, Grzywa M, Hambach M, Spirkl S, Volkmer D. From Micro to Nano: A Toolbox for Tuning Crystal Size and Morphology of Benzotriazolate-Based Metal–Organic Frameworks. *Crystal Growth & Design* 2016;16(6):3190–7.
- [48] Dong M, Miao X, Brisse R, Deng W, Joussetme B, Silly F. Molecular trapping in two-dimensional chiral organic Kagomé nanoarchitectures composed of Baravelle spiral triangle enantiomers. *NPG Asia Materials* 2020;12(1):20.
- [49] Owusu KA, Qu L, Li J, Wang Z, Zhao K, Yang C, et al. Low-crystalline iron oxide hydroxide nanoparticle anode for high-performance supercapacitors. *Nature Communications* 2017;8(1):14264.
- [50] Mohapatra J, Mitra A, Tyagi H, Bahadur D, Aslam M. Iron oxide nanorods as high-performance magnetic resonance imaging contrast agents. *Nanoscale* 2015;7(20):9174–84.
- [51] Grosvenor A, Kobe B, Biesinger M, McIntyre N. Investigation of multiplet splitting of Fe 2p XPS spectra and bonding in iron compounds. *Surface and Interface Analysis: An International Journal devoted to the development and application of techniques for the analysis of surfaces, interfaces and thin films* 2004;36(12):1564–74.
- [52] Yamashita T, Hayes P. Analysis of XPS spectra of Fe<sup>2+</sup> and Fe<sup>3+</sup> ions in oxide materials. *Applied surface science* 2008;254(8):2441–9.
- [53] Sing KS. Reporting physisorption data for gas/solid systems with special reference to the determination of surface area and porosity (Recommendations 1984). *Pure Appl Chem* 1985;57(4):603–19.

- [54] Zhang J, Han J, Wang M, Guo R. Fe<sub>3</sub>O<sub>4</sub>/PANI/MnO<sub>2</sub> core–shell hybrids as advanced adsorbents for heavy metal ions. *J Mater Chem A* 2017;5(8):4058–66.
- [55] Gulicovski JJ, Čerović LS, Milonjić SK. Point of Zero Charge and Isoelectric Point of Alumina. *Mater Manuf Processes* 2008;23(6):615–9.
- [56] Havlin JL, Schlegel AJ. Review of Phosphate as a Plant Nutrient and Fungicide 2021;5(3):52.
- [57] Jiang X, Guan Q, Feng M, Wang M, Yan N, Wang M, et al. Preparation and pH Controlled Release of Fe3O4/Anthocyanin Magnetic Biocomposites 2019;11(12):2077.
- [58] Andreas A, Winata ZG, Santoso SP, Angkawijaya AE, Yuliana M, Soetaredjo FE, et al. Bio-composite hydrogel beads from glutaraldehyde-crosslinked phytochemicals in alginate for effective removal of methylene blue. *J Mol Liq* 2021;329:115579.
- [59] Chubar N, Kanibolotskyy V, Strelko V, Gallios G, Samanidou V, Shaposhnikova T, et al. Adsorption of phosphate ions on novel inorganic ion exchangers. *Colloids Surf Physicochem Eng Aspects* 2005;255(1–3):55–63.
- [60] Giles CH, MacEwan TH, Nakhwa SN, Smith D. 786. Studies in adsorption. Part XI. A system of classification of solution adsorption isotherms, and its use in diagnosis of adsorption mechanisms and in measurement of specific surface areas of solids. *J Chem Soc* 1960(0):3973–93.
- [61] Piccin JS, Cadaval TRSA, de Pinto LAA, Dotto GL. Adsorption Isotherms in Liquid Phase: Experimental, Modeling, and Interpretations editors. In: Bonilla-Petriciolet A, Mendoza-Castillo DL, Reynel-Avila HE, editors. *Adsorption Processes for Water Treatment and Purification*. Cham: Springer International Publishing; 2017. p. 19–51.
- [62] Al-Ghouti MA, Da'ana DA. Guidelines for the use and interpretation of adsorption isotherm models: A review. *J Hazard Mater* 2020;393:122383.
- [63] Tanhaei B, Ayati A, Lahtinen M, Sillanpää M. Preparation and characterization of a novel chitosan/Al<sub>2</sub>O<sub>3</sub>/magnetite nanoparticles composite adsorbent for kinetic, thermodynamic and isotherm studies of Methyl Orange adsorption. *Chem Eng J* 2015;259:1–10.
- [64] Ajmal Z, Muhammad A, Usman M, Kizito S, Lu J, Dong R, et al. Phosphate removal from aqueous solution using iron oxides: adsorption, desorption and regeneration characteristics. *Journal of colloid and interface science* 2018;528:145–55.
- [65] Zeng H, Fisher B, Giamar DE. Individual and competitive adsorption of arsenate and phosphate to a high-surface-area iron oxide-based sorbent. *Environ Sci Technol* 2008;42(1):147–52.
- [66] Bozorgpour F, Ramandi HF, Jafari P, Samadi S, Yazd SS, Alibadi M. Removal of nitrate and phosphate using chitosan/Al<sub>2</sub>O<sub>3</sub>/Fe<sub>3</sub>O<sub>4</sub> composite nanofibrous adsorbent: comparison with chitosan/Al<sub>2</sub>O<sub>3</sub>/Fe<sub>3</sub>O<sub>4</sub> beads. *International journal of biological macromolecules* 2016;93:557–65.
- [67] Shen H, Wang Z, Zhou A, Chen J, Hu M, Dong X, et al. Adsorption of phosphate onto amine functionalized nano-sized magnetic polymer adsorbents: mechanism and magnetic effects. *RSC Advances* 2015;5(28):22080–90.
- [68] Jiang H, Chen P, Luo S, Tu X, Cao Q, Shu M. Synthesis of novel nanocomposite Fe<sub>3</sub>O<sub>4</sub>/ZrO<sub>2</sub>/chitosan and its application for removal of nitrate and phosphate. *Applied Surface Science* 2013;284:942–9.
- [69] Yan L-g, Yang K, Shan R-r, Yan T, Wei J, Yu S-j, et al. Kinetic, isotherm and thermodynamic investigations of phosphate adsorption onto core–shell Fe<sub>3</sub>O<sub>4</sub>@ LDHs composites with easy magnetic separation assistance. *Journal of colloid and interface science* 2015;448:508–16.
- [70] Jiang D, Amano Y, Machida M. Removal and recovery of phosphate from water by a magnetic Fe<sub>3</sub>O<sub>4</sub>@ASC adsorbent. *Journal of environmental chemical engineering* 2017;5(5):4229–38.
- [71] Wang F, Liu D, Zheng P, Ma X. Synthesis of rectorite/Fe<sub>3</sub>O<sub>4</sub>-CTAB composite for the removal of nitrate and phosphate from water. *Journal of Industrial and Engineering Chemistry* 2016;41:165–74.
- [72] Hu D, Wang L. Adsorption of amoxicillin onto quaternized cellulose from flax noil: Kinetic, equilibrium and thermodynamic study. *Journal of the Taiwan Institute of Chemical Engineers* 2016;64:227–34.
- [73] Liu X, Tian J, Li Y, Sun N, Mi S, Xie Y, et al. Enhanced dyes adsorption from wastewater via Fe<sub>3</sub>O<sub>4</sub> nanoparticles functionalized activated carbon. *J Hazard Mater* 2019;373:397–407.

# Evaluation of the potential removal of phosphate using rice husk ash-derived zeolite NaP1

**Phuong Lan Tran-Nguyen,<sup>a\*</sup>  Kim-Phung Ly,<sup>b</sup>  Thanh-Ty Nguyen,<sup>b</sup>  Shella Permatasari Santoso,<sup>c</sup>  Nguyen-Phuong-Dung Tran,<sup>d</sup>  Artik Elisa Angkawijaya,<sup>e</sup>  Maria Yuliana,<sup>c</sup>  Minh-Nhut Nguyen<sup>b</sup>  and Tuan Thi-Tran-Anh<sup>f</sup> **

## Abstract

**BACKGROUND:** Zeolite NaP1 with high crystalline intensity and good shape has been synthesized by utilizing rice husk ash. Several factors related to the formation of zeolite, such as mixing ratios, aging time, and reaction time, were investigated. Furthermore, the potential phosphate adsorption of the optimal synthesized zeolite was evaluated.

**RESULTS:** Under the optimal conditions ( $\text{SiO}_2/\text{Al}_2\text{O}_3$  molar ratio = 4.0,  $\text{NaOH}$  concentration = 1.5 M, aging time = 12 h, and reaction time = 8 h), the surface area and pore diameter of the zeolite NaP1 obtained were  $50 \text{ m}^2 \text{ g}^{-1}$  and  $40.77 \text{ \AA}$ , respectively. By varying the aging and reaction times, zeolite NaP1 with different surface areas could be created. Specifically, reducing the aging time and reaction time result in zeolite NaP1 with a lower surface area. The adsorption efficiency and adsorption capacity of the optimal synthesized zeolite NaP1 were 38.67% and  $19.97 \text{ mg g}^{-1}$ , respectively, at pH 6.0, with an initial phosphate concentration of  $100 \text{ mg L}^{-1}$ , an adsorbent dosage of  $2 \text{ g L}^{-1}$ , and a contact time of 120 min. The data are well described under the Temkin and Redlich-Peterson models, with the correlation coefficients of 0.991 and 0.995, respectively. The maximum adsorption capacity of the Langmuir model reached  $19.053 \text{ mg g}^{-1}$ .

**CONCLUSION:** The main contribution of this work is the direct use of rice husk ash without pretreatment to generate high crystalline zeolite NaP1 in a shorter time. The phosphate ion removal efficiency by zeolite NaP1 may be further improved by functionalizing zeolite surfaces and expanding its other applications.

© 2023 Society of Chemical Industry (SCI).

Supporting information may be found in the online version of this article.

**Keywords:** adsorption; phosphate; short aging time; rice husk ash; zeolite NaP1

## INTRODUCTION

The development of industries, agriculture, mining, and community activities has led to an increase in the level of phosphates entering water bodies.<sup>1</sup> An excess of phosphate in water can cause eutrophication, which is one of the most important issues affecting the ecological function and quality of water in rivers, lakes, and coastal areas.<sup>2</sup> Phosphate contamination in surface water and groundwater can be associated with human health problems, such as diarrhea, nausea, and skin irritation<sup>3</sup>; thus, the removal of excessive phosphate from water sources is a crucial concern. Common methods for treating phosphate are adsorption, ion exchange, chemical precipitation, and coagulation.<sup>4</sup> Among them, adsorption is well-known as a simple, economical, and high-performance process.<sup>1,2</sup> Zeolites, biochar,  $\text{ZrO}_2/\text{Fe}_3\text{O}_4$ , and La-Zr-Zn ternary oxide have been reported as effective adsorbents for removing phosphates.<sup>3,5-7</sup>

Zeolites are a family of inorganic minerals with aluminosilicate as their main component. The structure of zeolites consists of

frameworks that are built from  $[\text{SiO}_4]^{4-}$  and  $[\text{AlO}_4]^{5-}$  tetrahedrons linked together via oxygen atoms.<sup>8,9</sup> With their numerous unique

\* Correspondence to: PL Tran-Nguyen, Faculty of Mechanical Engineering, Can Tho University, Campus II, 3/2 street, Can Tho, 900100, Vietnam, E-mail: [tnplan@ctu.edu.vn](mailto:tnplan@ctu.edu.vn)

<sup>a</sup> Faculty of Mechanical Engineering, Can Tho University, Can Tho, Vietnam

<sup>b</sup> Faculty of Chemical Engineering, Can Tho University, Can Tho, Vietnam

<sup>c</sup> Department of Chemical Engineering, Widya Mandala Surabaya Catholic University, Surabaya, Indonesia

<sup>d</sup> Department of Materials Science and Engineering, National Taiwan University of Science and Technology, Taipei, Taiwan

<sup>e</sup> Center for Sustainable Resource Science, RIKEN, Yokohama, Japan

<sup>f</sup> School of Basic Sciences, Tra Vinh University, Tra Vinh, Vietnam

properties, zeolites play important roles in many industrial and agricultural fields.<sup>10</sup> Among many kinds of zeolites with diverse structures, zeolite NaP1 of the Gismondine family ( $\text{Na}_6\text{Al}_6\text{Si}_{10}\text{O}_{32}\cdot12\text{H}_2\text{O}$ ) is one of the most interesting structural zeolites with intersecting channels of  $3.1\text{ \AA} \times 4.4\text{ \AA}$  and  $2.6\text{ \AA} \times 4.9\text{ \AA}$ .<sup>11,12</sup> Zeolite NaP1 is commonly selected to separate small gas molecules due to its small and characteristic pore size. Furthermore, because of its durable structure, zeolite NaP1 is a promising adsorbent to treat heavy metals from wastewater, radioactive substances, and toxic waste.<sup>12,13</sup>

Zeolite NaP1 can be synthesized from a variety of feedstock, such as commercial silica, kaolin, pumice, fly ash, and rice husk ash (RHA).<sup>11,13-16</sup> In rice-producing countries, such as Vietnam, the amount of rice husk obtained from the rice milling process can reach tens of millions tons annually,<sup>17</sup> and this husk is utilized for different purposes.<sup>18</sup> This huge amount of RHA generated should be appropriately handled to avoid environmental pollution.<sup>19</sup> The use of RHA, which is a rich source of silica, to create valuable materials has become a popular trend of green chemistry.<sup>18,20,21</sup>

The most common methods for zeolite synthesis are hydrothermal and alkaline fusion, particularly the hydrothermal process.<sup>8</sup> The term hydrothermal is used in a broad sense, referring to the crystallization of zeolite from aqueous systems containing necessary chemical components, such as  $\text{SiO}_2$  and  $\text{Al}_2\text{O}_3$ ,<sup>8</sup> and requiring a reaction time of several days and a high temperature of  $80\text{--}200\text{ }^\circ\text{C}$ .<sup>11,13</sup> In addition, feedstock (like solid wastes) have to be pretreated before being subjected to reactions.<sup>19,22</sup> A mixture of zeolite NaP1 and analcime was synthesized from RHA in 2 h at  $140\text{--}170\text{ }^\circ\text{C}$ ; however, the RHA needed to be pretreated over several steps, such as soaking in HCl for 3 h and then burning at  $700\text{ }^\circ\text{C}$  for 2 h.<sup>22</sup> Bohra *et al.* carried out the synthesis of zeolite P1 at  $100\text{ }^\circ\text{C}$  for 48 h,<sup>13</sup> whereas Cardoso *et al.* successfully created zeolite P1 from fly ash in a shorter reaction time of 24 h at the same reaction temperature.<sup>23</sup> When a lower temperature ( $80\text{ }^\circ\text{C}$ ) was applied, a longer reaction time (26 h) was required.<sup>16</sup> For the fusion method, although the reaction time could be reduced, fusing at high temperatures was necessary before the reaction.<sup>24,25</sup> At the beginning, fly ash was mixed with solid NaOH, then fused at  $550\text{ }^\circ\text{C}$  for 1–2 h to release Si and Al in the form of sodium aluminate and sodium silicate. Lastly, a mixture at a suitable molar ratio was further reacted to obtain zeolite.<sup>24-26</sup> Additionally, aging time affects the synthesis of zeolite, and it is known that a prolonged time before heating the mixture to a required temperature benefited the crystallization of zeolites.<sup>27</sup> Aging time is a vital parameter of the reaction because it can cause changes to the material phase, especially the types, crystal sizes, and surface area of zeolites.<sup>28</sup> The aging time can be adjusted depending on the desired types and properties of zeolites.<sup>27,29</sup>

Following the procedure of Tran-Nguyen *et al.* regarding the synthesis of  $\text{NaX}$ ,<sup>29</sup> this work developed a synthesis process of zeolite NaP1 from RHA. The main goal of the study was to synthesize RHA-derived zeolite NaP1 and evaluate its adsorption capacity for phosphate removal. The first specific aim was to investigate the effects of factors on the formation of zeolite NaP1, including mixing ratios, aging time, and reaction time. The products are, then, characterized by X-ray diffraction (XRD), X-ray fluorescence (XRF), field emission scanning electron microscopy (FE-SEM), dynamic light scattering (DLS), and Brunauer–Emmett–Teller (BET). Additionally, the phosphate adsorption capacity and efficiency of zeolite NaP1 were evaluated. Lastly, the Langmuir, Freundlich, Temkin, Sips and Redlich-Peterson isotherm models were applied to elucidate the mechanism of the adsorption process.

## MATERIALS AND METHODS

### Materials

RHA collected from the local company at Can Tho City, Vietnam, was directly used for the NaP1 synthesis. The characteristics of RHA can be found in the study of Tran-Nguyen *et al.*<sup>29</sup> Analytical chemicals used in this work, such as sodium hydroxide pellets (purity 97%) and potassium dihydrogen phosphate (purity 99.5%), were bought from Acros (New Jersey, USA). Aluminum powder (purity 99%) was purchased at Union Chemical Industry Company Ltd. (Taipei, Taiwan), while ammonium molybdate tetrahydrate (purity 99%) and L-Ascorbic acid (purity 99%) were obtained from Sigma-Aldrich (MO, USA). Hydrochloric acid (purity 37%) was supplied by Xilong (Guangdong, China).

### Synthesis of zeolite NaP1

The synthesis process of this study (Fig. 1) followed that of Tran-Nguyen *et al.* and Bohra *et al.* with some modifications is depicted in (Fig. 1).<sup>13,29</sup> Firstly, for the preparation of  $\text{Na}_2\text{SiO}_3$  solution, 10 g RHA and NaOH solution (100 mL, 5 M) were placed into a round bottom flask and heated to  $90\text{ }^\circ\text{C}$  for 3 h. After reaction, the black solid was washed with deionized water and removed by vacuum filtration. Besides this, a certain amount of aluminum powder was dissolved into NaOH solution (25 mL, 3 M) to obtain a sodium aluminate solution. Afterward, the mixture of  $\text{NaSiO}_3$  and  $\text{NaAlO}_2$  was stirred at  $50\text{ }^\circ\text{C}$  and 500 rpm for 2 h to form the aluminosilicate gel. After being aged at room temperature for a pre-determined time, the suspension was heated to  $100\text{ }^\circ\text{C}$  and kept for 4 h. The reaction temperature was selected from the literature review and is invariant for all experiments.<sup>13,14,16,30-32</sup> The product was washed with deionized water until reaching a neutral pH and then separated using a centrifuge (Hanil Smart 15 Plus, Korea) for 10 min at 13 475 g. After product separation, the NaOH-rich solution was reused for the initial aluminum dissolution in the following experiments. The solid was dried until constant weight prior to storage. The imprecision or random error of the synthesis process was evaluated by the replication experiments.

### Characterizations

X-ray diffraction of NaP1 was analyzed by a D8 Advance diffractometer (Bruker, Germany) with CuK radiation ( $\lambda = 1.54056\text{ \AA}$ ) at 40 kV and 30 mA. Chemical composition of the synthesized zeolites was determined via a S8 Tiger X-Ray Fluorescence machine (Bruker, Germany). FE-SEM was conducted on a S-4800 instrument (Hitachi, Japan) to observe the morphology of the products. A Nova 2000 instrument (Quantachrome Instruments, USA) was applied for  $\text{N}_2$  adsorption-desorption at 77 K and the samples were degassed at 423 K for 6 h before measurement. The surface area and pore size were determined using the Brunauer–Emmett–Teller (BET) model.<sup>33</sup> The particle size distribution of NaP1 was examined via DLS (SZ-100, Horiba, Japan).

### Adsorption of phosphates

#### Determination of point of zero charge

The point of zero charge of NaP1 was determined by adding 0.2 g of adsorbent to 0.1 M KCl solutions at different pH. The pH of the solution was adjusted between 2 and 12 with 0.01 M NaOH or 0.01 M HCl. After the solution was kept at room temperature for 24 h, its final pH was determined. The difference between the initial and final pH can determine the isoelectric point.<sup>34</sup>

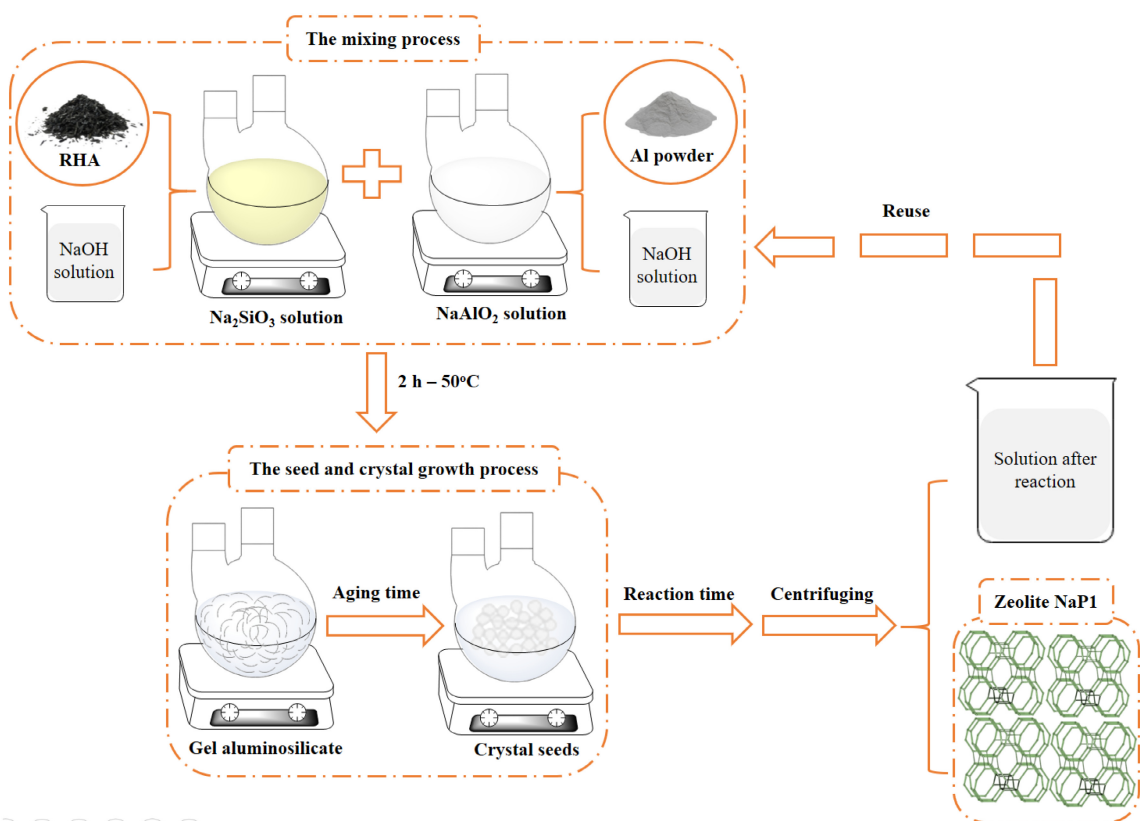


**Figure 1.** Schematic flowchart for zeolite NaP1 synthesis from RHA.

#### Batch adsorption experiments

The phosphate stock solution of  $1000 \text{ mg L}^{-1}$  was prepared by dissolving potassium dihydrogen phosphate in deionized water. The effect of pH on phosphate removal was examined by varying the pH from 2 to 10. The use of 0.01 M NaOH or 0.01 M HCl was for adjusting the pH value of the initial phosphate solutions. The adsorbent dosage of  $2 \text{ g L}^{-1}$  was subjected to the phosphate solutions and shaken at 200 rpm. After 45 min, the post-adsorption solutions were collected by centrifugation (10 min, 13 475 g). The effects of adsorbent dosage (0.5, 1.0, 2.0, 3.0, 4.0, and  $5.0 \text{ g L}^{-1}$ ) and concentration of initial phosphate solution (20 to  $400 \text{ mg L}^{-1}$ ) were investigated. The contact time was surveyed from 15–1440 min.

The concentrations of the solution before and after adsorption were measured using a UVS-2800 Spectrophotometer (Labomed, USA). The formation of a blue complex between phosphate ion and ammonium heptamolybdate in an acidic medium was observed in this method. The optical absorbance of the solutions could be determined at  $\lambda = 880 \text{ nm}$ .<sup>35</sup> The adsorption efficiency Y (%) and capacity  $Q_t$  ( $\text{mg g}^{-1}$ ) were calculated based on the following two formulas:

$$Y (\%) = \frac{(C_0 - C_e) \times 100}{C_0} \quad (1)$$

$$Q_t = \frac{(C_0 - C_e) \times V}{m} \quad (2)$$

where  $C_0$  is the initial concentration of phosphate ( $\text{mg L}^{-1}$ ),  $C_e$  is the equal concentration of phosphate ( $\text{mg L}^{-1}$ ),  $V$  and  $m$  are the

volume of the phosphate solution ( $\text{L}$ ) and the mass of NaP1 ( $\text{g}$ ), respectively.

#### Adsorption isotherms

The adsorption data were analyzed based on Langmuir, Freundlich, Temkin, Sips and Redlich-Peterson adsorption isotherm models. The Langmuir and Freundlich adsorption models described the monolayer and multilayer adsorption between the adsorbed molecules and the adsorbent.<sup>33</sup> The Temkin model expresses the physical or chemical adsorption process via the adsorption heat parameter.<sup>36</sup> The mathematical expressions of Langmuir, Freundlich, Temkin models are presented in Eqns. (3)–(5), respectively:

$$Q_t = \frac{Q_{\max} K_L C_e}{1 + K_L C_e} \quad (3)$$

$$Q_t = K_F C_e^{\frac{1}{n_F}} \quad (4)$$

$$Q_t = \frac{RT}{b_T} \ln(K_T C_e) \quad (5)$$

where  $Q_t$  ( $\text{mg g}^{-1}$ ) is the equilibrium adsorption capacity on the adsorbent,  $C_e$  ( $\text{mg L}^{-1}$ ) is the concentration of phosphate solution at equilibrium,  $Q_{\max}$  ( $\text{mg g}^{-1}$ ) is the Langmuir maximum adsorption capacity,  $K_L$  ( $\text{L mg}^{-1}$ ) is the Langmuir adsorption equilibrium constant,  $K_F$  ( $\text{mg g}^{-1}$ ) ( $\text{mg L}^{-1})^{1/n}$  is the Freundlich isotherm constant, and  $n_F$  is the constant related to the heterogeneity of the adsorbent surface;  $R$  is the gas constant ( $8.314 \times 10^{-3} \text{ kJ mol}^{-1} \text{ K}^{-1}$ ),  $T$  is the absolute temperature (K),  $b_T$  ( $\text{kJ mol}^{-1}$ ) is the Temkin

coefficient that characterizes the heat of adsorption, and  $K_t$  ( $\text{L g}^{-1}$ ) is a constant related to the maximum value of binding energy.<sup>37</sup>

Further, Sips and Redlich-Peterson three-factor adsorption models were used to explore the interactions occurring during the adsorption process. As mentioned, these two models were combined from the Langmuir model and the Freundlich model.<sup>36</sup> The mathematical expression of the Sips and Redlich-Peterson models are reported in Eqns. (6) and (7), respectively:

$$Q_t = \frac{Q_s \alpha_s C_e^{n_s}}{1 + \alpha_s C_e^{n_s}} \quad (6)$$

$$Q_t = \frac{K_{RP} C_e}{1 + \alpha_{RP} C_e^\beta} \quad (7)$$

where  $Q_s$  ( $\text{mg g}^{-1}$ ) and  $\alpha_s$  ( $\text{L mg}^{-1}$ ) are the Sips maximum adsorption capacity and the Sips equilibrium constant related to the adsorption affinity, respectively,  $n_s$  is the Sips model exponent that expresses the heterogeneity of the adsorbent;  $K_{RP}$  ( $\text{L g}^{-1}$ ) is the Redlich-Peterson isotherm constant,  $\alpha_{RP}$  ( $\text{L mg}^{-1}$ ) is a constant, and  $\beta$  is a parameter whose value ranges from 0 to 1. At  $\beta \sim 1$ , the isotherm is asymptotic to the Langmuir model. In contrast, the isotherm describing the adsorption process is like the Freundlich model at  $\sim 0$ .<sup>36</sup>

## RESULTS AND DISCUSSION

### Synthesis of NaP1 from RHA

#### Effects of mixing ratios

The molar ratio of  $\text{SiO}_2/\text{Al}_2\text{O}_3$  has been known as one of the key factors affecting the formation of zeolite phases.<sup>12,14,31,38</sup> The yield of zeolite NaP1 obtained by varying the molar ratio of  $\text{SiO}_2$  and  $\text{Al}_2\text{O}_3$  ( $\text{SiO}_2/\text{Al}_2\text{O}_3$ ) molar ratio from 3.0 to 7.0 is summarized in Table 1. The increase in  $\text{SiO}_2/\text{Al}_2\text{O}_3$  molar ratio is proportional with the increase of the product mass, except for that of molar ratio of 3.0 that result in a higher yield. Although the yield of synthesized zeolite was higher at  $\text{SiO}_2/\text{Al}_2\text{O}_3$  molar ratio of 3.0, it was noted that the intensity of its XRD characteristic peaks was low (Fig. 2(a)) compared to the zeolite NaP1 resulting from other

**Table 1.** Effects of reaction conditions on product yield

Reaction condition <sup>a</sup>		
$\text{SiO}_2/\text{Al}_2\text{O}_3$ (mol mol <sup>-1</sup> )	NaOH concentration (M)	Product yield (kg product/ kg RHA)
3.0	3.0	$1.482 \pm 0.042$
4.0	3.0	$1.194 \pm 0.036$
5.0	3.0	$0.918 \pm 0.034$
6.0	3.0	$0.714 \pm 0.045$
7.0	3.0	$0.570 \pm 0.028$
4.0	1.0	$1.086 \pm 0.034$
4.0	1.5	$1.190 \pm 0.047$
4.0	2.0	$1.187 \pm 0.038$
4.0	2.5	$1.176 \pm 0.035$
4.0	3.0	$1.171 \pm 0.027$
4.0	4.0	$1.174 \pm 0.037$

<sup>a</sup> All reactions were conducted at a reaction temperature of 100 °C and time of 4 h, without aging.

ratios, thus implying low crystallinity and low purity. An increase of molar ratio to 4.0 resulted in a rapid increase of intensity and in almost no impurities being found. Hildebrando *et al.* reported a similar result to this study on the effect of molar ratio towards the formation of zeolite.<sup>14</sup> All XRD results were compared to the standard card of zeolite NaP1 (JCPDS card No. 39-0219) in this work.

As the molar ratio was increased to 5.0 and 6.0, the peaks of zeolite NaP1 were still clearly present and their intensity seemed lower than those at the ratio of 4.0. At 7.0, the peak intensity of zeolite NaP1 was significantly reduced compared to those with molar ratios of 4.0–6.0 (Fig. 2(a)). An increase of  $\text{SiO}_2/\text{Al}_2\text{O}_3$  molar ratio from 3.8, 5.0 to 10.0 resulted in a decrease in peak intensity of zeolite NaP1.<sup>30</sup> Moreover, the structural order of zeolite NaP1 and its peak intensity significantly decreased as the  $\text{SiO}_2/\text{Al}_2\text{O}_3$  molar ratio was increased.<sup>31</sup> Besides this, some other types of zeolites might exist in the final crystalline phase, including zeolite NaY

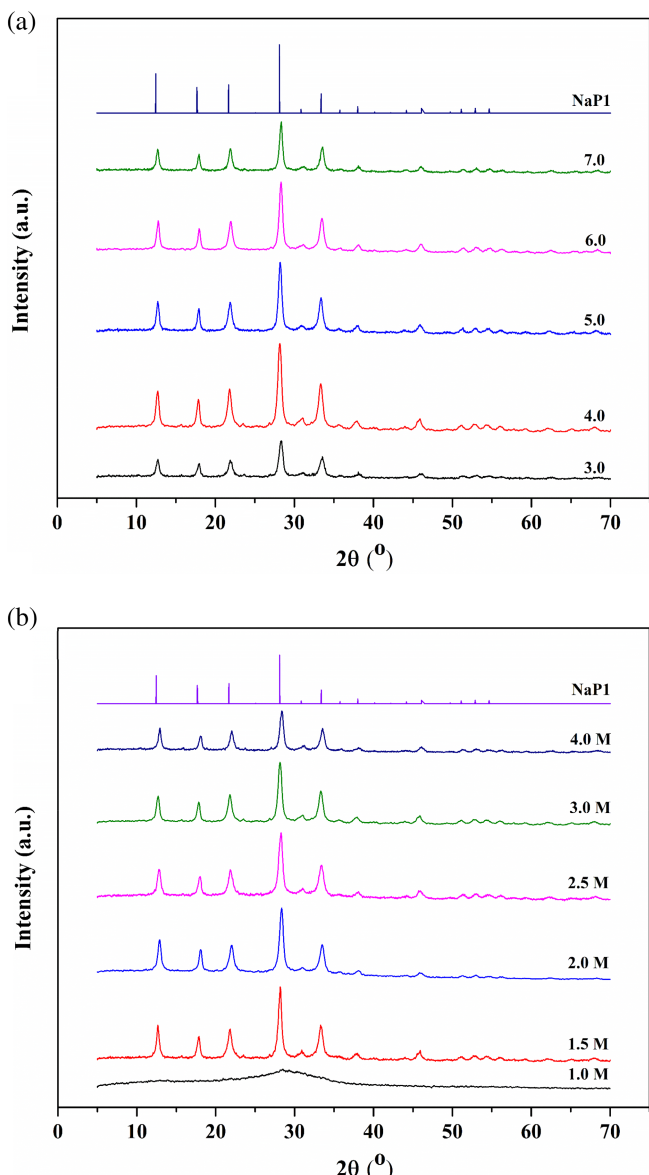


**Figure 2.** XRD patterns of NaP1 at different molar ratios of  $\text{SiO}_2/\text{Al}_2\text{O}_3$  (a) and at different NaOH concentrations (b).

and analcime, and the predominance of amorphous phases in the products was identified at higher  $\text{SiO}_2/\text{Al}_2\text{O}_3$  molar ratios.<sup>12,31,39</sup> In this study, only the reduction of zeolite NaP1 peak intensity was detected and no other zeolite phases appeared. The reason for this difference might be due to the source of the feedstock and to the experimental process.

Zeolite NaP1 was classified as a high silica zeolite,<sup>40</sup> thus, a higher concentration of  $\text{SiO}_2$  in solution favored the formation of zeolite NaP1. In addition,  $\text{Si}^{4+}$  ions were more easily dissolved than  $\text{Al}^{3+}$  ions in alkaline mixtures.<sup>31</sup> A further increase in the  $\text{SiO}_2/\text{Al}_2\text{O}_3$  molar ratio led to a decrease in the amount of  $\text{Al}^{3+}$  ions, while the alkalinity of the gel mixture was retained. The secondary structures of zeolite NaP1 cannot favorably be formed due to the different amounts of  $\text{Si}^{4+}$  and  $\text{Al}^{3+}$  ions in the mixture. As a result, the intensity of the characteristic peaks decreases at a molar ratio 4.0–7.0. The  $\text{SiO}_2/\text{Al}_2\text{O}_3$  ratio should be carefully controlled to achieve the expected zeolite phase. Furthermore, the main chemical composition of the synthesized NaP1 (including  $\text{SiO}_2$ ,  $\text{Al}_2\text{O}_3$ ,  $\text{Na}_2\text{O}$ , and other metal oxides) is reported in XRF results; particularly, the Si, Al, and Na oxides accounted for about 85.22–87.12% (Table 2). This agrees with the literature in that the chemical composition of the products and the appropriate  $\text{SiO}_2/\text{Al}_2\text{O}_3$  ratio range are similar to the values found in this work for most zeolites.<sup>28</sup> Additionally, the change of the initial  $\text{SiO}_2/\text{Al}_2\text{O}_3$  molar ratio of the reaction mixture will affect the chemical composition of zeolite NaP1. In fact, when these ratios were varied from 3 to 7, the molar ratios of the products increased between 2.27 and 3.42. The formation of zeolite NaP1 at various Si/Al molar ratios was also reported in previous works.<sup>16,41</sup> An increase of the Si/Al molar ratio resulted a corresponding increase of Si/Al molar ratio in zeolite NaP1.<sup>41</sup> Moreover, the typical oxide formula of zeolite NaP1 could be presented as follows:  $\text{M}_{2/n}\text{O} \cdot \text{Al}_2\text{O}_3 \cdot 1.8\text{--}5.0 \cdot \text{SiO}_2 \cdot 5\text{H}_2\text{O}$ , where M is the alkali metal and n is the valence of the corresponding metal.<sup>42</sup> According to the XRD and XRF results, a molar ratio of 4.0 was chosen as the optimal condition for further investigations.

The concentration of NaOH (or alkalinity) also affected the formation and the morphology of zeolites.<sup>12,43</sup> In this work, the concentration of NaOH ranged from 1.0 M to 4.0 M (Fig. 2(b)). At 1.0 M, the dominant amorphous phase was predicted to generate aluminosilicate gel.<sup>44</sup> Zeolite NaP1 generated at higher concentrations (between 1.5 M and 3.0 M) exhibited typical characteristic peaks with high intensity, whereas the intensity of peaks decreased at a concentration of 4.0. Gismondine structure of zeolite NaP1 was appropriately created at a low alkali concentration from 0.5 to 1 M,<sup>16</sup> which functioned as a medium for the release of Si and Al from precursors and acted as the supply source of  $\text{Na}^+$  and  $\text{OH}^-$  for the growth of zeolite crystals.<sup>12,45</sup> Zeolite NaP1

still has not yet been formed at low alkalinity ( $\sim 1.0$  M); nevertheless, the zeolite structures uniformly arrange and form zeolite frameworks at the appropriate alkalinity concentration. As a result, the characteristic peaks of zeolite NaP1 fully appeared at alkalinity levels of 1.5–3.0 M. However, the dissolving of zeolite NaP1 and the formation of by-products (such as zeolite NaX or sodalite) were also reported at high alkalinity.<sup>16,29,45,46</sup>

To confirm the above phenomenon, the morphology of zeolite NaP1 at different alkali concentrations was examined (Fig. 3). The amorphous parts of the aluminosilicate gel were firstly obtained (Fig. 3(a)). The fairly well-crystallized zeolite NaP1 was formed by the growth of spherical crystals with small knobs protruding on the surface at an appropriate NaOH concentration. This agrees with previous studies.<sup>41,47</sup> The morphology of crystals at different alkalinity samples was relatively uniform; nevertheless, the crystals of synthesized zeolite NaP1 at alkalinity concentrations above 1.5 M revealed cracking and cleavage. The FE-SEM results agreed with the previous works that too high alkalinity should not be applied for the synthesis of zeolite NaP1 because, in high alkaline environments, zeolite NaP1 can be dissolved to form other types of zeolite.<sup>16</sup> Based on the data from XRD and SEM, the milder synthesis condition with an alkaline concentration of 1.5 M was selected.

#### Effects of aging time

Aging is the transition process from aluminosilicate gel to the secondary building units of zeolite; it means that the primary building units of the zeolite will be assembled and the secondary building units (such as 4-membered rings and 8-membered rings) will be formed during this period.<sup>12,28,48</sup> The effects of aging time from 0 to 48 h on the XRD crystallinity pattern of zeolite NaP1 are given in Fig. 4. The typical characteristic peaks of zeolite NaP1 were clearly visible for the particles that underwent aging from 0 to 24 h; especially high intensity and purity were observed for aging from 0 to 12 h (Fig. 4). On the other hand, a decrease of the characteristic peak intensity at 24 h was observed and only the amorphous phase remained at 48 h. In fact, aging helped increase the zeolites crystallinity and the intensity of the characteristic peaks,<sup>12,31</sup> although the crystalline nuclei were dissolved and rearranged to generate other types of zeolites in the alkaline medium for a longer time.<sup>46</sup> This resulted in the low intensity of the characteristic peaks at a prolonged aging time of 24 h.

The surface area ( $S_{\text{BET}}$ ) increased from 20 to  $38 \text{ m}^2 \text{ g}^{-1}$  as the aging time was prolonged from 0 to 12 h (Table 3). The amount of crystal seeds proportionally increased with a longer aging time; thus, a significant increase of the surface area of zeolite NaP1 was obtained.<sup>28</sup> By varying the aging time, different surface areas of zeolite NaP1 can possibly be achieved.

**Table 2.** Chemical composition of zeolite NaP1 at different  $\text{SiO}_2/\text{Al}_2\text{O}_3$  ratios

$\text{SiO}_2/\text{Al}_2\text{O}_3$ ratio <sup>a</sup> (mol mol <sup>-1</sup> )	$\text{SiO}_2$	$\text{Al}_2\text{O}_3$	$\text{Na}_2\text{O}$	$\text{K}_2\text{O}$	$\text{Fe}_2\text{O}_3$	$\text{CaO}$	Others	Loss of Ignition	$\text{SiO}_2/\text{Al}_2\text{O}_3$ ratio <sup>b</sup> (mol mol <sup>-1</sup> )
3	41.02	29.82	16.28	0.31	0.08	0.03	0.06	12.4	2.27
4	42.89	27.48	15.52	0.34	0.08	0.03	0.06	13.6	2.77
5	46.09	25.19	13.94	0.35	0.04	0.02	0.07	14.3	3.17
6	47.28	25.34	13.70	0.31	0.08	0.04	0.05	13.2	3.25
7	49.53	24.38	12.84	0.38	0.08	0.05	0.04	12.7	3.42

<sup>a</sup> Initial  $\text{SiO}_2/\text{Al}_2\text{O}_3$  ratio of mixture before the reaction.

<sup>b</sup> Molar ratio of  $\text{SiO}_2/\text{Al}_2\text{O}_3$  of products.

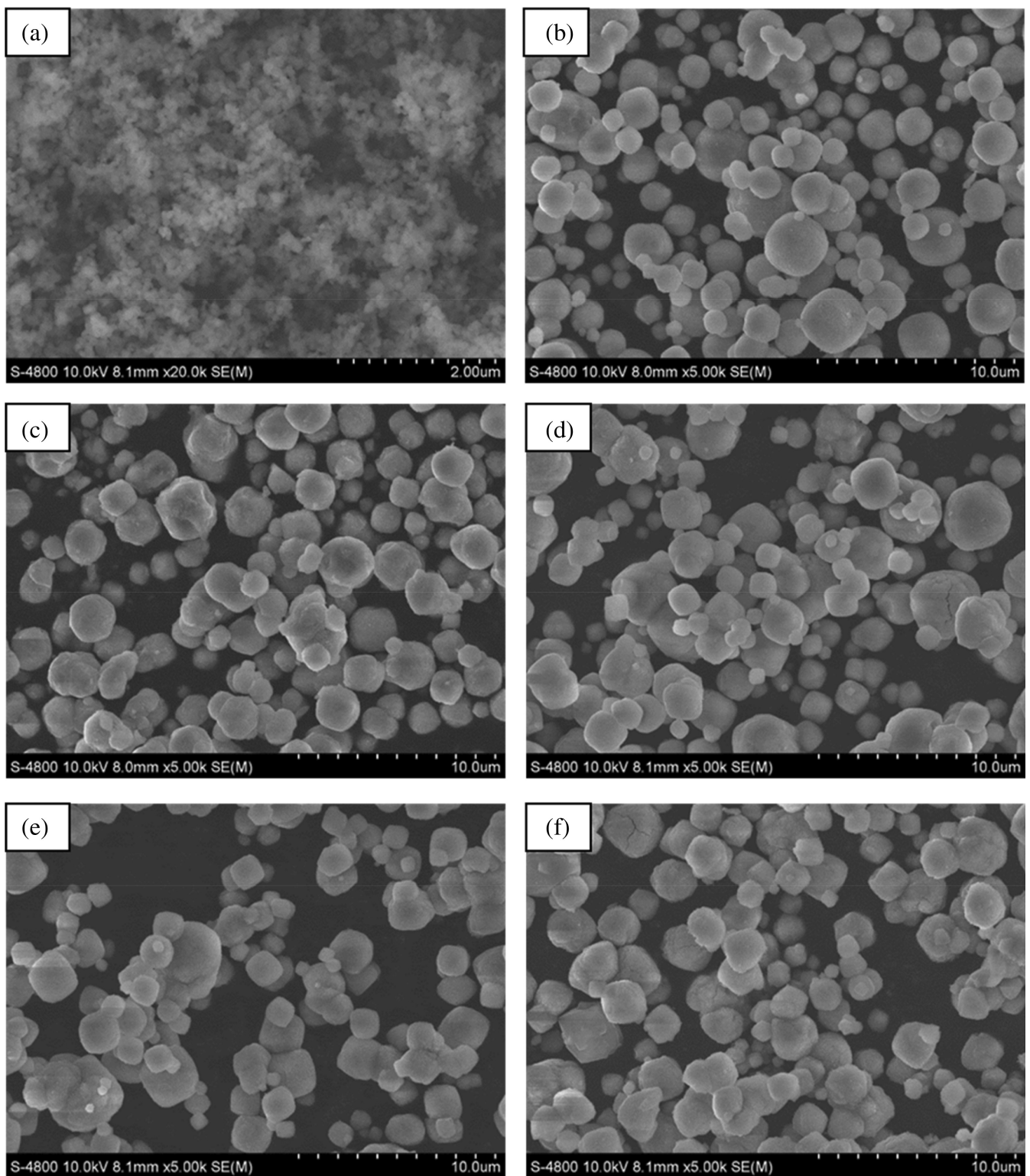


**Figure 3.** FE-SEM images of NaP1 at different NaOH concentrations: 1.0 M (a), 1.5 M (b), 2.0 M (c), 2.5 M (d), 3.0 M (e), and 4.0 M (f).

The pore sizes of zeolite NaP1 at different aging times are also presented in Table 3, where they are classified as a type IV isotherm according to The International Union of Pure and Applied Chemistry (IUPAC).<sup>49</sup> A pore size of 34.43 Å was achieved without aging, indicating that the structure of NaP1 belongs to meso-sized pores. At aging times of 6 and 12 h, the pore sizes were 77.57 and

64.76 Å, respectively. An increase of aging time can change the internal structure of zeolite, shifting asymptotic micropores to mesopores. The adsorption isotherms showed that a strong increase in nitrogen uptake above a relative pressure of about 0.8 revealed a more open surface area in the mesopore;<sup>13</sup> this behavior is typical for materials with type IV isotherm. Moreover,

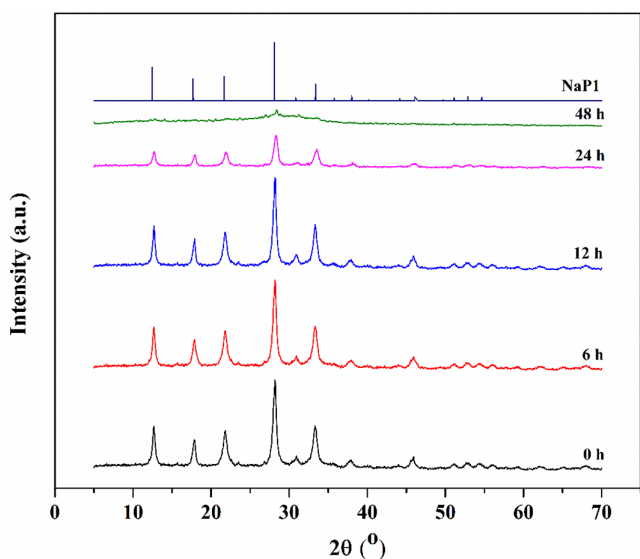


**Figure 4.** XRD patterns of NaP1 at different aging times.

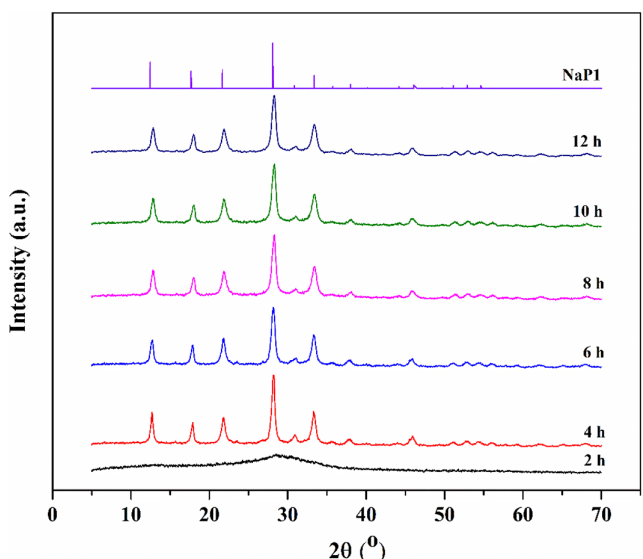


**Figure 5.** XRD patterns of zeolite NaP1 at different reaction times.

**Table 3.** BET results of zeolite NaP1 at different aging times

Aging time (h)	$S_{BET}$ ( $\text{m}^2 \text{ g}^{-1}$ )	Pore diameter (Å)
0	20	34.43
6	37	77.57
12	38	64.76

the adsorption properties of the synthesized NaP1 were also found to be quite similar to its desorption properties (Supporting Information, Fig. S1).

#### Effects of reaction time

Reaction time could affect the properties of products because the crystallinity increases at longer reaction times. Besides this, different types of zeolites can be created by changing the reaction time.<sup>16,28</sup> Fig. 5 shows the presence of an amorphous phase at a reaction time of 2 h, while the high intensity of characteristic peaks was fully achieved at 4 h and no significant difference was found from 6 to 12 h. Compared to the results of this study, the effects of reaction times between 2 and 26 h on the properties of zeolite synthesized from coal fly ash were evaluated.<sup>16</sup> The amorphous phases of aluminosilicate gel and coal fly ash phases were obtained in 2 h. Some characteristic peaks of zeolite NaP1 appeared at 4 h and strongly grew from 6 to 26 h. At the beginning, the impurity phases (mullite, quartz, and anatase) from the starting material (like the fly ash used for the zeolite synthesis) were still present in the products; then, the appearance of the characteristic peaks of zeolite NaP1 was found at longer reaction times.<sup>50</sup> However, in this work, there are no impurity phases present in the XRD results, which may be due to the different feedstocks and synthesis methods. A solution of  $\text{Na}_2\text{SiO}_3$  extracted from RHA is first obtained and then used as the precursor for zeolite synthesis, helping the reaction happen more easily and resulting in a shorter reaction time. Furthermore, this research also agrees with the study by Katsuki and Komarneni where the synthesis process also limited the existence of impurities derived from raw materials.<sup>51</sup>

The surface area was  $38 \text{ m}^2 \text{ g}^{-1}$  at a reaction time of 4 h and reached the maximum value of  $50 \text{ m}^2 \text{ g}^{-1}$  at 8 h (Table 4). A small change of surface area was found at 10 h; however, a significant decrease of surface area was found at 12 h. This trend is similar in the results of other works.<sup>13,16,44,50</sup> At  $100^\circ\text{C}$ , the surface area reached  $129 \text{ m}^2 \text{ g}^{-1}$  at 48 h and decreased to 92 and  $85 \text{ m}^2 \text{ g}^{-1}$  at 72 and 96 h, respectively.<sup>13</sup> The surface area of zeolite NaP1 was  $21 \text{ m}^2 \text{ g}^{-1}$  at an aging time of 24 h, a reaction time of 24 h, and reaction temperature of  $100^\circ\text{C}$ .<sup>44</sup> Zeolite was synthesized in the solid–liquid process and achieved a surface area of  $42 \text{ m}^2 \text{ g}^{-1}$  in 24 h,<sup>50</sup> and the synthesized zeolite NaP1 had a surface area of  $48 \text{ m}^2 \text{ g}^{-1}$  in 26 h.<sup>16</sup>

The effects of reaction time on the internal structure of NaP1 is reported from the adsorption and desorption isotherms (Supporting Information, Fig. S2). When the reaction time was prolonged between 4 and 8 h, the pore size decreased from 64.76 to 40.77 Å; however, they are not very different (74.57 and 74.58 Å) at reaction times of 10 and 12 h, respectively. Thereby, the change of reaction time dramatically affects the internal structure of NaP1. In addition, adsorption–desorption isotherms have also confirmed the reusability of NaP1 with a negligible hysteresis between these curves (type IV isotherm). This means that the loading and discharging properties of the mesopores system are similar.<sup>52</sup>

Zeolite NaP1 in this study had a surface area of  $50 \text{ m}^2 \text{ g}^{-1}$ , with uniform particle size distribution from 400 to 600 nm at the optimal conditions: 12 h aging time and 8 h reaction time. Specifically, the frequency of particles with sizes from 400–450 nm and 450–500 nm are 40% and 45%, respectively (Supporting Information, Fig. S3), and the remaining particles sizes (350–400 nm and 500–600 nm) made up 15%. In this work, one of the main objectives was to synthesize zeolite NaP1 for treating phosphate ions; therefore, the optimal conditions chosen are as follows: a  $\text{SiO}_2/\text{Al}_2\text{O}_3$  molar ratio of 4.0, a  $\text{NaOH}$  concentration of 1.5 M, an aging time of 12 h, and a reaction time of 8 h.

#### Comparison study on the preparation method of zeolite NaP1

Table 5 presents results from several methods for zeolite NaP1 synthesis from previous publications. A variety of feedstock (such as commercial  $\text{SiO}_2$ , natural minerals, agricultural/industrial by-products and wastes) was utilized to produce zeolite NaP1.

Regarding aging, the mixture was maintained at room temperature for 12 h before being reacted for 8 h in this work, while zeolite NaP1 usually needs a long reaction time from 12–96 h. Qiu *et al.*<sup>12</sup> spent 24 h to synthesize zeolite NaP1 at NaOH 2 M, while Liu *et al.*<sup>50</sup> annealed (at 750 °C) and pretreated feedstock using HCl to achieve a surface area of 42 m<sup>2</sup> g<sup>-1</sup>. Kunecki *et al.*<sup>16</sup> obtained a surface area of 48 m<sup>2</sup> g<sup>-1</sup> in 26 h. Zeolite NaP1 was compounded from RHA by first aging RHA for 15 h and then being reacted for 48 h, with a resulting surface area of 129 m<sup>2</sup> g<sup>-1</sup> and pore diameter of 35 Å.<sup>13</sup> In this study, for 12 h aging and 8 h reaction at 100 °C, the surface area and pore diameter were 50 m<sup>2</sup> g<sup>-1</sup> and 40.77 Å, respectively. Although a commercial SiO<sub>2</sub> was used, the surface area was only 13 m<sup>2</sup> g<sup>-1</sup> at a reaction time of 96 h.<sup>31</sup> To shorten the time to 4 h, the synthesis process required the help of thermo-sonochemical techniques.<sup>32</sup> The total spending time (20 h), including aging and reaction time, in this work is much shorter than those of previous studies<sup>12,13,16,50</sup> with comparable surface areas (50 m<sup>2</sup> g<sup>-1</sup>). Additionally, in the waste reduction perspective, this work utilizes the same alkaline solutions previously used for the preparation reactions of sodium aluminate and successfully achieves similar XRD results of zeolite NaP1, compared to the results of using fresh NaOH solution. This makes the procedure of zeolite NaP1 a facile, economical, and environmentally friendly process.

### Adsorption of phosphate onto zeolite NaP1

#### Point of zero charge of zeolite NaP1

Isoelectric point is one of the vital properties for evaluating adsorption capacity.<sup>53</sup> The change of zeolite NaP1 surface charge in different pH solutions is depicted in Fig. 6. The pH<sub>pzc</sub> of zeolite

NaP1 is 6.8, indicating that, in a solution with pH < pH<sub>pzc</sub>, the adsorbent is positively charged and vice versa.

#### Effects of pH

The highest adsorption efficiency of phosphate on zeolite NaP1 occurred at an acidic pH of 2 (Fig. 7(a)), with an adsorption efficiency of 81.81%. The increase of pH solution to 3 resulted in the efficiency decreasing to 56.89%. A significant decrease of adsorption efficiency occurred as the pH was further increased from 4 to 10. The phosphate removal efficiency has considerable potential at a low pH, which could be correlated to the surface charge of zeolite NaP1 and the distribution of phosphate species in water. At pH < pH<sub>pzc</sub>, zeolite NaP1 and phosphate ions are differently charged. Electrostatic interactions between NaP1 surface and phosphate ions easily occurred, enhancing the adsorption capacity of zeolite.<sup>54</sup> The surface of zeolite NaP1 carried a more negative charge at pH > pH<sub>pzc</sub>, resulting in a hindered adsorption ability for anions.<sup>33,55</sup>

Chen *et al.* described a decrease of phosphate adsorption capacity from pH 3 to pH 10 when using zeolite as the adsorbent. Some studies on the phosphate adsorption capacity of adsorbents with surface charges like those of zeolite also reported

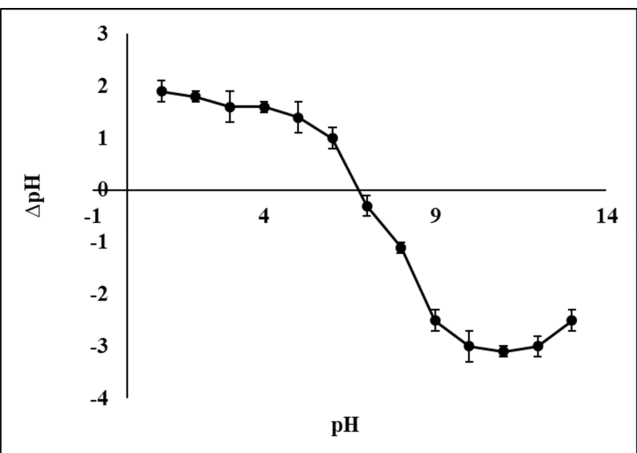


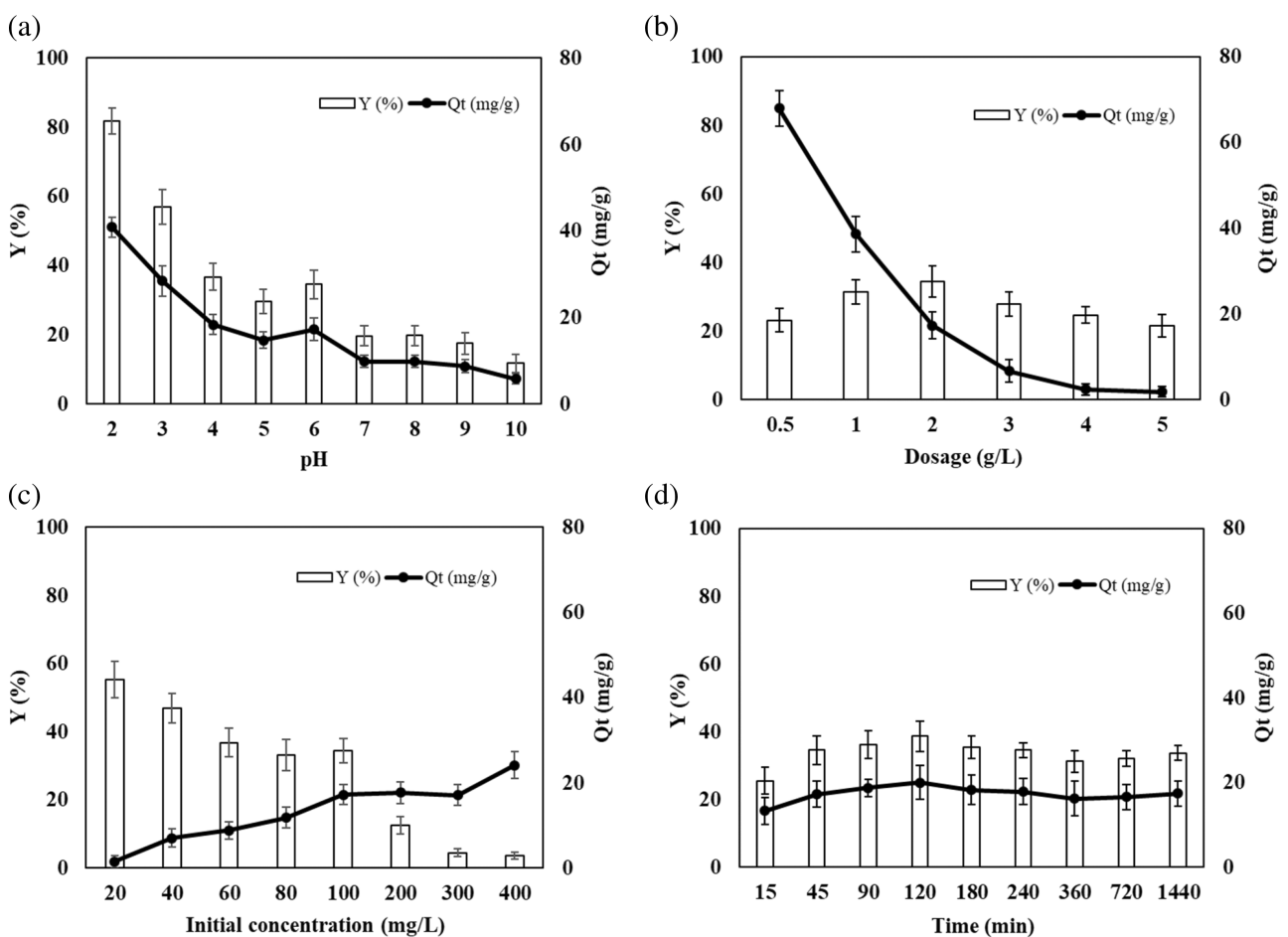
Figure 6. The pH of point of zero charge (pH<sub>pzc</sub>).

Table 5. Comparison of the zeolite NaP1 synthesized in this study with those of previous studies

Raw materials	Reaction conditions					
	Ratio of SiO <sub>2</sub> /Al <sub>2</sub> O <sub>3</sub>	NaOH concentration (M)	Aging time <sup>a</sup> (h)	Time (h)	S <sub>BET</sub> (m <sup>2</sup> g <sup>-1</sup> )	Pore diameter (Å)
SiO <sub>2</sub> commercial <sup>31</sup>	1.4	—	0.5	96	13	—
Coarse slag <sup>44</sup>	3.4	2.8	24	12	98	83.5
Kaolin <sup>14</sup>	4.0	1.0	—	20	—	—
Coal fly ash <sup>32</sup>	3.5	1.0	—	4 <sup>b</sup>	69	10.9
Coal fly ash <sup>16</sup>	5.0	3.0	—	26	48	116
Fly ash (annealed 750 °C-1.5 h, pretreated HCl 4 M-2 h) <sup>51</sup>	—	2.0	—	24	42	—
Fly ash <sup>12</sup>	1.4	2.0	—	24	50	111
RHA <sup>13</sup>	3.8	—	15	48	129	35
RHA without pretreatment (this study)	4.0	1.5	12	8	50	40.77

<sup>a</sup> Aging before reaction.

<sup>b</sup> Thermo-sonochemical process.



**Figure 7.** Effects of pH on phosphate adsorption with the adsorbent dosage of  $2\text{ g L}^{-1}$ , initial concentration of  $100\text{ mg L}^{-1}$ , and contact time of 45 min (a); effects of adsorbent dosage on phosphate adsorption with the initial concentration of  $100\text{ mg L}^{-1}$  and contact time of 45 min (b); effects of phosphate initial concentration on phosphate adsorption with the adsorbent dosage of  $2\text{ g L}^{-1}$  and contact time of 45 min (c); the effect of contact time on phosphate adsorption (d). Y (%): adsorption efficiency,  $Q_t$  (mg g $^{-1}$ ): adsorption capacity.

similar phenomena.<sup>54</sup> The removal of phosphate using iron oxide nanoflakes attained the maximum phosphate adsorption efficiency at  $\text{pH} < 6.3$  ( $\text{pH}_{\text{pzc}}$ ).<sup>56</sup> In a similar study, Angkawijaya *et al.* also reported that a low adsorption efficiency of phosphate occurred at  $\text{pH} > \text{pH}_{\text{pzc}}$ .<sup>33</sup> Based on the interpretation relating to the change in the adsorbent surface charge at different pH, the above results are consistent. Although the highest adsorption efficiency was recorded at pH 2, pH 6 was an appropriate selection for real wastewater treatment.

#### Effects of dosage

Adsorbent dosages from  $0.5$  to  $5\text{ g L}^{-1}$  were evaluated at pH 6 (Fig. 7(b)). At a dosage of  $0.5\text{ g L}^{-1}$ , the adsorption efficiency and adsorption capacity reached  $23.15\%$  and  $68.01\text{ mg g}^{-1}$ , respectively. An increase of dosage to  $1$  and  $2\text{ g L}^{-1}$  resulted in an increase of the adsorption efficiency to  $23.15\%$  and  $34.57\%$ , respectively; in contrast, the adsorption capacity dropped from  $68.01$  to  $17.28\text{ mg g}^{-1}$ . The adsorption efficiency and capacity simultaneously decreased at dosages higher than  $2\text{ g L}^{-1}$ . When a small amount of adsorbent was loaded and with a dense existence of phosphate ions in the solution, the ions could easily be adsorbed onto the surface of zeolite NaP1.

At low adsorbent dosages, it was impossible to significantly adsorb phosphate ions in the solution, leading to low adsorption

efficiency.<sup>57</sup> The more adsorbent mass was added in this process, more active sites were present in the solution; thus, the adsorption efficiency increased but the adsorption capacity declined. When excess adsorbent was used, the adsorption efficiency dramatically dropped due to the contrast of surface charge between zeolite NaP1 and phosphate ions. A similar phenomenon was reported when using more adsorbents in the solution: the diffusion of anions to negatively charged materials was hindered during the adsorption process.<sup>55</sup> Therefore, the optimal dosage for phosphate adsorption was chosen as  $2\text{ g L}^{-1}$ .

#### Effects of initial concentration

The adsorption efficiency and phosphate adsorption capacity of zeolite NaP1 at different initial concentrations are presented in Fig. 7(c) with an adsorbent dosage of  $2\text{ g L}^{-1}$ . The adsorption efficiency achieved the maximum value at an initial concentration of  $20\text{ mg L}^{-1}$ . The efficiency decreased from  $46.96\%$  and  $36.82\%$  when the initial concentration rose from  $40$  to  $60\text{ mg L}^{-1}$  and this value was an insignificant change between  $60$  and  $100\text{ mg L}^{-1}$ . However, at  $200\text{ mg L}^{-1}$ , the adsorption efficiency decreased by more than  $63\%$ .

At concentrations of  $300$  and  $400\text{ mg L}^{-1}$ , the efficiency decreased by about three times compared to that of  $200\text{ mg L}^{-1}$ . At low initial concentrations, less phosphate ions were used,

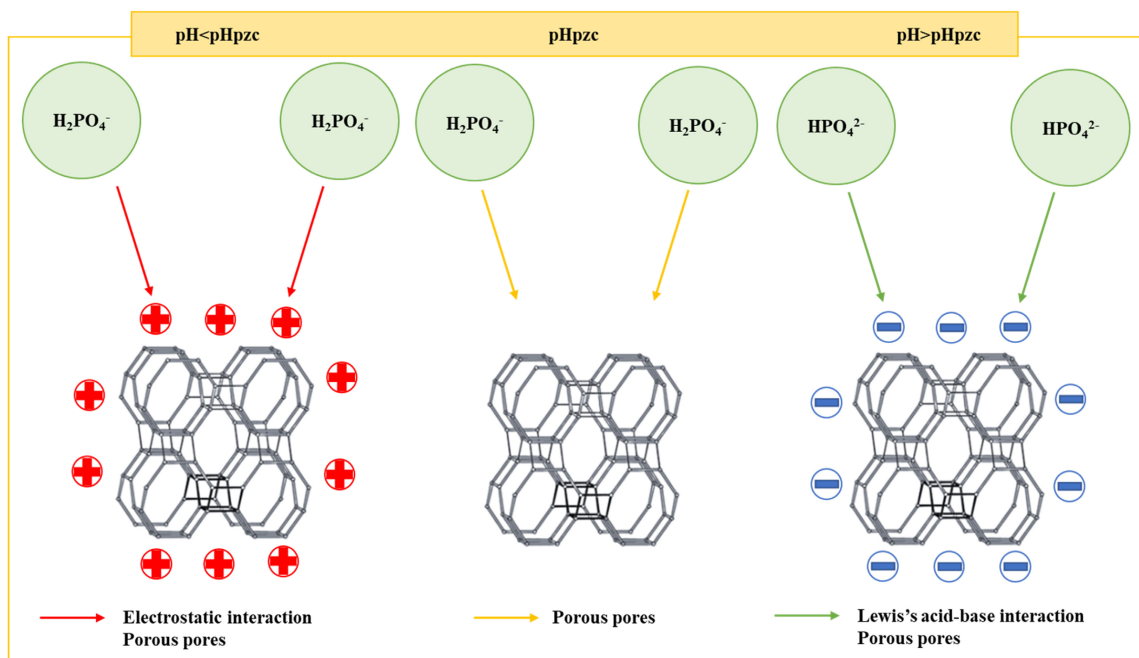


**Figure 8.** Proposed mechanism of pH effect on phosphate adsorption of zeolite NaP1.

**Table 6.** Comparison of phosphate adsorption capacity of several adsorbents

Materials	Adsorption conditions	$Q_t$ (mg g <sup>-1</sup> )
Iron oxide ( $\text{Fe}_2\text{O}_3$ and $\text{Fe}_3\text{O}_4$ ) <sup>57</sup>	pH 5.0, initial concentration 20 mg L <sup>-1</sup> , contact time 60 min	2.0
Zirconium-modified zeolite <sup>58</sup>	pH 7.0, dosage 1.5 g L <sup>-1</sup> , initial concentration 2 mg L <sup>-1</sup> , contact time 1440 min	1.73
Commercial zeolite <sup>55</sup>	pH 7.0, dosage 20 g L <sup>-1</sup> , initial concentration 100 mg L <sup>-1</sup> , contact time 1440 min	0.45
Clay derived-zeolite NaA <sup>56</sup>	pH 4.0, dosage 6.7 g L <sup>-1</sup> , initial concentration 500 mg L <sup>-1</sup> , contact time 120 min	34.0
Fly ash derived-zeolite NaP1 <sup>61</sup>	pH 1.8, dosage 50 g L <sup>-1</sup> , initial concentration 2000–8000 mg L <sup>-1</sup> , contact time 480 min	60.0
RHA derived-zeolite NaP1 (this study)	pH 6.0, dosage 2.0 g L <sup>-1</sup> , initial concentration 100 mg L <sup>-1</sup> , contact time 120 min	19.97

resulting in less competition between ions and the adsorption sites of zeolite; thus, the adsorption efficiency was high. This will waste zeolite NaP1 because the amount of phosphate ions loaded is negligible. At higher concentrations, the diffusion of phosphate ions on the surface of zeolite increased, making the adsorption capacity high. This trend also agrees with the study by Chen *et al.*<sup>54</sup> Additionally, Zhang *et al.* reported that the abundant vacant adsorption sites of zeolite were occupied when the initial concentration of phosphate was too high, resulting in a decrease in removal efficiency.<sup>58</sup>

#### Effects of contact time

The contact time was investigated from 15 to 1440 min at an initial concentration of 100 mg L<sup>-1</sup>. Fig. 7(d) shows that the adsorption efficiency and adsorption capacity gradually rose, attaining the maximum values of 38.67% and 19.96 mg L<sup>-1</sup>, respectively, in 120 min. After that, the efficiency did not significantly change and a similar trend for the adsorption capacity was observed. The highest adsorption capacity (35 mg g<sup>-1</sup>) for removing phosphate using clay-derived zeolite A at the adsorption equilibration time of 120 min was reported.<sup>55</sup> The surface area of 174 m<sup>2</sup> g<sup>-1</sup> in their work was 3.5 times higher than that of this study (50 m<sup>2</sup> g<sup>-1</sup>). Additionally, the higher adsorption capacity of natural zeolite for the removal of phosphate ions at an initial concentration of 100 mg L<sup>-1</sup> in 180 min was related to the zeolite structure and surface area.<sup>3</sup> Further increases of contact time revealed insignificant changes in adsorption efficiency and capacity.

#### Adsorption isotherm studies

The application of adsorption data to isotherm models is necessary to explore the mechanism of the adsorption process. To elucidate the phosphate adsorption behavior of zeolite NaP1, two-factor models (such as Langmuir, Freundlich and Temkin) were used. From the calculated data based on the adsorption models, the correlation coefficients of the models decrease in the order: Redlich-Peterson > Temkin > Freundlich > Sips > Langmuir (Supporting Information, Table S1). The Freundlich and Temkin isotherm models effectively described the experimental data with the correlation coefficients of 0.960 and 0.991, respectively. The Freundlich model assumes that there are interactions between adsorbed molecules on heterogeneous surfaces.<sup>59,60</sup> This suggests that phosphate adsorption mainly occurs following a multi-layer mechanism on the surface of zeolite NaP1. Additionally, the adsorption energy can be changed due to the heterogeneity of the adsorption surface.<sup>59,61</sup> The values of  $1/n_F$  and  $n_F$  are 0.537

and 1.862, respectively, while favorable adsorption will be processed at  $n_F$  values from 1 to 10, and  $n_F > 1$  can also predict the physical adsorption process.<sup>33,59</sup>

For the Temkin isotherm model, the adsorption heat of all molecules in the layer linearly decreased following an increase in surface coverage. At the same time, the interaction between adsorbent and adsorbate was characterized by a regular distribution of binding energy.<sup>37</sup> The  $b_T$  parameter, which is related to the adsorption heat, was 0.585 kJ mol<sup>-1</sup>, showing the weak interaction between the adsorbate and the adsorbent and indicating a physical adsorption process.<sup>59</sup> The calculated maximum adsorption capacity from the Langmuir model in this work was 19.053 mg g<sup>-1</sup> and its correlation coefficient was 0.922. Specifically, the correlation coefficients of both the Sips and Redlich-Peterson models were quite high at 0.959 and 0.995, respectively, suggesting that the real adsorption process can also be described according to these two models. The Sips and Redlich-Peterson three-parameter adsorption isotherms had the characteristics of both Langmuir and Freundlich isotherms; thus, the adsorption process may not exhibit an ideal multilayer adsorption state.<sup>36</sup> As a result, the Sips and Redlich-Peterson isotherms can be used in both homogeneous and heterogeneous systems. The  $n_S$  parameter of the Sips model and the  $\beta$  parameter of the Redlich-Peterson model also give values of 0.556 and 0.528, respectively, which are not clearly asymptotic to both of Langmuir and Freundlich models.<sup>33,36</sup> For this reason, the simultaneous occurrence of both monolayer and multilayer adsorption was present in the phosphate adsorption process onto zeolite NaP1, and this belonged to a predominant physical adsorption mechanism.

The mechanisms of phosphate adsorption onto zeolite NaP1 are elucidated in Fig. 8. The adsorption mechanism of phosphate ions onto the surface of zeolite NaP1 can be changed by the pH of the solution. At  $pH < pH_{pzc}$ , the surface of zeolite NaP1 was protonated, leading to many positive charges on the surface that significantly supported the adsorption of anions.<sup>55</sup> The adsorption capacity for  $H_2PO_4^-$  ions was high in acidic environments and gradually decreased near  $pH_{pzc}$ .<sup>33</sup> At  $pH_{pzc}$ , there were no charge interactions between the adsorbent and the adsorbate; therefore, the adsorption capacity was predicted to be caused by the pores of zeolite.<sup>61</sup> In the case of  $pH > pH_{pzc}$ , the phosphate ions were the negative divalent  $HPO_4^{2-}$  and the surface of NaP1 was also negatively charged at the same time. The adsorption of phosphate on the zeolite surface mainly happen at high pH values due to Lewis acid–base interactions, in which the active sites of aluminum played the role of weak base (Lewis base) and the phosphate ions were weak acid (Lewis acid).<sup>60</sup> However, interactions with the same charge resulted in the decrease of the adsorption capacity of zeolite when pH of solution was strongly higher than  $pH_{pzc}$ .

#### Comparison study on phosphate adsorption capacity

Table 6 reports previous studies on some typical adsorbents for phosphate removal. In these studies, zeolite often performed with a good adsorption efficiency, especially the synthesized zeolites from different kinds of feedstock. Chen *et al.* experimented with phosphate removal using commercial zeolite and found an adsorption capacity of 0.30–0.45 mg g<sup>-1</sup> at the initial concentration from 10–100 mg L<sup>-1</sup>.<sup>54</sup> Zeolite A synthesized from clay had the adsorption capacity of 34.0 mg g<sup>-1</sup> at pH 4.0.<sup>55</sup> Waste containing high concentrations of phosphate and metal ions was treated using fly ash derived-zeolite NaP1.<sup>58</sup> This study found that the simultaneous adsorption of zeolite NaP1 on anions and

cations with an adsorption capacity of 60 mg L<sup>-1</sup> and a favorable environment for electrostatic interactions between the zeolite surface and phosphate ions happened at pH 1.8. Meanwhile, in this work, the adsorption capacity was 19.97 mg g<sup>-1</sup> at pH 6.0. When zirconium oxide modified-zeolite was used as an adsorbent, the adsorption capacity reached 1.73 mg g<sup>-1</sup> at the initial concentration of 2.0 mg L<sup>-1</sup> within 60 min.<sup>57</sup> The surface modification of zeolite based on zirconium oxide presented a significant increase of adsorption capacity by ligand exchange mechanism.

In this study, the optimal adsorption efficiency and adsorption capacity of 38.67% and 19.97 mg g<sup>-1</sup>, respectively, were accomplished. However, to improve the adsorption efficiency and capacity of NaP1-derived from RHA on phosphate removal, the surface modification of NaP1 must be implemented to generate composites. Furthermore, the potential removal of anions, cations, and organic dyes by NaP1 and its composites should be evaluated. Finally, the selection of feedstock (especially wastes or agricultural by-product sources), the synthesis processes, and the use of obtained products for pollutants treatment should be targeted towards environmentally friendly application in various fields.

## CONCLUSIONS

Zeolite NaP1 was successfully synthesized under a facile, environmentally friendly, and mild *in-situ* process by using sodium silicate as a precursor. The synthesis process was operated at the following optimal conditions: a SiO<sub>2</sub>/Al<sub>2</sub>O<sub>3</sub> molar ratio of 4.0 and a NaOH concentration of 1.5 M. It is possible to collect zeolite NaP1 with different surface areas by changing the aging and reaction times. Likewise, the evaluation of the adsorption capacity of zeolite NaP1 (synthesis conditions: 12 h aging time and 8 h reaction time) is presented in this work. At pH 6, an initial phosphate concentration of 100 mg L<sup>-1</sup>, a dosage of 2 g L<sup>-1</sup>, and a contact time of 120 min, the adsorption efficiency and adsorption capacity were 38.67% and 19.97 mg g<sup>-1</sup>, respectively. The experimental data were well fitted with the Temkin ( $R^2 = 0.991$ ) and Redlich-Peterson ( $R^2 = 0.995$ ) models, and the calculated maximum adsorption capacity from the Langmuir model was 19.053 mg g<sup>-1</sup>. Although the zeolite NaP1 obtained in this study had satisfactorily good properties for the adsorption process, these results are still limited compared to some previous studies. For that reason, the surface modification of zeolite NaP1 is crucial to improve the removal efficiency of phosphate ions and widen its applications. Modified zeolite NaP1 can be created by combining with other materials to generate zeolite-based composites or by modifying using surfactants. With more functional groups and specialized properties, these materials are expected to serve well for various applications, such as the pollutant treatment, biomedical, and agriculture industries.

## AUTHOR CONTRIBUTIONS

Phuong Lan Tran-Nguyen: Conceptualization, Methodology, Investigation, Resources, Writing—original draft. Kim-Phung Ly: Conceptualization, Methodology, Writing—original draft. Thanh-Ty Nguyen: Methodology, Writing—review & editing. Shella Permatasari Santoso: Investigation, Writing—review & editing. Nguyen-Phuong-Dung Tran: Writing—review & editing. Artik Elisa Angkawijaya: Investigation, Writing—review & editing. Maria Yuliana: Writing—review & editing. Nguyen Minh Nhut: Methodology,

Writing—review & editing. Tuan Thi-Tran-Anh: Writing—review & editing.

## CONFLICT OF INTERESTS

The authors declare that there are no known competing financial interests or personal relationships that could have appeared to influence the work reported in this paper.

## ACKNOWLEDGEMENTS

This research was funded by the Vietnam National Foundation for Science and Technology Development (NAFOSTED) under Grant Number 103.02-2020.64.

## SUPPORTING INFORMATION

Supporting information may be found in the online version of this article.

## REFERENCES

- Goscianska J, Ptaszewska-Koniarsz M, Frankowski M, Franus M, Panek R and Franus WJ, Removal of phosphate from water by lanthanum-modified zeolites obtained from fly ash. *J Colloid Interface Sci* **513**: 72–81 (2018).
- Xu Q, Li W, Ma L, Cao D, Owens G and Chen Z, Simultaneous removal of ammonia and phosphate using green synthesized iron oxide nanoparticles dispersed onto zeolite. *Sci Total Environ* **703**:135002 (2020).
- Aljbour SH, Al-Harahsheh AM, Aliedeh MA, Al-Zboon K and Al-Harahsheh S, Phosphate removal from aqueous solutions by using natural Jordanian zeolitic tuff. *Adsorpt Sci Technol* **35**:284–299 (2017).
- Amiri MJ, Synthesis and optimization of spherical nZVI (20–60 nm) immobilized in bio-apatite-based material for efficient removal of phosphate: Box-Behnken design in a fixed-bed column. *Environ Sci Pollut Res* **29**:67751–67764 (2022).
- Almanassra IW, McKay G, Kochkodan V, Atieh MA and Al-Ansari T, A state of the art review on phosphate removal from water by biochars. *Chem Eng J* **409**:128211 (2021).
- Wang J, Shao X, Liu J, Zhang Q, Ma J and Tian G, Insight into the effect of structural characteristics of magnetic  $ZrO_2/Fe_3O_4$  nanocomposites on phosphate removal in water. *Mater Chem Phys* **249**:123024 (2020).
- Wei T, Zhang G, Long Z, Xian G and Niu L, Advanced phosphate removal by La–Zr–Zn ternary oxide: performance and mechanism. *J Alloys Compd* **817**:152745 (2020).
- de Andrade BR, de Sousa CL, Oliveira CP, Bohn F, do Nascimento RF, Sasaki JM et al., Kaolin-based magnetic zeolites A and P as water softeners. *Microporous Mesoporous Mater* **245**:64–72 (2017).
- Yoldi M, Fuentes-Ordoñez E, Korili S and Gil A, Zeolite synthesis from industrial wastes. *Microporous Mesoporous Mater* **287**:183–191 (2019).
- Nakhli SAA, Delkash M, Bakhshayesh BE and Kazemian H, Application of zeolites for sustainable agriculture: a review on water and nutrient retention. *Water, Air, Soil Pollut* **228**:1–34 (2017).
- Pal P, Das JK, Das N and Bandyopadhyay S, Synthesis of NaP zeolite at room temperature and short crystallization time by sonochemical method. *Ultrason Sonochem* **20**:314–321 (2013).
- Qiu X, Liu Y, Li D and Yan C, Preparation of NaP zeolite block from fly ash-based geopolymer via in situ hydrothermal method. *J Porous Mater* **22**:291–299 (2015).
- Bohra S, Kundu D and Naskar MK, Synthesis of cashew nut-like zeolite NaP powders using agro-waste material as silica source. *Mater Lett* **106**:182–185 (2013).
- Hildebrand EA, Andrade CGB, Rocha Junior CAF, Angélica RS, Valenzuela-Díaz FR and Neves RF, Synthesis and characterization of zeolite NaP using kaolin waste as a source of silicon and aluminum. *Mater Res* **17**:174–179 (2014).
- Prajaputra V, Abidin Z, Suryaningtyas D and Rizal H, Characterization of Na-P1 zeolite synthesized from pumice as low-cost materials and its ability for methylene blue adsorption, in *IOP Conference Series: Earth and Environmental Science*. IOP Publishing, United Kingdom, 012014 (2019).
- Kunecki P, Panek R, Koteja A and Franus W, Influence of the reaction time on the crystal structure of Na-P1 zeolite obtained from coal fly ash microspheres. *Microporous Mesoporous Mater* **266**:102–108 (2018).
- Anh DT, Tinh TV and Vang NN, *The Domestic Rice Value Chain in the Mekong Delta, White Gold: The Commercialisation of Rice Farming in the Lower Mekong Basin*. Springer, Berlin, pp. 375–395 (2020).
- Ng E-P, Awala H, Tan K-H, Adam F, Retoux R and Mintova S, EMT-type zeolite nanocrystals synthesized from rice husk. *Microporous Mesoporous Mater* **204**:204–209 (2015).
- Mohamed R, Mkhald I and Barakat M, Rice husk ash as a renewable source for the production of zeolite NaY and its characterization. *Arabian J Chem* **8**:48–53 (2015).
- Moayedi H, Aghel B, Nguyen H and Rashid ASA, Applications of rice husk ash as green and sustainable biomass. *J Cleaner Prod* **237**:117851 (2019).
- Amiri MJ, Bahrami M, Beigzadeh B and Gil A, A response surface methodology for optimization of 2,4-dichlorophenoxyacetic acid removal from synthetic and drainage water: a comparative study. *Environ Sci Pollut Res* **25**:34277–34293 (2018).
- Kongkachuchay P and Lohsoontorn P, Phase diagram of zeolite synthesized from perlite and rice husk ash. *Sci Asia* **32**:13–16 (2006).
- Cardoso AM, Paprocki A, Ferret LS, Azevedo CM and Pires M, Synthesis of zeolite Na-P1 under mild conditions using Brazilian coal fly ash and its application in wastewater treatment. *Fuel* **139**:59–67 (2015).
- Kazemian H, Naghdali Z, Kashani TG and Farhadi F, Conversion of high silicon fly ash to Na-P1 zeolite: alkaline fusion followed by hydrothermal crystallization. *Adv Powder Technol* **21**:279–283 (2010).
- Thuadaij P and Nuntiya A, Preparation and characterization of faujasite using fly ash and amorphous silica from rice husk ash. *Procedia Eng* **32**:1026–1032 (2012).
- Muriithi GN, Petrik LF and Doucet FJ, Synthesis, characterisation and CO<sub>2</sub> adsorption potential of NaA and NaX zeolites and hydrotalcite obtained from the same coal fly ash. *J CO<sub>2</sub> Util* **36**:220–230 (2020).
- Alfaró S, Rodríguez C, Valenzuela M and Bosch P, Aging time effect on the synthesis of small crystal LTA zeolites in the absence of organic template. *Mater Lett* **61**:4655–4658 (2007).
- Johnson E and Arshad SE, Hydrothermally synthesized zeolites based on kaolinite: a review. *Appl Clay Sci* **97**:215–221 (2014).
- Tran-Nguyen PL, Ly K-P, Thanh LHV, Angkawijaya AE, Santoso SP, Tsai M-L et al., Facile synthesis of zeolite NaX using rice husk ash without pretreatment. *J Taiwan Inst Chem Eng* **123**:338–345 (2021).
- Huo Z, Xu X, Lü Z, Song J, He M, Li Z et al., Synthesis of zeolite NaP with controllable morphologies. *Microporous Mesoporous Mater* **158**:137–140 (2012).
- Ali IO, El-Sheikh SM, Salama TM, Bakr MF and Fodial MH, Controllable synthesis of NaP zeolite and its application in calcium adsorption. *Sci China Mater* **58**:621–633 (2015).
- Aldahri T, Behin J, Kazemian H and Rohani S, Synthesis of zeolite Na-P from coal fly ash by thermo-sonochemical treatment. *Fuel* **182**:494–501 (2016).
- Angkawijaya AE, Tran-Chuong YN, Ha QN, Tran-Nguyen PL, Santoso SP, Bundjaja V et al., Studies on the performance of functionalized  $Fe_3O_4$  as phosphate adsorbent and assessment to its environmental compatibility. *J Taiwan Inst Chem Eng* **131**:104162 (2022).
- Djawad F, Djamel N, Elhadj M and Samira A, Adsorption of Ni<sup>2+</sup> ions onto NaX and NaY zeolites: equilibrium, kinetics, intra crystalline diffusion, and thermodynamic studies. *Iran J Chem Chem Eng* **38**:63–81 (2019).
- Lowry OH and Lopez JA, The determination of inorganic phosphate in the presence of labile phosphate esters. *J Biol Chem* **162**:421–428 (1946).
- Kalam S, Abu-Khamisin SA, Kamal MS and Patil S, Surfactant adsorption isotherms: a review. *ACS Omega* **6**:32342–32348 (2021).
- Shubair T, Tahara A and Khandaker S, Optimizing the magnetic separation of strontium ion using modified zeolite with nano iron particles. *Case Stud Chem Environ Eng* **6**:100243 (2022).
- Novembre D, Di Sabatino B, Gimeno D and Pace C, Synthesis and characterization of Na-X, Na-A and Na-P zeolites and hydroxysodalite from metakaolinite. *Clay Miner* **46**:339–354 (2011).
- Azizi SN, Alavi Daghagh A and Abrishamkar M, Phase transformation of zeolite P to Y and analcime zeolites due to changing the time and temperature. *J Spectrosc* **2013**:1–5 (2013).

- 40 Ismail A, El-Shafey O, Amr M and El-Maghrary MS, Pumice characteristics and their utilization on the synthesis of mesoporous minerals and on the removal of heavy metals. *Int Sch Res Notices* **2014**:1–9 (2014).
- 41 Sharma P, Song JS, Han MH and Cho CH, GIS-NaP1 zeolite microspheres as potential water adsorption material: influence of initial silica concentration on adsorptive and physical/topological properties. *Sci Rep* **6**:1–26 (2016).
- 42 Novembre D, Gimeno D and Del Vecchio A, Synthesis and characterization of Na-P1 (GIS) zeolite using a kaolinitic rock. *Sci Rep* **11**:4872 (2021).
- 43 Ji W, Zhang S, Zhao P, Zhang S, Feng N, Lan L et al., Green synthesis method and application of NaP zeolite prepared by coal gasification coarse slag from Ningdong, China. *Appl Sci* **10**:2694 (2020).
- 44 Sharma P, Yeo J-g, Han MH and Cho CH, knobby surfaced, mesoporous, single-phase GIS-NaP1 zeolite microsphere synthesis and characterization for H<sub>2</sub> gas adsorption. *J Mater Chem A* **1**:2602–2612 (2013).
- 45 Osacký M, Pálková H, Hudec P, Czímerová A, Galusková D and Vítková M, Effect of alkaline synthesis conditions on mineralogy, chemistry and surface properties of phillipsite, P and X zeolitic materials prepared from fine powdered perlite by-product. *Microporous Mesoporous Mater* **294**:109852 (2020).
- 46 Nazir LSM, Yeong YF and Chew TLJC, Controlled growth of Faujasite zeolite with NaX topology by manipulating solution aging and Na<sub>2</sub>O/Al<sub>2</sub>O<sub>3</sub> ratios. *Colloids Surf, A* **600**:124803 (2020).
- 47 Chen Y, Xu T, Xie C, Han H, Zhao F, Zhang J et al., Pure zeolite Na-P and Na-X prepared from coal fly ash under the effect of steric hindrance. *J Chem Technol Biotechnol* **91**:2018–2025 (2016).
- 48 Sayehi M, Garbarino G, Delahay G, Busca G and Tounsi H, Synthesis of high value-added Na-P1 and Na-FAU zeolites using waste glass from fluorescent tubes and aluminum scraps. *Mater Chem Phys* **248**:122903 (2020).
- 49 Nimmo JR, Porosity and pore size distribution, *Reference Module in Earth Systems and Environmental Sciences*; Elsevier, London, Vol. **3**, pp. 295–303 (2004).
- 50 Liu Y, Yan C, Zhao J, Zhang Z, Wang H, Zhou S et al., Synthesis of zeolite P1 from fly ash under solvent-free conditions for ammonium removal from water. *J Cleaner Prod* **202**:11–22 (2018).
- 51 Katsuki H and Komarneni S, Synthesis of Na-A and/or Na-X zeolite/porous carbon composites from carbonized rice husk. *J Solid State Chem* **182**:1749–1753 (2009).
- 52 Aysan H, Edebali S, Ozdemir C, Karakaya MC and Karakaya N, Use of chabazite, a naturally abundant zeolite, for the investigation of the adsorption kinetics and mechanism of methylene blue dye. *Microporous Mesoporous Mater* **235**:78–86 (2016).
- 53 Wen J, Dong H and Zeng G, Application of zeolite in removing salinity/sodicity from wastewater: a review of mechanisms, challenges and opportunities. *J Clean Prod* **197**:1435–1446 (2018).
- 54 Chen K, Zhao K, Zhang H, Sun Q, Wu Z, Zhou Y et al., Phosphorus removal from aqueous solutions using a synthesized adsorbent prepared from mineralized refuse and sewage sludge. *Environ Technol* **34**:1489–1496 (2013).
- 55 Hamdi N and Srasra E, Removal of phosphate ions from aqueous solution using Tunisian clays minerals and synthetic zeolite. *J Environ Sci* **24**:617–623 (2012).
- 56 Afriadi MN, Lee W-H and Kim J-O, Effect of phosphate concentration, anions, heavy metals, and organic matter on phosphate adsorption from wastewater using anodized iron oxide nanoflakes. *Environ Res* **171**:428–436 (2019).
- 57 Yang M, Lin J, Zhan Y and Zhang H, Adsorption of phosphate from water on lake sediments amended with zirconium-modified zeolites in batch mode. *Ecol Eng* **71**:223–233 (2014).
- 58 Zhang K, Van Dyk L, He D, Deng J, Liu S and Zhao H, Synthesis of zeolite from fly ash and its adsorption of phosphorus in wastewater. *Green Process Synth* **10**:349–360 (2021).
- 59 Wibowo E, Rokhmat M and Abdullah M, Reduction of seawater salinity by natural zeolite (clinoptilolite): adsorption isotherms, thermodynamics and kinetics. *Desalination* **409**:146–156 (2017).
- 60 Almasri DA, Saleh NB, Atieh MA, McKay G and Ahzi S, Adsorption of phosphate on iron oxide doped halloysite nanotubes. *Sci Rep* **9**:3232 (2019).
- 61 Jiang C, Jia L, He Y, Zhang B, Kirumba G and Xie J, Adsorptive removal of phosphorus from aqueous solution using sponge iron and zeolite. *J Colloid Interface Sci* **402**:246–252 (2013).



p-ISSN 1859-4794 \* e-ISSN 2615-9929

TẠP CHÍ

# KHOA HỌC & CÔNG NGHỆ Việt Nam

Vietnam Journal of Science and Technology - MOST

B

Tập 64 - Số 6 - Tháng 6 năm 2022

## HỘI ĐỒNG BIÊN TẬP

Châu Văn Minh - Viện Hàn lâm KH&CN Việt Nam  
Nguyễn Việt Anh - Trường Đại học Xây dựng  
Bùi Chí Bửu - Viện Khoa học Kỹ thuật Nông nghiệp miền Nam  
Vũ Dũng - Hội Tâm lý học Việt Nam  
Trần Thọ Đạt - Trường Đại học Kinh tế Quốc dân  
Nguyễn Đình Đức - Trường Đại học Công nghệ, Đại học Quốc gia Hà Nội  
Vũ Minh Giang - Đại học Quốc gia Hà Nội  
Trương Nam Hải - Viện Hàn lâm Khoa học và Công nghệ Việt Nam  
Trần Thanh Hải - Trường Đại học Mỏ - Địa chất  
Phạm Huy Khang - Trường Đại học Giao thông Vận tải  
Phạm Gia Khánh - Chủ tịch Hội ghép tạng Việt Nam  
Hồ Đắc Lộc - Trường Đại học Công nghệ TP Hồ Chí Minh  
Nguyễn Thị Mỹ Lộc - Trường Đại học Giáo dục, Đại học Quốc gia Hà Nội  
Bành Tiến Long - Trường Đại học Bách khoa Hà Nội  
Lê Quan Nghiêm - Trường Đại học Y Dược TP Hồ Chí Minh  
Mai Trọng Nhuận - Đại học Quốc gia Hà Nội  
Trần Hữu Phúc - Hội đồng GS Nhà nước  
Nguyễn Thanh Phương - Trường Đại học Cần Thơ  
Nguyễn Thanh Thủy - Trường Đại học Công nghệ, Đại học Quốc gia Hà Nội  
Phạm Hùng Việt - Trường Đại học Khoa học Tự nhiên, Đại học Quốc gia Hà Nội

## PHÓ TỔNG BIÊN TẬP PHỤ TRÁCH

Nguyễn Thị Hương Giang

## PHÓ TỔNG BIÊN TẬP

Nguyễn Thị Hải Hằng

## TRƯỞNG BAN BIÊN TẬP

Phạm Thị Minh Nguyệt

## TRƯỜNG BAN TẠP CHÍ ĐIỆN TỬ

Vũ Văn Hưng

## TRƯỜNG BAN TRỊ SỰ

Lương Ngọc Quang Hưng

## TRÌNH BÀY

Đinh Thị Luận

## EDITORIAL COUNCIL

Chau Van Minh - Vietnam Academy of Science and Technology  
Nguyen Viet Anh - National University of Civil Engineering  
Bui Chi Buu - Institute of Agricultural Science for Southern Vietnam  
Vu Dung - Vietnam Association of Social Psychology  
Tran Tho Dat - National Economics University  
Nguyen Dinh Duc - University of Engineering and Technology, VNU, Hanoi  
Vu Minh Giang - VNU, Hanoi  
Truong Nam Hai - Vietnam Academy of Science and Technology  
Tran Thanh Hai - Hanoi University of Mining and Geology  
Pham Huy Khang - University of Transport and Communications  
Pham Gia Khanh - President of Vietnam Society of Organ Transplantation  
Ho Dac Loc - Ho Chi Minh City University of Technology  
Nguyen Thi My Loc - University of Education, VNU, Hanoi  
Banh Tien Long - Hanoi University of Science and Technology  
Le Quan Nghiem - University of Medicine and Pharmacy of Ho Chi Minh City  
Mai Trong Nhuan - VNU, Hanoi  
Tran Huu Phuc - The State Council for Professorship  
Nguyen Thanh Phuong - Can Tho University  
Nguyen Thanh Thuy - University of Engineering and Technology, VNU, Hanoi  
Pham Hung Viet - University of Science, VNU, Hanoi

## EXECUTIVE DEPUTY EDITOR-IN-CHIEF

Nguyen Thi Huong Giang

## DEPUTY EDITOR

Nguyen Thi Hai Hang

## HEAD OF EDITORIAL BOARD

Pham Thi Minh Nguyet

## HEAD OF E-JOURNAL BOARD

Vu Van Hung

## HEAD OF ADMINISTRATION

Luong Ngoc Quang Hung

## ART DIRECTOR

Dinh Thi Luan

## TÒA SOẠN

113 Trần Duy Hưng - Cầu Giấy - Hà Nội  
Tel: (84.24) 39436793; Fax: (84.24) 39436794  
Email: khoahocvacacongnghevietnam@most.gov.vn  
Tạp chí điện tử: b.vjst.vn

## GIẤY PHÉP XUẤT BẢN

Số 459/GP-BTTTT ngày 20/7/2021

Giá: 18000<sup>d</sup>

## EDITORIAL OFFICE

113 Tran Duy Hung Str. - Cau Giay Dist. - Hanoi  
Tel: (84.24) 39436793; Fax: (84.24) 39436794  
Email: khoahocvacacongnghevietnam@most.gov.vn  
E-journal: b.vjst.vn

## PUBLICATION LICENCE

No. 459/GP-BTTTT 20<sup>th</sup> July 2021

# Xử lý methylene blue bằng zeolite NaX với silica có nguồn gốc từ tro trấu

Trần Nguyễn Phương Lan<sup>1\*</sup>, Lý Kim Phụng<sup>1</sup>, Lương Huỳnh Vũ Thanh<sup>1</sup>,  
Nguyễn Hồng Nam<sup>2</sup>, Trần Thị Bích Quyên<sup>1</sup>, Lê Phan Hưng<sup>3</sup>

<sup>1</sup>Trường Đại học Cần Thơ

<sup>2</sup>Trường Đại học Khoa học và Công nghệ Hà Nội, Viện Hàn lâm Khoa học và Công nghệ Việt Nam

<sup>3</sup>Trường Đại học Sư phạm Kỹ thuật TP Hồ Chí Minh

Ngày nhận bài 22/7/2021; ngày chuyển phản biện 26/7/2021; ngày nhận phản biện 27/8/2021; ngày chấp nhận đăng 31/8/2021

## Tóm tắt:

Nghiên cứu khảo sát các yếu tố ảnh hưởng đến quá trình hấp phụ methylene blue (MB) trong nước giã thải bằng zeolite NaX. Vật liệu zeolite được tổng hợp từ tro trấu (RHA) không thông qua tiền xử lý nhằm tận dụng nguồn phụ phẩm rẻ tiền và sẵn có tại Việt Nam. Các yếu tố ảnh hưởng đến quá trình hấp phụ như pH, nồng độ dung dịch MB, lượng chất hấp phụ và thời gian hấp phụ đã được khảo sát cụ thể. Bên cạnh đó, các mô hình đẳng nhiệt hấp phụ Langmuir, Freundlich, Dubinin - Radushkevich, mô hình động học hấp phụ giả kiến bậc 1 và 2 cũng được nghiên cứu. Kết quả là vật liệu zeolite NaX có khả năng hấp phụ MB với dung lượng hấp phụ cực đại và hiệu suất hấp phụ lần lượt là 16,67 mg/g và 87,03% ở pH 8, nồng độ MB là 15 mg/l, khối lượng vật liệu là 0,05 g và thời gian hấp phụ là 30 phút. Quá trình hấp phụ MB bằng zeolite NaX phù hợp với mô hình hấp phụ Freundlich và là quá trình hấp phụ vật lý tuân theo mô hình động học giả kiến bậc 2. Vật liệu zeolite NaX có thể được tái sử dụng 4 lần với độ giảm hiệu suất hấp phụ là 24,03%. Kết quả của nghiên cứu cho thấy tiềm năng ứng dụng của zeolite NaX trong xử lý chất màu hữu cơ và là tiền đề cho các nghiên cứu về xử lý kim loại nặng hay các loại chất khí.

**Từ khóa:** hấp phụ, methylene blue, tro trấu, zeolite NaX.

**Chỉ số phân loại:** 1.3

## Đặt vấn đề

Ngày nay, hệ quả của sự phát triển kinh tế là môi trường sống ngày càng bị ô nhiễm nghiêm trọng hơn, điển hình là ô nhiễm kim loại nặng, chất thải hữu cơ như thuốc nhuộm... Các loại thuốc nhuộm được sử dụng phổ biến là methylene blue (MB), methylene orange, crystal violet, malachite green, congo red... là những nguồn chất thải gây ô nhiễm nghiêm trọng đến môi trường nước. Vì vậy, việc xử lý các loại thuốc nhuộm một cách hợp lý với giá thành rẻ là một vấn đề đáng quan tâm. Một số phương pháp xử lý phổ biến cho ngành công nghiệp sử dụng thuốc nhuộm có thể kể đến như kết tủa hóa học, oxy hóa bậc cao (Fenton), keo tụ, thẩm thấu ngược, hấp phụ. Trong đó phương pháp hấp phụ đã được sử dụng rộng rãi và cho thấy hiệu suất xử lý cao với giá thành hợp lý [1].

Hàng năm, lượng trấu thải ra từ quá trình xay xát lúa gạo ước tính khoảng 9 triệu tấn [2]. Đa số trấu được sử dụng như một loại nhiên liệu thay cho than và khí gas, từ đó tạo thành một loại phụ phẩm khác là RHA. Lượng RHA còn lại sau khi đốt chiếm khoảng 25% trọng lượng trấu ban đầu và gây ra ô nhiễm môi trường. Đây là nguồn nguyên liệu tiềm năng và rẻ tiền có khối lượng vô cùng lớn tại nước ta. RHA có thể được tận dụng làm phân bón, vật liệu xây dựng [3]. Tuy nhiên, phần lớn RHA vẫn được thải trực tiếp ra môi trường, gây lãng phí nguồn tài nguyên. Do đó, việc sử dụng RHA để tạo ra các vật liệu có giá trị sẽ góp phần bảo vệ môi trường. RHA đã được biết đến như là một nguồn nguyên liệu chứa phần lớn silica, cụ thể các nghiên cứu về sử dụng trấu hoặc RHA làm nguyên liệu để tổng hợp các vật liệu như silica, zeolite,

cordierite... [4-6], trong đó các nghiên cứu về tổng hợp zeolite từ RHA đã được nhiều nhà khoa học đặc biệt chú ý.

Zeolite là vật liệu vô cơ có cấu trúc vi xốp với kích thước đồng đều và đã được nghiên cứu rộng rãi. Cấu trúc của zeolite gồm mạng lưới liên kết của các tứ diện  $[SiO_4]^{4-}$  và  $[AlO_4]^{5-}$ . Các tứ diện này liên kết với nhau qua các cầu nối oxygen tạo nên một cấu trúc mỏ với các hốc trống [7], vì thế zeolite có nhiều ứng dụng như hấp phụ, trao đổi ion, chất xúc tác cho một số phản ứng. Một số nghiên cứu như hấp phụ thuốc nhuộm MB, crystal violet, khí CO<sub>2</sub>, kim loại nặng bằng zeolite NaA và NaX [8-11] đã được công bố. Trong các loại zeolite này, zeolite NaX thuộc họ FAU với kích thước lỗ rỗng lớn (khoảng 8 Å) [7], thể hiện hiệu quả tích cực trong hấp phụ thuốc màu hữu cơ, hấp phụ khí hay kim loại nặng. Zeolite NaX có thể được tổng hợp từ các nguồn hóa chất thương mại, các nguồn khoáng tự nhiên hoặc các loại phụ phẩm trong sản xuất công nghiệp và nông nghiệp như diatomite, cao lanh, tro bay, và RHA [5, 8, 12].

Qua quá trình lược khảo tài liệu, nhóm tác giả nhận thấy chưa có công trình nghiên cứu nào về xử lý thuốc nhuộm MB bằng zeolite NaX tổng hợp từ RHA được công bố ở Việt Nam. Tiếp nối kết quả nghiên cứu của Tran-Nguyen và cs (2021) [13], nghiên cứu này nhằm tìm ra điều kiện tối ưu cho quá trình xử lý MB trong nước giã thải bằng zeolite NaX, với các yếu tố khảo sát như: pH, nồng độ dung dịch MB, lượng chất hấp phụ sử dụng, thời gian hấp phụ. Bản chất của quá trình hấp phụ và khả năng tái sử dụng của vật liệu NaX sau khi hấp phụ cũng được nhóm nghiên cứu đánh giá.

\*Tác giả liên hệ: Email: tplan@ctu.edu.vn

# Removal of methylene blue using zeolite NaX with silica derived from rice husk ash

Nguyen Phuong Lan Tran<sup>1\*</sup>, Kim Phung Ly<sup>1</sup>,  
Huynh Vu Thanh Luong<sup>1</sup>, Hong Nam Nguyen<sup>2</sup>,  
Thi Bich Quyen Tran<sup>1</sup>, Phan Hung Le<sup>3</sup>

<sup>1</sup>Can Tho University

<sup>2</sup>University of Science and Technology of Ha Noi,  
Vietnam Academy of Science and Technology

<sup>3</sup>Ho Chi Minh University of Technology and Education

Received 22 July 2021; accepted 31 August 2021

## Abstract:

This work investigates some parameters affecting the adsorption of methylene blue (MB) in synthesised wastewater using NaX. Zeolite has been synthesised from rice husk ash (RHA) without pretreatment to make use of cheap and readily available by-products in Vietnam. The parameters affecting the adsorption process such as pH, the concentration of MB, adsorbent dose, and contact time were specifically investigated. In addition, the adsorption isotherm models such as Langmuir, Freundlich, Dubinin - Radushkevich, pseudo-first-order kinetic, and pseudo-second-order kinetic were performed. The results showed that the maximum adsorption capacity and efficiency of NaX on MB were 16.67 mg/g and 87.03%, respectively, at pH 8, MB concentration of 15 mg/l, adsorbent dose of 0.05 g, and contact time of 30 min. The adsorption of MB by NaX has followed the Freundlich model and was physical adsorption fitted to pseudo-second-order kinetic. Zeolite NaX was reused four times with a decrease of adsorption yield by 24.03%. This study reveals the potential application of NaX on the removal of organic dyes and future researches on the removal of heavy metals or gases.

**Keywords:** adsorption, methylene blue, rice husk ash, zeolite NaX.

**Classification number:** 1.3

## Tổng hợp vật liệu NaX

Vật liệu NaX được tổng hợp từ RHA không nung theo điều kiện tối ưu của nghiên cứu Tran-Nguyen và cs (2021) [13]. Đầu tiên, RHA và dung dịch NaOH được khuấy ở 90°C trong 3 giờ với tỷ lệ rắn:lỏng phù hợp. Sau phản ứng, hỗn hợp được lọc rửa với nước cất và loại bỏ cặn rắn. Phần dung dịch thu được chủ yếu gồm  $\text{Na}_2\text{SiO}_3$ . Sau đó, thêm từ từ dung dịch  $\text{NaAlO}_2$  vào dung dịch trên ở 50°C và khuấy đồng nhất trong 2 giờ. Sau khi đồng nhất, hỗn hợp được gia nhiệt lên 90°C, giữ cố định nhiệt độ trong 4 giờ. Cuối cùng, hỗn hợp được lọc, ly tâm và sấy để thu được bột zeolite NaX. Điều kiện phản ứng tổng hợp NaX: tỷ lệ mol  $\text{SiO}_2:\text{Al}_2\text{O}_3=4$ , tỷ lệ mol  $\text{Na}_2\text{O}:\text{Al}_2\text{O}_3=10$ , thời gian phản ứng 4 giờ, nhiệt độ phản ứng 90°C và không già hóa.

## Hấp phụ MB của vật liệu NaX

Điện tích bề mặt và điểm đặng điện của NaX được xác định bằng cách cho 25 ml dung dịch KCl 0,1 M vào cốc thủy tinh, điều chỉnh pH dung dịch từ 3 đến 12 bằng dung dịch NaOH 0,01 M và HCl 0,01 M. Cân 0,2 g zeolite NaX cho vào các cốc thủy tinh. pH của dung dịch được đo sau 24 giờ. Điện tích bề mặt tại các pH khác nhau và điểm đặng điện của vật liệu được xác định bằng độ chênh lệch giữa pH trước và sau của dung dịch [14].

Các yếu tố ảnh hưởng đến quá trình hấp phụ MB của zeolite NaX được khảo sát gồm: pH (4-12), khối lượng vật liệu (0,025-0,2 g), nồng độ dung dịch của MB (5-50 mg/l) và thời gian hấp phụ (15-120 phút). Khảo sát sự ảnh hưởng của pH được thực hiện bằng cách cho 30 ml dung dịch MB có nồng độ 20 mg/l vào bình tam giác 250 ml, sau đó điều chỉnh pH của dung dịch từ 4 đến 12 bằng NaOH 0,01 M hoặc HCl 0,01 M. Cho 0,05 g vật liệu zeolite NaX vào bình và lắc đều với tốc độ 100 v/ph ở nhiệt độ phòng trong 30 phút. Kết thúc thí nghiệm, vật liệu được tách ra khỏi dung dịch bằng cách ly tâm. Thực hiện tương tự đối với các yếu tố còn lại. Độ hấp thụ quang trong các mẫu dung dịch sau quá trình hấp phụ được xác định bằng phương pháp phân tích phổ hấp thụ phân tử (Ultraviolet-visible spectroscopy, UV-Vis model V730 Jasco) [15].

Dung lượng hấp phụ (mg/g) và hiệu suất hấp phụ (%) được xác định theo công thức (1) và (2):

$$q = \frac{(C_0 - C_e) \times V}{m} \quad (1)$$

$$H = \frac{C_0 - C_e}{C_0} (\%) \quad (2)$$

với  $C_0$  (mg/l) là nồng độ ban đầu;  $C_e$  (mg/l) là nồng độ ở trạng thái cân bằng;  $V$  (l) là thể tích dung dịch và  $m$  (g) là khối lượng chất hấp phụ.

## Các mô hình đặng nhiệt hấp phụ và động học hấp phụ

Mô hình hấp phụ đặng nhiệt Langmuir, Freundlich và Dubinin - Radushkevich được sử dụng để đánh giá kết quả của quá trình hấp phụ MB bằng zeolite NaX [16].

Động học hấp phụ là một bộ thông số quan trọng trong việc áp dụng các quá trình hấp phụ vào xử lý nước thải, dùng để dự đoán tốc độ tách chất ô nhiễm ra khỏi dung dịch. Vì thế, phương trình động học giả định bậc 1 và 2 dạng tuyến tính đã được sử dụng trong nghiên cứu này [17].

## Phương pháp nghiên cứu

RHA được thu từ Công ty Cổ phần Nam Tiến (Khu công nghiệp Trà Nóc, TP Cần Thơ). Hóa chất sử dụng gồm lá nhôm 99% (Union Chemical Industry Company Ltd.), sodium hydroxide 96% (Xilong), hydrochloric acid 36-38% (Xilong), MB 98,5% (Xilong), potassium fluoride dihydrate 99% (Sigma Aldrich), disodium tetraborate decahydrate 99,5% (Merck), bromothymol blue (Merck). Các hóa chất có nguồn gốc thương mại và không cần tinh chế trước khi sử dụng.

### Khả năng tái sử dụng của zeolite NaX

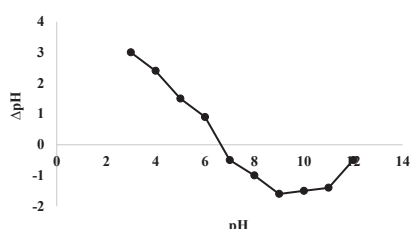
Vật liệu zeolite NaX được sử dụng cho quá trình hấp phụ MB theo các điều kiện tối ưu ở các khảo sát trên. Để khảo sát khả năng tái sử dụng, NaX được khuấy trong dung dịch NaOH 0,001 M trong 20 phút với tỷ lệ rắn:lỏng = 0,05:25 (g/ml) [18]. Sau đó, NaX được sấy đến khối lượng không đổi và tiếp tục được tái sử dụng cho lần hấp phụ MB tiếp theo. Sau khi tái sử dụng lần 1, vật liệu được giải hấp phụ và tái sử dụng lần 2. Các thí nghiệm tái sử dụng hấp phụ MB của zeolite NaX tiếp theo được thực hiện như đã mô tả.

### Kết quả và bàn luận

Vật liệu zeolite NaX tổng hợp có diện tích bề mặt riêng và kích thước lỗ rỗng lân lượt là  $388,41 \text{ m}^2/\text{g}$  và  $12,37 \text{ \AA}$ . Ngoài ra, kết quả phân tích kích thước hạt của zeolite NaX cho thấy kích thước hạt chủ yếu nằm trong khoảng  $0,3\text{-}0,7 \mu\text{m}$  và kích thước hạt trung bình tập trung ở khoảng  $0,5 \mu\text{m}$  [13].

#### Xác định diện tích bề mặt và điểm đắng điện của vật liệu

Điểm đắng điện là một yếu tố quan trọng khi nghiên cứu khả năng hấp phụ của vật liệu, vì vậy việc xác định thông số này là rất cần thiết. Ở pH thấp ( $\text{pH}<3$ ) vật liệu zeolite thường kém bền, do đó khoảng khảo sát được chọn từ 3 đến 12 [14] (hình 1).

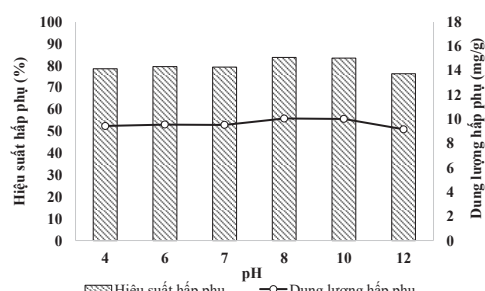


Hình 1. Điểm đắng điện của zeolite NaX.

Từ hình 1 có thể xác định được điểm đắng điện của vật liệu, tại pH 6,6 thì giá trị  $\Delta\text{pH}=0$ . Vây điểm đắng điện (pHPZC) của vật liệu zeolite NaX là 6,6, tại đây bề mặt vật liệu không tích điện. Kết quả này cho thấy, ở môi trường pH<6,6 bề mặt vật liệu mang điện tích dương và ngược lại.

#### Ảnh hưởng của pH

Ảnh hưởng của pH đến khả năng hấp phụ MB của vật liệu được thể hiện trong hình 2.

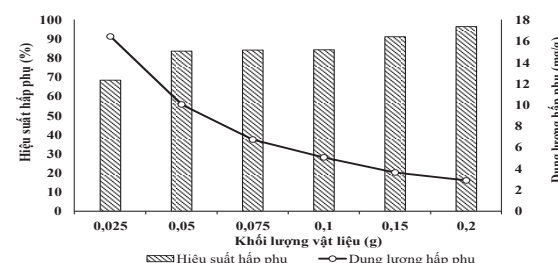


Hình 2. Sự ảnh hưởng của pH đến khả năng hấp phụ MB của zeolite NaX tại khối lượng vật liệu 0,05 g, nồng độ dung dịch 20 mg/l, thời gian hấp phụ 30 phút.

Khi thay đổi từ pH 4 đến 7 thì hiệu suất hấp phụ và dung lượng hấp phụ hầu như không có sự chênh lệch lớn. Tuy nhiên, khi thay đổi pH từ 8 đến 10, hiệu suất hấp phụ và dung lượng hấp phụ tăng và đạt cực đại tại 83,77% và 10,05 mg/g. Hiện tượng này là do trong môi trường acid ( $\text{pH}<7$ ) các ion  $\text{H}^+$  sẽ cạnh tranh với các phân tử cation MB dẫn đến lực tương tác tĩnh điện giữa MB và bề mặt vật liệu giảm dần [14, 17], do đó hấp phụ MB tại các khoảng pH lớn hơn 7 sẽ tốt hơn. Tại các khoảng pH quá cao ( $\text{pH} 12$ ), hiệu suất và dung lượng giảm (76,31% và 9,16 mg/g), có thể là do trong môi trường có nhiều ion  $\text{OH}^-$ , có sự cạnh tranh cation MB giữa ion  $\text{OH}^-$  và zeolite khiến vật liệu hấp phụ bị giải hấp một phần [18]. Nhìn chung, zeolite NaX có khả năng hấp phụ dung dịch MB ở môi trường acid và kiềm với hiệu suất trên 75%. Đây là một ưu điểm của vật liệu do quá trình hấp phụ xử lý nước thải nhiễm thuỷ nhuộm trong thực tế có thể ở nhiều khoảng pH khác nhau.

#### Ảnh hưởng của khối lượng vật liệu

Sự ảnh hưởng của khối lượng vật liệu đến khả năng hấp phụ MB của vật liệu được thể hiện ở hình 3.



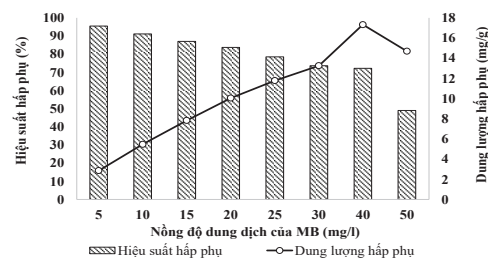
Hình 3. Sự ảnh hưởng của khối lượng vật liệu đến khả năng hấp phụ MB của zeolite NaX tại pH 8, nồng độ dung dịch 20 mg/l, thời gian hấp phụ 30 phút.

Từ kết quả có thể thấy rằng, hiệu suất hấp phụ tăng dần từ 68,58 đến 96,64% và dung lượng hấp phụ lại giảm (từ 16,46 đến 2,90 mg/g) khi tăng khối lượng chất hấp phụ từ 0,025 đến 0,2 g. Khi khối lượng chất hấp phụ ít (0,025 g), quá trình hấp phụ xảy ra với sự khuếch tán nhanh chóng của các phân tử MB lên bề mặt chất hấp phụ. Tuy nhiên, vì khối lượng vật liệu còn ít nên chưa thể hấp phụ đáng kể lượng MB có trong dung dịch, dẫn đến dung lượng hấp phụ cao nhưng hiệu suất lại thấp [15, 19].

Khi tăng khối lượng chất hấp phụ từ 0,05 đến 0,1 g, dung lượng hấp phụ lại giảm từ 10,05 đến 5,07 mg/g nhưng hiệu suất hấp phụ thay đổi không đáng kể vì quá trình hấp phụ dần đạt đến cân bằng. Hiệu suất tiếp tục tăng đến 96,64% khi khối lượng vật liệu là 0,2 g, nhưng dung lượng hấp phụ giảm còn 2,90 mg/g. Khi tăng khối lượng vật liệu, tần hấp phụ được bổ sung thêm, dẫn đến hiệu suất hấp phụ tăng. Jamil và cs (2011) [8] đã kết luận rằng, hiệu suất xử lý MB của vật liệu zeolite tăng nhanh khi thay đổi khối lượng từ 0,1 đến 0,3 g. Tuy nhiên, khi tiếp tục tăng khối lượng vật liệu từ 0,3 đến 1 g thì hiệu suất hấp phụ không có sự thay đổi đáng kể [8]. Kết quả này cũng tương tự với các kết quả nghiên cứu đã công bố [15, 20]. Mặc dù dung lượng hấp phụ đạt cực đại khi sử dụng 0,025 g vật liệu nhưng hiệu suất chỉ đạt 68,58%. Do đó, để xử lý dung dịch MB đạt hiệu suất và dung lượng hấp phụ tối ưu, khối lượng vật liệu được chọn là 0,05 g.

### Ảnh hưởng của nồng độ dung dịch

Ảnh hưởng của nồng độ dung dịch đến khả năng hấp phụ MB của zeolite NaX được trình bày ở hình 4.

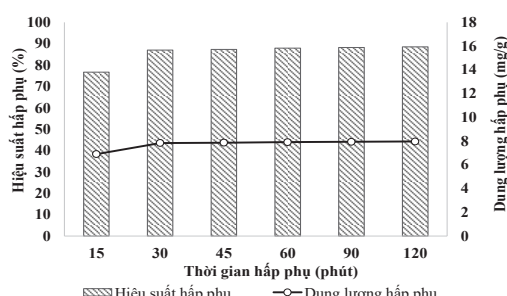


Hình 4. Sự ảnh hưởng của nồng độ dung dịch đến khả năng hấp phụ MB của zeolite NaX tại pH 8, khối lượng vật liệu 0,05 g, thời gian hấp phụ 30 phút.

Từ hình 4 có thể đánh giá được sự ảnh hưởng của nồng độ dung dịch đến khả năng hấp phụ MB của zeolite NaX. Khi tăng nồng độ dung dịch từ 5 đến 40 mg/l thì dung lượng hấp phụ tăng nhưng hiệu suất hấp phụ lại giảm. Tại các nồng độ từ 5 đến 30 mg/l, dung lượng hấp phụ tăng từ 2,86 đến 13,26 mg/g nhưng hiệu suất xử lý MB giảm 21,82% (từ 95,5 xuống 73,68%). Ở nồng độ thấp, các phân tử MB ít dẫn đến chúng dễ dàng bị hấp phụ bởi vật liệu zeolite, nên hiệu suất hấp phụ cao. Khi tăng nồng độ dung dịch, các phân tử MB tồn tại dày đặc hơn, đã lấp đầy các tâm hấp phụ và gây nên sự khó khuếch tán MB lên bề mặt vật liệu. Bên cạnh đó, các phân tử MB còn lại trong dung dịch có xu hướng cạnh tranh với các phân tử đã được hấp phụ nên hiệu suất hấp phụ giảm [15, 17, 21]. Do đó, nồng độ dung dịch là 15 mg/l đã được lựa chọn.

### Ảnh hưởng của thời gian

Ảnh hưởng của thời gian đến khả năng hấp phụ MB của zeolite NaX được trình bày ở hình 5.



Hình 5. Sự ảnh hưởng của thời gian đến khả năng hấp phụ MB của zeolite NaX với pH 8, khối lượng vật liệu 0,05 g, nồng độ dung dịch 15 mg/l.

Kết quả hình 5 cho thấy, các phân tử MB được hấp phụ nhanh chóng lên bề mặt của vật liệu, hiệu suất và dung lượng hấp phụ lần lượt là 76,66% và 6,90 mg/g ở 15 phút đầu tiên. Khi tiếp tục kéo dài thời gian từ 30 đến 120 phút, hiệu suất hấp phụ và dung lượng hấp phụ đạt trạng thái cân bằng ở 87,03% và 7,83 mg/g. Thời gian đạt cân bằng hấp phụ của vật liệu zeolite là khá ngắn (khoảng 30 phút) do các phân tử MB được khuếch tán vào trong các lỗ rỗng của zeolite NaX, dẫn tới các tâm hấp phụ được lấp đầy. NaX sử dụng

có diện tích bề mặt riêng khá lớn ( $388,41 \text{ m}^2/\text{g}$ ), giúp tăng khả năng khuếch tán và tiếp xúc của các phân tử MB đến bề mặt vật liệu so với các vật liệu cùng loại khác [8, 13]. Jamil và cs (2011) [8] đã sử dụng zeolite NaA và NaX để xử lý MB từ 5 đến 150 phút và cho thấy thời gian cân bằng hấp phụ tối ưu là 60 phút. Nhóm tác giả cũng khẳng định NaX có diện tích bề mặt riêng lớn hơn NaA nên hiệu quả xử lý MB của NaX tốt hơn.

### Cân bằng hấp phụ - các mô hình hấp phụ đẳng nhiệt

Dữ liệu của các mô hình hấp phụ đẳng nhiệt như Langmuir, Freundlich và Dubinin - Radushkevich được tính toán dựa trên các kết quả thực nghiệm và được miêu tả ở bảng 1. Qua đó, có thể thấy được sự tương tác của các phân tử MB và bề mặt zeolite NaX tại thời điểm cân bằng ở nhiệt độ không đổi [16]. Từ phương trình đường đẳng nhiệt Langmuir có thể xác định được  $q_{\max} = 16,67 \text{ mg/g}$ ,  $k_L = 0,67 \text{ l/mg}$ ,  $R^2 = 0,9843$ , trong khi các tham số của phương trình Freundlich là  $k_F = 5,69 \text{ l/g}$ ,  $n = 2,28$  và  $R^2 = 0,9936$ . Hệ số hồi quy tuyến tính của cả hai mô hình đẳng nhiệt Langmuir ( $R^2 = 0,9843$ ) và Freundlich ( $R^2 = 0,9936$ ) đều khá cao (bảng 1).

Bảng 1. Các giá trị tham số của các phương trình đẳng nhiệt.

Các tham số	Langmuir	Freundlich	Dubinin - Radushkevich
$k_L (\text{l}/\text{mg})$	0,67	-	-
$q_{\max} (\text{mg}/\text{g})$	16,67	-	-
$R^2$	0,9843	0,9936	0,7992
$k_F (\text{l}/\text{g})$	-	5,69	-
$n$	-	2,28	-
$\beta (\text{mol}^2/\text{J}^2)$	-	-	0,075
$E (\text{kJ/mol})$	-	-	2,58

Đồng thời, khi xem xét giá trị  $n$  được tính toán từ phương trình đẳng nhiệt Freundlich cho thấy  $n < 10$ . Từ các kết quả trên, có thể kết luận rằng quá trình hấp phụ MB của vật liệu zeolite NaX tuân theo cả hai mô hình đẳng nhiệt Langmuir và Freundlich, trong đó mô hình Freundlich chiếm ưu thế do hệ số  $R^2$  cao hơn. Nghiên cứu về quá trình hấp phụ MB của zeolite chỉ ra rằng bề mặt của zeolite được bao phủ không đồng nhất về mặt năng lượng, dẫn đến sự phân bố không đều của các phân tử MB tại các vị trí hấp phụ trên zeolite đã được trình bày ở những công bố trước đây [8, 22]. Từ mô hình đẳng nhiệt, có thể kết luận rằng quá trình hấp phụ MB của zeolite NaX diễn ra hiệu quả. Ngoài ra, giá trị năng lượng  $E$  được tính từ mô hình Dubinin - Radushkevich là  $2,58 \text{ kJ/mol}$  ( $< 8 \text{ kJ/mol}$ ) cho thấy quá trình hấp phụ MB của zeolite NaX phù hợp với quá trình hấp phụ vật lý. Một trong những yếu tố quan trọng giúp vật liệu zeolite NaX có thể hấp phụ vật lý thuận lợi đó là nhờ vào diện tích bề mặt riêng lớn và kích thước lỗ rỗng tương đối lớn, phù hợp với phân tử MB.

### Động học hấp phụ

Bảng 2 biểu diễn phương trình động học giả định bậc 1 của quá trình hấp phụ với  $R^2 = 0,7742$  và  $q_e = 0,953 \text{ (mg/g)}$ . Hệ số hồi quy tuyến tính  $R^2$  thấp và sự khác biệt giữa dung lượng hấp phụ cân bằng tính toán so với dung lượng hấp phụ cân bằng thực nghiệm lớn cho thấy phương trình bậc 1 không phù hợp với quá trình xử lý MB của zeolite NaX. Bảng 2 cũng cho thấy phương trình giả

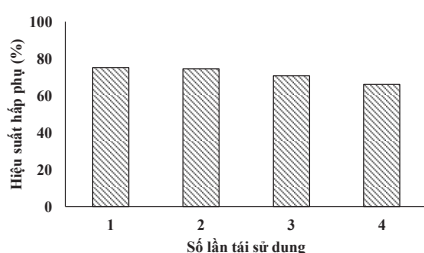
kiến bậc 2 có  $R^2=0,9998$  và giá trị dung lượng hấp phụ cân bằng tính toán rất gần so với giá trị dung lượng hấp phụ cân bằng thực nghiệm. Vì vậy, phương trình động học bậc 2 phù hợp với quá trình hấp phụ MB của zeolite NaX. Hệ số góc của phương trình động học bậc 2 ( $a=0,123$ ) tương đối nhỏ, cho thấy khả năng hấp phụ khá tốt của zeolite NaX. Khi hệ số góc càng nhỏ thì dung lượng hấp phụ của vật liệu càng cao. Đồng thời, hệ số tốc độ hấp phụ  $k_2$  tỷ lệ nghịch với dung lượng hấp phụ,  $k_2$  càng nhỏ dung lượng hấp phụ được trong thời gian t càng lớn, tốc độ hấp phụ nhanh. Điều này phù hợp với kết quả thí nghiệm khi  $k_2=0,073$  thì  $q_e=8,13 \text{ mg/g}$ .

**Bảng 2. Các tham số của phương trình giải kiến bậc 1 và bậc 2.**

a	b	$q_e$ tính toán (mg.g <sup>-1</sup> )	$k_1$ (phút <sup>-1</sup> )	$k_2$ (g.mg <sup>-1</sup> .phút <sup>-1</sup> )	$R^2$
Bậc 1	-0,042	-0,048	0,953	-0,042	-
Bậc 2	0,123	0,207	8,130	-	0,9998

### Khả năng tái sử dụng của zeolite NaX

Khả năng tái sử dụng của vật liệu được trình bày ở hình 6.

**Hình 6. Đồ thị thê hiện khả năng tái sử dụng của zeolite NaX.**

Kết quả hình 6 cho thấy, hiệu suất xử lý MB của vật liệu sau quá trình giải hấp phụ nhìn chung vẫn khá cao (75,14-66,12% qua 4 lần tái sử dụng). Hiệu suất hấp phụ chỉ chênh lệch khoảng 0,7% ở lần 1 và lần 2. Khi so với hiệu suất hấp phụ ban đầu thì hiệu suất hấp phụ lần 2 giảm khoảng 13,65%. Hiệu suất hấp phụ chỉ đạt khoảng 70,76-66,12% (lần 3 và lần 4) và được dự đoán sẽ tiếp tục giảm ở những lần tái sử dụng sau. Do đó, có thấy thấy rằng vật liệu zeolite NaX có khả năng tái sử dụng sau quá trình hấp phụ MB, tuy nhiên hiệu quả cao chỉ ở lần 1 và 2. Khi tiếp tục tái sử dụng zeolite NaX thì hiệu suất hấp phụ sẽ giảm.

### Kết luận

Vật liệu zeolite NaX tổng hợp từ nghiên cứu có khả năng hấp phụ hiệu quả MB trong nước giả thai với dung lượng hấp phụ và hiệu suất hấp phụ lần lượt là 16,67 mg/g và 87,03%. Điểm đáng điện của vật liệu ở pH 6,6 và quá trình hấp phụ MB của vật liệu cho thấy hiệu quả ở môi trường kiềm. Các điều kiện tối ưu cho quá trình hấp phụ MB là ở pH 8, nồng độ MB 15 mg/l, khối lượng vật liệu 0,05 g và thời gian hấp phụ 30 phút. Kết quả cũng cho thấy quá trình hấp phụ MB bằng zeolite NaX phù hợp với mô hình hấp phụ Freundlich và hấp phụ vật lý, cũng như phù hợp với phương trình động học bậc 2. Những kết quả trong nghiên cứu cho thấy tiềm năng của zeolite NaX trong hấp phụ các loại thuốc nhuộm, kim loại nặng và chất khử.

### LỜI CẢM ƠN

Nghiên cứu này được tài trợ bởi Quỹ Phát triển KH&CN quốc gia (NAFOSTED) thông qua đề tài mã số 103.02-2020.64. Nhóm nghiên cứu xin trân trọng cảm ơn.

### TÀI LIỆU THAM KHẢO

- [1] M. Mohammed, et al. (2014), “Removal of methylene blue using low cost adsorbent: a review”, *Res. J. Chem. Sci.*, **4(1)**, pp.91-102.
- [2] Đỗ Năng Vinh và cs (2020), “Nghiên cứu năng suất hạt và tiềm năng sinh khối cây lúa và một số định hướng ứng dụng”, *Tạp chí Khoa học Nông nghiệp Việt Nam*, **18(8)**, tr.570-579.
- [3] S.S. Hossain, et al. (2018), “Rice husk/rice husk ash as an alternative source of silica in ceramics: a review”, *J. Asian Ceram. Soc.*, **6(4)**, pp.299-313.
- [4] V. Shelke, et al. (2010), “Mesoporous silica from rice husk ash”, *Bull. Chem. React. Eng. Catal.*, **5(2)**, pp.63-67.
- [5] H. Katsuki, et al. (2009), “Synthesis of Na-A and/or Na-X zeolite/porous carbon composites from carbonized rice husk”, *J. Solid State Chem.*, **182(7)**, pp.1749-1753.
- [6] S. Sembiring, et al. (2016), “Preparation of refractory cordierite using amorphous rice husk silica for thermal insulation purposes”, *Ceram. Int.*, **42(7)**, pp.8431-8437.
- [7] Z. Qiang, et al. (2019), “A simple hydrothermal synthesis of zeolite X from bauxite tailings for highly efficient adsorbing CO<sub>2</sub> at room temperature”, *Micropor. Mesopor. Mat.*, **287**, pp.77-84.
- [8] T.S. Jamil, et al. (2011), “Removal of methylene blue by two zeolites prepared from naturally occurring Egyptian kaolin as cost effective technique”, *Solid State Sci.*, **13(10)**, pp.1844-1851.
- [9] S. Sivalingam, et al. (2019), “Efficient removal of textile dye using nanosized fly ash derived zeolite - X: kinetics and process optimization study”, *J. Taiwan Inst. Chem. Eng.*, **96**, pp.305-314.
- [10] S. Krachuanram, et al. (2021), “Synthesis and characterization of NaX - type zeolites prepared by different silica and alumina sources and their CO<sub>2</sub> adsorption properties”, *Micropor. Mesopor. Mat.*, **310**, pp.110632.
- [11] S.M. Al-Jubouri, et al. (2019), “Effect of synthesis parameters on the formation 4A zeolite crystals: characterization analysis and heavy metals uptake performance study for water treatment”, *Desalin. Water Treat.*, **165**, pp.290-300.
- [12] G. Yao, et al. (2018), “One-step hydrothermal synthesis of zeolite X powder from natural low-grade diatomite”, *Mater.*, **11(6)**, pp.1-14.
- [13] P.L. Tran-Nguyen, et al. (2021), “Facile synthesis of zeolite NaX using rice husk ash without pretreatment”, *J. Taiwan Inst. Chem. Eng.*, **123**, pp.338-345.
- [14] X. Jin, et al. (2008), “Adsorption of methylene blue and orange II onto unmodified and surfactant-modified zeolite”, *J. Colloid Interface Sci.*, **328(2)**, pp.243-247.
- [15] D.M. EL-Mekkawi, et al. (2016), “Removal of methylene blue from water using zeolites prepared from Egyptian kaolins collected from different sources”, *J. Environ. Chem. Eng.*, **4(2)**, pp.1417-1422.
- [16] M.A. Al-Ghouti, et al. (2020), “Guidelines for the use and interpretation of adsorption isotherm models: a review”, *J. Hazard. Mater.*, **393**, pp.122383.
- [17] C. Li, et al. (2015), “Removal of basic dye methylene blue from aqueous solution using zeolite synthesized from electrolytic manganese residue”, *J. Ind. Eng. Chem.*, **23**, pp.344-352.
- [18] H. Mahmud, et al. (1997), “Rice husk ash—an alternative material in producing high strength concrete”, *Proceedings of International Conference on Engineering Materials*, pp.275-284.
- [19] Nguyễn Văn Hưng và cs (2015), “Điều chế vật liệu nano SiO<sub>2</sub> cấu trúc xốp từ tro trấu để hấp thụ xanh metylen trong nước”, *Tạp chí Hóa học*, **53(4)**, tr.491-496.
- [20] X.B. Li, et al. (2018), “Microwave digestion and alkali fusion assisted hydrothermal synthesis of zeolite from coal fly ash for enhanced adsorption of Cd(II) in aqueous solution”, *J. Cent. South Univ.*, **25(1)**, pp.9-20.
- [21] K. Rida, et al. (2013), “Adsorption of methylene blue from aqueous solution by kaolin and zeolite”, *Appl. Clay Sci.*, **83**, pp.99-105.
- [22] C.D.D. Sundari, et al. (2018), “Synthesis of zeolite L using rice husk ash silica for adsorption of methylene blue: kinetic and adsorption isotherm”, *MATEC Web of Conferences - EDP Sciences*, **197**, DOI: 10.1051/matecconf/201819705002.

## SYNTHESIS OF NaX/Fe<sub>3</sub>O<sub>4</sub> COMPOSITE AND EVALUATION OF ITS NITRATE REMOVAL

**Tran Nguyen Phuong Lan<sup>\*</sup>, Ly Kim Phung, Nguyen Thanh Ty, Nguyen Minh Nhut,  
Tran Thi Bich Quyen, Duong Thi My Tuyen, Doan Van Hong Thien**  
*Can Tho University*

ARTICLE INFO	ABSTRACT
<b>Received:</b> 19/12/2023	This study presented a simple, time and energy saving process to synthesize NaX/Fe <sub>3</sub> O <sub>4</sub> composite, with a mass ratio of zeolite NaX:Fe <sub>3</sub> O <sub>4</sub> = 1.5:1 (w/w), mixing time of 2 h, at room temperature and tetraethyl orthosilicate (TEOs) as a cohesion of 1 % v/v. In this work, the analysis methods such as XRD, TEM, and FTIR used reported the sphere shape and uniform sizes of the composite. Besides, all of the functional groups of composites such as -OH, Al-O-Si, T-O-T, and Fe-O could be seen in the final product. The saturation magnetization of NaX/Fe <sub>3</sub> O <sub>4</sub> composite is 2.135 emu/g, which is determined by VSM. The specific surface area and pore diameter are 322.449 m <sup>2</sup> /g and 32.4 Å, respectively. The removal ability of NaX/Fe <sub>3</sub> O <sub>4</sub> composite onto NO <sub>3</sub> <sup>-</sup> anion was performed at pH 6, an anion concentration of 20 mg/L, adsorbent dose of 0.02 g within 40 min. The adsorption capacity and adsorption yield of the composite are 36.28 mg/g and 72.55%, respectively. The adsorption of this work was fitted to Langmuir isotherm model, and physical adsorption. The adsorption experiments proved that NaX/Fe <sub>3</sub> O <sub>4</sub> composite is a potential adsorbent for removing NO <sub>3</sub> <sup>-</sup> anion in wastewater.
<b>Published:</b> 11/01/2023	
<b>KEYWORDS</b>	
NaX/Fe <sub>3</sub> O <sub>4</sub> composite NO <sub>3</sub> <sup>-</sup> ion Adsorption Rice husk ash Tetraethyl orthosilicate	

## TỔNG HỢP VẬT LIỆU COMPOSITE NaX/Fe<sub>3</sub>O<sub>4</sub> VÀ ĐÁNH GIÁ KHẢ NĂNG HẤP PHỤ NITRATE

**Trần Nguyễn Phương Lan<sup>\*</sup>, Lý Kim Phụng, Nguyễn Thành Tý, Nguyễn Minh Nhựt,  
Trần Thị Bích Quyên, Dương Thị Mỹ Tuyên, Đoàn Văn Hồng Thiện**  
*Trường Đại học Cần Thơ*

THÔNG TIN BÀI BÁO	TÓM TẮT
<b>Ngày nhận bài:</b> 19/12/2023	Nghiên cứu này trình bày một quy trình đơn giản, tiết kiệm thời gian và năng lượng để tổng hợp vật liệu composite NaX/Fe <sub>3</sub> O <sub>4</sub> , với tỷ lệ khối lượng zeolite NaX:Fe <sub>3</sub> O <sub>4</sub> = 1.5:1 (g/g), thời gian khuấy trộn 2 giờ, nhiệt độ phòng, và nồng độ chất kết tetraethyl orthosilicate (TEOs) 1%. Các phương pháp phân tích XRD, TEM, và FTIR cho thấy vật liệu NaX/Fe <sub>3</sub> O <sub>4</sub> có dạng hình cầu, kích thước khá đồng đều và đầy đủ các dao động đặc trưng của vật liệu composite. Độ từ hóa bão hòa của composite là 2,135 emu/g, được xác định bằng phương pháp VSM. Diện tích bề mặt riêng và kích thước lỗ rỗng của vật liệu NaX/Fe <sub>3</sub> O <sub>4</sub> lần lượt là 322,449 m <sup>2</sup> /g và 32,4 Å. Đánh giá khả năng xử lý ion NO <sub>3</sub> <sup>-</sup> của vật liệu composite ở điều kiện pH 6, nồng độ nitrate 20 mg/L, khối lượng vật liệu là 0,02 g, thời gian hấp phụ 40 phút, cho thấy rằng dung lượng hấp phụ và hiệu suất hấp phụ lần lượt là 36,28 mg/g và 72,55%. Quá trình hấp phụ trong nghiên cứu này phù hợp với lý thuyết đẳng nhiệt Langmuir, hấp phụ đồng nhất, đơn lớp, độc lập và là hấp phụ vật lý. Các thí nghiệm về hấp phụ chứng tỏ composite NaX/Fe <sub>3</sub> O <sub>4</sub> có tiềm năng xử lý ion NO <sub>3</sub> <sup>-</sup> trong nước.
<b>Ngày hoàn thiện:</b> 11/01/2023	
<b>Ngày đăng:</b> 11/01/2023	
<b>TỪ KHÓA</b>	
Composite NaX/Fe <sub>3</sub> O <sub>4</sub> Ion NO <sub>3</sub> <sup>-</sup> Hấp phụ Tro trấu Tetraethyl orthosilicate	

**DOI:** <https://doi.org/10.34238/tnu-jst.7145>

\* Corresponding author. Email: [tnplan@ctu.edu.vn](mailto:tnplan@ctu.edu.vn)

## 1. Giới thiệu

Hiện nay, xử lý chất thải chứa nitrate đang thu hút sự quan tâm của nhiều nhà khoa học. Ô nhiễm nitrate chủ yếu từ quá trình sử dụng quá mức lượng phân bón hữu cơ, thuốc trừ sâu, hay lượng thức ăn dư thừa trong các ao nuôi thủy sản [1]. Nồng độ nitrate cao sẽ gây các tác hại nghiêm trọng đến con người và sinh vật, đồng thời cũng là nguyên nhân gây ra nhiều bệnh hiểm nghèo như ung thư, đột biến,... [2].

Việt Nam là nước nông nghiệp nên lượng vỏ trấu thải ra hàng năm là rất lớn, được sử dụng làm chất đốt, thu được tro trâu (RHA) [3], [4]. Do đó, tận dụng nguồn RHA để chế tạo vật liệu hấp phụ, trong đó có zeolite NaX và ứng dụng trong xử lý các chất gây ô nhiễm đang được quan tâm. Nghiên cứu vật liệu zeolite NaX từ tính để xử lý Pb (II) được thực hiện, với dung lượng hấp phụ là 196,8 mg/g [5]. Tổng hợp zeolite từ tính/chitosan để loại bỏ Cr (VI) đã được nghiên cứu [6]. Vật liệu zeolite- $\text{Fe}_3\text{O}_4$  được ứng dụng để xử lý Pb (II) [7]. Vật liệu  $\text{Fe}_3\text{O}_4/\text{ZrO}_2/\text{chitosan}$  với diện tích bề mặt riêng là 212,9 m<sup>2</sup>/g có khả năng hấp phụ nitrate hấp phụ tối đa là 89,3 mg/g ở pH 3, nồng độ 500 mg/L, 25°C trong 24 giờ [8]. Vật liệu GO- $\text{Fe}_3\text{O}_4$  được ứng dụng để xử lý nitrate với hiệu suất 89% tại pH 2, nồng độ ion 100 mg/L, 0,5 g chất hấp phụ và thời gian 120 phút [9]. Nghiên cứu này nhằm tổng hợp vật liệu composite NaX/ $\text{Fe}_3\text{O}_4$  với zeolite NaX được tổng hợp từ RHA. Bên cạnh đó, đánh giá khả năng xử lý  $\text{NO}_3^-$  trong nước giả thải của vật liệu composite NaX/ $\text{Fe}_3\text{O}_4$  cũng được thực hiện.

## 2. Phương pháp nghiên cứu

### 2.1. Hóa chất và nguyên liệu

RHA được thu gom tại công ty Cổ phần Nam Tiên, Khu Công nghiệp Trà Nóc, Cần Thơ. Bột nhôm (Al), sodium hydroxide 96% (NaOH), hydrochloric acid 36-38% (HCl), iron (III) chloride hexahydrate 99% ( $\text{FeCl}_3 \cdot 6\text{H}_2\text{O}$ ), iron (II) chloride tetrahydrate 99% ( $\text{FeCl}_2 \cdot 4\text{H}_2\text{O}$ ), ammonium hydroxide 99% ( $\text{NH}_4\text{OH}$ ), ethanol 96% ( $\text{C}_2\text{H}_5\text{OH}$ ), tetraethyl orthosilicate 99% ( $\text{Si}(\text{OC}_2\text{H}_5)_4$ ), potassium chloride 99% (KCl), các hóa chất này có nguồn gốc từ Xilong. Potassium nitrate ( $\text{KNO}_3$ ) được sản xuất tại Merck.

### 2.2. Tổng hợp vật liệu composite NaX/ $\text{Fe}_3\text{O}_4$

Quy trình tổng hợp zeolite NaX được thura hướng từ kết quả nghiên cứu đã công bố, với điều kiện tổng hợp: tỷ lệ mol  $\text{SiO}_2:\text{Al}_2\text{O}_3 = 4$ , ở 90°C, 4 giờ và khuấy 300 vòng/phút [10]. Nano sét từ  $\text{Fe}_3\text{O}_4$  được tổng hợp bằng phương pháp đồng kết tủa ở điều kiện: tỷ lệ mol  $\text{Fe}^{2+}:\text{Fe}^{3+}:\text{NH}_3 = 1:2:8$  ở 80°C trong 1 giờ, khuấy 300 vòng/phút và sục khí  $\text{N}_2$  [11]. Quy trình tổng hợp composite NaX/ $\text{Fe}_3\text{O}_4$  được thực hiện với các tiền chất ban đầu là zeolite NaX và  $\text{Fe}_3\text{O}_4$  ở tỷ lệ khói lượng x:y (g/g). 80 mL ethanol được thêm vào hỗn hợp và siêu âm dung dịch trong 30 phút. Tiếp theo, V mL dung dịch TEOs được cho vào dung dịch trên và khuấy trong thời gian t giờ. Sau đó, hỗn hợp được lọc rửa đến pH trung tính và sấy ở 60°C đến khói lượng không đổi, sản phẩm là composite NaX/ $\text{Fe}_3\text{O}_4$ . Các yếu tố ảnh hưởng đến quá trình tổng hợp composite được khảo sát như sau: tỷ lệ khói lượng zeolite NaX: $\text{Fe}_3\text{O}_4 = 1:1; 1,5:1$ ; và 2:1 g/g; thời gian khuấy t = 1; 2; 4; 6 và 8 giờ; phần trăm thể tích TEOs = 0,5; 1,0; 1,5 và 2,0%.

### 2.3. Đánh giá tính chất của vật liệu composite

Composite NaX/ $\text{Fe}_3\text{O}_4$  được xác định cấu trúc mạng tinh thể bằng phương pháp nhiễu xạ tia X (XRD) trên thiết bị D8-Advance. Sự liên kết giữa zeolite NaX và  $\text{Fe}_3\text{O}_4$  được kiểm tra bằng Phô hồng ngoại biến đổi Fourier (FTIR) - đo bằng máy Thermo Nicolet 6700. Hình dạng của hạt vật liệu, diện tích bề mặt riêng và kích thước lỗ rỗng của composite được xác định bằng phương pháp kính hiển vi điện tử truyền qua (TEM) - đo bằng thiết bị TEM TECNAI G2-20 và BET Nova 1000e (Quantachrome Instruments). Tính chất từ của  $\text{Fe}_3\text{O}_4$  và composite trong nghiên cứu được thực hiện trên hệ từ kế mẫu rung (VSM).

#### 2.4. Đánh giá khả năng xử lý $\text{NO}_3^-$ của composite $\text{NaX}/\text{Fe}_3\text{O}_4$

Điểm đăng điện của composite  $\text{NaX}/\text{Fe}_3\text{O}_4$  ( $\text{pH}_{\text{pzc}}$ ) xác định bằng cách: cân 0,02 g composite cho vào 20 mL dung dịch KCl 0,1 M. pH của dung dịch được điều chỉnh từ 3-12 bằng KOH 0,1 M hoặc HCl 0,1 M, xác định pH của dung dịch sau khi ngâm 24 giờ và tính toán  $\text{pH}_{\text{pzc}}$  của composite. Trong nghiên cứu này, các yếu tố ảnh hưởng đến quá trình hấp phụ  $\text{NO}_3^-$  của composite được khảo sát ở pH 4-6; khối lượng vật liệu = 0,02-0,2 g; thời gian hấp phụ 20-60 phút; nồng độ của dung dịch 20-100 mg/L với thể tích mỗi mẫu thí nghiệm là 50 mL. Nồng độ nitrate trước và sau khi hấp phụ được xác định bằng phương pháp trắc quang hấp thụ phân tử (Thermo Scientific Evolution 60S) ở bước sóng  $\lambda = 543$  nm theo tiêu chuẩn ISO 6777-1984 (E) và ISO 14673-1:2004. Dung lượng hấp phụ  $q$  (mg/g) và hiệu suất hấp phụ  $H$  (%) được tính toán:

$$q = \frac{(C_o - C_e) \times V}{m} \quad (1)$$

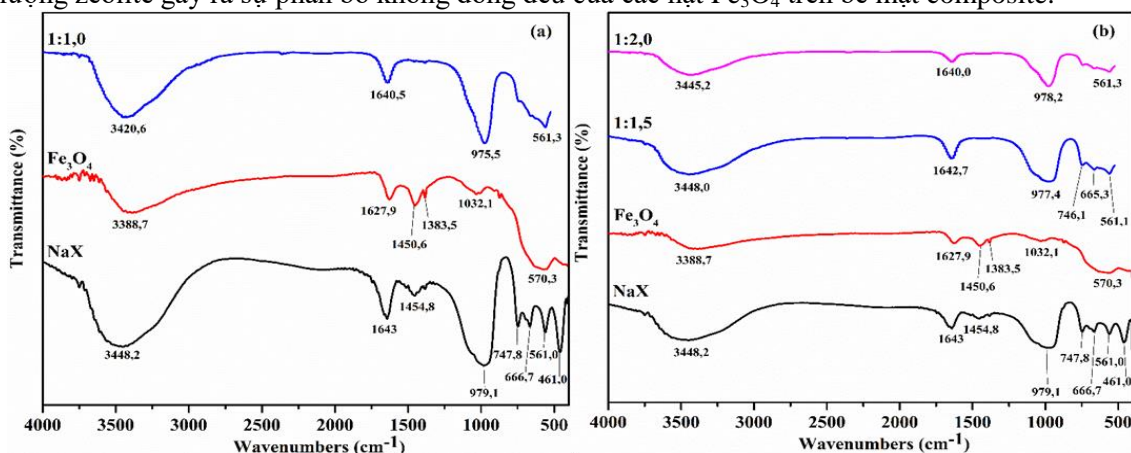
$$H = \frac{C_o - C_e}{C_o} (\%) \quad (2)$$

với  $C_o$  (mg/L) và  $C_e$  (mg/L) lần lượt là nồng độ ban đầu và nồng độ ở trạng thái cân bằng;  $V$  (L) là thể tích dung dịch và  $m$  (g) là khối lượng chất hấp phụ.

### 3. Kết quả và thảo luận

#### 3.1. Ảnh hưởng của tỷ lệ khối lượng $\text{NaX}: \text{Fe}_3\text{O}_4$

Tỷ lệ khối lượng  $\text{NaX}: \text{Fe}_3\text{O}_4$  ảnh hưởng trực tiếp đến khả năng tạo thành composite, được đánh giá thông qua khả năng tải  $\text{Fe}_3\text{O}_4$  lên zeolite NaX. Hình 1 trình bày sự dao động của nhóm -OH được thể hiện ở các số sóng từ 3420,6-3448,0  $\text{cm}^{-1}$  [12]. Các dải hấp thụ ở số sóng từ 1640-1642,7  $\text{cm}^{-1}$  đặc trưng cho nhóm -OH trong liên kết Si-OH của composite [13]. Các số sóng từ 975,5-978,2  $\text{cm}^{-1}$  là sự dao động bất đối xứng của liên kết Al-O-Si đặc trưng của zeolite [14]. Ngoài ra, số sóng 665,3  $\text{cm}^{-1}$  và 746,1  $\text{cm}^{-1}$  thể hiện liên kết T-O-T (T = Si hoặc Al) đối xứng [15]. Các dao động trên chứng minh sự tồn tại của zeolite NaX trong composite. Dao động của liên kết Fe-O tại các số sóng 561,1  $\text{cm}^{-1}$  và 561,3  $\text{cm}^{-1}$  [5], cho thấy  $\text{Fe}_3\text{O}_4$  đã gắn thành công trên zeolite. Để xác định hàm lượng  $\text{Fe}_3\text{O}_4$  tải lên zeolite, kết quả EDX (bảng 1) cho thấy composite có hàm lượng sắt ở tỷ lệ 1:1 chiếm khoảng 8,89%, tỷ lệ 1,5:1 chiếm 8,60% và tỷ lệ 2:1 khoảng 2,23%. Hàm lượng sắt ở tỷ lệ 1:1 và 1,5:1 không có sự chênh lệch nhiều và tỷ lệ 2:1, lượng sắt chỉ chiếm khoảng 2,23%, thấp nhất trong khoảng khảo sát. Nguyên nhân có thể là do khi tăng lượng zeolite gây ra sự phân bố không đồng đều của các hạt  $\text{Fe}_3\text{O}_4$  trên bề mặt composite.



**Hình 1.** Kết quả FTIR của các mẫu vật liệu có tỷ lệ khối lượng  $\text{NaX}: \text{Fe}_3\text{O}_4 = 1:1-2:1$  g/g  
ở 8 giờ, TEOS 1,0 % v/v

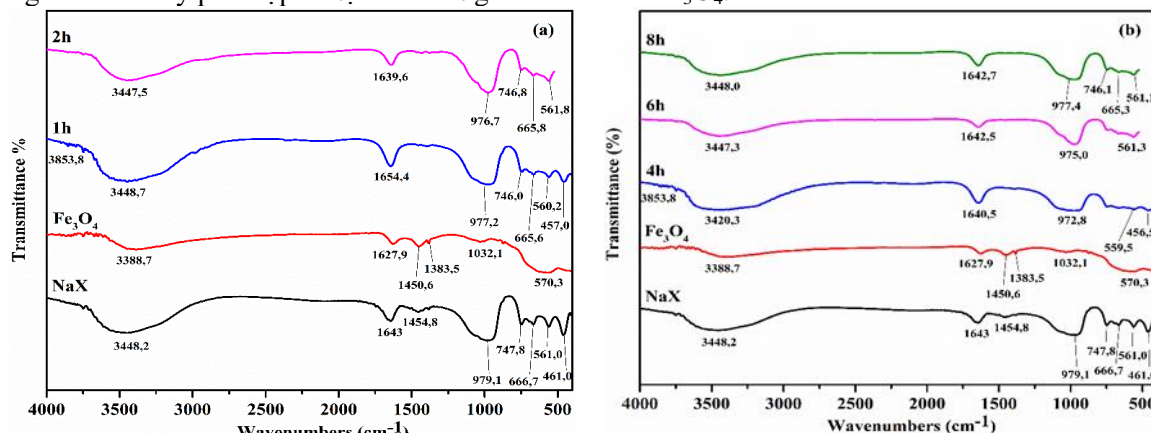
Các kết quả trên cho thấy các peak đặc trưng của NaX và  $\text{Fe}_3\text{O}_4$  được thể hiện rõ ràng nhất ở tỷ lệ 1,5:1, đặc biệt là các liên kết T-O-T đối xứng so với 2 tỷ lệ còn lại, chứng tỏ zeolite NaX và  $\text{Fe}_3\text{O}_4$  đã liên kết một cách đồng đều và thuận lợi. Kết quả EDX cho thấy thành phần các nguyên tố C, O, Na, Al, Si của cả 3 mẫu không có sự khác biệt lớn, nên cần quan tâm đến lượng Fe có thể tải lên zeolite. Vật liệu composite được tổng hợp với hàm lượng sắt phủ lên zeolite khoảng 3,50% [16], thấp hơn so với hàm lượng sắt có trong composite của khảo sát này, khẳng định sự gắn kết giữa hạt  $\text{Fe}_3\text{O}_4$  trên NaX trong nghiên cứu này là phù hợp. Mục tiêu của nghiên cứu là lựa chọn tỷ lệ phối trộn thích hợp để tạo thành composite, do đó tỷ lệ khối lượng 1,5:1 được lựa chọn.

**Bảng 1.** Thành phần hóa học của các mẫu vật liệu có tỷ lệ khối lượng  $\text{NaX}:\text{Fe}_3\text{O}_4$  khác nhau; điều kiện khuấy trộn: 8 giờ, TEOs = 1,0 %v/v

Tên mẫu	Thành phần nguyên tố (%)					
	C	O	Na	Al	Si	Fe
NaX : $\text{Fe}_3\text{O}_4$ = 1,0 : 1	4,64	59,18	8,85	8,35	10,10	8,89
NaX : $\text{Fe}_3\text{O}_4$ = 1,5 : 1	10,40	55,33	7,87	8,17	9,63	8,60
NaX : $\text{Fe}_3\text{O}_4$ = 2,0 : 1	9,79	58,10	9,53	9,47	10,88	2,23

### 3.2. Ảnh hưởng của thời gian khuấy

Thời gian tạo liên kết trong composite được thực hiện từ 1-8 giờ (hình 2). Có thể thấy rằng không có sự khác biệt nhiều về kết quả FTIR các mẫu có thời gian khuấy trộn khác nhau. Các số sóng đặc trưng của bộ khung zeolite được quan sát trong khoảng  $650$ - $760\text{ cm}^{-1}$ ,  $950$ - $1250\text{ cm}^{-1}$ ,  $1639,6$ - $1654,4\text{ cm}^{-1}$  và  $3000$ - $3600\text{ cm}^{-1}$  [8], [13] – [15]. Dao động của liên kết Fe-O tại khoảng số sóng  $570\text{ cm}^{-1}$  [5]. Mẫu 1 giờ và 4 giờ có các số sóng ở vị trí từ  $3853,8$ - $3747,7\text{ cm}^{-1}$  là dao động của nhóm chức -OH trong phân tử  $\text{H}_2\text{O}$  [15], [17]. Mẫu 2 giờ có sự hiện diện của các liên kết đặc trưng cho composite và tương đồng với mẫu 6 và 8 giờ. Vật liệu composite  $\text{NaX}:\text{Fe}_3\text{O}_4$  có thể được tổng hợp thành công trong thời gian khuấy từ 1-4 giờ, đồng thời được ứng dụng hấp phụ thuốc nhuộm hữu cơ, Pb, và Cu [15], [18] – [20]. Điều này chứng tỏ thời gian khuấy 2 giờ trong nghiên cứu này phù hợp để tạo liên kết giữa zeolite và  $\text{Fe}_3\text{O}_4$ .



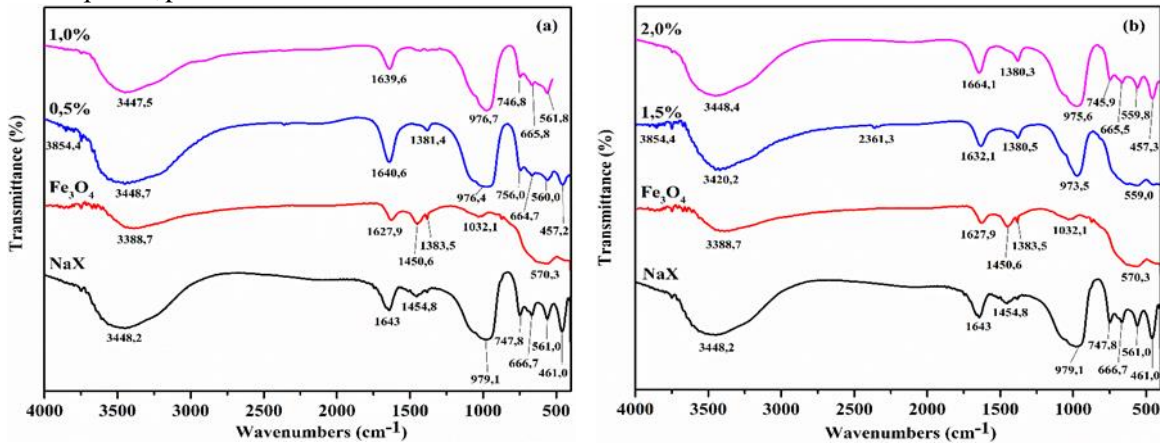
**Hình 2.** Kết quả FTIR của các mẫu vật liệu có tỷ lệ khối lượng  $\text{NaX}:\text{Fe}_3\text{O}_4$  = 1,5:1; thời gian khuấy 1-8 giờ, % thể tích TEOs 1,0

### 3.3. Ảnh hưởng của tỷ lệ phần trăm TEOs

TEOs đã được sử dụng rộng rãi trong tổng hợp các vật liệu composite  $\text{Fe}_3\text{O}_4/\text{SiO}_2$  và zeolite/ $\text{Fe}_3\text{O}_4$  [21], [22]. TEOs có thể dễ dàng được thuỷ phân và hình thành các lớp  $\text{SiO}_2$  bao quanh các hạt vật liệu [21], [22], đây là tiền đề cho sự kết hợp của  $\text{Fe}_3\text{O}_4$  và zeolite.

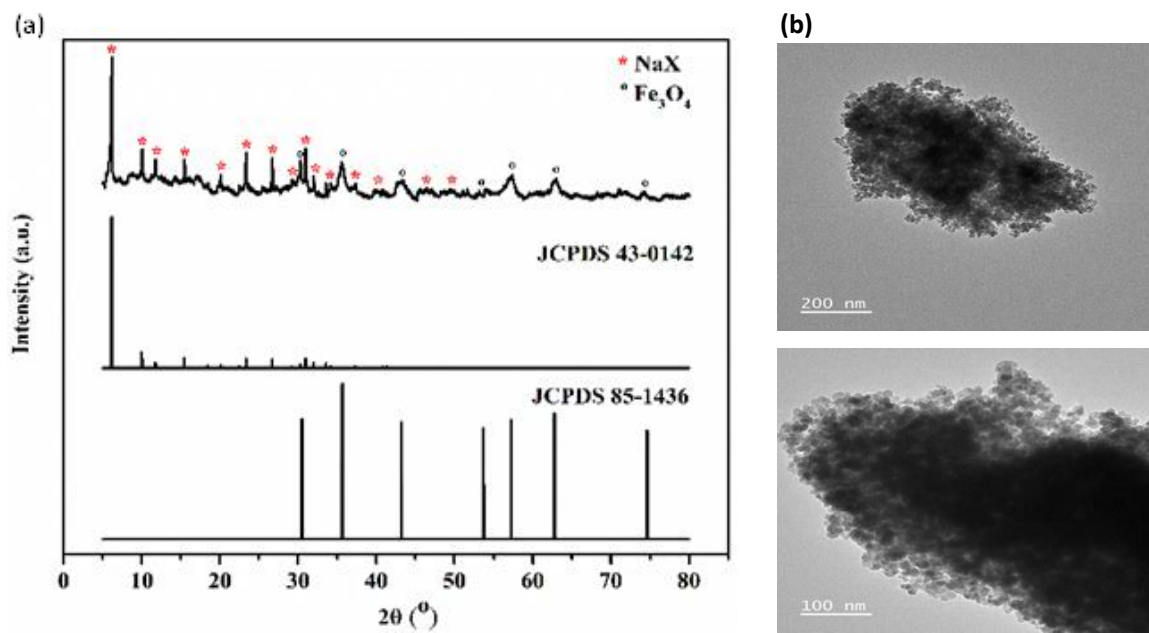
Ảnh hưởng của hàm lượng TEOs được khảo sát từ 0,5%-2,0% (hình 3). Các đỉnh từ  $559$ - $561,8\text{ cm}^{-1}$  là dao động uốn cong của liên kết Fe-O [5]. Ngoài ra, các dải hấp thụ ở số sóng  $650$ -

760 cm<sup>-1</sup>, 950-1000 cm<sup>-1</sup>, 1632,1-1644,1 cm<sup>-1</sup> và 3000-3600 cm<sup>-1</sup> thể hiện các nhóm chức đặc trưng trong bộ khung zeolite [5], [12], [14], [15]. Tuy nhiên, ở các tỷ lệ TEOs 0,5%, 1,5% và 2,0% có sự xuất hiện các số sóng 457,2 và 457,3 cm<sup>-1</sup> là dao động uốn cong của liên kết T-O [5], [14]. Đồng thời các số sóng 1380,3 cm<sup>-1</sup> và 1381,4 cm<sup>-1</sup> là đặc trưng cho dao động kéo căng bất đối xứng của liên kết Si-CH<sub>3</sub>. Ngoài ra, số sóng 3747,7-3854,4 cm<sup>-1</sup> là sự dao động của nhóm chức -OH có trong phân tử H<sub>2</sub>O. Ở tỷ lệ TEOs 1,5% và 2,0%, dao động của liên kết C-H ở vị trí số sóng 2361,3 cm<sup>-1</sup> cũng được tìm thấy. Cao và các cộng sự (2020) đã tổng hợp thành công vật liệu Fe<sub>3</sub>O<sub>4</sub>@zeolite NaA với phần trăm TEOs là 2% [21]. Trong nghiên cứu này, phần trăm TEOs phù hợp nhất là 1%.



**Hình 3.** Kết quả FTIR của các mẫu vật liệu có tỷ lệ khói lượng  $NaX:Fe_3O_4 = 1,5:1$ ; thời gian khuấy 2 giờ, % thể tích TEOs 0,5-2,0

### **3.4. Kết quả XRD, TEM và VSM của mẫu composite NaX/Fe<sub>3</sub>O<sub>4</sub>**



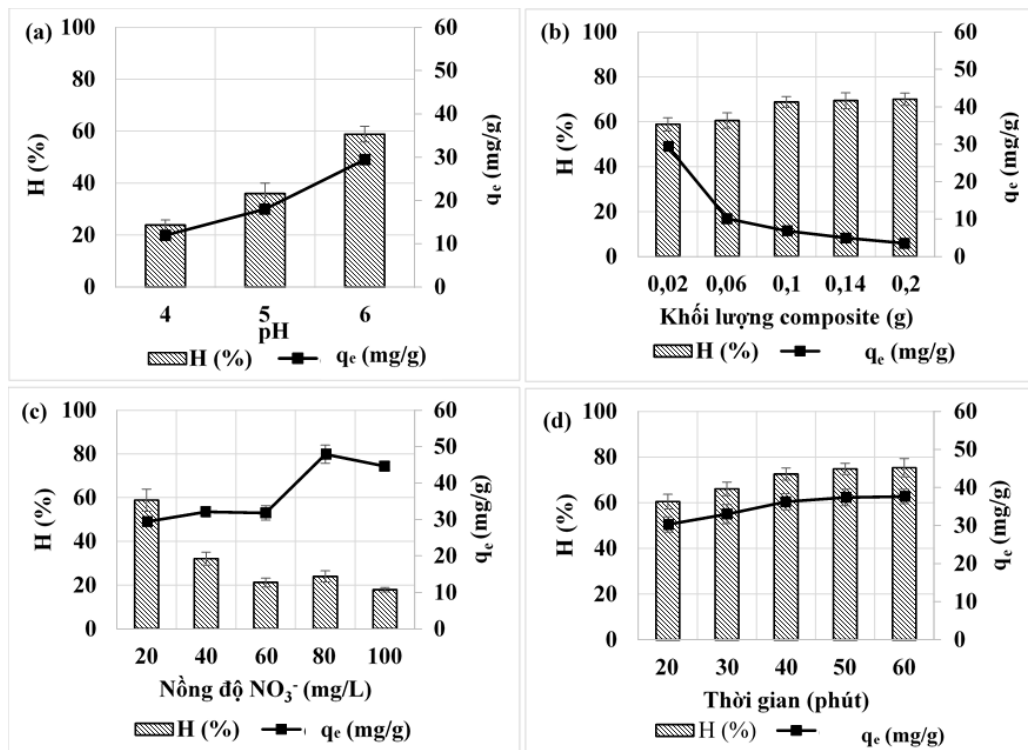
**Hình 4.** Giản đồ XRD (a) và ảnh TEM (b) của mẫu composite có tỷ lệ khối lượng  $NaX:Fe_3O_4 = 1,5:1$ ; thời gian khuấy 2 giờ, % thể tích TEOs 1,0

Vật liệu composite thu được sau quá trình khảo sát với các thông số xác định được tiến hành phân tích nhằm xác định chính xác các tính chất của vật liệu. Hình 4 cho thấy các đỉnh đặc trưng

của mẫu composite tổng hợp được ở góc  $2\theta = 6,08^\circ; 10,12^\circ; 11,26^\circ; 20,16^\circ; 23,28^\circ; 26,68^\circ; 30,94^\circ$  phù hợp với thẻ chuẩn NaX (JCPDS 43-0142); giá trị  $2\theta = 30,5^\circ; 35,4^\circ; 43,6^\circ; 53,6^\circ$  và  $62,7^\circ$  đặc trưng cho vật liệu  $\text{Fe}_3\text{O}_4$  tương ứng với các mặt phẳng (220), (311), (400), (422) và (440) (JCPDS 85-1436). Cường độ peak cao và rõ ràng chứng tỏ vật liệu composite kết tinh tốt, phù hợp với nghiên cứu của Kouli và các cộng sự [23]. Ảnh TEM ở các độ phóng đại khác nhau cho thấy composite có dạng hình cầu và kích thước khá đồng đều, nhưng độ phân tán chưa rõ ràng nên dẫn đến sự kết tụ. Độ từ hóa của composite là 2,135 emu/g và thấp hơn so với  $\text{Fe}_3\text{O}_4$  (68,56 emu/g), là do sự hiện diện của zeolite NaX đã che chấn từ tính của  $\text{Fe}_3\text{O}_4$ . Din và các cộng sự cũng đã tổng hợp nanocomposite zeolite/ $\text{Fe}_3\text{O}_4$  với độ từ hóa khoảng 30 emu/g [24]. Composite có diện tích bề mặt riêng là  $322,449 \text{ m}^2/\text{g}$  và kích thước lỗ rỗng là  $32,4 \text{ \AA}$ , thấp hơn so với kết quả nghiên cứu của Yuan và cộng sự [5] là  $571,5 \text{ m}^2/\text{g}$ , có thể là do sự phân bố không đồng đều của hạt  $\text{Fe}_3\text{O}_4$  trên bề mặt của zeolite.

### 3.5. Đánh giá khả năng hấp thụ nitrat

Trong nghiên cứu này, điểm đึง điện của composite là 6,46, có nghĩa là khi  $\text{pH} < 6,46$  thì bề mặt composite tích điện dương và ngược lại. Vì vậy, quá trình hấp thụ sẽ diễn ra thuận lợi ở khoảng  $\text{pH} < 6,46$ . Khả năng hấp thụ  $\text{NO}_3^-$  của composite phụ thuộc vào pH được khảo sát ở pH 4-6 (hình 5a). Hiệu suất hấp thụ tăng 35% (từ 23,85 đến 58,85%) và dung lượng hấp thụ tăng khoảng 2,46 lần (từ 11,925 đến 29,425 mg/g). Dung lượng hấp thụ của ion  $\text{NO}_3^-$  tăng khi pH tăng [25]. Ở môi trường acid, lượng  $\text{H}^+$  được thêm vào nên bề mặt chất hấp thụ tích điện dương, nhờ vào lực tương tác tĩnh điện, vật liệu có thể hấp thụ những ion có điện tích âm. Trong nghiên cứu này, pH 6 được lựa chọn là giá trị phù hợp cho các khảo sát tiếp theo [25]. Hiệu suất hấp thụ nitrat cũng đã đạt tối ưu tại pH 5 khi sử dụng composite của  $\text{Fe}_3\text{O}_4$ /bentonite và zeolite Clinoptilolite được chức năng hóa bề mặt là chất hấp thụ [25], [26].

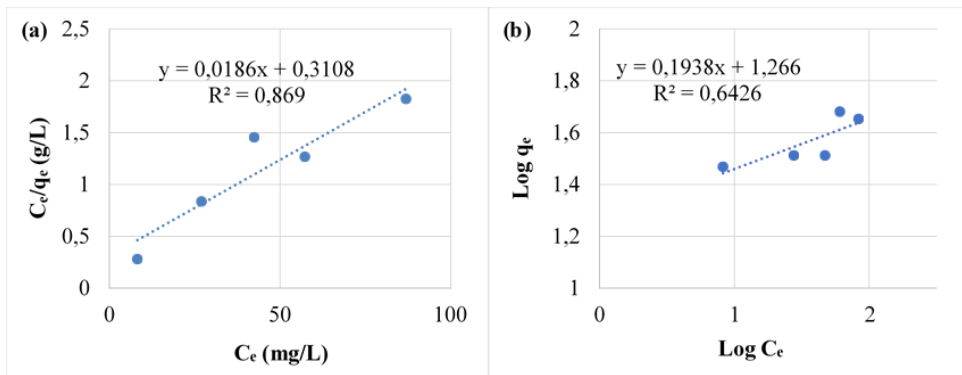


**Hình 5.** Ảnh hưởng của pH (a), khối lượng composite(b), nồng độ ion nitrat (c) và thời gian (d) đến khả năng hấp thụ  $\text{NO}_3^-$

Kết quả khảo sát ảnh hưởng của khối lượng chất hấp phụ (hình 5b) cho thấy khi tăng khối lượng từ 0,02-0,2 g, hiệu suất hấp phụ tăng 16,05% (từ 58,85% đến 70,1%) và dung lượng hấp phụ giảm 8,38 lần (từ 29,43 mg/g đến 3,51 mg/g). Khi khối lượng chất hấp phụ tăng từ 0,02-0,1 g, dung lượng hấp phụ giảm từ 29,43-6,88 mg/g. Hiệu suất hấp phụ dao động tăng từ 58,85-68,8% là do số tóm hấp phụ đã đủ. Hiệu suất tiếp tục tăng và đạt 70,1% ở khối lượng 0,2 g nhưng dung lượng hấp phụ chỉ đạt 3,51 mg/g. Điều này là do tăng khối lượng vật liệu thì số tóm hấp phụ được bổ sung dần đến hiệu suất hấp phụ tăng. Vì vậy, tăng khối lượng composite nhưng hàm lượng  $\text{NO}_3^-$  không đổi và hệ đã đạt trạng thái cân bằng nên dung lượng giảm. Dựa vào sự tương quan giữa hiệu suất và dung lượng hấp phụ, khối lượng chất hấp phụ là 0,02 g đã được lựa chọn.

Ảnh hưởng của nồng độ dung dịch  $\text{NO}_3^-$  đến quá trình hấp phụ (hình 5c) cho thấy khi tăng nồng độ từ 20-80 mg/L, hiệu suất hấp phụ giảm từ 58,85%-17,86% và dung lượng hấp phụ tăng. Nồng độ ion  $\text{NO}_3^-$  thấp sẽ dễ dàng hấp phụ lên vật liệu nên hiệu suất xử lý đạt hiệu quả cao. Khi nồng độ dung dịch cao, các ion  $\text{NO}_3^-$  trong dung dịch tương đối nhiều dẫn đến hiệu suất xử lý thấp. Ở nồng độ dung dịch cao, các ion  $\text{NO}_3^-$  tồn tại nhiều và dễ dàng hấp phụ lên bề mặt composite, dẫn đến dung lượng hấp phụ tăng dần. Tuy nhiên, khi nồng độ dung dịch quá cao (100 mg/L), các ion  $\text{NO}_3^-$  trong dung dịch có xu hướng cạnh tranh với các ion đã được hấp phụ lên bề mặt vật liệu, do đó nhận thấy hiệu suất và dung lượng hấp phụ giảm đồng thời. Xu hướng của nghiên cứu này hoàn toàn phù hợp với các nghiên cứu xử lý nitrate khác [25], [26]. Nồng độ nitrate 20 mg/L được lựa chọn cho khảo sát tiếp theo.

Khả năng hấp phụ  $\text{NO}_3^-$  của composite được khảo sát từ 20-60 phút (hình 5d). Dung lượng và hiệu suất hấp phụ tăng từ 20-40 phút. Ở 40 phút, hiệu suất và dung lượng hấp phụ đạt trạng thái cân bằng lần lượt tại 72,55% và 36,28 mg/g. Khi kéo dài thời gian hấp phụ (>40 phút), hiệu suất và dung lượng gần như không thay đổi, do đó thời gian hấp phụ cần thiết là 40 phút.



Hình 6. Đường đẳng nhiệt (a) Langmuir và (b) Freundlich

Hình 6 thể hiện đồ thị của các mô hình đẳng nhiệt hấp phụ dựa trên lý thuyết Langmuir và Freundlich. Từ kết quả tính toán, hệ số hồi quy của phương trình Langmuir  $R^2 = 0,8694$  lớn hơn hệ số hồi quy của phương trình Freundlich, do đó quá trình hấp phụ phù hợp với lý thuyết đẳng nhiệt Langmuir. Quá trình hấp phụ trong nghiên cứu này là hấp phụ đồng nhất, đơn lớp, độc lập, không có sự tương tác lẫn nhau, tức là quá trình hấp phụ và giải hấp phụ có tốc độ bằng nhau khi đạt trạng thái cân bằng [27], [28].

Bảng 2 trình bày khả năng hấp phụ nitrate của nghiên cứu này so với một số nghiên cứu khác. Nhìn chung khả năng hấp phụ của vật liệu zeolite NaX/ $\text{Fe}_3\text{O}_4$  khá tốt. Tuy vật liệu sử dụng nguồn tiên chất là phụ phẩm RHA nhưng hiệu suất hấp phụ (72,55%) và dung lượng hấp phụ cực đại (53,76 mg/g) khá cao so với các nghiên cứu đã công bố. Trong nghiên cứu này, thời gian hấp phụ khá ngắn, đồng thời khối lượng vật liệu sử dụng ít hơn so với một số nghiên cứu khác. Điều này giúp tiết kiệm nguyên liệu và có ý nghĩa về mặt kinh tế. Tuy nhiên, điều kiện tối ưu để đạt hiệu suất và dung lượng hấp phụ này chỉ ở nồng độ thấp (20 mg/L).

**Bảng 2.** So sánh khả năng hấp phụ nitrate của nghiên cứu này và các nghiên cứu khác

Vật liệu	Tiền chất	Điều kiện hấp phụ					H (%)	TLTK
		pH	Nồng độ (mg/L)	Khối lượng (g/L)	Thời gian (phút)	$q_{\max}$ (mg/g)		
Zeolite Clinoptilolite	Thương mại	5	50	16	180	21,66	37,01	[26]
Fe <sub>3</sub> O <sub>4</sub> /bentonite	Thương mại	5	30	12	90	6,44	79,00	[25]
Zeolite modified potassium permanganate	Thương mại	5	150	2	60	6,70	60,00	[29]
NaX/Fe <sub>3</sub> O <sub>4</sub>	Tro trâu	6	20	0,4	40	53,76	72,55	Nghiên cứu này

#### 4. Kết luận

Nghiên cứu đã tổng hợp thành công composite NaX/Fe<sub>3</sub>O<sub>4</sub> với tỷ lệ khối lượng zeolite NaX:Fe<sub>3</sub>O<sub>4</sub> = 1:1,5 (g/g) trong 2 giờ khuấy trộn, ở nhiệt độ phòng, sử dụng TEOs là chất đệm liên kết. Các hạt composite có dạng hình cầu và kích thước khá đồng đều, diện tích bề mặt riêng và kích thước lỗ rỗng lần lượt là 322,449 m<sup>2</sup>/g và 32,4 Å. Điều kiện tối ưu để composite có thể xử lý ion NO<sub>3</sub><sup>-</sup> ở pH 6, nồng độ 20 mg/L, khối lượng vật liệu 0,02 g, thời gian hấp phụ 40 phút, với dung lượng hấp phụ và hiệu suất hấp phụ lần lượt là 36,28 mg/g và 72,55%. Nghiên cứu tạo tiền đề cho các nghiên cứu xử lý nitrate trong tương lai.

#### Lời cảm ơn

Nghiên cứu này được hỗ trợ bởi Quỹ phát triển khoa học và công nghệ quốc gia (NAFOSTED) thông qua đề tài mã số 103.02-2020.64. Nhóm tác giả xin trân trọng cảm ơn.

#### TÀI LIỆU THAM KHẢO/ REFERENCES

- [1] P. Loganathan, S. Vigneswaran and J. Kandasamy, "Enhanced removal of nitrate from water using surface modification of adsorbents—a review," *Journal of Environmental Management*, vol. 131, pp. 363-374, 2013.
- [2] M. AL-Housni1, A.H. Hussein, D. Yeboah, R. A. Khaddar, B. Abdulhadi, A. A. Shubbar, and K.S. Hashim, "Electrochemical removal of nitrate from wastewater," *IOP Conference Series: Materials Science and Engineering*, vol. 888, no. 1, 2020, Art. no. 012037.
- [3] T. T. Nguyen, H. M. P. Nguyen, N. T. T. Ho, T. B. T. Pham, T. K. C. Nguyen, V. N. Le, T. T. Nguyen, and X. A. T. Trinh, "Synthesis of SiO<sub>2</sub> nanoparticles from rice husk ash by precipitation method," (in Vietnamese), *Can Tho University Journal of Science*, vol. 32, pp. 120-124, 2014.
- [4] V. H. Le, C. N. H. Thuc, and H. H. Thuc, "Synthesis of silica nanoparticles from Vietnamese rice husk by sol-gel method," *Nanoscale Research Letters*, vol. 8, no. 1, pp. 1-10, 2013.
- [5] L. Yuan, C. Song, and G. J. Yan, "Some research on the magnetic X zeolite composites," *Advanced Materials Research*, vol. 311, pp. 2040-2047, 2011.
- [6] A. Gaffer, A. A. Al Kahlawy, and D. Aman, "Magnetic zeolite-natural polymer composite for adsorption of chromium (VI)," *Egyptian Journal of Petroleum*, vol. 26, no. 4, pp. 995-999, 2017.
- [7] T. Pambudi, E. Wahyuni, and M. Mudasir, "Recoverable adsorbent of natural zeolite/Fe<sub>3</sub>O<sub>4</sub> for removal of Pb (II) in water," *Journal of Materials and Environmental Science*, vol. 11, no. 1, pp. 69-78, 2020.
- [8] H. Jiang, P. Chen, S. Luo, X. Tu, Q. Cao, and M. Shu, "Synthesis of novel nanocomposite Fe<sub>3</sub>O<sub>4</sub>/ZrO<sub>2</sub>/chitosan and its application for removal of nitrate and phosphate," *Applied Surface Science*, vol. 284, pp. 942-949, 2013.
- [9] S. Perveen, R. Nadeem, M. Iqbal, S. Bibi, R. Gill, R. Saeed, S. Noreen, K. Akhtar, T. M. Ansari, and N. Alfryyan, "Graphene oxide and Fe<sub>3</sub>O<sub>4</sub> composite synthesis, characterization and adsorption efficiency evaluation for NO<sub>3</sub><sup>-</sup> and PO<sub>4</sub><sup>3-</sup> ions in aqueous medium," *Journal of Molecular Liquids*, vol. 339, 2021, Art. no. 116746.

- [10] P. L. Tran-Nguyen, K. -P. Ly, L. H. V. Thanh, A. E. Angkawijaya, S. P. Santoso, M.-L. Tsai, and Y.-H. Ju, "Facile synthesis of zeolite NaX using rice husk ash without pretreatment," *Journal of the Taiwan Institute of Chemical Engineers*, vol. 123, pp. 338-345, 2021.
- [11] H. V. T. Luong, N. Y. Nguyen, N. T. C. Tien, N. P. L. Tran, L. N. H. Cao, and T. N. M. Ngo, "The synthesis of nano  $\text{Fe}_3\text{O}_4@\text{SiO}_2$  functionalized with chitosan," (in Vietnamese), *Can Tho University Journal of Science*, vol. 57, no. 2, pp. 10-20, 2021.
- [12] X. Mou, Y. Li, B. Zhang, L. Yao, X. Wei, D. S. Su, and W. Shen, "Crystal phase and morphology controlled synthesis of  $\text{Fe}_2\text{O}_3$  nanomaterials," *European Journal of Inorganic Chemistry*, vol. 2012, no. 16, pp. 2684-2690, 2012.
- [13] I. Karimzadeh, M. Aghazadeh, M. R. Ganjali, P. Norouzi, T. Doroudi, and P.H. Kolivand, "Saccharide-coated superparamagnetic  $\text{Fe}_3\text{O}_4$  nanoparticles (SPIONs) for biomedical applications: An efficient and scalable route for preparation and in situ surface coating through cathodic electrochemical deposition (CED)," *Materials Letters*, vol. 189, pp. 290-294, 2017.
- [14] S. Setiadji, C. Sundari, V. Aprilia, E. Sumiyanto, I. Noviantia, and A. Ivansyah, "Synthesis of zeolite NaX using elephant grass (*pennisetum purpureum*) as a silica source and its characterization," *Journal of Physics: Conference Series*, vol. 1402, no. 6, 2019, Art. no. 066016.
- [15] Z. Majid, A. A. AbdulRazak, and W. A. H. Noori, "Modification of zeolite by magnetic nanoparticles for organic dye removal," *Arabian Journal for Science Engineering*, vol. 44, no. 6, pp. 5457-5474, 2019.
- [16] N. Xu, H. Yan, X. Jiao, L. Jiang, R. Zhang, J. Wang, Z. Liu, Z. Liu, Y. Gu, and F. Gang, "Effect of  $\text{OH}^-$  concentration on  $\text{Fe}_3\text{O}_4$  nanoparticle morphologies supported by first principle calculation," *Journal of Crystal Growth*, vol. 547, 2020, Art. no. 125780.
- [17] P. Chutia, S. Kato, T. Kojima, and S. Satokawa, "Arsenic adsorption from aqueous solution on synthetic zeolites," *Journal of Hazardous Materials*, vol. 162, no. 1, pp. 440-447, 2009.
- [18] M. Khodadadi, A. Malekpour, and M. Ansaritabar, "Removal of Pb (II) and Cu (II) from aqueous solutions by NaA zeolite coated magnetic nanoparticles and optimization of method using experimental design," *Microporous Mesoporous Materials*, vol. 248, pp. 256-265, 2017.
- [19] R. Bosinceanu and N. Sulitanu, "Synthesis and characterization of  $\text{FeO(OH)/Fe}_3\text{O}_4$  nanoparticles encapsulated in zeolite matrix," *Journal of Optoelectronics and Advanced Materials*, vol. 10, no. 12, pp. 3482-3486, 2008.
- [20] J. Cao, Q. Sun, P. Wang, J. Shen, and X. Dai, "Synthesize and characterize of  $\text{Fe}_3\text{O}_4$ /zeolite 4A magnetic nanocomposite," *Journal of Dispersion Science Technology*, vol. 43, no. 4, pp. 517-525, 2022.
- [21] J. Cao, P. Wang, J. Shen, and Q. Sun, "Core-shell  $\text{Fe}_3\text{O}_4@\text{zeolite NaA}$  as an Adsorbent for  $\text{Cu}^{2+}$ ," *Materials Chemistry Physics*, vol. 13, no. 21, 2020, Art. no. 5047.
- [22] Munasir and A. Terraningtyas, "Synthesis and characterization of  $\text{Fe}_3\text{O}_4/\text{SiO}_2$  composite with in-situ method: TEOs as  $\text{SiO}_2$  NPs precursor," *Journal of Physics: Conference Series*, vol. 1171, no. 1, 2019, Art. no. 012050.
- [23] M.-E. Kouli, G. Banis, M. G. Savvidou, A. Ferraro, and E. Hristoforou, "A study on magnetic removal of hexavalent chromium from aqueous solutions using magnetite/zeolite-X composite particles as adsorbing material," *International Journal of Molecular Sciences*, vol. 21, no. 8, 2020, Art. no. 2707.
- [24] T. S. El-Din, A. A. Elzatahry, D. M. Aldhayyan, A. M. Al-Enizi, and S. S. Al-Deyab, "Synthesis and characterization of magnetite zeolite nano composite," *International Journal of Electrochemical Science*, vol. 6, pp. 6177-6183, 2011.
- [25] M. Khatamian, B. Divband, and R. Shahi, "Ultrasound assisted co-precipitation synthesis of  $\text{Fe}_3\text{O}_4$ /bentonite nanocomposite: performance for nitrate, BOD and COD water treatment," *Journal of Water Process Engineering*, vol. 31, 2019, Art. no. 100870.
- [26] A. Azari, A. H. Mahvi, S. Naseri, K. R. Rezaei, and M. Saberi, "Nitrate removal from aqueous solution by using modified clinoptilolite zeolite," *Archives of Hygiene Sciences*, vol. 3, no. 1, pp. 21-29, 2014.
- [27] K.Y. Foo and B. H. Hameed, "Insights into the modeling of adsorption isotherm systems," *Chemical Engineering Journal*, vol. 156, no. 1, pp. 2-10, 2010.
- [28] O. Hamdaoui and E. Naffrechoux, "Modeling of adsorption isotherms of phenol and chlorophenols onto granular activated carbon: Part I. Two-parameter models and equations allowing determination of thermodynamic parameters," *Journal of Hazardous Materials*, vol. 147, no. 1-2, pp. 381-394, 2007.
- [29] A. Mohsenibandpe, A. Alinejad, H. Bahrami, and M. Ghaderpoori, "Water solution polishing of nitrate using potassium permanganate modified zeolite: parametric experiments, kinetics and equilibrium analysis," *Global Nest Journal*, vol. 18, no. 3, pp. 546-58, 2016.



## Green and facile synthesis of $\text{Fe}_3\text{O}_4$ nanoparticles using the *Citrus aurantifolia* fruit juice associated with $\text{NaBH}_4$ and its adsorption of Cr(VI) in aqueous solution

Luong Huynh Vu Thanh<sup>1</sup>, Dao Lam Gia Hao<sup>1</sup>, Phan Thi Diem Trang<sup>1</sup>, Pham Minh Tien<sup>1</sup>, Tran Thi Bich Quyen<sup>1</sup>, Dang Huynh Giao<sup>1</sup>, Tran Nguyen Phuong Lan<sup>2,\*</sup>

<sup>1</sup> Department of Chemical Engineering, Can Tho University, Can Tho, VIETNAM.

<sup>2</sup> Department of Mechanical Engineering, Can Tho University, Can Tho, VIETNAM

\*Email: tnplan@ctu.edu.vn

### ARTICLE INFO

Received: 15/7/2021

Accepted: 18/8/2021

Published: 20/8/2021

### Keywords:

*Citrus aurantifolia* extract, Adsorption of Cr(VI), Facile synthesis, Green method, Magnetite nanoparticles

### ABSTRACT

This work presents a facile and green method using *Citrus aurantifolia* fruit extract for the biosynthesis of magnetite nanoparticles (MNs). The effects of some effective parameters such as temperature, reaction time and the ratio of *Citrus aurantifolia* extract to sodium borohydride on the synthesis were investigated. The synthesized  $\text{Fe}_3\text{O}_4$  nanoparticles were characterized by X-ray diffraction (XRD), Fourier-transform infrared spectroscopy (FTIR), field emission scanning electron microscopy (FE-SEM), energy-dispersive X-ray spectroscopy (EDX), transmission scanning electron microscopy (TEM), and vibrating sample magnetometer (VSM). The results showed that the MNs were well-monodisperse with the mean size of 50 nm and superparamagnetism value of 40.1 emu/g. Adsorption of Cr(VI) in aqueous solution at pH 2.5 using MNs reached 94.9% for removal of Cr(VI). The main contribution of this work was the synthesis of MNs in an economical and environmental friendly way, achieving size-controlled MNs at mild conditions. A possible mechanism of MNs synthesis was also presented.

### Introduction

Hexavalent chromium (Cr(VI)) is one of the most toxic cations which can cause damage to public health and the environment [1]. There are various methods for the treatment of heavy metals in contaminated water, including chemical precipitation, membrane filtration, ion exchange, electrodialysis and photocatalytic degradation [2-4]. Although these methods possess high efficiency but they are costly; thus are restricted in practical applications. Differently, adsorption method is widely used because it is simple and easy to scale up in industrial application. There are plenty of adsorbents that have been applied to remove heavy metal ions,

such as zeolite, activated carbon, agricultural by-products. Among these adsorbents, magnetite nanoparticles (MNs) have high potential in the removal of toxic contaminants, such as As(V) [5], methylene blue [6], and Hg(II) [7, 8].

Magnetite nanoparticles (MNs) are widely used in hazardous waste treatment due to its magnetic property, high surface area, chemical stability and low toxicity [9]. For example,  $\text{Fe}_3\text{O}_4$  nanoparticles were synthesized and functionalized with several functional groups to remediate aqueous solution contaminated by heavy metals [5, 10, 11]. Many reports on MNs synthesis methods are available [12]. However, several limitations and drawbacks were indicated in these

methods which usually required special equipment, expensive chemicals and extreme conditions such as inert gas environment, vacuum atmosphere, long reaction time and high reaction temperature. For instance, toxic, corrosive, and flammable chemical substances such as sodium borohydride ( $\text{NaBH}_4$ ) was used as a reducing agent to form zero-valence iron nanoparticles before  $\text{Fe}_3\text{O}_4$  nanoparticles were formed by oxidation [16].  $\text{Fe}_3\text{O}_4$  nanoparticles were synthesized at high temperature ( $120^\circ\text{C}$ ) with long reaction time (2 h) before being annealed at  $400^\circ\text{C}$  for 4 h [14]. Furthermore, in conventional methods the synthesized magnetite nanoparticles were oxidized easily due to the presence of oxidizing agents in solvent (e.g., dissolved oxygen or water); hence stability of these nanoparticles was reduced significantly. To solve this issue, MNs were normally functionalized on their surfaces by using graphene or  $\text{SiO}_2$  [15, 16]. Consequently, new synthesis processes using natural extracts have been developed in recent years. These green synthesis methods are not only less harmful to the environment but also are low-cost approach, conform to the trend of sustainable development [17, 18].

However, using extracts of natural products as the sole reducing agent usually resulted in nanoparticles containing impurities and with low crystallinity [19]. Therefore, combining natural extract and chemical reducing agent have been employed to synthesize magnetite nanoparticles, e.g., combining  $\alpha$ -D-glucose and  $\text{NH}_3$  solution [20]; green tea extract and  $\text{NaOH}$  [19]. In the past two decades, there has been an increased focus on green chemistry and cleaner processes. Utilization of natural extracts, environmentally benign solvents and renewable materials are some of the main emphases in a green process. In Vietnam, *Citrus aurantifolia* fruit is popular and inexpensive. Using *Citrus aurantifolia* fruit extract as a reducing agent is more environmental friendly and suitable for sustainable development. These green methods to synthesize MNs are expected to replace or reduce the utilization of sodium borohydride which was a commonly used reducing agent in MNs synthesis.

In this work, mixture of *Citrus aurantifolia* fruit extract and  $\text{NaBH}_4$  was used in producing MNs using to remove Cr(VI) in aqueous solution. The parameters of synthesis reaction investigated include the volume ration of *Citrus aurantifolia* extract to  $\text{NaBH}_4$ , reaction time and temperature. For the adsorption of Cr(VI), the effects of pH, reaction time, adsorbent dose and

concentration of Cr(VI) on removal efficiency were studied.

## Experimental

### Materials

The following reagents and chemicals were needed in ferromagnetic synthesis and adsorption experiments: potassium dichromate ( $\text{K}_2\text{Cr}_2\text{O}_7$ ), 1,5-diphenylcarbazide (DPC), sulfuric acid ( $\text{H}_2\text{SO}_4$ ), ferrous chloride tetrahydrate ( $\text{FeCl}_2 \cdot 4\text{H}_2\text{O}$ , 98%), sodium borohydride ( $\text{NaBH}_4$ , 98%), polyethylene glycol (PEG), Poly(vinylpyrrolidinone) (PVP), hexadecyltrimethylammonium bromide (CTAB, 98%), and ethanol (96%). They were purchased from Sigma Aldrich and directly used without further purification. Limes were collected from the local markets in Can Tho city, Vietnam. Freshly prepared double distilled water was used throughout the experiments.

### Green synthesis of iron nanoparticles

A flow chart depicting  $\text{Fe}_3\text{O}_4$  synthesis by using *Citrus aurantifolia* (lime) extract and  $\text{NaBH}_4$  is given Fig 1. The solution of lime extracts was firstly prepared. Limes were bought in the local market in Can Tho city and carefully washed with clean water. After squeezing the limes, the collected juice was vacuum filtered using Whatman No.1, 90 nm filter paper. Centrifugation was applied to remove suspended non-solubles. The extracts of lime were used immediately after centrifugation to minimize oxidation. Moreover, pH of each lime extract was determined and properly adjusted to keep it constant.

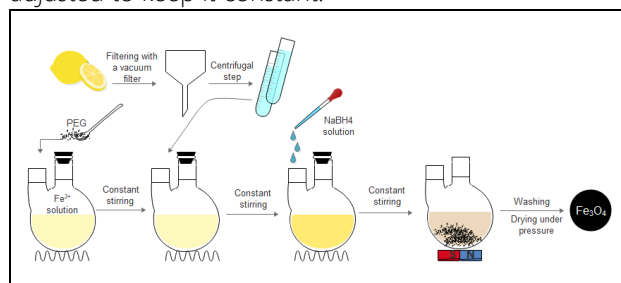


Figure 1: Flow chart of  $\text{Fe}_3\text{O}_4$  synthesis using *Citrus aurantifolia* fruit extract and sodium borohydride

In the synthesis of MNs, the precursor and the reducing agent were mixed in a beaker. A desired amount of  $\text{FeCl}_2 \cdot 4\text{H}_2\text{O}$  solution (0.2 M) and PEG surfactant solution (1% of the total volume of reactive solution) were added and stirred at room temperature for 60 min. Then 10 mL of the prepared lime extract

was added to the above mixture and stirred continuously for 15 min. When the color of the solution changed from light green to lemon yellow, 20 mL of 0.3 M aqueous NaBH<sub>4</sub> solution was added dropwise into the solution. The color of the solution changed to black, indicating the formation of Fe<sub>3</sub>O<sub>4</sub>. The precipitate of Fe<sub>3</sub>O<sub>4</sub> nanoparticles were collected by applying an external magnet, and the nanoparticles were washed with water and ethanol 96% until the neutral pH. The nanoparticles were dried at 60 °C until the mass was constant. Each reaction was repeated at least two times.

### *Characterization of magnetic nanoparticles*

Fe<sub>3</sub>O<sub>4</sub> nanoparticles obtained were characterized. X-ray diffraction (XRD) was performed on a D8 Advance instrument (Bruker), with an X-ray diffractometer using CuK radiation ( $\lambda=1.54056 \text{ \AA}$ ) scanned at 7.0000 degree/min, accelerating voltage of 40 kV and applied current of 30 mA. Fourier transform infrared (FTIR) spectra were obtained using a NICOLET 6700 (Thermo) spectrophotometer (frequency range from 4000 to 500 cm<sup>-1</sup>) with KBr pellet. Field emission scanning electron microscopy (FE-SEM) measurements and energy dispersive X-ray spectroscopy module ADAX (EDX) were taken with a Hitachi S-4800 scanning electron microscopy at accelerating voltage of 10 kV, working distance of 1.8 mm, low magnification mode. Transmission electron microscopy (TEM) were taken on a JEOL-1010 (Japan Electron Co.) and operated at operating voltage of 80 kV, magnification of 60.000x to 100.000x. UV-vis absorption spectra were recorded on a V730 Jasco spectrophotometer operated with single monochromator, silicon photodiode detectors, wide wavelength range of 190 to 1100 nm, fixed bandpass 1.0 nm, speed scanning speed at 8,000 nm/min. The magnetic properties of the sample were investigated using a vibrating sample magnetometer (VSM) on Microsense EZ9, USA operated with maximum field of 22.5 kOe, field resolution of 0.001 Oe, signal noise of 0.1  $\mu\text{emu}$  and at room temperature.

### *Adsorption experiments*

A stock of Cr(VI) solution (1000 mg/L) was firstly prepared by dissolving K<sub>2</sub>Cr<sub>2</sub>O<sub>7</sub> in deionized water. All working solutions at the desired concentration were prepared from this stock solution by diluting with deionized water. The initial pH was adjusted to between 2.0 and 6.0 with 0.1 M HCl or 0.1 M NaOH solution. The concentration of Cr(VI) and adsorbent

dose were varied from 20 – 150 mg/L and 0.01 – 0.2 mg, respectively. Contact time of adsorbent and the solution studied was from 15 to 75 min. Concentrations of Cr(VI) were determined by using a UV-Vis spectrophotometer at  $\lambda= 540 \text{ nm}$  after reacting with DPC. The removal capacity of MNs (H%) and the equilibrium adsorption amount ( $q_e$ , mg/g) were calculated using the following equations [21].

$$H(\%) = \frac{(C_0 - C_e)}{C_0} \times 100 \quad (1)$$

$$q_e = \frac{(C_0 - C_e) \times V}{m} \quad (2)$$

where  $C_0$  (mg/L) and  $C_e$  (mg/L) are the initial concentration and the equilibrium concentration of Cr(VI) solution, respectively. V (L) is the volume of the solution and m (g) is the adsorbent dose.

## Results and discussion

### *Synthesis mechanism*

Superparamagnetic Fe<sub>3</sub>O<sub>4</sub> nanoparticles could be obtained by the Fe<sup>2+</sup> controlled particle reduction using Citrus aurantifolia fruit extract which is rich in citric acid. A possible formation mechanism of magnetite nanoparticles by this green method is described in Fig 2. In the reaction system containing FeCl<sub>2</sub> and the Citrus aurantifolia extract, the C=O of carboxylic group in citric acid chelated with Fe<sup>2+</sup> to form complex COO<sup>-</sup>...Fe<sup>2+</sup>, while Fe<sup>2+</sup> was also partially oxidized by H<sup>+</sup> from citric acid to form COO<sup>-</sup>...Fe<sup>3+</sup> complex. Besides, NaBH<sub>4</sub> was dispersed in the aqueous solution (Reaction 1), which was the main source to produce OH<sup>-</sup> [22].

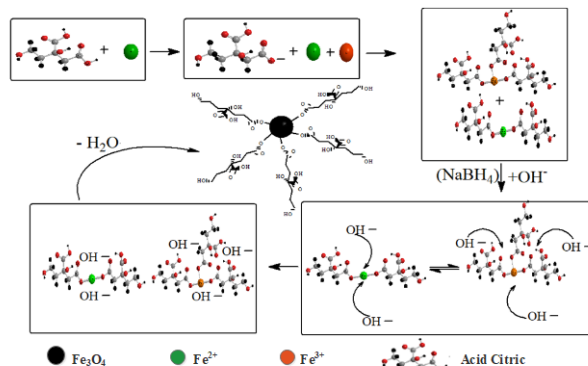


Figure 2: A schematic illustration of the formation mechanism of magnetite nanoparticles

Interaction between  $\text{COO}^- \dots \text{Fe}^{2+}$  bonding and  $\text{COO}^- \dots \text{Fe}^{3+}$  bonding by  $\text{OH}^-$  in solution formed  $\text{OH}^- \dots \text{Fe}^{2+}$  bonding and  $\text{OH}^- \dots \text{Fe}^{3+}$  bonding, resulting in the formation of both ferric hydroxide,  $\text{Fe(OH)}_3$  and ferrous hydroxide,  $\text{Fe(OH)}_2$ . Magnetite nanoparticle crystals were formed by dehydrating between ferric hydroxide and ferrous hydroxide [23]. The change of solution color from light green to greenness-yellow, as Citrus aurantifolia extract was added, possibly caused the appearance of the complex of both  $\text{Fe}^{2+}$  and  $\text{Fe}^{3+}$ . The  $\text{Fe}_3\text{O}_4$  magnetite nanoparticles could be drawn from the solution to the wall of the vial by applying an external magnetic field (Fig 3). MNs were obtained after washing with water and ethanol (96%), then dried in atmospheric pressure. These processes were summarized in Reaction 2:



Figure 3: Digital photograph of the  $\text{Fe}_3\text{O}_4$  nanoparticles synthesized in the presence of a magnet

#### *Evaluation of synthesized MNs properties*

##### *X-ray Diffraction (XRD)*

MNs prepared from different Citrus aurantifolia extract volume of 2, 5, 8, 10 and 15 mL are referred to as MNs-2, MNs-5, MNs-8, MNs-10 and MNs-15, respectively (Fig 4a). MNs-60m, MNs-90m and MNs-120m represents reaction time of 60 min, 90 min and 120 min, respectively (Fig 4b), while MNs-30t, MNs-55t and MNs-80t represents reaction temperature of 30 °C, 55 °C and 80 °C, respectively (Fig 4c). The effects of surfactants such as PEG, CTAB, PVP on MNs formation were also investigated.

In Fig 4, the peaks at  $2\theta = 30.1^\circ, 35.4^\circ, 43.1^\circ, 53.4^\circ, 56.9^\circ$  and  $62.5^\circ$  refer to (220), (311), (400), (422), (511)

and (440) lactic planes, respectively. This observation matched well with the inverse spinel structure of  $\text{Fe}_3\text{O}_4$  (JCPDS card no. 75–1610) according to the reflection peak positions and relative intensities, which confirmed that the nanoparticles synthesized in this study were the  $\text{Fe}_3\text{O}_4$  nanoparticles. This indicates that  $\text{Fe}_3\text{O}_4$  magnetite nanoparticles can be synthesized by green method. Meanwhile, the Bragg reflection peaks were all relatively broad because of the extremely small dimensions of the  $\text{Fe}_3\text{O}_4$  nanoparticles. The average size of the products could be obtained from Scherrer's equation (3). The calculated size was 43.3 nm.

$$d = \frac{k \cdot \lambda}{\beta \cdot \cos(\theta)} \quad (3)$$

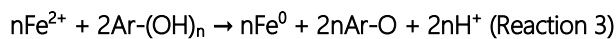
where d is particle diameter,  $\lambda$  is X-ray wave length,  $\beta$  is the peak width of half-maximum, and  $\theta$  is diffraction angle – Bragg angle, k is the Scherrer constant with the value from 0.9 to 1.

The XRD patterns of MNs synthesized using different extract volumes show stronger and clearer intensity as more Citrus aurantifolia extract was added, and the XRD patterns of MNs-10 and MNs-15 are very similar (Fig 4a). Base on the mechanism, the more  $\text{H}^+$  ions from citric acid were dissociated, the more  $\text{Fe}^{3+}$ -complexes oxidized from  $\text{Fe}^{2+}$  complexes were formed. These complexes were, then, dehydrated to form  $\text{Fe}_3\text{O}_4$  nanoparticles (Reaction 2). In Fig 4a, MNs-10 showed the highest crystallinity among all MNs. Hence, 10 mL extract was chosen for further experiments.

Figure 4b reveals that the capacity of CTAB and PVP affecting the crystallization of MNs. In aqueous solution, CTAB is a cationic surfactant and forms micelles. Lipophilic biomolecules like polyphenol and flavonoid (which are the major components in Citrus aurantifolia extract) tend to be incorporated into the micellar phase. This progress will prevent the formation of crystalline MNs. PVP is a non-ionic surfactant which can be dissolved in a wide range of organic solvents and water. Characterization of the oxidized nano-fluids revealed the formation of amorphous ferromagnetic ferric oxide phase in the presence of PVP. Thus, PVP is unable to protect the surface oxidation of MNs. In this work, PEG showed better protection MNs oxidation than PVP and CTAB. Besides, PEG is more environmental friendly so PEG is the best option for MNs synthesis.

In Figure 4c and Fig 4d, the appearance of nanoscale zero-valent iron (nZVI) is obvious due to the observed characteristic peaks at  $2\theta = 44.9^\circ$  corresponding to

nZIV ( $\alpha$ -Fe) [24, 25]. Actually, Figure 4c shows phase transition of  $\text{Fe}_3\text{O}_4$  to nZVI as reaction temperature was elevated from ambient temperature to higher temperature (55 °C and 80 °C). At 55 °C, a mixture of MNs and nZVI was observed, but the only nZVI was found at 80 °C. Thus, ambient temperature was selected in studying the effect of reaction time. In other studies which synthesized MNs mostly were conducted under high temperatures [26, 27], yet this study indicated that MNs can be synthesized at room temperature. As can be seen in Fig 4d, as reaction time was extended to 90 min and 120 min, nZVI was again appeared. The presence of nZVI can be attributed to aromatic groups derived from lime extract as shown in Reaction 3 [28], where Ar stands for aromatic group.



As temperature increases, the reaction rate of Reaction 3 increases, resulting in concomitant reduction reaction of  $\text{Fe}_3\text{O}_4$  nanoparticles to nZVI. The presence of aromatic groups in lime extract was confirmed by FTIR analysis (Figure 5) and EDS analysis (Figure 7).

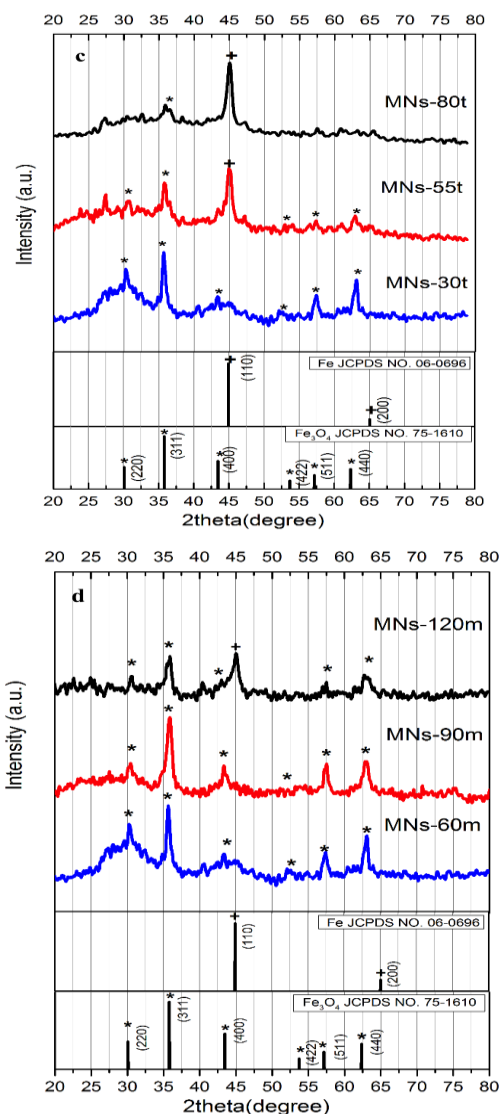
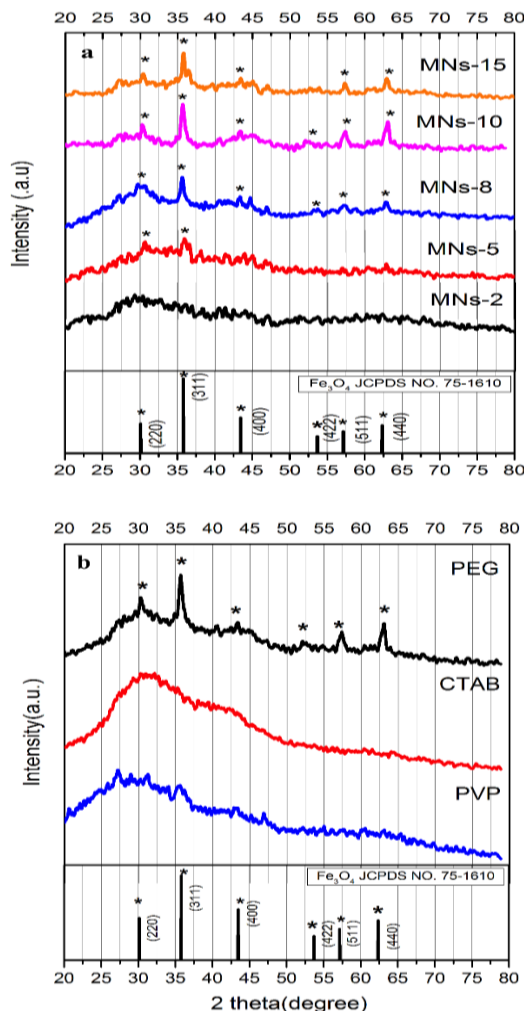


Figure 4: XRD of synthesized magnetite nanoparticles. Different volumes of lime extract (2 mL, 5 mL, 8 mL, 10 mL and 15 mL); (b) Different surfactants (PEG, CTAB, and PVP) (c) Different reaction temperatures (30 °C, 55 °C and 80 °C); (d) Different reaction times (60 min, 90 min, and 120 min)

#### Fourier Transform Infrared Spectroscopy (FT-IR)

The FTIR spectrum (Fig 5) reveals a broadband at 3381.8  $\text{cm}^{-1}$ , corresponding to traces of water on MNs surface, which was assigned to O-H stretching vibrations. The absorption peaks at 1622.5 and 1422.8  $\text{cm}^{-1}$ , respectively indicate the C=C and C-C aromatic ring stretching vibration of polyphenolic compounds which are abundant in many plant extracts [17, 29, 30]. The absorption peak at 1384.1  $\text{cm}^{-1}$  can be assigned to O-H bending vibration. The aromatic ring showed a characteristic signal at 873.6  $\text{cm}^{-1}$ . The intensive absorption band at 575.3  $\text{cm}^{-1}$  was assigned to Fe-O

bonding in  $\text{Fe}_3\text{O}_4$  nanoparticles [7, 28, 31]. Table 1 is a summary of the FTIR peaks and the corresponding mode assignments. Therefore, MNs formed by using *Citrus aurantifolia* extract was confirmed by FTIR analysis and this MNs adsorbed polyphenolic compounds onto its surface.

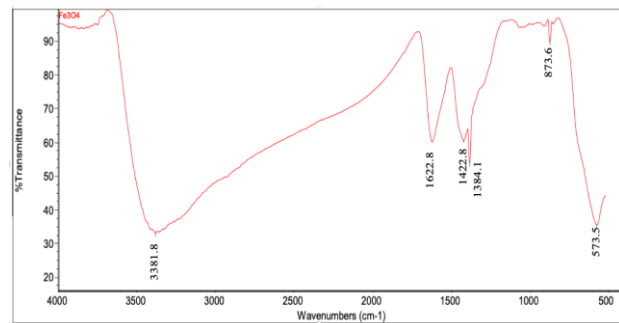


Figure 5: FTIR profile of green synthesized nanoparticles

Table 1: FTIR peaks and corresponding mode assignments for MNs from lime extract

No	Wavenumber ( $\text{cm}^{-1}$ )	Peak assignment
1	3381.8	O-H stretching
2	1622.5	C=C stretching (aromatic)
3	1422.8	C-C stretching (aromatic)
4	1384.1	O-H bending
5	873.6	Aromatic ring
6	573.3	Fe–O bonding

#### Transmission Electron Microscopy (TEM) and Field Emission Scanning Electron Microscope (FE-SEM)

Surface morphology of MNs synthesized using 10 mL lime extract and 40 mL 0.3 M  $\text{NaBH}_4$  solution was analyzed by FE-SEM. The FE-SEM image (Fig 6a) shows that as-synthesized MNs were roughly spherical with narrow size distribution. These spherical shapes were formed due to isotropic nucleation rate per unit area at the interface between MNs [32] which was the driving force for Ostwald ripening. The surface free energy was minimum by reduction of total surface area per volume, resulting in equivalent growth rate along with nucleation in different directions because sphere has the smallest surface area per unit volume of any shape [20]. Additionally, surface energy increased by the great number of charges distributed on the MNs

surface, so the spherical shape indicated that surface tension is higher than larger particles [17]

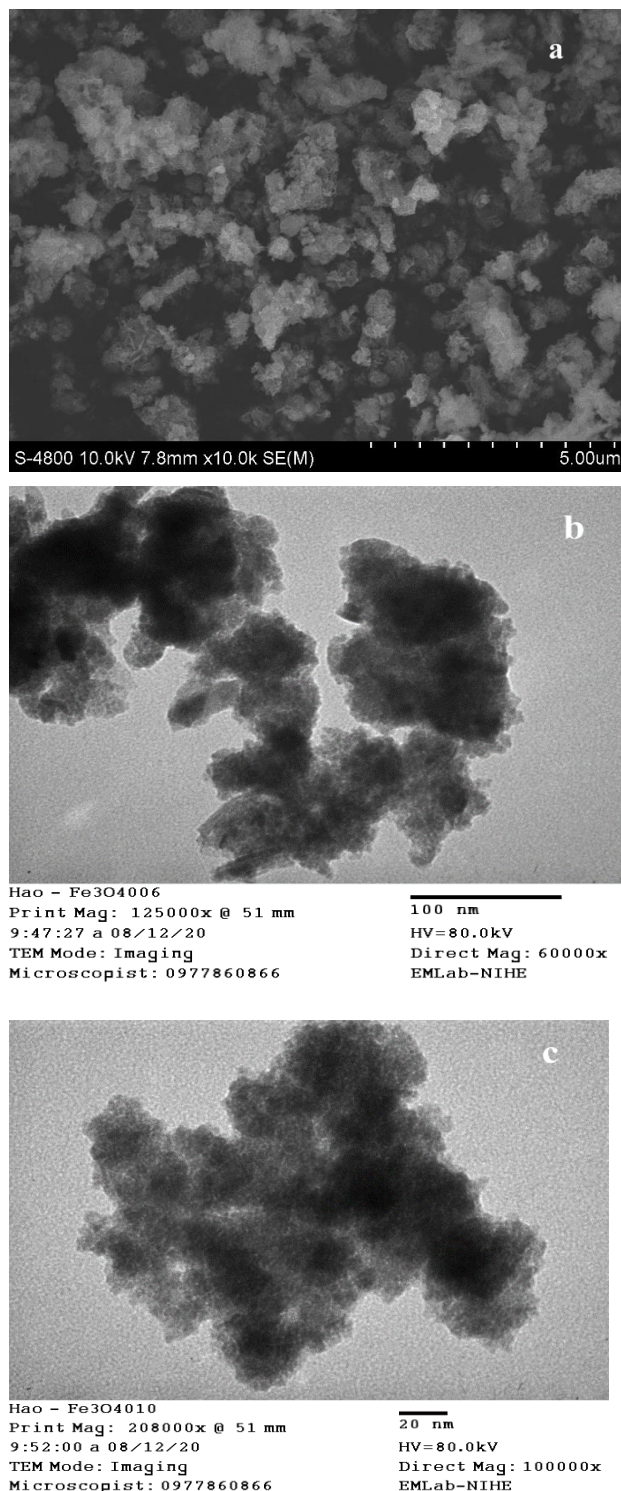


Figure 6: Images of synthesized MNs using lime extract and  $\text{NaBH}_4$  at optimal condition: 90 min, 30 °C and 10 mL of lime extract; a. FE-SEM, b. TEM (scale 100 nm), c. TEM (scale 20 nm)

The size and shape of MNs were determined by TEM analysis. As shown in Fig 6b and Fig 6c, TEM analysis

reveals that MNs both spherical and elliptical particles were formed. The TEM image shows that the sizes of the MNs were approximately between 40 and 60 nm. The good correlation of particle sizes obtained from the Scherrer's equation in XRD pattern and TEM supports the crystalline structure of  $\text{Fe}_3\text{O}_4$  nanoparticles.

#### *Energy Dispersive X – ray Fluorescence Spectrometry (EDX)*

The EDX spectrum of the powder MNs sample (Fig 7) shows the presence of Fe, O, and C elements with 53%, O 41.74%, and 4.96% composition, respectively (Table 2). The strong peaks of Fe observed at around 0.8, 6.2 and 6.9 keV, and the intensive peak of O at 0.6 keV were related to the binding energies of O. Therefore, these peaks correspond to the presence of  $\text{Fe}_3\text{O}_4$ . However, the impurity peak of C was found at 0.4 keV due to the presence of bio-organic components in Citrus aurantifolia extract, which were adsorbed on the surface of  $\text{Fe}_3\text{O}_4$  nanoparticles. This finding was also observed by FTIR spectra in Fig 5. FTIR peaks at 1622.5, 1422.8 and 873.6 show the appearance of aromatic rings. Due to significant amount of acid citric presented in the reaction, acid ascorbic likely remained in solution. Table 3 shows compounds predicted in MNs base on atomic ratios.

Table 2: Percentages of weight and atomic by EDX spectra

Element	%Weight	%Atomic
C K	4.96	10.38
O K	41.74	65.62
Fe K	53.30	24.00
Total	100.00	

Table 3: Compounds predicted in MNs base on atomic ratio

Compounds	%Fe	%O	%C
$\text{Fe}_3\text{O}_4$	24.00	32.00	-
$\text{C}_6\text{H}_8\text{O}_6$ (Ascorbic acid)	-	10.38	10.38
$\text{H}_2\text{O}$	-	23.24	-
Total	24.00	65.62	10.38

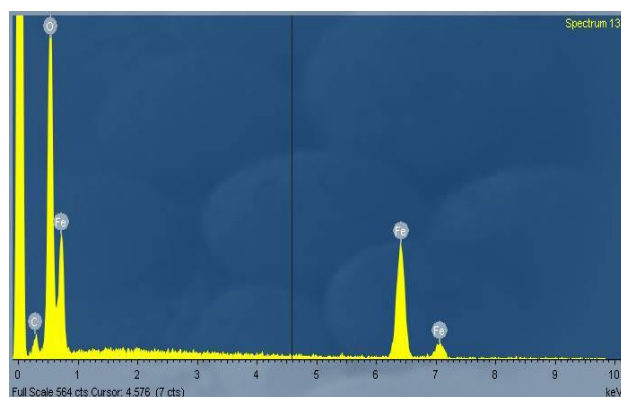


Figure 7: EDX spectra of  $\text{Fe}_3\text{O}_4$  synthesized at optimal reaction conditions

#### *Vibrating Sample Magnetometer (VSM)*

The magnetization curve measured for the as-synthesized  $\text{Fe}_3\text{O}_4$  nanoparticles in this study is presented in Fig 8. The measured specific saturation magnetization value of MNs was 40.1 emu/g. The low specific saturation magnetization in MNs with particle size of several tens of nanometers was feasibly due to the presence of non-magnetic layer on the particle surface, cation distribution and superparamagnetic relaxation. However, the negligible coercivity  $H_c$  of hysteresis loop (195.7 Oe) and consequently low remanence  $M_s$  (5 emu/g) indicate the superparamagnetic nature of the MNs.

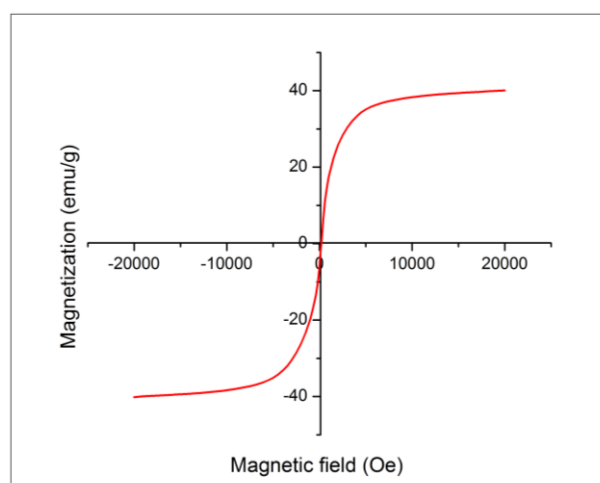


Figure 8: Magnetization curve of  $\text{Fe}_3\text{O}_4$  synthesized using lime extract and  $\text{NaBH}_4$

In this work, experiments were carried out at room temperature ( $30^\circ\text{C}$ ) compared to those reported under higher temperatures (Table 4). MNs in this study can be produced easily at room temperature. The synthesized nanoparticle sizes were bigger than those of other studies but with more uniform size achieved

by using surfactants. In conclusion, the process was evaluated as a simple method for MNs synthesis.

### Hexavalent Chromium adsorption

#### Effect of pH on Cr(VI) removal

The adsorption ability of MNs toward Cr(VI) in a pH range of 2.0 to 8.0 and the results are presented in

Figure. 9 and Table 5. As can be seen, pH of the solution significantly influenced the adsorption capacity. Both adsorption yield (~94.8%) and capacity (47.4 mg/g) were almost constant in the pH range of 2.0 to 3.0. The yield decreased to about 88% as pH was increased to 4.0 ~ 5.0. After that the yield dropped sharply as pH continued to increase, reaching 71.2% at pH 8. Similar trend was also observed for adsorption capacity.

Table 4: The comparison of the obtained results between this work and the published works

Reactants (Fe <sup>2+</sup> /Fe <sup>3+</sup> )	Reaction conditions			Temperature (°C)	Time (min)	Size of MNs (nm)	References
	Reducing agent	Using of plant extract					
Fe <sup>2+</sup> /Fe <sup>3+</sup>	NaOH	Ipomoea aquatica leaf extract		N.R.	N.R.	18	[10]
Fe <sup>2+</sup> /Fe <sup>3+</sup>	NH <sub>4</sub> OH and α-D-glucose	N.R.		60	30	0.25	[13]
Fe <sup>2+</sup>	NaOH	Camellia angustifolia leaves		60	120	5-10	[30]
Fe <sup>2+</sup>	NaBH <sub>4</sub>	Citrus aurantifolia extract		Room temperature	90*	40	This work

\*90 min include 60 min for homogenously stirring and 30 min for time reaction between Citrus aurantifolia extract and Fe<sup>2+</sup>, N.R.: not reported

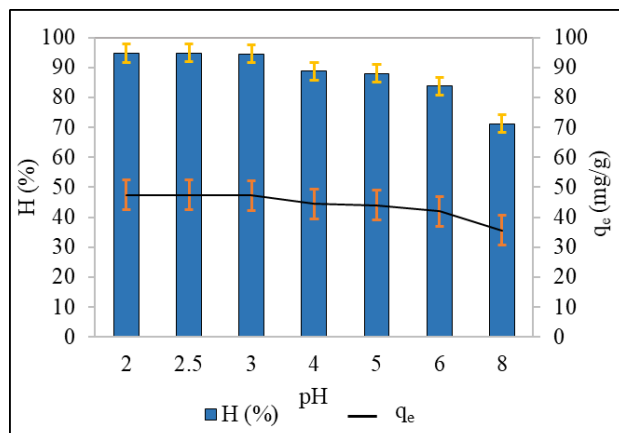


Figure 9: Effect of pH on Cr(VI) removal (Initial concentration: 100 mg/L, reaction temperature: 25 °C, adsorbent dose: 0.15 g, reaction time: 45 min)

From the above observation, MNs showed strong adsorption at pH less than 3.0. The main reason could be that Cr(VI) mainly existed in the form of Cr<sub>2</sub>O<sub>7</sub><sup>2-</sup> and HCrO<sub>4</sub><sup>-</sup> in a pH range of 2.0 to 6.0, and then the CrO<sub>4</sub><sup>2-</sup> species became dominant at higher pH [33]. In the meantime, Figure 10 shows that the surface of MNs is

strongly protonated in a solution containing more protons. The positive surface charge of MNs was high in pH range of 2.0 to 3.0 and then slightly reduced as pH rose. The significant reduction of positive surface charge of MNs occurred as pH was higher than 6.0. In other words, the adsorption capacity of MNs toward negatively charged species could be significantly decreased as pH of the solution increased higher than 6.0 due to a weak electrostatic interaction [21].

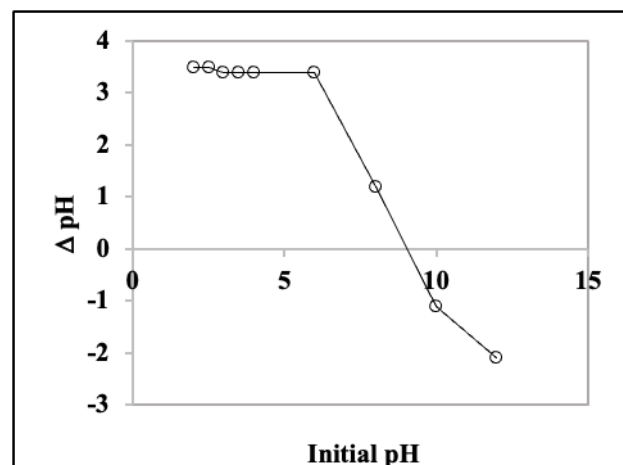


Figure 10: Surface charge of Fe<sub>3</sub>O<sub>4</sub> nanoparticles as a function of initial pH

Based on the above explanation, the main mechanism of the adsorption in this work was electrostatic interaction. In conclusion, the adsorption ability of MNs is highly depended on pH of the solution. The highest adsorption yield (94.6%) and capacity (47.5 mg/g) of MNs was obtained at pH 2.5. Therefore, all the further experiments were conducted at pH 2.5.

#### *Effect of contact time on Cr(VI) removal*

Contact time (reaction time) has significant effect on adsorption. In this work, reaction time varied from 15 to 75 min and the adsorption results are presented in Fig 11 and Table 6. The Cr(IV) removal raised from 83.7% to 94.7% as reaction time increased from 15 min to 45 min, the change in Cr(VI) removal was insignificant after 45 min. Similar trend was observed for the equilibrium adsorption amount  $q_e$ . Apparently 45 min was enough for Cr(VI) to diffuse from bulk solution to the surface of  $\text{Fe}_3\text{O}_4$  nanoparticles and be adsorbed [34].

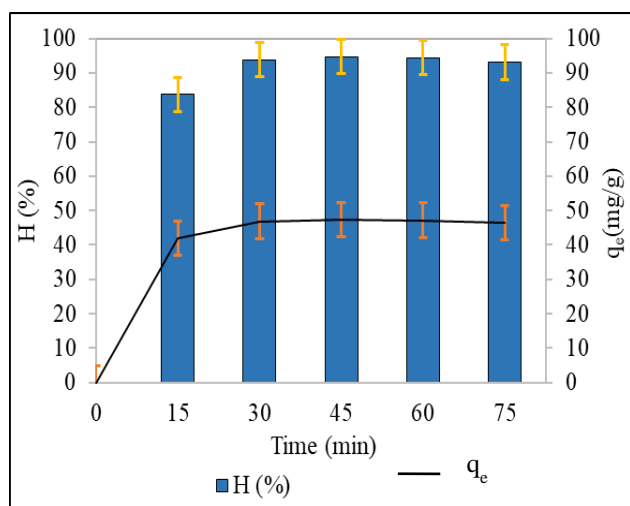


Figure 11: Effect of reaction time on Cr(VI) removal (Initial concentration: 100 mg/L, pH 2.5, reaction temperature: 25 °C, adsorbent dose: 0.15 g)

#### *Effect of $\text{Fe}_3\text{O}_4$ nanoparticles dose on Cr(VI) removal*

As seen from Figure 12, adsorbent dose strongly affect the removal yield of Cr(VI). As the adsorbent dose was increased from 0.01 to 0.1 g, the removal percentage of Cr(IV) increased from 16.8% to 94.8% (a 5.64-fold increase). Removal capacity remained constant after that. On the other hand, as dose was increased from 0.01 to 0.2 g, equilibrium adsorption amount decreased from 84.0 to 23.8 mg/g. This result shows at low dose the active adsorption sites were not enough, so multilayer adsorption occurred. On the other hand,

single layer adsorption was the predominant adsorption mechanism at high adsorbent dose. A dose of 0.1 g were applied for further experiments.

#### *Effect of Cr(VI) concentration*

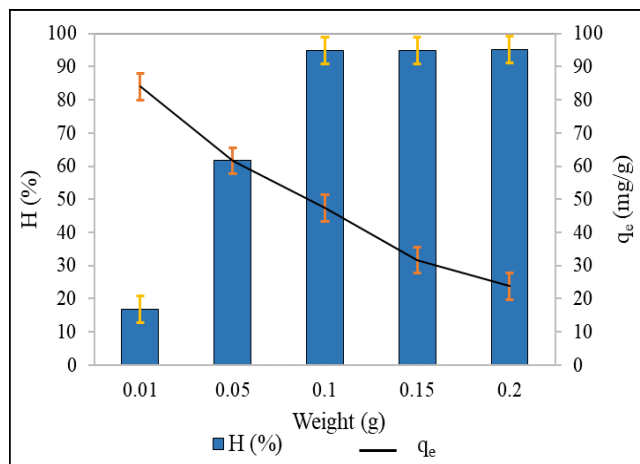


Figure 12: Effect of  $\text{Fe}_3\text{O}_4$  nanoparticles dose on Cr(VI) removal (Initial concentration: 100 mg/L, pH 2.5, reaction temperature: 25 °C, reaction time: 45 min)

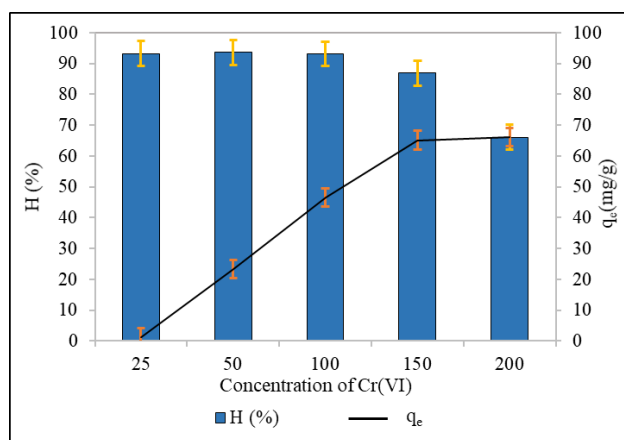


Figure 13: Effect of Cr(VI) concentration on the removal (pH 2.5, reaction temperature: 25 °C, reaction time: 45 min, adsorbent dose: 0.1g)

Figure 13 shows that removal capacity of Cr(IV) was constant (~ 93%) as Cr(VI) concentration was increased from 25 to 100 mg/L, it then decreased to 47.1% as Cr(VI) concentration was increased to 200 mg/L. For equilibrium adsorption amount ( $q_e$ ), it increased from 11.7 mg/g at a Cr(VI) concentration of 25 mg/L to 65.2 mg/g at a Cr(VI) concentration of 150 mg/L, then slightly increased to 66.1 mg/g as Cr(VI) concentration was at 200 mg/L (Table 8). The results indicate that at low Cr(VI) concentration (<100 mg/L), there were enough active sites for Cr(VI) adsorption, hence almost constant adsorption yield was observed. However, at Cr(VI) concentration >100 mg/L, the active sites of MNs

were not enough to adsorb more Cr(VI) due to saturation. Consequently, the optimum concentration for Cr(VI) adsorption is 150 mg/L.

### Adsorption isotherms

To gain insight of adsorption mechanism of Cr(VI) onto MNs, data were fitted with Langmuir, Freundlich, and Dubinin-Radushkevich models. As shown in Table 9, Langmuir isotherm model gave the best fit in term of its highest value of  $R^2$ . This result suggests that the monolayer adsorption of Cr(VI) occurred. The maximum adsorption capacity of Cr(VI) onto MNs from the fitted Langmuir model is 72.46 mg/g (Table 9). In Table 9, in the Freundlich model a n value of 2.18 confirms the removal Cr(VI) ability of MNs is a good fit. Besides, the dimensionless parameter (RL) also evaluates the favorability of adsorption of Cr(VI) onto MNs following the Langmuir isotherm model. The value of RL for Cr(VI) adsorption onto MNs were between 0 and 1, indicating that the process is favorable. More detail can be obtained from the Dubinin-Radushkevich isotherm model. The free energy in Cr(VI) adsorption by MNs surface was 0.87 kJ/mol. A value of E under 8 kJ/mol indicates physical adsorption [35-36].

Table 9: Fitted isotherm models for Cr(VI) adsorption onto  $\text{Fe}_3\text{O}_4$

Isotherms	Unit	Information
<i>Freundlich model:</i> <i>Fitted model</i>		$\log q_e = 1.164 + 0.4568 \ln C_e$
$K_F$	-	13.07
$n$	$(\text{mg/g})^{1/n}$	2.18
$R^2$	-	0.806
<i>Langmuir model:</i> <i>Fitted model</i>		$C_e/q_e = 0.0786 + 0.0138C_e$
$K_L$	L/mg	0.176
$Q_{\max}$	mg/g	72.46
$R^2$	-	0.9911
$RL = 1/(1+K_L C_i)$		From 0.05 to 0.76
<i>D-R: Fitted model</i>		$\ln q_e = 2.6043 - 0.6557\epsilon^2$
$E$	kJ/mol	0.87
$K_{DR}$	$\text{mol}^2/\text{kJ}^2$	0.6557
$R^2$	-	0.6822

### Conclusions

Magnetite nanoparticles ( $\text{Fe}_3\text{O}_4$ ) were synthesized by *Citrus aurantifolia* extract combined with  $\text{NaBH}_4$  in this study. Although the phenolic and acid citric level in *Citrus aurantifolia* extract were not stable, the combination of plant extract and  $\text{NaBH}_4$  was able to synthesize MNs. The green method in the present work has advantageous in the synthesis of magnetite nanoparticles such as it is economical, environmentally friendly, non-toxic. The spherical and elliptical magnetite nanoparticles in size of 40-60 nm can be obtained in one-pot reaction at mild conditions, namely 10 mL extract combined with 20 mL  $\text{NaBH}_4$  0.3 M with the present of PEG at room temperature for 60 min. The as-synthesis magnetite nanoparticles ( $\text{Fe}_3\text{O}_4$ ) were capable of removal Cr(VI) in solution with a  $q_{\max}$  of 71.94 mg/g, suggesting potential application in environmental treatment.

### Acknowledgments

This research is funded by Vietnam National Foundation for Science and Technology Development (NAFOSTED) under grant number 103.02-2020.64.

### References

- Z. Rahman, V.P. Singh, Environ. Monit. Assess. 191 (2019) 419-439.  
<https://doi.org/10.1007/s10661-019-7528-7>
- S. Mahdavi, S.R. Allahkaram, J. Alloy. Compd. 635 (2015) 150-157.  
<https://doi.org/10.1016/j.jallcom.2015.02.119>
- X.F. Lei, X.X. Xue, H. Yang, C. Chen, X. Li, J.X. Pei, M.C. Niu, Y.T. Yang, X.Y. Gao, J. Alloy. Compd. 646 (2015) 541-549.  
<https://doi.org/10.1016/j.jallcom.2015.04.233>
- P. Yuan, D. Liu, M. Fan, D. Yang, R. Zhu, F. Ge, J. Zhu, H. He, J. Hazard. Mater. 173 (2010) 614-621.  
<https://doi.org/10.1016/j.jhazmat.2009.08.129>
- S. Aredes, B. Klein, M. Pawlik, J. Clean. Prod., 60 (2013) 71-76.  
<https://doi.org/10.1016/j.jclepro.2012.10.035>
- J. Saini, V.K. Garg, R.K. Gupta, J. Mol. Liq. 250 (2018) 413-422.  
<https://doi.org/10.1016/j.molliq.2017.11.180>
- S.N. Wang, F.D. Zhang, A.M. Huang, Q. Zhou, De Gruyter 70 (2016) 503-510.  
<https://doi.org/10.1515/hf-2015-0125>

8. Z. Wang, J. Xu, Y. Hu, H. Zhao, J. Zhou, Y. Liu, Z. Lou, X. Xu, *J. Taiwan Inst. Chem. E.* 60 (2016) 394-402.  
<https://doi.org/10.1016/j.jtice.2015.10.041>
9. H. Zhang, G. Zhu, *Appl. Surf. Sci.* 258 (2012) 4952-4959.  
<https://doi.org/10.1016/j.apsusc.2012.01.127>
10. J. Wang, S. Zheng, Y. Shao, J. Liu, Z. Xu , D. Zhu, J. Colloid. Interf. Sic. 349 (2010) 293-299.  
<https://doi.org/10.1016/j.jcis.2010.05.010>
11. C.M. Babu, Babu, B. Palasinamy, B. Sundaravel, M. Palachinamay, V. Murugesa, *J. Nanosci. Nanotechno.* 13 (2013) 2517-2527.  
<https://doi.org/10.1166/jnn.2013.7376>
12. S.H. Chaki, T.J. Malek, M.D. Chaudhary, J.P. Tailor, M.P. Deshpande, *Adv. Nat. Sci: Nanosci. Nanotechnol.* 6 (2015) 035009-035014.  
<http://dx.doi.org/10.1088/2043-6262/6/3/035009>
13. A. Ruiz-Baltazar, R. Esparza, G. Rosas, R. Pérez, *J. Nanomater.* 2015 (2015) 1-8.  
<https://doi.org/10.1155/2015/240948>
14. S.A. Jayanthi, D.M.G.T. Nathan, J. Jayashainy, P. Sagayaraj, *Mater. Chem. Phys.* 162 (2015) 316-325.  
<https://doi.org/10.1016/j.matchemphys.2015.05.073>
15. C. Meng, W. Zhikun, L. Qiang, L. Chunling, S. Shuangqing, H. Songqing, *J. Hazard. Mater.* 341 (2018) 198-206.  
<https://doi.org/10.1016/j.jhazmat.2017.07.062>
16. T.T. Tung, J. Feller, T. Kim, H. Kim, W.S. Yang, K.S. Suh, *J. Polym. Sic. A1.* 50 (2012) 927-935.  
<https://doi.org/10.1002/pola.25847>
17. M.M. Zaman, D.M.A.S Karal, D.M.N.I. Khan, A.R.M. Tareq, S. Ahammed, D.M. Akter, A. Hossain, A.K.M.A. Ullah, *ChemistrySelect.* 4 (2019) 7824-7831.  
<https://doi.org/10.1002/slct.201901594>
18. S. Ahmadian-Fard-Fini, M. Salavati-Niasari, D. Ghanbari, *SAA.* 2203 (2018) 481-493.  
<https://doi.org/10.1016/j.saa.2018.06.021>
19. T. Shahwan, S.A. Sirriah, M. Nairat, E. Boyaci, A.E. Eroğlu, T.B. Scott, K.R. Hallam, *Chem. Eng. J.* 172 (2011) 258-266.  
<https://doi.org/10.1016/j.cej.2011.05.103>
20. W. Lu, Y. Shen, A. Xie, W. Zhang, *J. Magn. Magn. Mater.* 322 (2010) 1828-1833.  
<https://doi.org/10.1016/j.jmmm.2009.12.035>
21. S. Li, L. Liu, Y. Yu, G. Wang, H. Zhang, A. Chen, *J. Alloy. Compd.* 698 (2017) 20-26.  
<https://doi.org/10.1016/j.jallcom.2016.12.163>
22. S. Chandrasekhar, A. Shrinidhi, *Synthetic Commun.*, 44 (2014) 2051-2056.  
<https://doi.org/10.1080/00397911.2014.888751>
23. A.M. Awwad, N.M. Salem, *Nanosci. Nanotechnol.* 2 (2012) 208-213.  
<https://doi.org/10.5923/j.nn.20120206.09>
24. T. Wang, J. Su, X. Jin, Z. Chen, M. Megharaj, R. Naidu, *J. Hazard. Mater.* 262 (2013) 819-825.  
<https://doi.org/10.1016/j.jhazmat.2013.09.028>
25. Y. Kuang, Q. Wang, Z. Chen, M. Megharaj, R. Naidu, *J. Coll. Interf. Sci.* 410 (2013) 67-73.  
<https://doi.org/10.1016/j.jcis.2013.08.020>
26. M. Krajewski, K. Brzozka, W.S. Lin, H.M. Lin, M. Tokarczyk, J. Borysiuk, G. Kowalska, D. Wasik, *Phys. Chem. Chem. Phys.* 18(2016) 3900-3909.  
<https://doi.org/10.1039/C5CP07569F>
27. L.Y. Zhang, T. Chu, *Bulletin of the Korean Chemical Society,* 34 (2013) 1457-1461.  
<https://doi.org/10.5012/bkcs.2013.34.5.1457>
28. T. Wang, J. Lin, Z. Chen, M. Megharaj, R. Naidu, J. *Clean. Prod.* 83 (2014) 413-419.  
<https://doi.org/10.1016/j.jclepro.2014.07.006>
29. M. Mahdavi, F. Namvar, M.B. Ahmad, R. Mohamad, *Molecules* 18 (2013) 5954-5964.  
<https://doi.org/10.3390/molecules18055954>
30. A.S.Y. Ting, J.E. Chin, *Water Air Soil Pollut.* 231 (2020) 278.  
<https://doi.org/10.1007/s11270-020-04658-z>
31. R.K. Das, B.B. Borthakur, U. Bora, *Mater. Lett.* (2010) 64 1445-1447.  
<https://doi.org/10.1016/j.matlet.2010.03.051>
32. D.K. Kim, M. Mikhaylova, Y. Zhang, M. Muhammed, *Chem. Mater.* 15 (2003) 1617-1627.  
<https://doi.org/10.1021/cm021349j>
33. C.V. Gherasim, G. Bourceanu, R.I. Olariu, C. Arsene, *J. Hazard. Mater.* 197 (2011) 244-253.  
<https://doi.org/10.1016/j.jhazmat.2011.09.082>
34. F. Ghorbani, S. Kamari, *Environ. Technol. Innov.* 14 (2019) 100333.  
<https://doi.org/10.1016/j.eti.2019.100333>
35. G. Moussavi, B. Barikbin, *Chem. Eng. J.* 162 (2010) 893-900.  
<https://doi.org/10.1016/j.cej.2010.06.032>
36. Q. Hu, Z. Zhang, *J. Mol. Liq.* 277 (2019) 646-648.  
<https://doi.org/10.1016/j.molliq.2019.01.005>



## REMOVAL OF ION Cu<sup>2+</sup> AND Pb<sup>2+</sup> USING ZEOLITE NAP1 WITH THE SILICA SOURCE UTILIZED FROM RICE HUSK ASH

Tran Nguyen Phuong Lan<sup>1,\*</sup>, Nguyen Thanh Ty<sup>1</sup>, Ly Kim Phung<sup>1</sup>, Hong Nam Nguyen<sup>2</sup>, Cao Thi Xuan Vy<sup>1</sup>, Huynh Quoc Khanh<sup>1</sup>, Tran Thi Bich Quyen<sup>1</sup>

<sup>1</sup>College of Engineering, Can Tho University, Can Tho, VIETNAM

<sup>2</sup>University of Science and Technology of Ha Noi, Vietnam Academy of Science and Technology, Ha Noi, VIETNAM

\*Email: [tnplan@ctu.edu.vn](mailto:tnplan@ctu.edu.vn)

### ARTICLE INFO

Received:

Accepted:

**Keywords:**

zeolite NaP1, rice husk ash, without aging, energy-saving, adsorption

### ABSTRACT

Zeolite, as chemical essence, is an aluminosilicate mineral synthesized by rich-silica source, such as rice husk ash (RHA). This study focuses on the synthesis of zeolite NaP1 under a facial hydrothermal method using the silica source utilized from RHA without any -pretreatment steps. The **synthesis conditions** of the synthesis are achieved at the molar ratio of 8 Na<sub>2</sub>O: 6 SiO<sub>2</sub>: 1 Al<sub>2</sub>O<sub>3</sub>, at 100°C, 8 hours, and without aging. Scanning electron microscope (SEM), dynamic light scattering (DLS), Brunauer-Emmett-Teller (BET), and X-ray diffraction (XRD) are used to determine the physical and chemical properties of the product. Adsorption results show that the optimal conditions are the initial concentration of 75 mg/L, adsorbent dose of 0.5 g/L, and contact time of 30 mins. Ion Cu<sup>2+</sup> removal can reach a capacity and efficiency of 57.4 mg/g and 95.7%, respectively while Pb<sup>2+</sup> adsorption can achieve a capacity and efficiency of 59.2 mg/g and 98.6%, respectively. Besides, Langmuir, Freundlich, Dubinin – Radushkevich (D-R), Temkin, Sips, and Redlich - Peterson models are also applied to describe the adsorption process.

### Introduction

Nowadays, the rapid development of industries causing the pollution of heavy metals in the aquatic environment is more and more critical. The heavy metals such as copper, lead, arsenic, cobalt, nickel etc. used in batteries, metal plating and mining, can be of dangerous effects on plants, animals and humans [1]. There are many methods to remove heavy metals such as coagulation, membrane filtration, oxidation, biological and adsorption. Among them, the adsorption method shows the effective removal of heavy metals [2]. The choice of adsorbent is important for the adsorption process to achieve good efficiency. Porous materials belonging to the zeolite families are

well-known as potential and effective adsorbents for the removal of heavy metals [2]. Zeolite is a family of inorganic mineral materials with aluminosilicates as the main component. Its structure consists of an anionic network with porous pores; thus, zeolite can be applied for many fields, especially environmental applications [1].

The amount of RHA discharged in Mekong Delta, Vietnam is often millions of tons annually [3]. This by-product can cause the pollution owing to its small sizes, lightweight and unreasonable utilization [3]. The main component of RHA is silicon oxide (~90%), which is utilized to synthesize valuable materials [4]. Zeolite has the general formula M<sub>2/n</sub>.O.Al<sub>2</sub>O<sub>3</sub>.xSiO<sub>2</sub>.mH<sub>2</sub>O, M is the compensating cation with valence n, x is the ratio

between  $\text{SiO}_2:\text{Al}_2\text{O}_3$  and  $m$  is the moles of  $\text{H}_2\text{O}$  [5]. Therefore, the combination between heavy metals removal and the utilization of agricultural by-product for limiting environmental pollution is practical significance. In Vietnam, there are many previous studies on zeolite synthesis from minerals and by-products, and using zeolite as the adsorbent for heavy metals removal [6-9]. In 2015, zeolite A was successfully synthesized from RHA [10]. Rice husks were firstly pretreated and calcinated at the temperature range of 600-800°C for 90 mins, after RHA was mixed with sodium hydroxide to obtain a suspension. And then,  $\text{Na}_2\text{SiO}_3$  solution was collected by separating liquid and solid. This solution and  $\text{NaAlO}_2$  were mixed together, stirred for 1 hour to obtain a homogeneous gel mixture, and heated to 100°C and kept for 6 hours to obtain the crystallized product. Meanwhile, kaolin was used as a precursor source for the preparation of zeolite NaX [11]. The synthesis was carried out by aging a mixture of precursors and sodium hydroxide for 144 h. Then, the mixture was crystallized at 80°C for 72 hours. The obtained results revealed that zeolite X has good crystallinity and large specific surface area. As a whole, there are several studies on zeolite in Vietnam; however, the synthesis of zeolite NaP from RHA is still relatively new. Besides, zeolite NaP1 was usually synthesized over a long period ranging from one day to several days [12]. Thus, this study implements the zeolite NaP1 synthesis at a simpler process, short reaction and aging time, and obtains good adsorption capacity for heavy metal ions. The properties of zeolite NaP1 derived from RHA are also determined via SEM, DLS, BET, and XRD. Besides, the factors affecting the adsorption experiments of Cu and Pb ions are also investigated. Furthermore, the experimental data are described with isotherm models such as Langmuir, Freundlich, D-R, Temkin, Sips and Redlich - Peterson to understand the adsorption process.

## Experimental

### Materials

RHA collected from Nam Tien Joint Stock Company, Tra Noc Industrial Park, Can Tho City, Vietnam was directly used for the zeolite synthesis. Additionally, chemicals for the synthesis and ion removal included sodium hydroxide ( $\text{NaOH}$ , 96%), hydrochloric acid ( $\text{HCl}$ , 36-38%), bromothymol blue, potassium fluoride dihydrate ( $\text{KF} \cdot 2\text{H}_2\text{O}$ , 99%), sodium tetraborate decahydrate ( $\text{Na}_2\text{B}_4\text{O}_7 \cdot 10\text{H}_2\text{O}$ , 99.5%), copper sulfate ( $\text{CuSO}_4 \cdot 5\text{H}_2\text{O}$ , 99%), lead nitrate ( $\text{Pb}(\text{NO}_3)_2$ , 99%), potassium chloride ( $\text{KCl}$ , 99%) and potassium

hydroxide ( $\text{KOH}$ , 85%). All reagents and chemicals were purchased from Xilong, China and high purity without any purification steps. Besides, aluminum powder ( $\text{Al}$ , 99% purity) was obtained from Union Chemical Industry Company Ltd.).

### Synthesis of zeolite NaP1

In this work, zeolite NaP1 is synthesized by sol-gel method, using silica source from RHA, alumina source from commercial, and  $\text{NaOH}$  as a mineralizer. The synthesis process was based on previous studies with fine modification [10, 13] (Fig 1). Silica is firstly extracted from RHA by a reaction of RHA and  $\text{NaOH}$  5M with a ratio of 1:10 (g/mL), 90°C for 3 hours. The obtained solution mainly possesses  $\text{Na}_2\text{SiO}_3$  in composition (as rich-silica solution) after removing the solid phase. Additionally,  $\text{NaAlO}_2$  solution is prepared by dissolving aluminum in  $\text{NaOH}$  solution. 50 mL  $\text{Na}_2\text{SiO}_3$  solution and 25 mL  $\text{NaAlO}_2$  solution are placed into a round bottom flask to obtain a gel mixture with a molar ratio of  $\text{Na}_2\text{O}:\text{SiO}_2:\text{Al}_2\text{O}_3 = 8:6:1$ . After homogenizing stirring step with a speed of 500 rpm, 50 °C, within 2 hours, the reaction is undergone at 100°C in 8 hours. When the reaction is complete, the solid phase is filtered and washed several times by distilled water to neutralize product pH value. A dry step at 60 °C until constant weight is required to obtain zeolite powder.

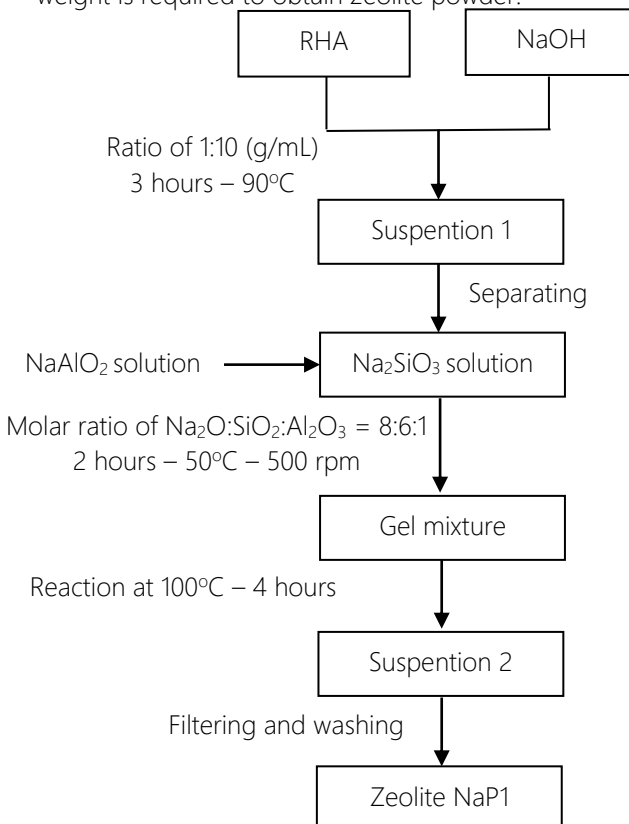


Fig. 1: Schematic diagram of the synthesis of zeolite NaP1

### Characterization of zeolite NaP1

Products are characterized by several methods such as SEM (6500F), DLS (SZ-100 Horiba), XRD (D8 Advance), and BET (Nova 1000e Quantachrome). Scherrer equation was applied as,

$$D = \frac{K \cdot \lambda}{\beta \cdot \cos(\theta)} \quad (1)$$

where, D is crystallite size, K is a numerical factor frequently referred to as the crystallite-shape factor,  $\lambda$  is the wavelength of X-rays,  $\beta$  and  $\theta$  are the width (full-width at half-maximum) of diffraction peak in radians and the angle, respectively.

### Experiments of $Cu^{2+}$ , $Pb^{2+}$ removal

Zeolite NaP1 is firstly determined the surface charge by determining the point of zero charge ( $pH_{pzC}$ ) method. Ten beakers containing 25 mL KCl (0.1 M) solution are adjusted pH value of 3-12 by using KOH and HCl 0.01 M. Then, 0.2 g zeolite is added to each solution and the pH value is double-checked after 24 hours. Surface charges at different pH and  $pH_{pzC}$  are calculated by the pH value disparity of pre- and post-solution.

Removal of  $Cu^{2+}$  and  $Pb^{2+}$  is performed at room temperature (isothermal adsorption) with some parameters such as the initial concentration of 10-100 mg/L, adsorbent dose of 0.25-4 g/L, and contact time of 30-150 mins. The adsorbates having pH value of 5 are chosen for all experiments and discussed in the next section. The concentrations of ion  $Cu^{2+}$  and  $Pb^{2+}$  ions in solution are detected by using Inductively Coupled Plasma (ICP, Optima 7300 DV). The adsorption result is presented as adsorption efficiency and capacity calculated by:

$$H(\%) = \frac{C_0 - C_t}{C_0} \cdot 100 \quad (2)$$

$$q_t (\text{mg/g}) = \frac{(C_0 - C_t) \cdot V}{m} \quad (3)$$

where, H (%) and  $q_t$  (mg/g) are adsorption efficiency and capacity, respectively.  $C_0$  and  $C_t$  (mg/L) are liquid phase concentration at initial and at any time t (min), respectively. m (g) is dose of zeolite and V (mL) is the volume of the solution.

### Adsorption models

Adsorption models are applied to describe the adsorption process, including two-parameter (Langmuir, Freundlich, Dubinin-Redushkevich, and Temkin) and three-parameter (Sips and Redlich-Peterson) [-[14]. Besides, coefficient ( $R^2$ ) is determined (Eq.4) to check the validity of the models used in describing the experimental data [15]

$$R^2 = \left( \frac{\sum_{i=1}^N (q_{i,\text{exp}} - \bar{q}_{i,\text{exp}})^2 - \sum_{i=1}^N (q_{i,\text{exp}} - \bar{q}_{i,\text{theo}})^2}{\sum_{i=1}^N (q_{i,\text{exp}} - \bar{q}_{i,\text{exp}})^2} \right) \quad (4)$$

### Results and discussion

#### Synthesis of zeolite NaP1

Obtained zeolite is analyzed by XRD to examine the crystalline structure as well as collate with pure zeolite NaP1. XRD result in Fig 2 reveals the fine crystalline structure of zeolite with the obvious sharp peak and high intensity. In comparison of the standard peak of NaP1 (JCPDS card No. 39-0219), the synthesized zeolite possesses full of peaks fitting the standard ones. It illustrates the good transferring of silica into zeolite structure due to no finding of non-crystalline reagents. Besides, the crystalline size of zeolite NaP1 (16.23 nm) is identified by the Scherrer equation.

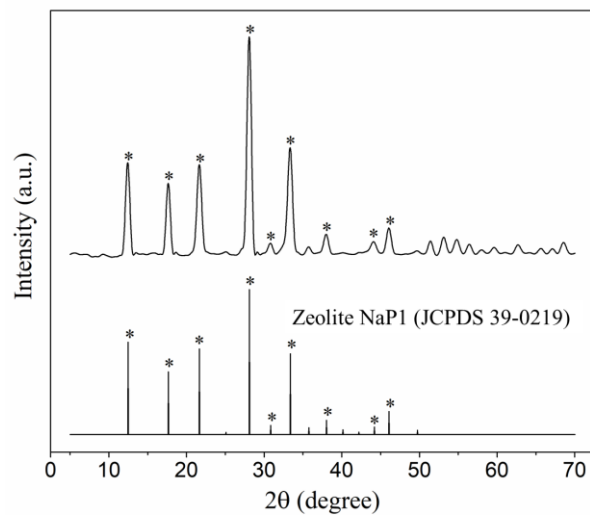


Fig 2: XRD pattern of zeolite NaP1

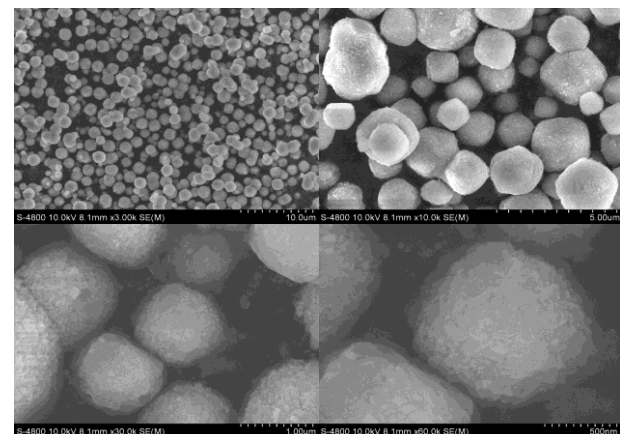


Fig 3: SEM images of zeolite NaP1 at different magnifications

To determine the crystal structure and morphology of zeolite NaP1, SEM is carried out and presented in Fig 3 at different magnifications. In general, the SEM images

suggest a well-crystal growth of the synthesized zeolite. Zeolite NaP1 with the regular sphere shape was similar to other study [12]. The zeolite NaP1 particles were categorized to the Gismondine group, well-known microspheres. In this study, synthesized zeolite NaP1 is also sphere-shaped with a regular size of about 1.3  $\mu\text{m}$ . Moreover, DLS result (Fig 4) also indicates the narrow distribution and particle size of about 1.123  $\mu\text{m}$ . Nano crystallites are found as well-grown on microsphere surface with the size of each crystallite size of few nanometers (Fig 3). This dimension agrees with the Scherrer calculation based on the XRD peak. However, the sphere particles are isolatedly dispersed but may be still aggregated. The presence of the aggregation and self-assembling may be due to the excess amount of an alkaline solution used during the synthesis reaction, resulting in an increased electrolyte concentration and it causes the condensation of primary particles in the solution phase [16]

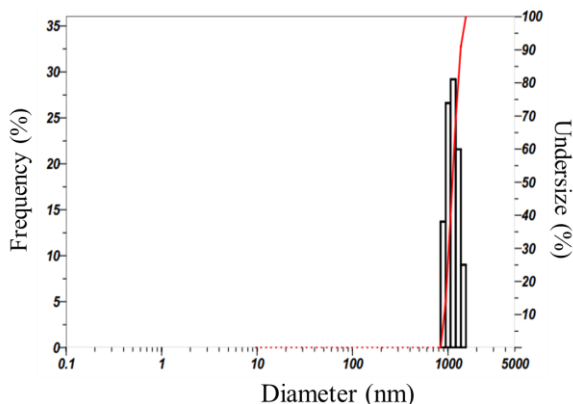


Fig 4: DLS result demonstrating the particle size distribution of zeolite NaP1

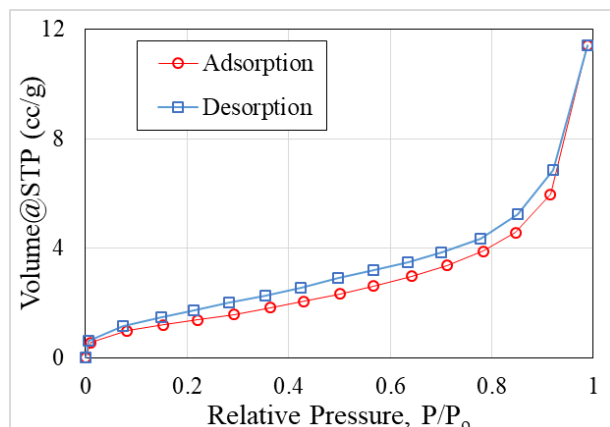


Fig 5:  $\text{N}_2$  adsorption-desorption isotherms of zeolite NaP1

Surface texture of zeolite NaP1 is determined by  $\text{N}_2$  adsorption/desorption and presented in Fig 5. Zeolite

NaP1 expresses a type I isotherm with no step-wise behavior. This behavior suggests the uniform pore size of material which is in agreement with the observed/pretended pore size distribution in Fig 3 and Fig 4. The observed hysteresis was assigned to the mesopore character of the material, but zeolite NaP1 does not have mesoporous structure. This phenomenon can be described owing to the smaller pore size of NaP1, compared to the kinetic diameter of nitrogen, the observed BET surface areas may not reflect the intrinsic zeolite microporosity. The surface area and pore diameter are  $14 \text{ m}^2/\text{g}$  and  $19.4 \text{ \AA}$ , respectively. The surface area is relatively small, similar to reported values, which could be illustrated that the structure of zeolite NaP1 only had 8-membered rings [17].

#### Removal of cation $\text{Cu}^{2+}$ and $\text{Pb}^{2+}$

$\text{pH}_{\text{pzc}}$  of zeolite NaP1 was presented at 6.41 in Fig 6. At  $\text{pH}_{\text{solution}} < \text{pH}_{\text{pzc}}$ , the surface of zeolite NaP1 has a positive-charge, and versa. This study focuses on removal cation ( $\text{Cu}^{2+}$ ,  $\text{Pb}^{2+}$ ); thus,  $\text{pH}_{\text{solution}} > 6.41$  should be favourable for the adsorption process. However, the high pH value of the solution causes the presence of hydroxide precipitation (Eq 5 and Eq 6), which makes the adsorption meaningless (pH 5.3 and pH 5.4 in the case of  $\text{Cu}^{2+}$  and  $\text{Pb}^{2+}$ , respectively). From the experimental study, a pH value of 5 is chosen for all adsorption experiments in this work.

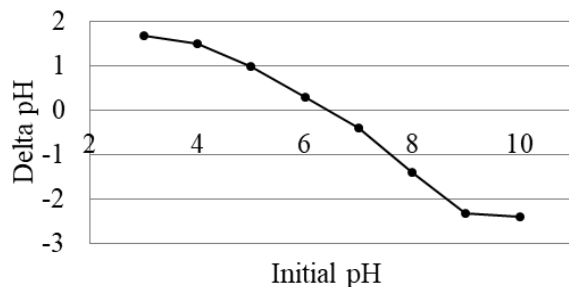
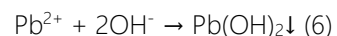
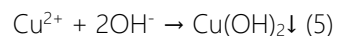


Fig 6: Point of zero charge plot for zeolite NaP1

#### Effect of zeolite NaP1 dose

Adsorption experiment is carried out at the different doses of zeolite NaP1 between 0.25 and 4 mg/L. The increase of zeolite dose from 0.25 to 4 mg/L provides more total surface area as well as the number of active sites that help the adsorption process conveniently happen, so the adsorption efficiency increased from 89.0 to 99.3 %, and 92.1 to 99.1% for  $\text{Cu}^{2+}$  and  $\text{Pb}^{2+}$  adsorption, respectively (Fig 7). At the dose of 1 g/L,

the adsorption process may reach the equilibrium state due to the slight increase in efficiency. However, considering the adsorption capacity, a rise of zeolite dose causes a decrease in capacity (Fig 8). At high adsorbent dose loaded, particles trended to form aggregation because of their high surface energy which leads to decrease total surface area and the number of active sites, and to increase diffusion path length as well [18], so adsorption is obstructed. Correlating to adsorption efficiency and capacity, a 0.5 g/L absorbent dose is selected for the subsequent evaluation.

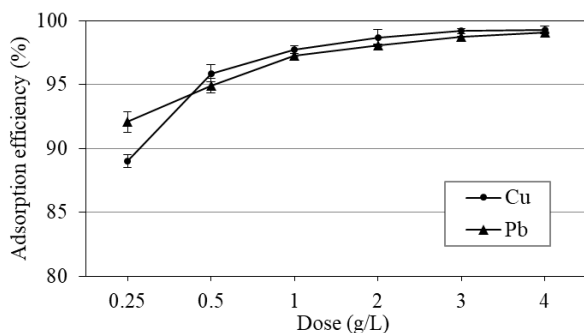


Fig 7: Adsorption efficiency corresponding with different doses of zeolite NaP1 (initial concentration 20 mg/L, pH 5, 30 mins)

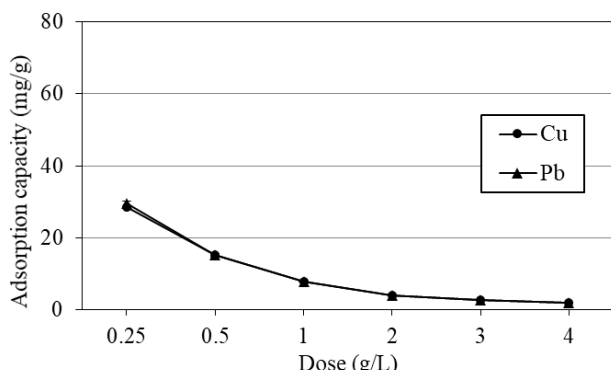


Fig 8: Adsorption capacity corresponding with different doses of zeolite NaP1 (initial concentration 20 mg/L, pH 5, 30 mins)

#### Effect of initial concentration

The adsorption process at different initial concentrations of cations is evaluated in Fig 9 and Fig 10. The initial concentrations are adjusted from 10 to 100 mg/L. At period of 10-75 mg/L, the adsorption efficiency increases 82.5-95.7% ( $\text{Cu}^{2+}$  adsorption) and 95.0-98.6% ( $\text{Pb}^{2+}$  adsorption). The efficiency slightly decreases at 100 mg/L with both cations. This can be explained due to the overload of adsorbate that zeolite is not able to catch or retain. At the initial concentration of 75 mg/L, the adsorption efficiency

achieved the maximum value of 95.7% ( $\text{Cu}^{2+}$ ) and 98.6% ( $\text{Pb}^{2+}$ ), respectively, and decreased at 100 mg/L concentration owing to the loading effect [15]. It signifies that energetically less favorable sites become involved with an increase of metal concentrations in the aqueous solution. For adsorption capacity, the increase of initial concentration results in the increased capacity of 6.6-71.7 mg/g ( $\text{Cu}^{2+}$ ), 7.6-73.9 mg/g ( $\text{Pb}^{2+}$ ). Based on the adsorption efficiency and capacity, the concentration of 75 mg/L is used for next study.

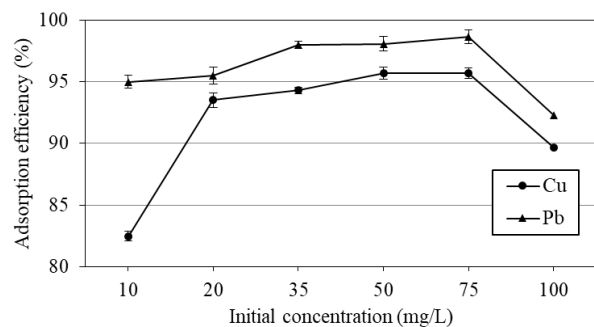


Fig 9: Adsorption efficiency corresponding with different initial concentrations (dose of zeolite 0.5 g/L, pH 5, 30 mins)

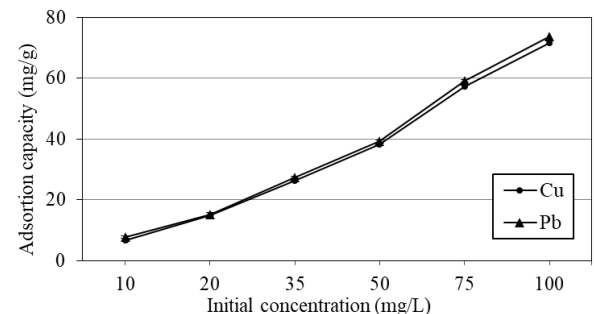


Fig 10: Adsorption capacity corresponding with different initial concentrations (dose of zeolite 0.5 g/L, pH 5, 30 mins)

#### Effect of contact time

The  $\text{Cu}^{2+}$  and  $\text{Pb}^{2+}$  cation uptake is regarded to different mechanisms of ion-exchange processes and the adsorption process. For the ion-exchange process, ions have to move into the pores of zeolite, and then through channels of the lattice, and replace exchangeable cations, typically sodium ions in zeolite NaP1). Diffusion happens faster when the ions move through the pores and are retarded through the smaller diameter channels. For that reason, contact time is investigated from 30 to 150 mins (Fig 11 and Fig 12). The adsorption got the highest value at 90 mins and the obtained results reported that the efficiency and capacity of  $\text{Cu}^{2+}$  and  $\text{Pb}^{2+}$  are 97.2% and 58.3 mg/g, 98.9 % and 59.3 mg/g, respectively. However,

the adsorption seems to reach the equilibrium state at 30 mins due to insignificant changes during the prolonged contact time. The capacity and efficiency of  $\text{Cu}^{2+}$  removal are 57.4 mg/g and 95.7%, respectively.  $\text{Pb}^{2+}$  adsorption can reveal a capacity and efficiency of 59.2 mg/g and 98.6%, respectively. At this time, the cations uptake could be mainly attributed to ion-exchange mechanism in the microporous system of zeolite [19]

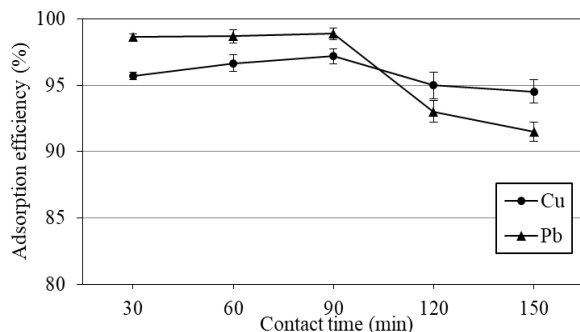


Fig 11: Adsorption efficiency corresponding with different contact time (dose of zeolite 0.5 g/L, pH 5, initial concentration 75 mg/L)

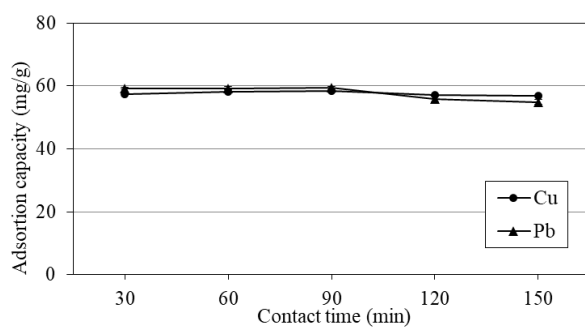


Fig 12: Adsorption capacity corresponding with different contact time (dose of zeolite 0.5 g/L, pH 5, initial concentration 75 mg/L)

#### Adsorption models

To describe the adsorption process, the adsorption models (two- and three-parameter) are applied and presented in Table [Table 1](#) and [Table 2](#).

Generally, experimental data fit in theoretical models but is not high reliability. To two of the adsorption process, the  $R^2$  of the Temkin model achieved the highest value at 0.919 for  $\text{Cu}^{2+}$  and 0.871 for  $\text{Pb}^{2+}$ . This model contains  $b_T$ -a factor that explicitly takes into account of adsorbent-adsorbate interactions [14]. The value of  $b_T < 8 \text{ kJ/mol}$ , so the adsorption process is suggested as physical adsorption. Besides, the Langmuir model obtains the low  $R^2$  value, proving that the complex of real adsorption may be an experimental error. In concentration of  $Q_{\max}$  (Langmuir

model) and  $Q_s$  (Sips one) seem to be equivalent that can be considered.

Table 1: The adsorption models for  $\text{Cu}^{2+}$  adsorption

Type	Model	Parameters		$R^2$
Two-para*	Langmuir	$K_L$	0.072	0.596
		$Q_{\max} (\text{mg/g})$	245.190	
	Freundlich	$1/n_F$	1.587	0.799
		$K_F$	9.378	
D-R		$Q_{D-R} (\text{mg/g})$	76.732	0.724
		$\beta_{D-R} (\text{mol}^2/\text{J}^2)$	0.853	
Temkin		$b_T (\text{J/mol})$	0.060	0.919
		$K_T$	1.080	
Three-para*	Sips	$Q_s (\text{mg/g})$	268.774	0.801
		$\alpha_s$	0.034	
		$1/s_p$	1.793	
	Redlich-Peterson	$K_{RP} (\text{L/g})$	14.892	0.906
		$\alpha_{RP} (\text{L/mg})$	$0.576 \times 10^{-5}$	
		B	0	

\* parameter

Table 2: The adsorption models for  $\text{Pb}^{2+}$  adsorption

Type	Model	Parameters		$R^2$
Two-para*	Langmuir	$K_L$	0.118	0.400
		$Q_{\max} (\text{mg/g})$	392.105	
	Freundlich	$1/n_F$	2.492	0.606
		$K_F$	50.251	
D-R		$Q_{D-R} (\text{mg/g})$	161.101	0.556
		$\beta_{D-R} (\text{mol}^2/\text{J}^2)$	0.398	
Temkin		$b_T (\text{J/mol})$	0.044	0.871
		$K_T$	2.290	
Three-para*	Sips	$Q_s (\text{mg/g})$	510.010	0.602
		$\alpha_s$	0.109	
		$1/s_p$	2.642	
	Redlich-Peterson	$K_{RP} (\text{L/g})$	41.505	0.845
		$\alpha_{RP} (\text{L/mg})$	$0.85 \times 10^{-3}$	
		B	0	

\* parameter

#### Comparison of $\text{Cu}^{2+}$ , $\text{Pb}^{2+}$ adsorption of zeolite NaP1

As above investigation, zeolite NaP1 is proved as the good absorbent for the removal of both  $\text{Cu}^{2+}$  and  $\text{Pb}^{2+}$ . The adsorption capacity of synthesized zeolite NaP1 is comparable to that of other kinds of zeolites (Table 3 and Table 4). For the case of  $\text{Cu}^{2+}$  removal, NaP1 adsorption capacity in this work is comparable to zeolite X synthesized from coal gangue and zeolite NaP from fly ash; however, the adsorption reaches the equilibrium in the shorter time (30 mins) and the

adsorption dose used (0.5 g/L) is smaller than that of other works.

Table 3: Comparison of Cu<sup>2+</sup> adsorption

Type	Precursor	Adsorption condition			q <sub>e</sub> (mg/g)	Ref
		pH	C <sub>0</sub> (mg/L)	Dose (g/L)		
NaP1	fly ash	5	230	2	120	68.9 [20] <sup>a</sup>
NaP1	fly ash	6	100	2	180	138.1** [21] <sup>a</sup>
NaX	comm*	5	100	2.5	30	147.2** [15]
NaX	coal gang-ue	4	100	2	40	45.76 [22]
NaP1	RHA	5	75	0.5	30	57.41 245.19** ***

\*commercial; \*\*maximum theoretical capacity for Langmuir model' \*\*\* this work; <sup>a</sup>JCPDS card No. 39-0219 of zeolite NaP1

For the Pb<sup>2+</sup> adsorption (Table 4), the precursor like commercial silica was used to produce the zeolite NaP which had the high adsorption capacity (144.70 mg/g), compared to that of this work (59.21 mg/g). Moreover, a comparison between zeolite sodalite (SOD) synthesized from diatomite and zeolite NaP1 in this work, the zeolite NaP1 adsorption capacity of Pb<sup>2+</sup> is quite lower. It can be explained because the zeolite NaP1 in this work is directly synthesized from RHA without any treatment, the pores of zeolite may be locked, resulted in the lower adsorption capacity of Pb<sup>2+</sup> and Cu<sup>2+</sup>. However, the adsorption equilibrium of zeolite NaP1 reaches at shorter time (30 minutes), compared to 60 mins [9]. Generally, zeolite NaP1 is of a smaller surface area due to its structure (compared to other zeolites), but the removal capacity of heavy metals is still satisfactory. The short contact time of 30 mins is also an interesting point of this study. Lastly, zeolite NaP1 generated from RHA, an abundant agricultural by-product, performs the good adsorption capacity.

Table 4: Comparison of Pb<sup>2+</sup> adsorption

Type	Pre-cursor	Adsorption condition			q <sub>e</sub> (mg/g)	Ref
		pH	C <sub>0</sub> (mg/L)	Dose (g/L)		
NaP1	comm*	4	200	1	45	144.70 [23]
NaX	comm*	5-7	100	2.5	30	198.72** [15]
NaX	comm*	6	10	4	144 0	14.22 [24]
NaA	Fly ash	8	100	10	30	178.00 [25]
SOD	dia-tomite	-	1200	10	60	107.64 [9]

NaP1	RHA	5	75	0.5	30	59.21 392.11**	***
------	-----	---	----	-----	----	-------------------	-----

\*commercial; \*\*maximum theoretical capacity for Langmuir model; \*\*\* this work

## Conclusions

Zeolite NaP1 is successfully synthesized from RHA source using a facile sol-gel method. Physicochemical properties of zeolite NaP1 are analyzed by techniques including XRD, SEM, BET, and DLS. The results have the well-crystalline of zeolite, a sphere-shape of 1.123 μm, surface area of 14.034 m<sup>2</sup>/g and pore diameter of 19.4 Å. Additionally, zeolite NaP1 is also applied for removing Cu<sup>2+</sup> and Pb<sup>2+</sup> cations at the optimal condition: initial concentration of 75 mg/L, adsorbent dose of 0.5 g/L, and contact time of 30 mins. Ion Cu<sup>2+</sup> removal has the capacity and efficiency of 57.4 mg/g and 95.7%, respectively while Pb<sup>2+</sup> adsorption obtains a capacity and efficiency of 59.2 mg/g and 98.6%, respectively. Adsorption processes are much fitted in Temkin model and the maximum theoretical capacity reaches 245.19 mg/g for Cu<sup>2+</sup> adsorption and 392.11 mg/g for Pb<sup>2+</sup> adsorption.

## Acknowledgments

This research is funded by Vietnam National Foundation for Science and Technology Development (NAFOSTED) under grant number 103.02-2020.64.

## References

1. S. Khan, M. Idrees, M. Bilal, Colloids Surf. A Physicochem. Eng. Asp. 623 (2021) 126711. <https://doi.org/10.1016/j.colsurfa.2021.126711>
2. L.R. Rad, M. Anbia, Environ. Chem. Eng. 95 (2021) 106088. <https://doi.org/10.1016/j.jece.2021.106088>
3. S.S. Hossain, L. Mathur, P. Roy, J. Asian Ceram. Soc. 64 (2018) 299-313. <https://doi.org/10.1080/21870764.2018.1539210>
4. R. Mohamed, I. Mkhald, M. Barakat, Arab. J. Chem. 81 (2015) 48-53. <https://doi.org/10.1016/j.arabjc.2012.12.013>
5. T. Barakat, J.C. Rooke, H.L. Tidahy, M. Hosseini, R. Cousin, J.F. Lamonier, J.M. Giraudon, G. De Weireld, B.L. Su,S. Siffert, ChemSusChem 410 (2011) 1420-1430. <https://doi.org/10.1002/cssc.201100282>
6. D.H.L. Thanh, D.T.T. Ha, TNU Journal of Science and Technology 226 (2021) 93-99. <https://doi.org/10.34238/tnu-jst.4345>

7. P.T.M. Huong, N.M. Ha, Vietnam Journal of Catalysis and Adsorption 11 (2022) 92-97. <https://doi.org/10.51316/jca.2022.076>
8. D.Q. Huy, D.Q. Khanh, N.X. Truong, N.D. Hue, VNU Journal of Science: Natural Sciences and Technology 23 (2007) 160-165. <https://js.vnu.edu.vn/NST/article/view/2186>
9. N.X. Hai, N.N. Minh, L.V. Kireycheva, P.A. Hung, P.D. Pha, V.T.H. Ha, D.K. Van, VNU Journal of Science: Natural Sciences and Technology 27 (2011) 171-178. <https://js.vnu.edu.vn/NST/article/view/1324>
10. P.T.H. Oanh, N.B. Nguyen, Ho Chi Minh City University of Education-Journal of Science 2 (2015) 21-30. [https://doi.org/10.54607/hcmue.js.0.2\(67\).618\(2015\)](https://doi.org/10.54607/hcmue.js.0.2(67).618(2015))
11. T.N. Don, H.T.L. Anh, T.X. Bai, T. Vu, L.V. Duong, Vietnam Journal of Chemistry 48 (2010) 475-479. <https://doi.org/10.15625/2149>
12. P. Sharma, J.-S. Song, M.H. Han,C.-H. Cho, Scientific Reports 61 (2016) 1-26. DOI: 10.1038/srep22734
13. P.L. Tran-Nguyen, K.P. Ly, L.H.V. Thanh, A.E. Angkawijaya, S.P. Santoso, M.-L. Tsai,Y.-H. Ju, J. Taiwan Inst. Chem. Eng. (2021) 1-8. <https://doi.org/10.1016/j.jtice.2021.05.009>
14. K.Y. Foo, B.H. Hameed, Chem. Eng. J. 1561 (2010) 2-10. <https://doi.org/10.1016/j.cej.2009.09.013>
15. Y. Yurekli, J. Hazard. Mater. 378 (2019) 120743. <https://doi.org/10.1016/j.jhazmat.2019.120743>
16. P. Sharma, J.-g. Yeo, M.H. Han, C.H. Cho, J. Mater. Chem. 17 (2013) 2602-2612. <https://doi.org/10.1039/C2TA01311H>
17. I.O. Ali, S.M. El-Sheikh, T.M. Salama, M.F. Bakr,M.H. Fodial, Sci. China Mater 58 (2015) 621-633. <https://doi.org/10.1007/s40843-015-0075-9>
18. V.S. Raghuwanshi, U.M. Garusinghe, J. Ilavsky, W.J. Batchelor, G. Garnier, J. Colloid Interface Sci. 510 (2018) 190-198. <https://doi.org/10.1016/j.jcis.2017.09.064>
19. E. Erdem, N. Karapinar, R. Donat, J. Colloid Interface Sci. 2802 (2004) 309-314. <https://doi.org/10.1016/j.jcis.2004.08.028>
20. X. Pu, L. Yao, L. Yang, W. Jiang, X. Jiang, J. Clean. Prod. 265 (2020) 121822. <https://doi.org/10.1016/j.jclepro.2020.121822>
21. Y. Liu, G. Wang, L. Wang, X. Li, Q. Luo, P. Na, Chin. J. Chem. Eng. 272 (2019) 341-348. <https://doi.org/10.1016/j.cjche.2018.03.032>
22. X. Lu, D. Shi, J. Chen, Environ. Earth Sci. 76 (2017) 1-10. <https://doi.org/10.1007/s12665-017-6923-z>
23. A. Utami, S. Sugiarti, P. Sugita, J. Rasayan J. Chem 122 (2019) 650-658. <http://dx.doi.org/10.31788/RJC.2019.1222056>
24. P.K. Pandey, S. Sharma, S. Sambi, J. Environ. Chem. Eng. 34 (2015) 2604-2610. <https://doi.org/10.1016/j.jece.2015.09.008>
25. T. Hussain, A.I. Hussain, S.A.S. Chatha, A. Ali, M. Rizwan, S. Ali, P. Ahamd, L. Wijaya, M.N. Alyemeni, Int. J. Environ. Res. Public Health 187 (2021) 3373. <https://doi.org/10.3390/ijerph18073373>



International Conference on Environmental Engineering  
and Renewable Energy  
(ICENVERE-2023)

Taipei City, Taiwan  
23<sup>rd</sup> - 24<sup>th</sup> June, 2023

Research Plus

[www.researchplus.co](http://www.researchplus.co)

Publisher: Research Plus Explore

Copyright © 2023 Research Plus-International Conference, Taipei City, Taiwan

All rights reserved. No part of this publication may be reproduced, stored in a retrieval system or transmitted in any form or by any means, electronic, mechanical, photocopying, recording or otherwise, without the prior written permission of the publisher.

This edition is produced in India and is intended for worldwide distribution. However, no part of this publication may be exported without the prior permission of the publisher, Research Plus-Explore.

**Editorial:**

We are delighted to extend a warm welcome to all participants attending the International Conference on Environmental Engineering and Renewable Energy (ICENVERE-23), taking place in Taipei City, Taiwan on June 23<sup>rd</sup> - 24<sup>th</sup>, 2023. This conference provides a vital platform for researchers, students, academicians, and industry professionals from all over the world to share their latest research results and development activities in the field of Environmental Engineering and Renewable Energy. It offers delegates an opportunity to exchange new ideas and experiences, establish business or research relationships, and explore global collaborations.

The proceedings for ICENVERE-23 contain the most up-to-date, comprehensive, and globally relevant knowledge in the field of Environmental Engineering and Renewable Energy. All submitted papers were subject to rigorous peer-reviewing by 2-4 expert referees, and the papers included in these proceedings have been selected for their quality and relevance to the conference. We are confident that these proceedings will not only provide readers with a broad overview of the latest research results in Environmental Engineering and Renewable Energy but also serve as a valuable summary and reference for further research in this field.

We are grateful for the support of many universities and research institutes, whose contributions were vital to the success of this conference. We extend our sincerest gratitude and highest respect to the many professors who played an important role in the review process, providing valuable feedback and suggestions to authors to improve their work. We also extend our appreciation to the external reviewers for providing additional support in the review process and to the authors for contributing their research results to the conference.

Since April 2023, the Organizing Committees have received more than 60 manuscript papers, covering all aspects of Environmental Engineering and Renewable Energy. After review, approximately 20 papers were selected for inclusion in the proceedings of ICENVERE-2023.

We would like to thank all participants at the conference for their significant contribution to its success. We express our gratitude to the keynote and individual speakers and all participating authors for their dedication and hard work. We also sincerely appreciate the efforts of the technical program committee and all reviewers, whose contributions made this conference possible. Finally, we extend our thanks to all the referees for their constructive comments on all papers, and we express our deepest gratitude to the organizing committee for their tireless work in making this conference a reality.

## **Acknowledgement**

The International Conference on Environmental Engineering and Renewable Energy, organized by Research Plus, was successfully held in June. We extend our heartfelt gratitude to our colleagues, staff, professors, reviewers, and members of the organizing committee for their unwavering support in making this conference a success.

We would also like to thank all the delegates who travelled far and wide to attend this conference, making it a truly global event. This conference provided a platform for students, professional engineers, academicians, and scientists to share their latest research and developments in the field of Environmental Engineering and Renewable Energy.

The aim of the conference was to promote research and development activities and to encourage scientific information exchange between researchers, developers, engineers, students, and practitioners from all around the world. Once again, we thank everyone who contributed to making this conference a resounding success.



**Sukumar Sen**  
**Program Manager**  
**Research Plus**

## CONTENTS

1.	<b>Renewable Energy and Electricity Incapacitation in Sub-Saharan Africa: Analysis of a 100% Renewable Electrification in Chad .....</b>	1
	❖ Olusola Bamisile	
	❖ Cai Dongsheng	
	❖ Jian Li	
2.	<b>Optimizing Planning and Operation of Renewable Energy Communities with Genetic Algorithms .....</b>	2
	❖ Florencia Lazzari	
	❖ Gerard Mor	
	❖ Jordi Cipriano	
3.	<b>The Role of Renewable Energy and Total Factor Productivity in Reducing CO<sub>2</sub> Emissions in Azerbaijan. Fresh Insights from a New Theoretical Framework Coupled with Autometrics .....</b>	3
	❖ Fakhri J. Hasanova	
4.	<b>Long-Term Planning for the Integration of Electric Mobility with 100% Renewable Energy Generation under Various Degrees of Decentralization: Case Study Cuenca, Ecuador .....</b>	4
	❖ Daniel Icaza-Alvarez	
	❖ Francisco Jurado	
5.	<b>Liquified Hydrogen vs. Liquified Renewable Methane: Evaluating Energy Consumption and Infrastructure for Sustainable Fuels.....</b>	5
	❖ Mohammed Al-Breiki	
	❖ Yusuf Bicer	
6.	<b>Feasibility and Optimal Sizing Analysis of Hybrid Renewable Energy Systems: A Case Study of Al-Karak, Jordan .....</b>	6
	❖ Rafat Al Afif	
7.	<b>Worldwide Carbon Neutrality Transition? Energy Efficiency, Renewable, Carbon Trading and Advanced Energy Policies .....</b>	7
	❖ Yuekuan Zhou	
8.	<b>An Efficient Renewable Hybridization Based on Hydrogen Storage for Peak Demand Reduction: A Rule-Based Energy Control and Optimization using Machine Learning Techniques .....</b>	8
	❖ Amirmohammad Behzadi	
	❖ Seyed Mojtaba Alirahmi	
9.	<b>Assessing Motivations and Barriers to Renewable Energy Development: Insights from a Survey of Municipal Decision-Makers in Alberta, Canada.....</b>	9
	❖ Sonak Patel	
	❖ John R. Parkins	
10.	<b>A Comparison and Methodological Proposal for Hybrid Approaches to Quantify Environmental Impacts: A Case Study for Renewable Energies .....</b>	10
	❖ A.R. Gamarra	
	❖ Y. Lechón	
	❖ S. Banacloche	
	❖ B. Corona	

11. Reliability Index Based Optimal Sizing and Statistical Performance Analysis of Stand-Alone Hybrid Renewable Energy System using Metaheuristic Algorithms .....	11
❖ M. Thirunavukkarasu	
❖ Himadri Lala	
12. Renewable Energy Public-Private Partnership Projects in Egypt: Perception of the Barriers and Key Success Factors by Sector .....	12
❖ Kareem Othman	
❖ Rana Khallaf	
13. Hydrogen Production, Storage and Transport for Renewable Energy and Chemicals: An Environmental Footprint Assessment .....	13
❖ Robert Hren	
❖ Annamaria Vujanović	
14. Drivers and Challenges of Off-Grid Renewable Energy-Based Projects in West Africa: A Review .....	14
❖ Kofi Nyarko	
❖ Jonathan Whale	
❖ Tania Urmee	
15. Techno-Economic Analysis of a Renewable-Based Hybrid Energy System for Utility and Transportation Facilities in a Remote Community of Northern Alberta .....	15
❖ Tazrin Jahan Priyanka	
❖ Shivam Atre	
16. Optimal Sorting and Recycling of Plastic Waste as a Renewable Energy Resource Considering Economic Feasibility and Environmental Pollution.....	16
❖ Jonghun Lim	
17. Evaluation of Dynamic Growth Trend of Renewable Energy Based on Mathematical Model.....	17
❖ Jiaona Li	
18. Energy Policy Simulation in Times of Crisis: Revisiting the Impact of Renewable and Non-Renewable Energy Production on Environmental Quality in Germany .....	18
❖ Festus Fatai Adedoyin	
❖ Naila Erum	
❖ Dilvin Taşkin	
❖ Daouia Chebab	
19. Impacts of Integrating Engineering Design Process into STEM Makerspace on Renewable Energy Unit to Foster Students' System Thinking Skills.....	19
❖ Abdurrahman Abdurrahman	
20. The Removal of Phosphate using NaP / Chitosan Composite .....	20
❖ Phuong Lan Tran-Nguyen	
❖ Kim-Phung Ly	
❖ Xuan Vy Cao-Thi	
❖ Minh-Tien Pham	
❖ Duc-Duy Le	
❖ Minh Thu Tran-Thi	
❖ Nguyen Thi Nhu Y	

# International Conference on Environmental Engineering and Renewable Energy (ICENVERE-23)

## Renewable Energy and Electricity Incapacitation in Sub-Saharan Africa: Analysis of a 100% Renewable Electrification in Chad

### Olusola Bamisile

Sichuan Industrial Internet Intelligent Monitoring and Application Engineering Research Center,  
Chengdu University of Technology, Sichuan, China

### Cai Dongsheng

Sichuan Industrial Internet Intelligent Monitoring and Application Engineering Research Center,  
Chengdu University of Technology, Sichuan, China

### Jian Li

Sichuan Provincial Lab for Power System Wide-Area Measurement and Control,  
University of Electronic Science and Technology of China, Sichuan, China

### Abstract:

Despite the global push for net-zero emission and the power system's decarbonization, there are still a lot of developing countries (especially in sub-Saharan Africa) with electricity crises or inadequate electrification. Coincidentally, these countries have enormous renewable energy potential. Therefore, this paper presents a brief summary of the electricity incapacitation and renewable energy potential in many sub-Saharan African countries. This study is novel as it presents a techno-analysis of 100% renewable electrification in Chad which is one of the countries with the least electricity access globally. Also, the models developed are simulated using the EnergyPLAN tool with targeted implementation years set as 2030, 2040, and 2050 based on different global decarbonization targets. From the result of this study, the use of biomass power plants is the only scenario that does not have critical excess electricity production (CEEP) in the power system. Also, these scenarios require the least power capacities (270 MW for 2030, 650 MW for 2040, and 1600 MW for 2050) out of all the scenarios in this study. Solar PV and wind power can be categorized as the most probable options as they are matured technologies and in application in many countries, however, they will require pumped hydro storage integration.

### Keywords:

EnergyPLAN, Electrification, Electricity demand estimation, Renewable energy, Sub-Saharan Africa.

# International Conference on Environmental Engineering and Renewable Energy (ICENVERE-23)

## Optimizing Planning and Operation of Renewable Energy Communities with Genetic Algorithms

### Florencia Lazzari

Department of Computer Science and Industrial Engineering, University of Lleida, Lleida, Spain  
International Center for Numerical Methods in Engineering. Building Energy and Environment Group. CIMNE-Lleida.  
Lleida. Spain

### Gerard Mor

International Center for Numerical Methods in Engineering. Building Energy and Environment Group. CIMNE-Lleida.  
Lleida. Spain

### Jordi Cipriano

International Center for Numerical Methods in Engineering. Building Energy and Environment Group. CIMNE-Lleida.  
Lleida. Spain

### Abstract:

Renewable Energy Communities (REC) have the potential to become a key agent for the energy transition. Since consumers have different consumption patterns depending on their habits, their grouping allows for a better use of the resource. REC provide both economic and environmental benefits. However, its potential drastically diminishes when grouping of prosumers and energy al- location is performed improperly, as the energy generated ends up not being consumed. Given the importance of extracting the maximum potential of REC, this study presents a tool to assist in both the planning and the operation phases. We present a combinatorial optimization method for participant selection and a multi-objective (MO) optimization of solar energy allocation. Specific Genetic Algorithms (GA) were developed including problem-specific approaches for reducing the search space, encoding, techniques for space ordering, fitness functions, special operators to replace duplicate individuals and decoding for equality constraints. The performance of the novel solution approach was exper- imentally proved with an electrical solar installation and electricity consumers from Northern east Spain. The results show that the developed tool achieves energy sharing in REC with low solar energy excess, high self-consumption and high avoided CO<sub>2</sub> emissions while assuring low payback periods for all partic- ipants. This tool will be essential to increase revenues of REC schemes and boost their beneficial environmental impact.

### Keywords:

Renewable Energy Communities, Solar energy, Optimization, Genetic Algorithm.

# International Conference on Environmental Engineering and Renewable Energy (ICENVERE-23)

## The Role of Renewable Energy and Total Factor Productivity in Reducing CO<sub>2</sub> Emissions in Azerbaijan. Fresh Insights from a New Theoretical Framework Coupled with Autometrics

**Fakhri J. Hasanov**

Institute of Control Systems, Bakhtiyar Vahabzadeh, Baku, Azerbaijan

### **Abstract:**

Environmental issues, such as carbon dioxide (CO<sub>2</sub>) emissions, are humanity's most critical issues. Emissions released by oil-producing countries is not small. This is because these countries have an abundance of fossil fuels with considerably low prices, and the cost of using these natural sources to obtain energy is significantly cheaper than using alternative energy sources. This study examined pollution in Azerbaijan, an oil-producing country. It uses a new theoretically grounded framework in which consumption-based CO<sub>2</sub> emissions are a function of renewable energy consumption (REC) and total factor productivity (TFP), as well as income, exports, and imports. REC and TFP have not only emission-reducing properties but also growth-enhancing benefits and are, therefore, very useful to be considered in environmental policies. Econometric analysis was conducted with robustness checks and the state-of-the-art econometric methodology called *Autometrics* – a machine learning algorithm for model discovery – was employed. CO<sub>2</sub> was found to be negatively affected by TFP and REC. Exports also exert a negative impact on CO<sub>2</sub>, while the effects of income and imports are positive. Our key policy insights are that Azerbaijani policymakers may wish to implement policies that further promote technological improvements, efficiency gains, and transitions to renewable energy.

### **Keywords:**

Azerbaijan, Consumption-based CO<sub>2</sub>, Total factor productivity, Renewable energy, Exports, Imports, GDP, Cointegration, Autometrics.

# International Conference on Environmental Engineering and Renewable Energy (ICENVERE-23)

## Long-Term Planning for the Integration of Electric Mobility with 100% Renewable Energy Generation under Various Degrees of Decentralization: Case Study Cuenca, Ecuador

**Daniel Icaza-Alvarez**

Department of Electrical Engineering, University of Jaen, Linares, Spain

**Francisco Jurado**

Department of Electrical Engineering, University of Jaen, Linares, Spain

### **Abstract:**

Urban borders are expanding in cities, solar photovoltaic and wind energy are being used and decentralized more and more, while the electrification of transport systems is in permanent progress. Users trust more in the modernization of electrical systems giving rise to various applications. The efforts made by both the public and private sectors are isolated and are not framed within comprehensive planning. For this reason, cities must be fully planned and contemplated in their land use plans. This article presents a long-term roadmap for the comprehensive electrification of mobility. To achieve a proper approach, it is based on the EnergyPLAN tool that uses the concept of smart energy and determines the long-term scenarios, the case of study is for the City of Cuenca in Ecuador. It seeks to take advantage of the potential of renewable energies available in the territory, which are evaluated and provide the necessary energy to feed future decentralized transport systems with a view to 2050. The long-term results show that the energy mix would be composed of wind with 37.3%, followed by solar photovoltaic with 33.9% and hydroelectric with 25.4%. There are others technologies such as biomass that do not exceed 3.4%.

### **Keywords:**

Clean energy, Energy planning, Smart energy, Power sources, Energy transition, Electric mobility.

# International Conference on Environmental Engineering and Renewable Energy (ICENVERE-23)

## Liquified Hydrogen vs. Liquified Renewable Methane: Evaluating Energy Consumption and Infrastructure for Sustainable Fuels

**Mohammed Al-Breiki**

Division of Sustainable Development, College of Science and Engineering, Hamad Bin Khalifa University,  
Qatar Foundation, Doha, Qatar

**Yusuf Bicer**

Division of Sustainable Development, College of Science and Engineering, Hamad Bin Khalifa University,  
Qatar Foundation, Doha, Qatar

### **Abstract:**

This study aims to assess the energy consumption characteristics of various fuels, namely liquified natural gas, liquefied renewable methane, and liquefied hydrogen from production to overseas transportation, by covering broad color spectra of grey, blue, and green. A quantitative assessment is implemented to calculate how much energy is consumed to produce, store, and transport fuels. Carbon capture scenarios are also considered, along with boil-off gas recovery and utilization options for increased value chain effectiveness. Thereafter, a qualitative assessment is performed to compare the use of fuels from four perspectives: (i) technology, (ii) infrastructure, (iii) scalability, and (iv) regulations. The obtained quantitative results indicate that the energy consumption to produce liquified natural gas, liquefied renewable methane, and liquefied green hydrogen is about 0.49, 31.4, and 62.3 kWh/kg of fuel, respectively. The energy consumption to store liquified hydrogen in a 2,000 m<sup>3</sup> on-land storage tank for one day while recovering 100% of the generated boil-off gas is about 4,840 kWh. Moreover, the qualitative results indicate that the infrastructure is ready, and regulations are available to use liquefied renewable methane as fuel, whereas the infrastructure of liquified hydrogen still needs to be ready, and the associated regulations require amendments.

### **Keywords:**

Boil-off gas, Carbon capture, Clean energy, Energy carrier, Liquefaction, Synthetic natural gas.

# International Conference on Environmental Engineering and Renewable Energy (ICENVERE-23)

## Feasibility and Optimal Sizing Analysis of Hybrid Renewable Energy Systems: A Case Study of Al-Karak, Jordan

**Rafat Al Afif**

Institute of Chemical and Energy Engineering, University of Natural Resources and Life Sciences, Muthgasse,  
Vienna, Austria

### **Abstract:**

The aim of this research is to examine the techno-economic viability of both off-grid and on-grid hybrid renewable energy systems for Jordan's Al-Karak governorate. Hybrid Optimization of Multiple Energy Resources (HOMER) Pro software was used in this article to evaluate the carry feasibility to maximize the renewable energy (RE) integration in hybrid energy systems based on different configurations, grid-connected and stand-alone systems of the wind turbine, biogas plant, photovoltaic (PV) panels, flywheel, and batteries while minimizing the net present cost, the Levelized cost of energy and CO<sub>2</sub> emissions mitigation. The results showed that the PV/Wind system, connected to the grid with batteries for storage is the optimal configuration for sustainable Al-Karak governorate electrification whilst achieving environmental benefits and guaranteeing reliable and continuous energy access with the lowest net present cost and the Levelized cost, 298,359 USD\$ and 0.024 USD\$/kWh respectively, and high RE share, 71.8% of electricity is generated from wind and 28.2% is purchased from the grid and emits 220 tons of CO<sub>2</sub> per year, 53% less than a grid alone system. Such a system would provide advantages in terms of energy independence and improved environmental quality.

### **Keywords:**

Hybrid renewable energy systems, Techno economic, Net present cost, Al Karak governorate.

# International Conference on Environmental Engineering and Renewable Energy (ICENVERE-23)

## Worldwide Carbon Neutrality Transition? Energy Efficiency, Renewable, Carbon Trading and Advanced Energy Policies

**Yuekuan Zhou**

Sustainable Energy and Environment Thrust, Function Hub,  
The Hong Kong University of Science and Technology (Guangzhou), Nansha, Guangzhou, Guangdong, China  
Department of Mechanical and Aerospace Engineering, The Hong Kong University of Science and Technology,  
Clear Water Bay, Hong Kong Special Administrative Region of China  
HKUST Shenzhen-Hong Kong Collaborative Innovation Research Institute, Futian, Shenzhen, China

**Abstract:**

Climate change and energy shortage crisis promptly necessitate achievement of sustainable development goals. However, there is no straightforward pathways for low-carbon transformation on building sectors, and energy/carbon trading and reverse promotion on decarbonization strategies are not clear. In this study, a literature enumeration method with dialectical analysis was adopted for state-of-the-art literature review and comparison. Low-carbon transformation pathways in buildings were holistically reviewed, with a series of integrated techniques, such as energy saving, clean energy supply, flexible demand response for high self-consumption, and even smart electric vehicle (EV) integration. Afterwards, energy/carbon flows and trading in building-related systems were provided, such as peer-to-peer energy trading, building and thermal/power grids, building and energy-integrated EVs, and carbon trading in buildings. Last but not the least, worldwide decarbonization roadmaps across regions and countries are analysed, to identify the most critical aspects and immediate actions on decarbonization. Results indicate that tradeoff strategies are required to compromise the conflict between insufficient feed-in tariff (FiT) incentives (low renewable penetration in the market) and great economic pressures (high investment in renewable systems). Low-carbon building pathway is further enhanced with first priority given to passive/active energy-saving strategies, onsite clean energy supply and then flexible demand response. Energy/carbon trading will significantly affect renewable energy utilization, and acceptance from end-users to actively install renewable systems or participate in EV interactions. Worldwide decarbonization pathways mainly focus on industries, transportation, buildings, renewable sources, carbon sink and carbon capture, utilization and storage (CCUS). This study can contribute to technical roadmaps and strategies on carbon neutrality transition in both academia and industry, together with advanced policies in grid feed-in tariff, energy/carbon trading and business models worldwide.

**Keywords:**

Carbon neutrality, Energy policy, Renewable energy, Energy storage, Energy flexible buildings, Energy/carbon trading.

# International Conference on Environmental Engineering and Renewable Energy (ICENVERE-23)

## **An Efficient Renewable Hybridization Based on Hydrogen Storage for Peak Demand Reduction: A Rule-Based Energy Control and Optimization using Machine Learning Techniques**

**Amirmohammad Behzadi**

Department of Civil and Architectural Engineering, KTH Royal Institute of Technology, Stockholm, Sweden

**Seyed Mojtaba Alirahmi**

Department of Chemistry and Bioscience, Aalborg University, Esbjerg, Denmark

### **Abstract:**

The present study proposes and thoroughly examines a novel approach for the effective hybridization of solar and wind sources based on hydrogen storage to increase grid stability and lower peak load. The parabolic trough collector, vanadium chloride thermochemical cycle, hydrogen storage tank, alkaline fuel cells, thermal energy storage, and absorption chiller make up the suggested smart system. Additionally, the proposed system includes a wind turbine to power the electrolyzer unit and minimize the size of the solar system. A rule-based control technique establishes an intelligent two-way connection with energy networks to compensate for the energy expenses throughout the year. The transient system simulation (TRNSYS) tool and the engineering equation solver program are used to conduct a comprehensive techno-economic-environmental assessment of a Swedish residential building. A four-objective optimization utilizing MATLAB based on the grey wolf algorithm coupled with an artificial neural network is used to determine the best trade-off between the indicators. According to the results, the primary energy saving, carbon dioxide reduction rate, overall cost, and purchased energy are 80.6 %, 219 %, 14.8 \$/h, and 24.9 MWh at optimal conditions. From the scatter distribution, it can be concluded that fuel cell voltage and collector length should be maintained at their lowest domain and the electrode area is an ineffective parameter. The suggested renewable-driven smart system can provide for the building's needs for 70 % of the year and sell excess production to the local energy network, making it a feasible alternative. Solar energy is far less effective in storing hydrogen over the winter than wind energy, demonstrating the benefits of combining renewable energy sources to fulfill demand. By lowering CO<sub>2</sub> emissions by 61,758 kg, it is predicted that the recommended smart renewable system might save 7719 \$ in environmental costs, equivalent to 6.9 ha of new reforestation.

### **Keywords:**

Hydrogen storage, Thermal energy storage, Multi-objective optimization, Energy management, Fuel cell, Solar collector.

# International Conference on Environmental Engineering and Renewable Energy (ICENVERE-23)

## Assessing Motivations and Barriers to Renewable Energy Development: Insights from a Survey of Municipal Decision-Makers in Alberta, Canada

**Sonak Patel**

Department of Resource Economics and Environmental Sociology, University of Alberta, Canada

**John R. Parkins**

Department of Resource Economics and Environmental Sociology, University of Alberta, Canada

### **Abstract:**

Municipal renewable energy development is a component of community energy that remains under-examined. Particularly, within jurisdictions like Alberta, Canada, where fossil fuels remain dominant, transition to decentralized and renewable energy systems can be challenging. To gain a deeper understanding of the motivations and the barriers to building renewable energy projects within municipalities, we utilize a province-wide survey of municipal decision-makers ( $n = 101$ ). Results are examined through a framework that combines the theory of planned behaviour with transition theory to identify specific motivations and challenges associated with renewable energy development in this jurisdiction. Consistent with other research, results highlight the perception of economic value that encourages municipal renewable development. Key constraints on the development of renewable projects are associated with difficulties in accessing grants, limited support from the provincial government, and a concern about aesthetics and negative impacts on natural landscapes. Results are discussed in the context of published literature on this topic, with insights on the value of this blended theoretical framework for unpacking and understanding constraints and opportunities for renewable energy development at the municipal level.

### **Keywords:**

Community energy, Transition theory, Theory of planned behaviour, Municipal decision-making.

# International Conference on Environmental Engineering and Renewable Energy (ICENVERE-23)

## A Comparison and Methodological Proposal for Hybrid Approaches to Quantify Environmental Impacts: A Case Study for Renewable Energies

### **A.R. Gamarra**

Universidad Politécnica de Madrid (UPM), C/ José Gutiérrez Abascal, Madrid, Spain  
Research Centre for Energy, Environment and Technology (Ciemat), Madrid, Spain

### **Y. Lechón**

Research Centre for Energy, Environment and Technology (Ciemat), Madrid, Spain

### **S. Banacloche**

Research Centre for Energy, Environment and Technology (Ciemat), Madrid, Spain

### **B. Corona**

Copernicus Institute of Sustainable Development, Utrecht University, Princetonlaan, Utrecht, Netherlands

### **Abstract:**

The transition towards a more sustainable and decarbonised energy system is mandatory for achieving global climate objectives, and counting on proper tools to evaluate sustainability is essential. Among sustainability assessment methodologies, hybrid approaches integrating Input-Output analysis (IOA) and Life Cycle Assessment (LCA) are often proposed to overcome limitations and take advantage of strengths of both methodologies. In this paper we propose a new hybrid tiered approach, named Identification and Subtraction Method (ISM). Through a case study of Concentrated Solar Power (CSP) technology, we test the proposed method assessing seven environmental indicators and compare the results obtained by different methodological approaches: Environmental Extended Multiregional Input-Output (EMRIO), LCA and two hybrid approaches.

Results showed that, in general, LCA and EMRIO provide the lowest and upper impact values, respectively. The ISM method expands the LCA boundaries by including indirect impacts, avoiding double-counting and retaining the technological detail and representativeness of the LCA. The main advantage is the ability to establish with high accuracy the impact coming from the LCA system boundaries. Furthermore, ISM is easy to undertake for LCA practitioners, is a low time-consuming hybrid approach once the LCA and EMRIO models are run, and it does not require the alteration of the IO matrix as other hybrid methods. However, the need to perform the EMRIO and LCA analysis could imply high detailed data needs. An additional limitation of the model is that it is not be able to include partial contributions from EMRIO sectors. The highest differences between results obtained by the different methods are found in the assessment of local impacts and the resources depletion, while the methods tend to agree more on global and regional impacts quantification. However, there are limitations to the implementation of the impact characterization methods that should be borne in mind when comparing the results of the different methods.

### **Keywords:**

Multiregional input-output, Life cycle assessment, Environmental impact assessment, Hybrid life cycle assessment, Concentrated solar power.

**International Conference on  
Environmental Engineering and Renewable Energy  
(ICENVERE-23)**

**Reliability Index Based Optimal Sizing and Statistical Performance Analysis of Stand-Alone Hybrid Renewable Energy System using Metaheuristic Algorithms**

**M. Thirunavukkarasu**

School of Electrical Engineering, Vellore Institute of Technology, Vellore, India

**Himadri Lala**

School of Electrical Engineering, Vellore Institute of Technology, Vellore, India

**Abstract:**

Integration of renewable energy systems can provide reliable, environmentally sustainable, and cost-effective alternatives for meeting the demand for electricity in remote locations. In this study, recently developed meta-heuristic techniques are explored to find the optimal design for two combinations of off-grid hybrid renewable energy systems. To evaluate the performance, the Tasmanian devil Optimization (TDO) was compared to three meta-heuristic algorithms, called the COOT bird optimization algorithm (COOT), the Grey wolf algorithm (GWO), and the Beluga whale optimization (BWO), and determined the optimal design of the proposed off-grid energy system in terms of best and worst-case solutions. The system consisting of a solar-battery is more cost-effective, with the lowest total annual cost (TAC) of 36,859 \$ and the lowest levelized cost of electricity (LCOE) of 0.0930 \$/kWh for 0% LPSP<sub>max</sub> level as compared to the wind turbine-battery-diesel generator with the highest TAC (102580 \$) and LCOE (0.2589 \$/kWh). Hence, a solar-battery hybrid system is more viable for producing clean energy with effective storage and better power system reliability enhancement. Also, the obtained simulation results reveal the supremacy of the TDO compared to the other three meta-heuristic algorithms, where it achieved the optimal solution with a quick convergence time and fewer oscillations.

**Keywords:**

Hybrid renewable energy system, Sizing optimization, Loss of power supply probability, Renewable fraction, Meta-heuristic techniques, Convergence rate.

# International Conference on Environmental Engineering and Renewable Energy (ICENVERE-23)

## Renewable Energy Public-Private Partnership Projects in Egypt: Perception of the Barriers and Key Success Factors by Sector

**Kareem Othman**

Civil Engineering Department, University of Toronto, Toronto, Canada

Public Works Department, Faculty of Engineering, Cairo University, Giza, Egypt

**Rana Khallaf**

Future University in Egypt, Cairo, Egypt

### **Abstract:**

Given its location, Egypt has a tremendous potential for renewable energy resources such as wind, solar, and hydropower. On the other hand, renewable energy projects require huge upfront costs which makes it difficult for the Egyptian government to fulfill. Thus, renewable energy projects in Egypt are conducted in the form of public-private partnership (PPP) projects to take advantage of the private entity's financial support. Thus, this study focuses on studying and analyzing renewable energy PPPs in Egypt using a questionnaire survey. First, the main barriers and keys success factors (KSFs) were identified by collecting previous studies in the area to build the survey. The survey was then created and disseminated to experts involved in renewable energy PPPs in Egypt. A total of 25 responses were collected from experts in the public and private sectors. The results show that the main barriers for renewable energy PPPs in Egypt are regulatory and political barriers, while well prepared contact documents and skilled and efficient parties are the main KSFs. Additionally, the different sectors perceive the barriers and KSFs differently. Finally, the results show that unlike the public sector, the private sector is efficient in identifying and valuing risks appropriately.

### **Keywords:**

Renewable energy, Public-private partnership, Barriers, Key success factors, Key performance indicators, Egypt.

# International Conference on Environmental Engineering and Renewable Energy (ICENVERE-23)

## **Hydrogen Production, Storage and Transport for Renewable Energy and Chemicals: An Environmental Footprint Assessment**

**Robert Hren**

Faculty of Chemistry and Chemical Engineering, University of Maribor, Maribor, Slovenia

**Annamaria Vujanović**

Faculty of Chemistry and Chemical Engineering, University of Maribor, Maribor, Slovenia

### **Abstract:**

Hydrogen applications range from an energy carrier to a feedstock producing bulk and other chemicals and as an essential reactant in various industrial applications. However, the sustainability of hydrogen production, storage and transport are neither unquestionable nor equal. Hydrogen is produced from natural gas, biogas, aluminium, acid gas, biomass, electrolytic water splitting and others; a total of eleven sources were investigated in this work. The environmental impact of hydrogen production, storage and transport is evaluated in terms of greenhouse gas and energy footprints, acidification, eutrophication, human toxicity potential, and eco-cost. Different electricity mixes and energy footprint accounting approaches, supported by sensitivity analysis, are conducted for a comprehensive overview. H<sub>2</sub> produced from acid gas is identified as the production route with the highest eco-benefit (-41,188 €/t H<sub>2</sub>), while the biomass gasification method incurred the highest eco-cost (11,259 €/t H<sub>2</sub>). The water electrolysis method shows a net positive energy footprint (60.32 GJ/t H<sub>2</sub>), suggesting that more energy is used than produced. Considering the operating footprint of storage, and transportation, gaseous hydrogen transported via a pipeline is a better alternative from an environmental point of view, and with a lower energy footprint (38 %–85%) than the other options. Storage and transport (without construction) could have accounted for around 35.5% of the total GHG footprint of a hydrogen value chain (production, storage, transportation and losses) if liquefied and transported via road transport instead of a pipeline. The identified results propose which technologies are less burdensome to the environment.

### **Keywords:**

Hydrogen producing technologies, Hydrogen storage, Hydrogen transport, Life cycle assessment, Different electricity sources, Energy and environmental footprints, Eco-benefit and eco-cost, Comparative impact assessment.

# International Conference on Environmental Engineering and Renewable Energy (ICENVERE-23)

## Drivers and Challenges of Off-Grid Renewable Energy-Based Projects in West Africa: A Review

**Kofi Nyarko**

Department of Energy Systems Engineering, Faculty of Engineering, Koforidua Technical University, Koforidua, Ghana

**Jonathan Whale**

Discipline of Engineering and Energy, Murdoch University, Murdoch, Australia

**Tania Urmee**

Discipline of Engineering and Energy, Murdoch University, Murdoch, Australia

### **Abstract:**

Off-grid hybrid power systems with renewable energy as the primary resource remain the best option to electrify rural/remote areas in developing countries to help attain universal electricity access by 2030. However, deploying these systems in West Africa faces several challenges and regularly fail to transition from pilot, donor-sponsored projects to sustainable large-scale implementations. The study examined the drivers and challenges by conducting a review of previous studies done in the region and a short survey in Ghana. Using Political, Economic, Social, Technical, Legal and Environmental dimensions, the review and survey showed that economic challenges have the worst impacts on the sustainable development of off-grid renewable energy-based power systems in WA. Further, the analysis revealed patterns and linkages among the challenges that make it detrimental to focus solely on the most pressing challenges.

### **Keywords:**

Off-grid hybrid power system, Sustainable energy, Renewable energy, Rural area power system, West Africa, PESTLE analysis.

# International Conference on Environmental Engineering and Renewable Energy (ICENVERE-23)

## Techno-Economic Analysis of a Renewable-Based Hybrid Energy System for Utility and Transportation Facilities in a Remote Community of Northern Alberta

**Tazrin Jahan Priyanka**

Department of Mechanical Engineering, Donadeo Innovation Centre for Engineering, University of Alberta, Edmonton, Alberta, Canada

**Shivam Atre**

Department of Mechanical Engineering, Donadeo Innovation Centre for Engineering, University of Alberta, Edmonton, Alberta, Canada

### **Abstract:**

Many off-grid communities in Canada are dependent on diesel generators to fulfill their utility and transportation needs, causing destructive environmental impact. This study aims to optimize and investigate the techno-economic feasibility of a hybrid renewable energy system to satisfy the 1.6 MWh/day electricity, 184.2 kWh/day thermal, and 428.38 kg/year hydrogen demand simultaneously, Trout Lake, a remote community of Northern Alberta. A novel hybrid energy system consisting of solar PV, wind turbine, electrolyzer, hydrogen tank, battery, fuel cell, hydrogen boiler, and thermal load controller has been proposed to generate electricity, heat, and hydrogen by renewables which reduce carbon emission utilizing the excess energy (EE). Five different scenarios were developed in HOMER Pro software, and the results were compared to identify the best combination of hybrid renewable energy systems. The results indicate that the fifth scenario is the optimal renewable energy system that provides a lower cost of energy (COE) at \$0.675/kWh and can reduce 99.99% carbon emission compared to the diesel-based system. Additionally, the utilization of thermal load controller, battery, and fuel cell improved the system's reliability, increasing renewable fraction (RF) (93.5%) and reducing EE (58.3%) significantly. In comparison to the diesel-based systems, it is also discovered that battery energy storage is the most affordable option, while fuel cells are the more expensive choice for remote community. Sensitivity analyses are performed to measure the impact of different dominating factors on COE, EE, and RF.

### **Keywords:**

Hybrid energy system, Off-grid, Cost of energy, Excess energy, Renewable energy, HOMER, Sensitivity analysis.

# International Conference on Environmental Engineering and Renewable Energy (ICENVERE-23)

## Optimal Sorting and Recycling of Plastic Waste as a Renewable Energy Resource Considering Economic Feasibility and Environmental Pollution

**Jonghun Lim**

Green Materials and Processes R&D Group, Korea Institute of Industrial Technology, Ulsan, Republic of Korea  
Department of Chemical and Biomolecular Engineering, Yonsei University, Seoul, Republic of Korea

### **Abstract:**

This work suggests an optimal strategy to sort and recycle plastic waste as a renewable energy resource with maximizing economic feasibility and mitigating environmental pollution. To derive the optimal sorting and recycling strategies of plastic waste, a novel optimization model is developed; it calculates the overall profit by subtracting the profit of recycling plastic from the total annualized cost. Then the model is used to identify the optimal strategy to sort and recycle plastic waste as a renewable energy resource in mixed-integer nonlinear programming that maximizes the overall profit. In the derived optimal sorting and recycling strategy, high-density polyethylene is recycled to produce downgrade plastic; low-density polyethylene, polypropylene, and polystyrene are recycled as pyrolysis oil; and polyethylene terephthalate is recycled to produce refuse plastic fuel. The derived optimal case can significantly increase the overall profit by about 3,137% (i.e., 35 US\$/1 kg of recycled plastic), and 492% (i.e., 29 US\$/1 kg of recycled plastic) compared to conventional case in South Korea and Japan respectively.

### **Keywords:**

Plastic waste, Sorting, Recycling, Optimization.

# International Conference on Environmental Engineering and Renewable Energy (ICENVERE-23)

## Evaluation of Dynamic Growth Trend of Renewable Energy Based on Mathematical Model

**Jiaona Li**

School of General Education and International Studies, Chongqing College of Electronic Engineering, Chongqing, China

**Abstract:**

Energy is an important basis for economic growth and social development and plays a vital role in the modern economic system. Due to the overuse and consumption of fossil fuels, and the overreliance of economic growth on fossil fuels, fossil fuels not only play an important role in the current economic system, it is also the main cause of environmental problems. The CO<sub>2</sub> emissions from the combustion of fossil fuels account for 85% of the total emissions, and the greenhouse effect contributes 50% of all greenhouse gases, causing a serious greenhouse effect problem. It releases 45% of sulfur dioxide emissions and 35% of particulate matter into the atmosphere, causing severe acid rain pollution. If the power structure cannot be effectively repaired, the environmental pollution would increase. At present, energy development is faced with two major problems: resource scarcity and environmental pollution. In the 21st century, renewable energy has increasingly become the preferred strategy for energy development in many countries in the world due to its unique resources and environmental benefits. As technology improves and production costs decrease, renewable energy would greatly replace fossil fuels. Renewable energy is predicted by analyzing and comparing commonly used mathematical models using grey system theory, engineering statistical software, and relevant analysis principles. Theoretical and practical research in this field is essential due to the serious conflict between energy demand and environmental issues. Through experiments and algorithms, the application results of the mathematical model in the dynamic growth trend of renewable energy were obtained, and it can be concluded that the mathematical model analysis had a 24.8% improvement in the dynamic growth trend of renewable energy.

**Keywords:**

Mathematical model analysis, Renewable energy, Dynamic growth, Renewable energy dynamic growth.

# International Conference on Environmental Engineering and Renewable Energy (ICENVERE-23)

## Energy Policy Simulation in Times of Crisis: Revisiting the Impact of Renewable and Non-Renewable Energy Production on Environmental Quality in Germany

**Festus Fatai Adedoyin**

Department of Computing and Informatics, Bournemouth University, United Kingdom

**Naila Erum**

Accounting Research Institute, Universiti Teknologi Mara (UiTM), Malaysia

**Dilvin Taşkin**

Faculty of Business, Yasar University, Turkey

**Daouia Chebab**

College of Business Administration, University of Bahrain, Kingdom of Bahrain

### **Abstract:**

In this paper, we examine for the first time in the literature the implications of energy policy alternatives for Germany considering the aftermath of coronavirus as well as Electricity and Gas energy supply shortages. Whilst several policy options are open to the government, the choice of investment in renewable energy generation versus disinvestment in non-renewable energy such as coal energy generation provides divergent impacts in the long term. We utilize data from British Petroleum and the World Bank Development Indicator database for Germany covering 1981 to 2020 to explore a Carbon function by applying a battery of Autoregressive distributed lag model (ARDL), dynamic ARDL and Kernel-Based Regularized Least squares approaches. The particular policy tested is the pledge by Germany to decrease emissions by ~100% in 2050, and this was integrated through the estimation of dynamic ARDL estimation. The simulation result shows that a +61% shock in renewable energy production decreases carbon emissions unlike coal energy production which increases carbon emissions in the beginning but the carbon emissions decrease thereafter. The findings highlight the inevitability of cutting down on coal production, and recommends energy investment alternatives. Hence, Germany's energy policy should contemplate more thoroughly on these factors.

### **Keywords:**

Renewable energy production, Carbon dioxide emissions, Coal consumption, Air transportation, Dynamic ARDL, Simulation.

# International Conference on Environmental Engineering and Renewable Energy (ICENVERE-23)

## Impacts of Integrating Engineering Design Process into STEM Makerspace on Renewable Energy Unit to Foster Students' System Thinking Skills

**Abdurrahman Abdurrahman**

Physics Education Department, University of Lampung, Indonesia

### **Abstract:**

Currently, science education systems around the world are faced with global challenges, especially in anticipating environmental changes related to sustainable development programs. Complex system problems related to climate change, reduced fossil-based energy reserves, and social environmental problems that have an impact on the economy have made stakeholders aware of the Education for Sustainability Development (ESD) program. This study aims to examine the effectiveness of STEM-PBL integrated Engineering Design Process (EDP) in renewable energy learning units to improve students' system thinking skills. The quantitative experimental research with a non-equivalent control group design was conducted on 67 high school students in XI grades. The results showed that the performance of students who were taught with STEM-EDP was better than students who studied with traditional STEM learning approach. In addition, this learning strategy also encourages students to be actively involved in every EDP process so that they show good performance in mind-on and hands-on activities which have an impact on increasing students' system thinking abilities. Furthermore, the STEM-EDP learning is implemented to develop students' ability to design through applied technology and engineered activities, paying special attention to design-based theory. It does not require students and teachers to prepare super-sophisticated technology, because the integration of technology in this learning design used cheap, simple and 'easy to find' equipments, to create more meaningful learning packages. In the critical pedagogy, STEM-PBL integrated EDP can be used to systematically foster students' STEM literacy and thinking skills through the engineering design thinking process, thus expanding students' cognitive building and perspectives in reducing the routine in conventional pedagogy.

### **Keywords:**

Education for sustainable development, STEM, Systems thinking.

# International Conference on Environmental Engineering and Renewable Energy (ICENVERE-23)

## The Removal of Phosphate using NaP / Chitosan Composite

**Phuong Lan Tran-Nguyen**

Faculty of Mechanical Engineering, Can Tho University, Vietnam

**Kim-Phung Ly**

Faculty of Chemical Engineering, Can Tho University, Vietnam

**Xuan Vy Cao-Thi**

Faculty of Chemical Engineering, Can Tho University, Vietnam

**Minh-Tien Pham**

Faculty of Chemical Engineering, Can Tho University, Vietnam

**Duc-Duy Le**

Faculty of Chemical Engineering, Can Tho University, Vietnam

**Minh Thu Tran-Thi**

Can Tho University of Technology, Vietnam

**Nguyen Thi Nhu Y**

Can Tho University of Technology, Vietnam

### **Abstract:**

Nowadays, the penetration of phosphate ions into the aquatic environment becomes more serious. This can increase the growth of algae and aquatic plants, leading to a decrease in dissolved oxides known as eutrophication. Furthermore, high phosphate concentration can also cause algal bloom, which is harmful to animals and humans if exposed. Rice husk ash (RHA), an agricultural by-product, is a potential raw material for the synthesis of zeolite - a superior adsorbent for removing pollutants. Zeolite-based composite materials have gained prominence and popularity in recent years. In this study, NaP/chitosan (ZPCS) composite was prepared based on a simple and cost-efficient method with zeolite NaP derived from RHA. The composite was synthesized under conditions as follows: mass ratio of zeolite:chitosan = 1:2 (w/w), reaction time = 2.5 h. Physicochemical properties of the composite were analyzed via methods such as Fourier transform infrared spectroscopy (FTIR), thermogravimetric analysis (TGA), scanning electron microscopy (SEM) and zeta potential. Moreover, the phosphate adsorption capacity of ZPCS composite was also evaluated with the adsorption efficiency and capacity of 40.72% and 99.55 mg/g, respectively, at an initial phosphate concentration of 110 mg/L and a contact time of 30 min. The adsorption process was fitted with Langmuir and Freundlich isotherm models and the maximum adsorption capacity obtained from Langmuir model reaches a high value of 297.00 mg/g. The pseudo-first-order and pseudo-second-order models also proposed well the adsorption mechanism of phosphate onto composite.

### **Keywords:**

Adsorption, chitosan, phosphate removal, NaP/chitosan composite.



# **HƯỚNG DẪN LUẬN VĂN TỐT NGHIỆP THẠC SĨ**

1. Quyết định hướng dẫn Luận văn Thạc sĩ cho học viên Phạm Minh Tiến
2. Quyết định công nhận tốt nghiệp Thạc sĩ của học viên Phạm Minh Tiến
3. Bằng tốt nghiệp Thạc sĩ của học viên Phạm Minh Tiến

BỘ KHOA HỌC VÀ CÔNG NGHỆ  
QUỸ PHÁT TRIỂN KHOA HỌC VÀ CÔNG NGHỆ QUỐC GIA



**PHỤ LỤC KẾT QUẢ THỰC NGHIỆM**  
**BÁO CÁO TỔNG HỢP**

**KẾT QUẢ THỰC HIỆN ĐỀ TÀI NGHIÊN CỨU CƠ BẢN  
TRONG KHOA HỌC TỰ NHIÊN**

Tên đề tài: Nghiên cứu tổng hợp vật liệu zeolite từ tính  $\text{Fe}_3\text{O}_4/\text{NaP}$  có nguồn gốc từ tro trấu không nung và ứng dụng hấp phụ ion ion  $\text{Cu}^{2+}$ ,  $\text{Pb}^{2+}$ ,  $\text{NO}_3^-$  và  $\text{PO}_4^{3-}$  trong nước của ao nuôi tôm

Mã số đề tài: 103.02-2020.64

Chủ nhiệm đề tài: TS. Trần Nguyễn Phương Lan

Thành viên chính: GS. TS. Ju Yi-Hsu

TS. Lương Huỳnh Vũ Thanh

TS. Trần Thị Bích Quyên

Thư ký khoa học: TS. Nguyễn Hoàng Anh

Cần Thơ, tháng 8 năm 2023

# **NỘI DUNG BÁO CÁO**

## **1. Đánh giá tính chất của RHA và tổng hợp NaP1 từ RHA không nung**

### **1.1. Tình hình nghiên cứu trong và ngoài nước về tổng hợp zeolite từ tro trấu nung và không nung**

Những nghiên cứu về xử lý nước thải của ao nuôi tôm cho thấy rằng một số ion kim loại nặng như Cd và Pb được tìm trong bùn thải của ao nuôi [1]. Ngoài ra, sự tích tụ của đạm, lân vô cơ và hữu cơ cũng được tìm thấy trong ao nuôi cá tra thảm canh ở ĐBSCL [2]. Ngoài ra, khảo sát các chỉ tiêu lý hóa của nước và trầm tích ao nuôi tôm tại một số vùng ven biển tỉnh Quảng Ninh cho thấy rằng hàm lượng  $\text{PO}_4^{3-}$  vượt tiêu chuẩn cho phép từ 22 – 23 lần [3]. Do đó, vấn đề tìm ra những giải pháp cải thiện nguồn nước của ao nuôi tôm là đang rất cần thiết. Có nhiều phương pháp xử lý ô nhiễm các kim loại nặng, các ion nitrate và phosphate, trong đó phổ biến nhất là phương pháp hấp phụ. Phương pháp hấp phụ giúp thu hồi vật liệu hấp phụ dễ dàng, quy trình đơn giản và cho hiệu quả hấp phụ cao [4-6]. Zeolites được biết đến như vật liệu hấp phụ có khả năng trao đổi ion cao, độ chon lọc cao và tính tương thích [2-8].

Với những tính năng hấp phụ vượt trội nên zeolite NaP đã được nghiên cứu và tổng hợp từ các nguồn nguyên liệu khác nhau như từ hóa chất thương mại đến các khoáng vật tự nhiên như phlogopite, diatomite, kaolinite, hay phế phẩm tro bay, tro trấu (RHA). Nguyên liệu tổng hợp zeolite NaP rất phổ biến và rẻ tiền, chủ yếu từ các nguồn nguyên liệu giàu silica như tro trấu, tro bay, cao lanh... Zeolite NaP đã được nghiên cứu rất nhiều trên thế giới từ những năm 1990, 1993, 1998 đến nay và được tổng hợp thành công với nguyên liệu chủ yếu là từ tro bay [9-18]. Một số nghiên cứu khác cho thấy zeolite NaP cũng được tổng hợp từ cao lanh, khoáng sét phlogopite và tro trấu đã qua nung [19-21]. Đồng thời, tùy nguồn nguyên liệu và mục tiêu nghiên cứu hướng đến mà các nghiên cứu lựa chọn những phương pháp tổng hợp và điều kiện phản ứng phù hợp. Ngoài phương pháp tổng hợp truyền thống, zeolite NaP còn có thể được tổng hợp bằng cách phương pháp thủy nhiệt kết hợp bức xạ siêu âm nhằm rút ngắn thời gian phản ứng (Bảng 1-1).

Bảng 1-1 cho thấy rằng hầu hết các nghiên cứu về zeolite NaP được thực hiện bởi các nhà khoa học trên thế giới với sự đa dạng của các nguồn nguyên liệu như silica thương mại, diatomite, kaolinite thải, tro bay, metakaolinite, RHA. Ở Việt Nam, có một

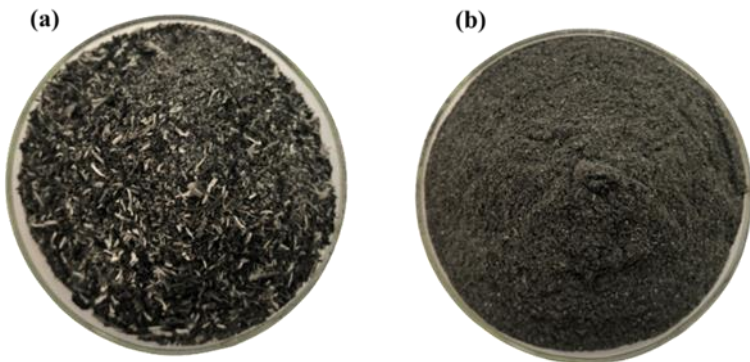
công trình nghiên cứu tổng hợp zeolite NaP từ phlogopite với độ kết tinh là 65.7% [28]. Nhìn chung, quá trình tổng hợp zeolite NaP đòi hỏi thời gian phản ứng dài từ 12 – 96 h, tuy nhiên nếu có sự hỗ trợ của sóng siêu âm thì thời gian phản ứng sẽ được giảm xuống còn 4 h. Nhiệt độ của phản ứng tổng hợp chủ yếu từ 90 – 140 °C và phản ứng đòi hỏi quá trình già hóa trước phản ứng.

**Bảng 1-1 Một số điều kiện tổng hợp zeolite NaP từ các nguồn nguyên liệu khác nhau**

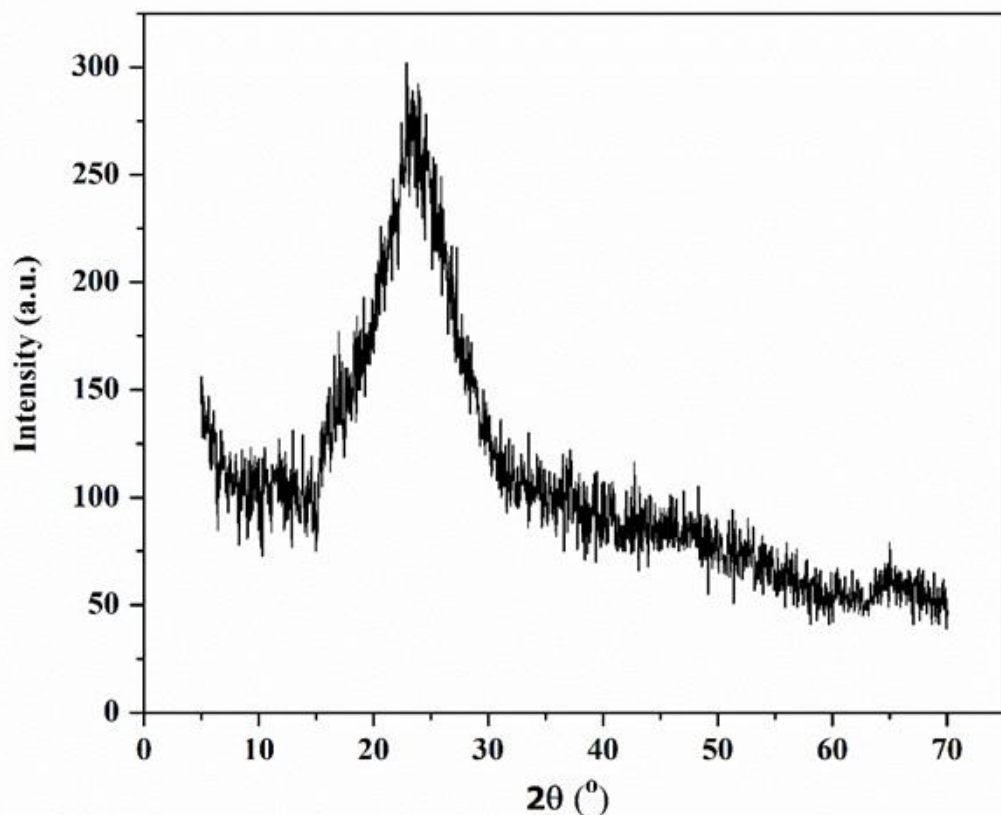
Nguyên liệu	Điều kiện tổng hợp					Độ kết tinh (%)	Tài liệu tham khảo
	Si:Al	Già hóa trước phản ứng (h)	Nhiệt độ phản ứng (°C)	Thời gian phản ứng (h)	Già hóa sau phản ứng (h)		
Silica thương mại	0.7	0.5 <sup>c</sup>	100	96 <sup>a</sup>	-	-	[30]
Silica thương mại	5	24 (25°C) <sup>b</sup> bước 1: 1 (30°C) <sup>b</sup>	100	24 <sup>b</sup>	-	-	[25]
Silica thương mại	2.5	bước 2: 3 (80°C, siêu âm)	100	12	-	-	[31]
Phlogopite	1.67	96 <sup>a,c</sup>	90	96 <sup>b</sup>	-	65.7	[28]
Diatomite	3.7	-	90	6-24 <sup>b</sup>	-	-	[32]
Tro bay	1.39	48 (47°C) <sup>b</sup>	140	48 <sup>a</sup>	-	-	[26]
Tro bay	1.1	-	100	4, siêu âm	-	-	[33]
Kaolinite phè thải (nung 700°C, 2h)	2	-	100	20	-	-	[24]
Metakaolinite (nung 650°C, 5h)	2-3.5	-	68 ± 1	38 <sup>b</sup>	-	-	[34]
Kaolinite không nung	4	-	95	48	-	92	[29]
RHA không nung	1.9	0.25 <sup>b,c</sup>	100	48 <sup>b</sup>	-	-	[35]
RHA (HCl 1N, 3h, nung 700°C, 2h)	2.5-4.5	-	140	2 <sup>a</sup>	-	-	[27]

<sup>a</sup>Không khuấy, <sup>b</sup>Có khuấy, <sup>c</sup>Nhiệt độ phòng

## 1.2. Tính chất hóa lý của RHA



Hình 1-1 RHA (a) thu gom từ khu công nghiệp và (b) đã loại bỏ tạp và nghiên mịn



Hình 1-2 Giản đồ XRD của RHA

Bảng 1-2 Thành phần hóa học của RHA

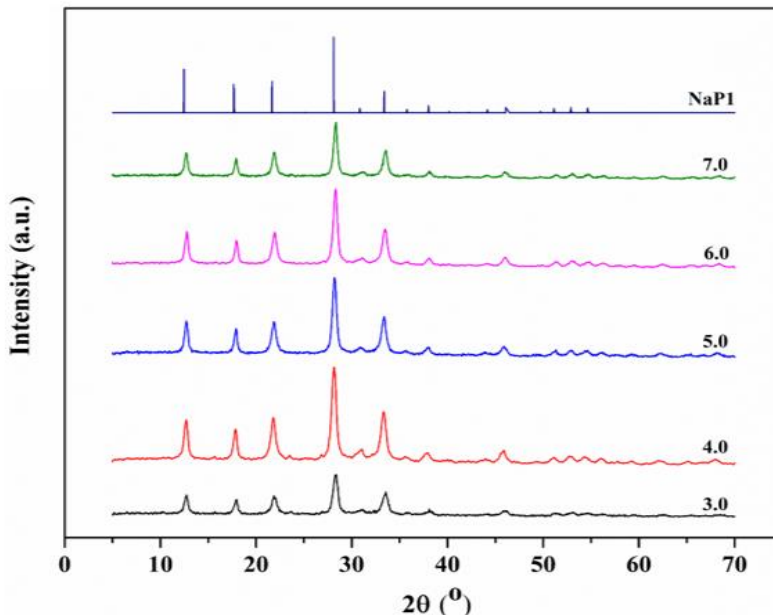
Thành phần	SiO <sub>2</sub>	K <sub>2</sub> O	Al <sub>2</sub> O <sub>3</sub>	CaO	P <sub>2</sub> O <sub>5</sub>	MnO	Fe <sub>2</sub> O <sub>3</sub>	Na <sub>2</sub> O	Khác
Hàm lượng (%)	96.11	1.47	1.16	0.48	0.2	0.19	0.15	0.11	0.11

### 1.3. Ảnh hưởng của các yếu tố đến quá trình tổng hợp zeolite NaP1

Bảng 1-3 Ảnh hưởng của tỷ lệ phôi trộn đến hiệu suất thu sản phẩm

Mẫu	Tỷ lệ $\text{SiO}_2:\text{Al}_2\text{O}_3$ (mol:mol)	Nồng độ $\text{NaOH}$ (M)	Thời gian già hoá (h)	Nhiệt độ phản ứng (°C)	Thời gian phản ứng (h)	Hiệu suất (kg sản phẩm/ kg RHA)
1	3.0	3.0	0	100	4	1.482 ± 0.042
2	4.0	3.0	0	100	4	1.194 ± 0.036
3	5.0	3.0	0	100	4	0.918 ± 0.034
4	6.0	3.0	0	100	4	0.714 ± 0.045
5	7.0	3.0	0	100	4	0.570 ± 0.028
6	4.0	1.0	0	100	4	1.086 ± 0.034
7	4.0	1.5	0	100	4	1.190 ± 0.047
8	4.0	2.0	0	100	4	1.187 ± 0.038
9	4.0	2.5	0	100	4	1.176 ± 0.035
10	4.0	3.0	0	100	4	1.171 ± 0.027
11	4.0	4.0	0	100	4	1.174 ± 0.037

#### **4.3.1. Ảnh hưởng của tỷ lệ $\text{SiO}_2:\text{Al}_2\text{O}_3$**

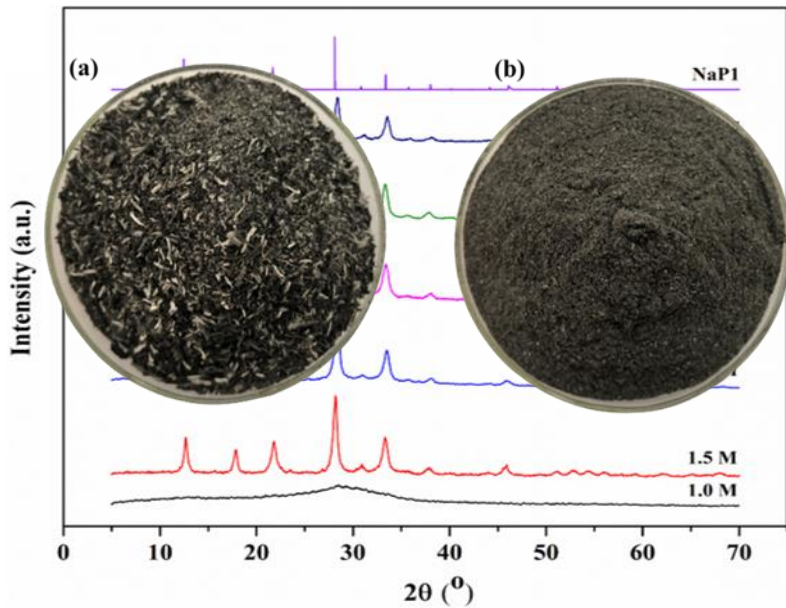


**Hình 1-3 Giản đồ XRD của zeolite NaP1 ở các tỷ lệ mol  $\text{SiO}_2/\text{Al}_2\text{O}_3$  khác nhau và thẻ chuẩn của zeolite NaP1**

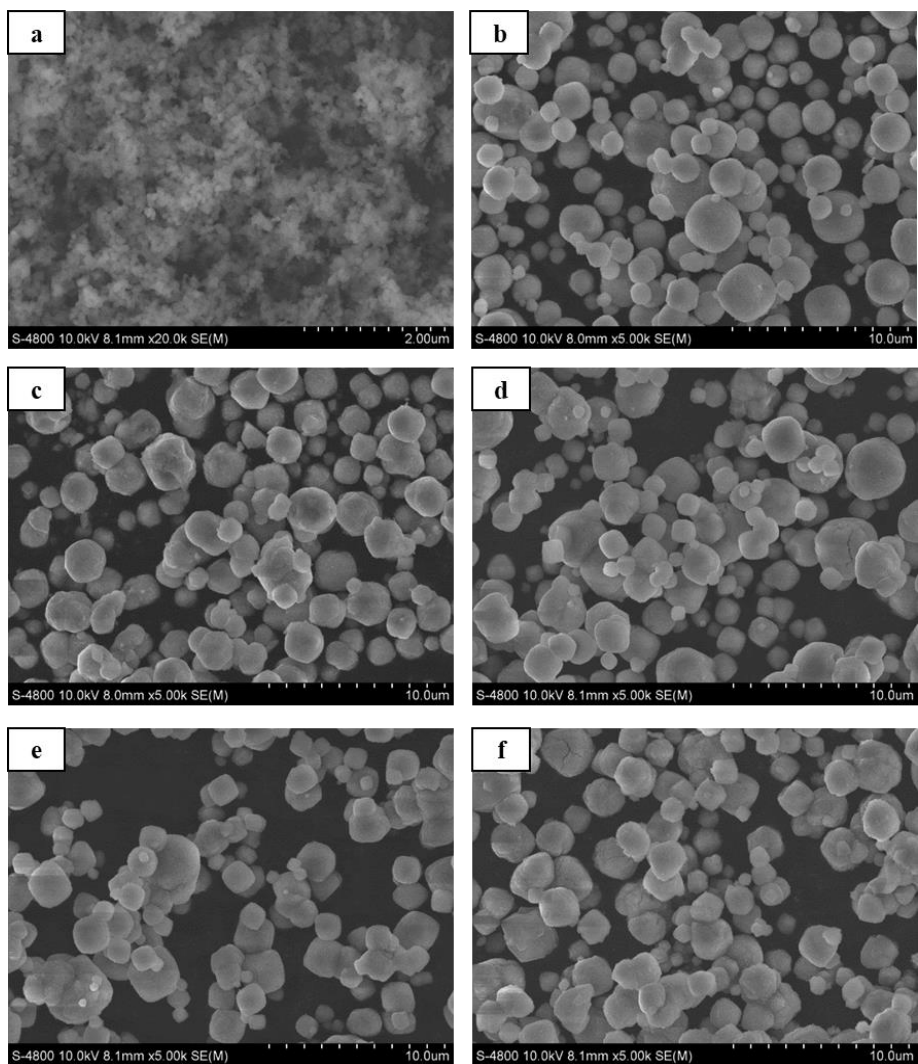
#### **4.3.2. Ảnh hưởng của nhiệt độ phản ứng**

Qua quá trình lược khảo tài liệu, thấy rằng với nhiều loại nguyên liệu ban đầu khác nhau như silica thương mại, tro trâu, tro bay, kaolin,... nhiệt độ phản ứng tối ưu phổ biến là 100°C. Do đó, nhiệt độ này được cố định trong tất cả các thí nghiệm tổng hợp zeolite NaP1.

#### **4.3.3. Ảnh hưởng của nồng độ $\text{NaOH}$**

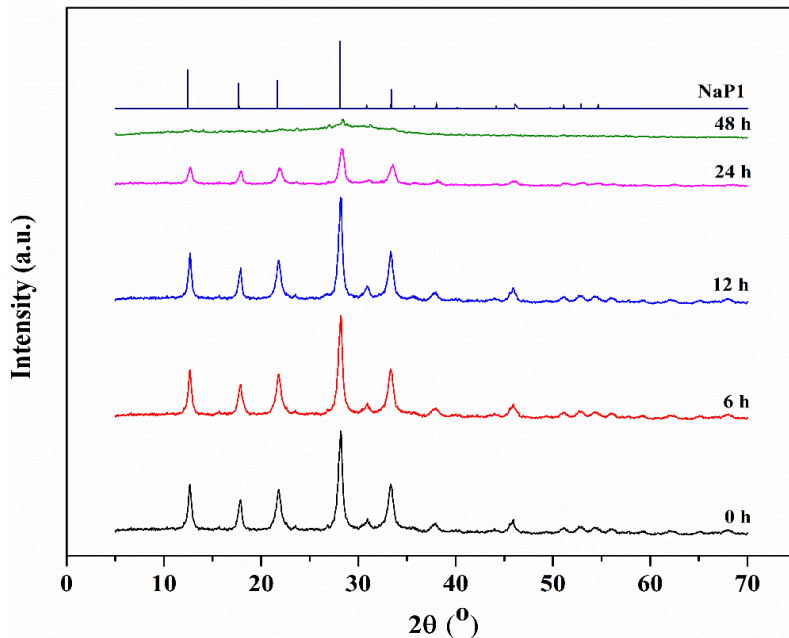


**Hình 1-4 Giản đồ XRD của zeolite NaP1 ở các nồng độ NaOH khác nhau và thẻ chuẩn của zeolite NaP1**



**Hình 1-5 Hình FE-SEM của zeolite NaP1 tại các nồng độ NaOH từ 1.0 M - 4.0 M (a-f)**

#### 4.3.4. Ảnh hưởng của thời gian già hóa

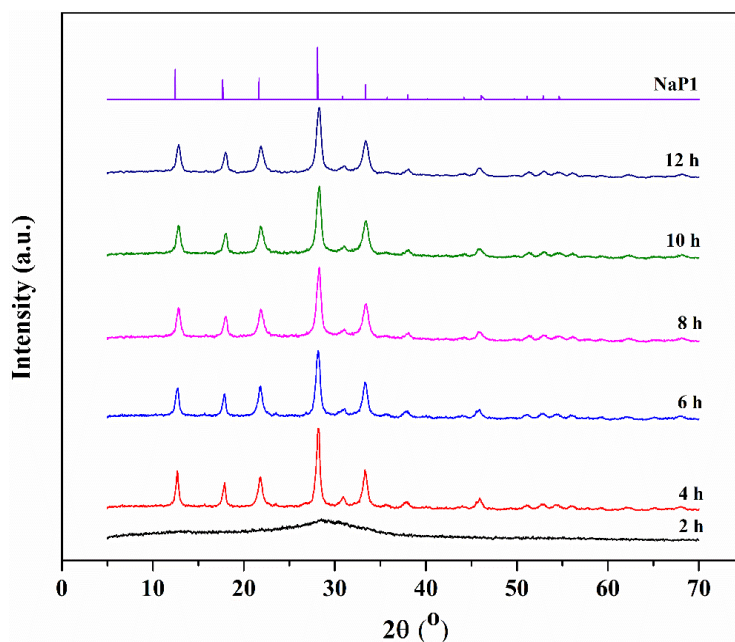


Hình 1-6 Giản đồ XRD của zeolite NaP1 ở các thời gian già hóa khác nhau và thê chuẩn của zeolite NaP1

Bảng 1-4 Kết quả BET của zeolite NaP1 tại các thời gian già hóa khác nhau

Thời gian già hóa (h)	Diện tích bề mặt ( $\text{m}^2/\text{g}$ )	Kích thước lỗ rỗng (nm)
0	20.39	34.43
6	36.95	77.57
12	37.57	64.76

#### 4.3.5. Ảnh hưởng của thời gian phản ứng



Hình 1-7 Giản đồ XRD của zeolite NaP1 ở các thời gian phản ứng khác nhau và thê chuẩn của zeolite NaP1

**Bảng 1-5 Kết quả BET của zeolite NaP1 ở các thời gian phản ứng khác nhau**

<b>Thời gian phản ứng (h)</b>	<b>Diện tích bề mặt (m<sup>2</sup>/g)</b>	<b>Kích thước lỗ rỗng (nm)</b>
4	37.57	64.76
6	38.83	42.79
8	49.62	40.77
10	47.45	74.57
12	41.56	74.58

## **2. Tổng hợp vật liệu Fe<sub>3</sub>O<sub>4</sub> và vật liệu từ tính Fe<sub>3</sub>O<sub>4</sub>/NaP1**

### **2.1. Tình hình nghiên cứu trong và ngoài nước về tổng hợp Fe<sub>3</sub>O<sub>4</sub>**

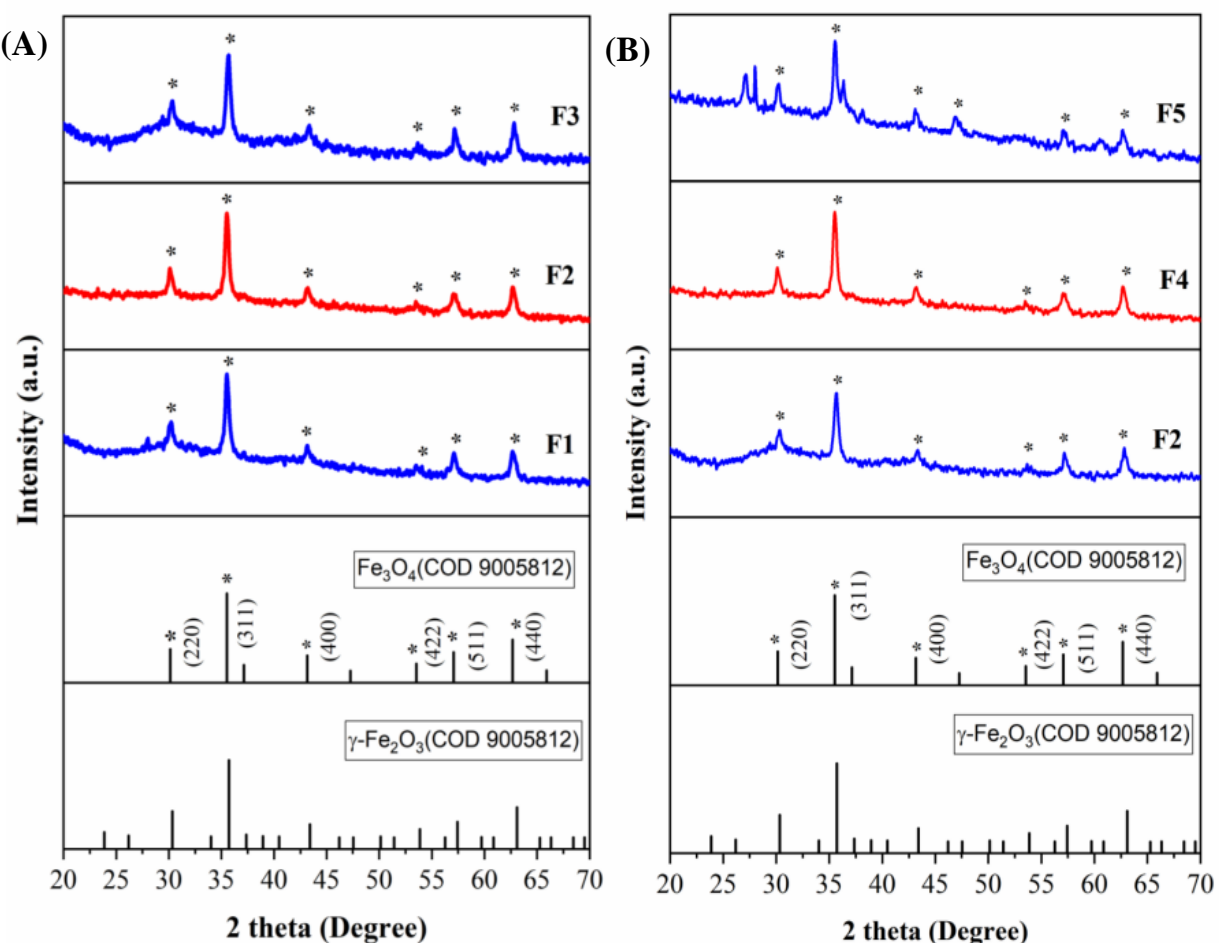
Năm 2007, Nguyễn Hữu Đức cùng cộng sự đã nghiên cứu chế tạo thành công hạt nano oxit sắt siêu thuận từ bằng phương pháp đồng kết tủa, kích thước trung bình của các hạt khoảng 10-15nm [36]. Năm 2016, Phạm Xuân Núi cùng các cộng sự đã tiến hành tổng hợp các hạt nano sắt từ bằng phương pháp vi nhũ tương ở 300 rpm trong 30 phút ở nhiệt độ phòng, dung dịch muối sắt FeCl<sub>3</sub>.6H<sub>2</sub>O và FeSO<sub>4</sub>.7H<sub>2</sub>O tỉ lệ mol 2:1 trong hỗn hợp tween-80/butan-1-ol/n-heptane [37]. Năm 2015, Nguyễn Hữu Hiếu cùng các cộng sự sử dụng phương pháp đồng kết tủa để tổng hợp các hạt nano sắt từ bằng cách khuấy trong 1 giờ ở pH 10 dung dịch muối sắt II và III [38]. Tùy vào nhu cầu ứng dụng mà kích thước hạt nano từ được điều chỉnh cho phù hợp. Trong lĩnh vực khoa học kỹ thuật, các hạt nano từ tính được ứng dụng chủ yếu để hấp phụ kim loại nặng trong xử lý nước thải như vật liệu nano Fe<sub>3</sub>O<sub>4</sub>/graphene oxide loại bỏ ion Pb<sup>2+</sup> [38]. Do diện tích bề mặt riêng lớn, độ từ tính cao và sức cản khuếch tán bên trong không đáng kể nên nano Fe<sub>3</sub>O<sub>4</sub> được nghiên cứu ứng dụng mạnh mẽ như một chất hấp phụ ion kim loại nặng trong xử lý nước thải. Hấp phụ Cd<sup>2+</sup> và Cu<sup>2+</sup> bằng vật liệu nano Fe<sub>3</sub>O<sub>4</sub>/hydroxyapatite/β-cyclodextrin được thực hiện bởi Ansari (2019) [39]. Vật liệu Fe<sub>3</sub>O<sub>4</sub>/hydroxyapatite/chitosan được sử dụng để thu hồi pherc hợp thuốc nhuộm kim loại AY220 [40]. Bên cạnh đó, vật liệu nano từ tính Fe<sub>3</sub>O<sub>4</sub>/hydroxyapatite được nghiên cứu để hấp phụ ion Hg<sup>2+</sup> trong nước thải [41]. Do vật liệu Fe<sub>3</sub>O<sub>4</sub> có khả năng hấp phụ ion kim loại và những chất hữu cơ khác nên sự kết hợp của vật liệu này và zeolite NaP là cần thiết.

Có một số công trình nghiên cứu về sự kết hợp của nano từ tính Fe<sub>3</sub>O<sub>4</sub> với zeolites và được ứng dụng trong xử lý nước thải hữu cơ hoặc kim loại nặng. Nyankson (2019) tổng hợp zeolite NaA/Fe<sub>3</sub>O<sub>4</sub> để xử lý methylene blue cho hiệu suất hấp phụ là 97.5% và hiệu suất này là 82.6% sau 3 lần tái sử dụng [42]. Nghiên cứu của Liu et al. (2013) cho

thấy rằng khi thêm 3.4%  $\text{Fe}_3\text{O}_4$  sẽ ảnh hưởng đến quá trình tách ion  $\text{NH}_4^+$  trong zeolite NaA. Nghiên cứu này cũng nhận định là zeolite từ tính NaA là một vật liệu đầy tiềm năng để xử lý ion  $\text{NH}_4^+$  trong dung dịch với khả năng hấp phụ cao, chi phí thấp và quá trình phân tách dễ dàng [43]. Zendehdel et al. (2019) nghiên cứu khả năng hấp phụ Pb (II) and Cd (II) bằng vật liệu  $\text{Fe}_3\text{O}_4/\text{NaP}/\text{NH}_2$  cho hiệu suất hấp phụ hơn 95% [44]. Quá trình thu hồi vật liệu hấp phụ cũng rất dễ dàng dựa vào tính chất từ và tái sinh bằng cách xử lý với acid.

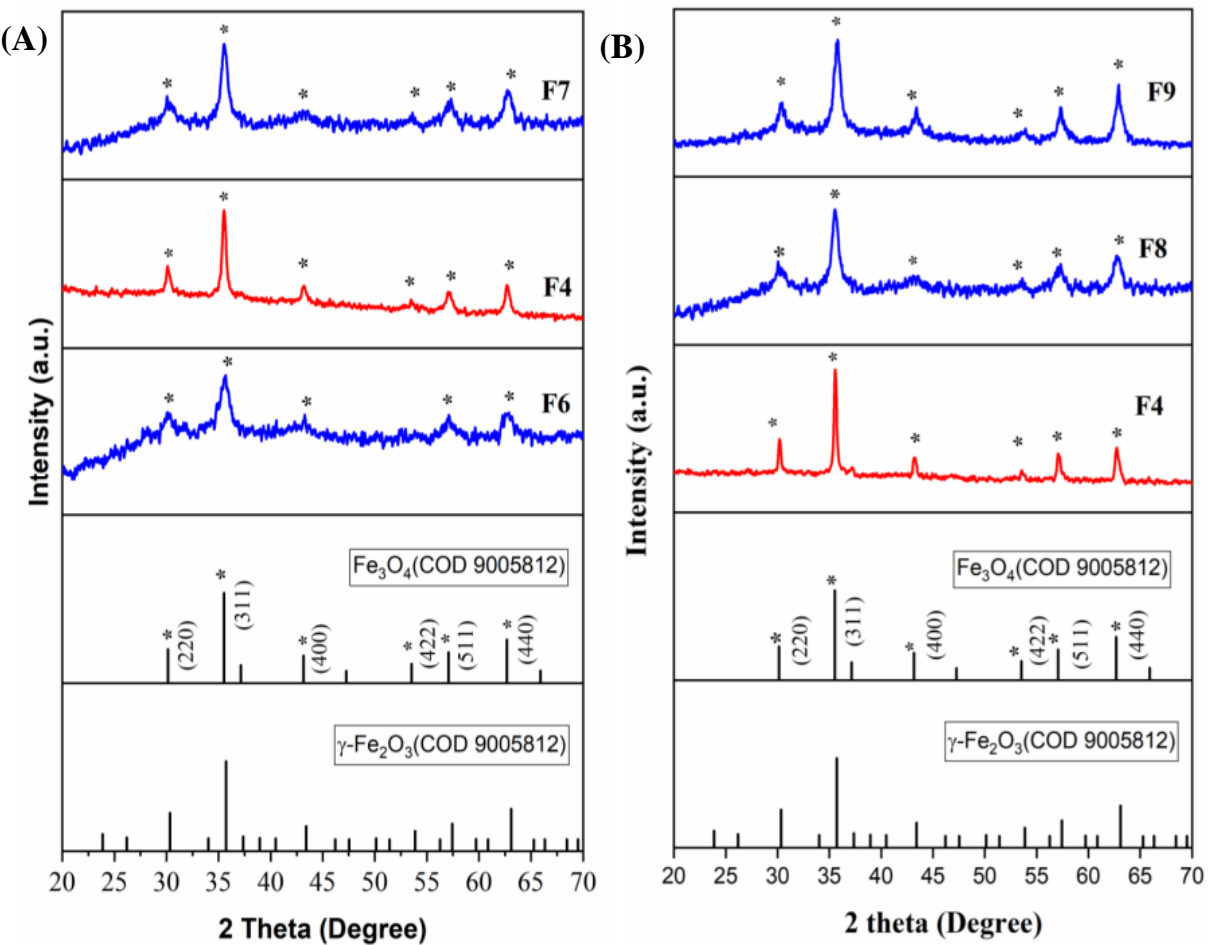
## 2.2 Ảnh hưởng của các yếu tố đến quá trình tổng hợp $\text{Fe}_3\text{O}_4$

### *Ảnh hưởng của tỷ lệ mol $\text{NaBH}_4:\text{FeCl}_3.6\text{H}_2\text{O}$ và các loại chất hoạt động bề mặt*

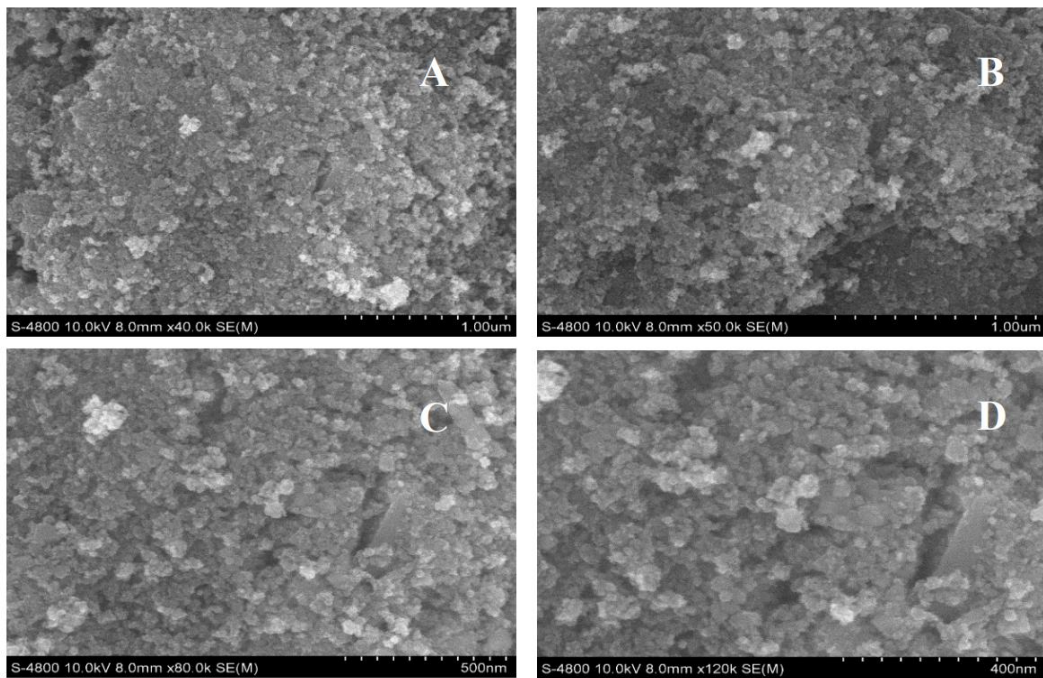


Hình 2-1 Giản đồ nhiễu xạ tia X (XRD) của các mẫu  $\text{Fe}_3\text{O}_4$  (A) ở các tỷ lệ mol  $\text{NaBH}_4:\text{FeCl}_3.6\text{H}_2\text{O} = 5:1$  (F1),  $\text{NaBH}_4:\text{FeCl}_3.6\text{H}_2\text{O} = 10:1$  (F2) và  $\text{NaBH}_4:\text{FeCl}_3.6\text{H}_2\text{O} = 15:1$  (F3). Điều kiện phản ứng:  $T (^\circ\text{C}) = 30$ ,  $t (\text{phút}) = 30$ , CHDBM CTAB 1% (v/v) và (B) ở các loại CHDBM như CHDBM = CTAB (F2), CHDBM = PEG (F4) và CHDBM = PVP (F5). Điều kiện phản ứng: tỷ lệ mol  $\text{NaBH}_4:\text{FeCl}_3.6\text{H}_2\text{O} = 10:1$ ,  $T (^\circ\text{C}) = 30$ ,  $t (\text{phút}) = 30$ , phần trăm thể tích CHDBM = 1% (v/v)

## Ảnh hưởng của phần trăm thể tích CHDBM trong dung dịch và thời gian phản ứng



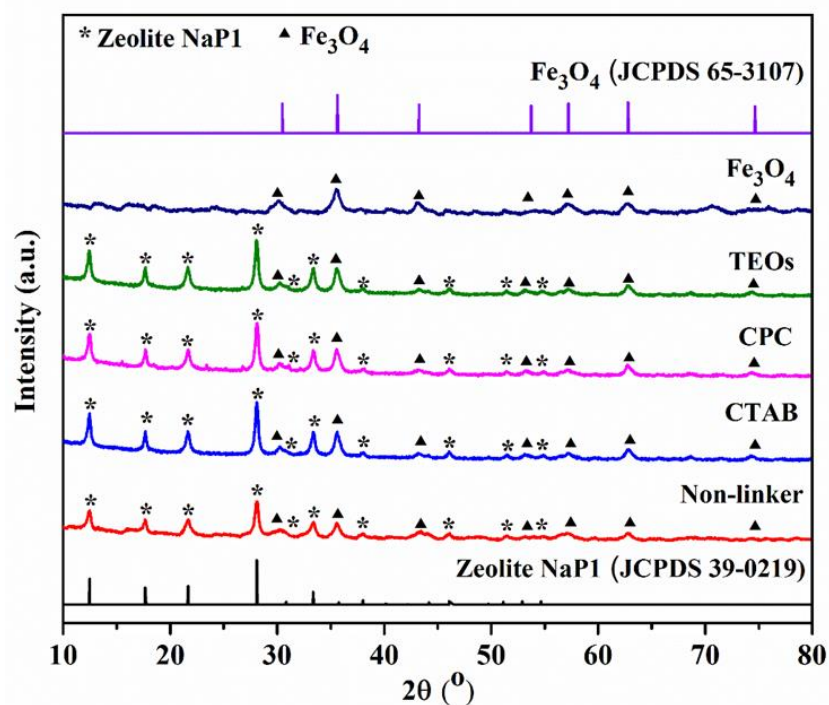
**Hình 2-2** Giản đồ nhiễu xạ tia X của các mẫu  $\text{Fe}_3\text{O}_4$  (A) ở các phần trăm thể tích (v/v) CHDBM = 0.5% (F6), CHDBM = 1% (F4) và CHDBM = 2% (F7). Điều kiện phản ứng: tỷ lệ mol  $\text{NaBH}_4:\text{FeCl}_3\cdot 6\text{H}_2\text{O} = 10:1$ , T ( $^{\circ}\text{C}$ ) = 30, t (phút) = 30, CHDBM = PEG và (B) ở các thời gian phản ứng t (phút) = 30 (F4), t (phút) = 60 (F8) và t (phút) = 90 (F9). Điều kiện phản ứng: tỷ lệ mol  $\text{NaBH}_4:\text{FeCl}_3\cdot 6\text{H}_2\text{O} = 10:1$ , T ( $^{\circ}\text{C}$ ) = 30, CHDBM = PEG 1% (v/v)



**Hình 2-3 Hình FE-SEM của nano sắt từ  $\text{Fe}_3\text{O}_4$**

### 2.3. Ảnh hưởng của các yếu tố đến quá trình tổng hợp vật liệu zeolite từ tính $\text{Fe}_3\text{O}_4/\text{NaP1}$

#### Ảnh hưởng của loại chất phân tán



**Hình 2-4 Giản đồ XRD của  $\text{Fe}_3\text{O}_4$ ,  $\text{Fe}_3\text{O}_4$ /zeolite NaP1 với các chất phân tán TEOs, CPC, CTAB và không tác nhân phân tán**

**Bảng 2-1 Kết quả BET của  $\text{Fe}_3\text{O}_4/\text{NaP1}$  với các chất phân tán khác nhau**

Mẫu	Diện tích bê mặt ( $\text{m}^2/\text{g}$ )	Thể tích lỗ rỗng ( $\text{cm}^3/\text{g}$ )	Kích thước lỗ rỗng (nm)
$\text{Fe}_3\text{O}_4/\text{NaP1}$ (TEOs)	35.935	0.090	10.024
$\text{Fe}_3\text{O}_4/\text{NaP1}$ (CTAB)	30.499	0.084	9.753
$\text{Fe}_3\text{O}_4/\text{NaP1}$ (CPC)	34.626	0.043	9.463
$\text{Fe}_3\text{O}_4/\text{NaP1}$ (Không chất phân tán)	34.382	0.079	9.177

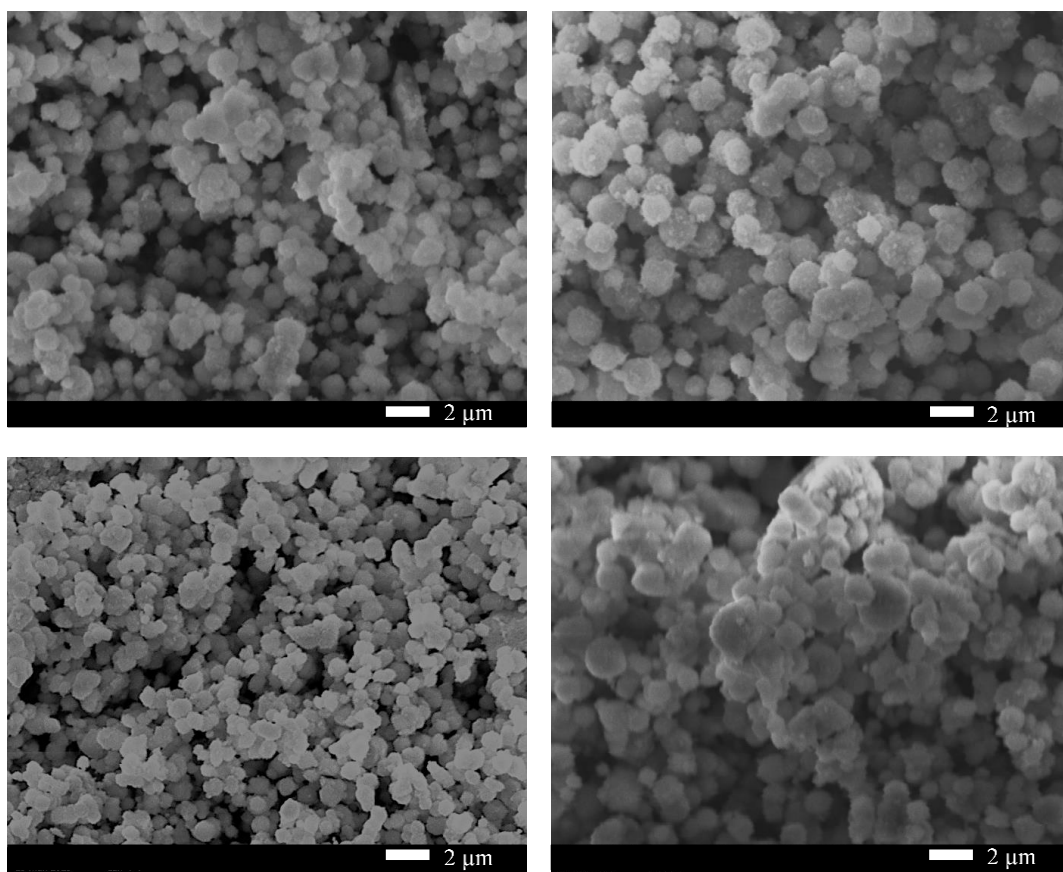
**Bảng 2-2 Thành phần hoá học của  $\text{Fe}_3\text{O}_4/\text{NaP1}$  với các chất phân tán khác nhau**

Thành phần (%)	TEOs	CTAB	CPC	Không chất phân tán
$\text{SiO}_2$	40,01	39,50	39,51	39,63
$\text{Al}_2\text{O}_3$	21,13	22,46	21,83	23,48
$\text{Na}_2\text{O}$	5,48	4,57	3,93	4,81
$\text{Fe}_2\text{O}_3$	32,55	32,59	32,76	31,18
Khác	0,83	0,88	0,97	0,90

### *Ảnh hưởng của nồng độ phần trăm của dung dịch chất phân tán*

**Bảng 2-3 Thành phần hoá học của  $\text{Fe}_3\text{O}_4/\text{NaP1}$  với các nồng độ dung dịch chất phân tán khác nhau**

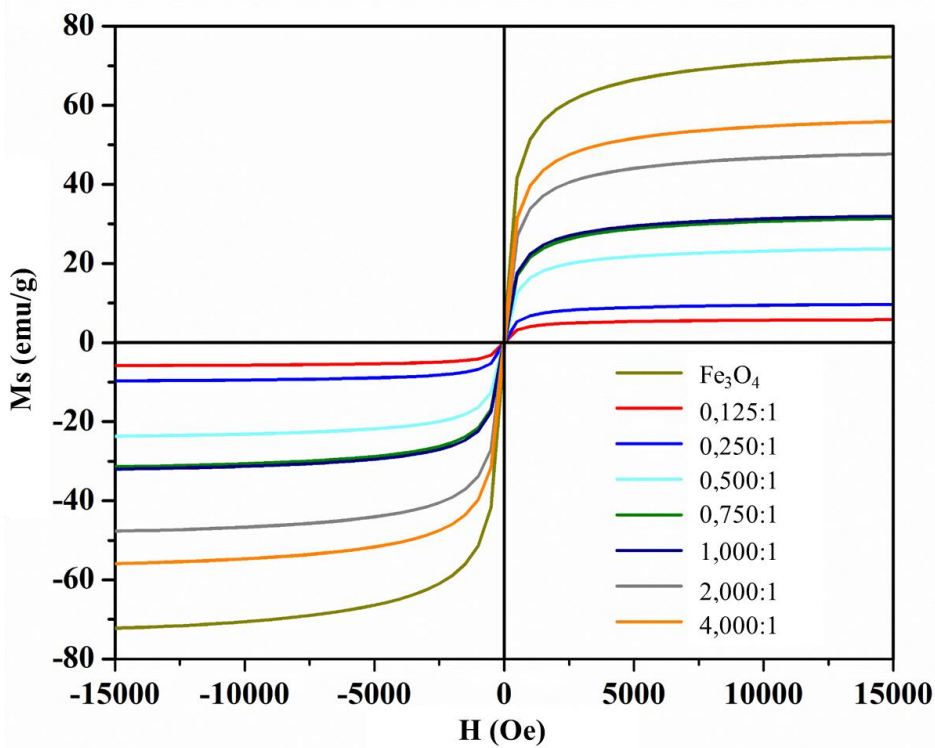
Thành phần (%)	0,5 %	1,0 %	1,5 %	2,0 %
$\text{SiO}_2$	38,54	39,08	40,75	39,51
$\text{Al}_2\text{O}_3$	23,45	22,87	20,87	21,83
$\text{Na}_2\text{O}$	4,56	3,51	3,75	3,93
$\text{Fe}_2\text{O}_3$	32,64	33,69	33,76	32,76
Khác	0,81	0,85	0,87	0,97



**Hình 2-5 Hình SEM của  $\text{Fe}_3\text{O}_4/\text{NaP1}$  với các nồng độ dung dịch chất phân tán khác nhau  
Ảnh hưởng của khối lượng  $\text{Fe}_3\text{O}_4$**

**Bảng 2-4 Kết quả BET của  $\text{Fe}_3\text{O}_4/\text{NaP1}$  với các tỷ lệ khối lượng  $\text{Fe}_3\text{O}_4:\text{NaP1}$  khác nhau**

Mẫu	Diện tích bề mặt ( $\text{m}^2/\text{g}$ )	Thể tích lỗ rỗng ( $\text{cm}^3/\text{g}$ )	Kích thước lỗ rỗng (nm)
$\text{Fe}_3\text{O}_4$	76	0,220	11,28
0,125:1	21	0,056	11,03
0,250:1	35	0,068	11,70
0,500:1	43	0,111	12,63
0,750:1	41	0,148	14,31
1,000:1	57	0,179	12,82
2,500:1	58	0,226	15,59
4,000:1	78	0,279	14,38



Hình 2-6 Momen từ của các mẫu  $\text{Fe}_3\text{O}_4/\text{NaP1}$  với các tỷ lệ khói lượng  $\text{Fe}_3\text{O}_4:\text{NaP1}$  khác nhau

### 3. Đánh giá khả năng hấp phụ các ion $\text{Cu}^{2+}$ , $\text{Pb}^{2+}$ , $\text{NO}_3^-$ và $\text{PO}_4^{3-}$ trong nước giả thải và nước ao nuôi tôm của $\text{NaP1}$ và $\text{Fe}_3\text{O}_4/\text{NaP1}$

#### 3.1. Thành phần hóa học của nước ao nuôi tôm

Bảng 3-1 Thông số hóa lý của một số loại nước ao nuôi tôm

Thông số	Loại nước			
	<sup>a</sup> MĐ 250 con/m <sup>3</sup>	<sup>a</sup> MĐ 300 con/m <sup>3</sup>	<sup>a</sup> MĐ 400 con/m <sup>3</sup>	<sup>b</sup> MĐ 250 con/m <sup>3</sup>
pH	7	7	7	7
$\text{Cu}^{2+}$ (mg/L)	$0,17 \pm 0,02$	$0,19 \pm 0,02$	$0,12 \pm 0,03$	$0,21 \pm 0,02$
$\text{Pb}^{2+}$ (mg/L)	$0,04 \pm 0,003$	$0,03 \pm 0,006$	$0,03 \pm 0,002$	$0,07 \pm 0,001$
$\text{NO}_3^-$ (mg/L)	$46,98 \pm 1,31$	$51,62 \pm 4,05$	$37,69 \pm 4,88$	$11,85 \pm 1,44$
$\text{PO}_4^{3-}$ (mg/L)	$21,63 \pm 3,18$	$29,05 \pm 2,72$	$8,93 \pm 1,36$	$48,41 \pm 5,14$

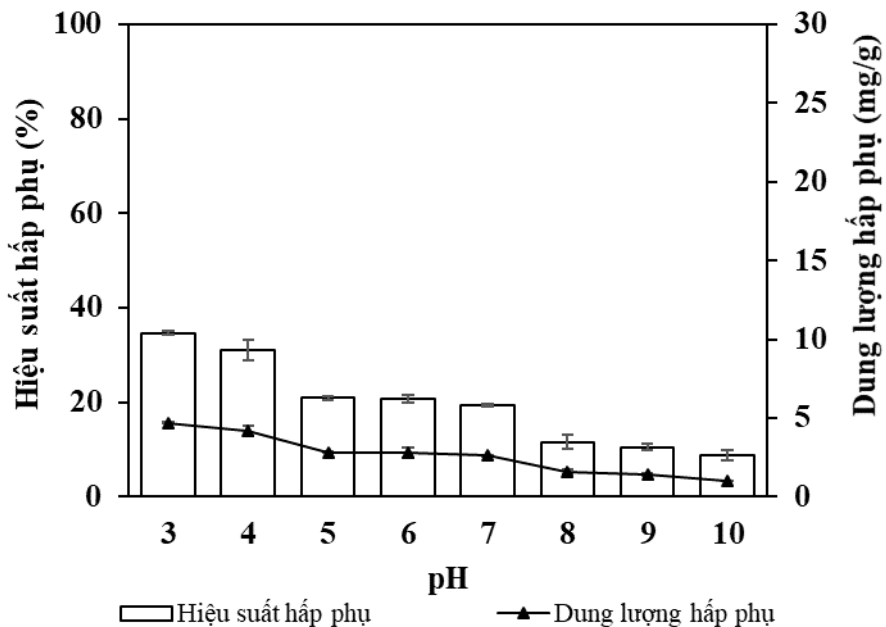
<sup>a</sup>MĐ Mật độ, <sup>a</sup>Đa loài, <sup>b</sup>Đơn loài

#### 3.2. Các yếu tố ảnh hưởng đến khả năng hấp phụ của $\text{NaP1}$ và $\text{Fe}_3\text{O}_4/\text{NaP1}$

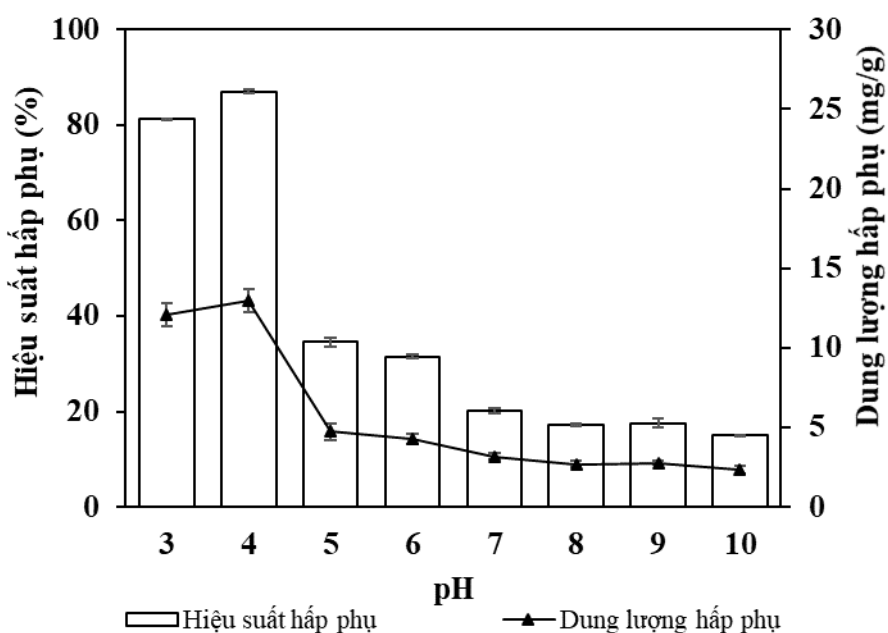
##### 3.2.1. Khả năng hấp phụ của $\text{Fe}_3\text{O}_4/\text{NaP1}$ đối với nước giả thải

## *Ảnh hưởng của pH*

Khả năng hấp phụ của  $\text{Fe}_3\text{O}_4/\text{NaP1}$  đối với hai ion  $\text{Cu}^{2+}$  và  $\text{Pb}^{2+}$  được thực hiện tại pH 5. Khả năng hấp phụ của  $\text{Fe}_3\text{O}_4/\text{NaP1}$  đối với hai ion  $\text{NO}_3^-$  và  $\text{PO}_4^{3-}$  được khảo sát với khoảng pH từ 3 – 10.

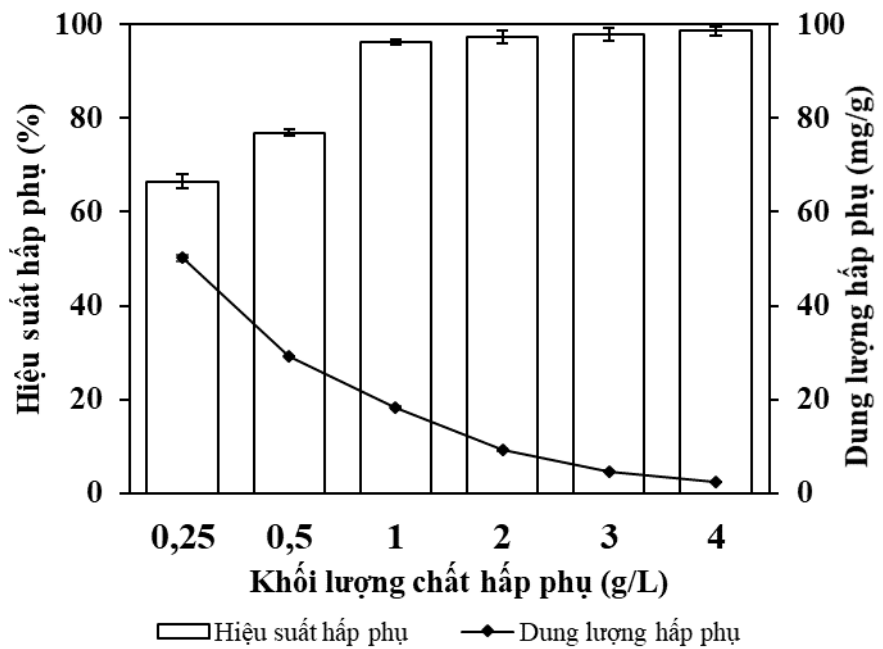


Hình 3-1 *Ảnh hưởng của pH đến khả năng hấp thụ  $\text{NO}_3^-$  của  $\text{Fe}_3\text{O}_4/\text{NaP1}$*

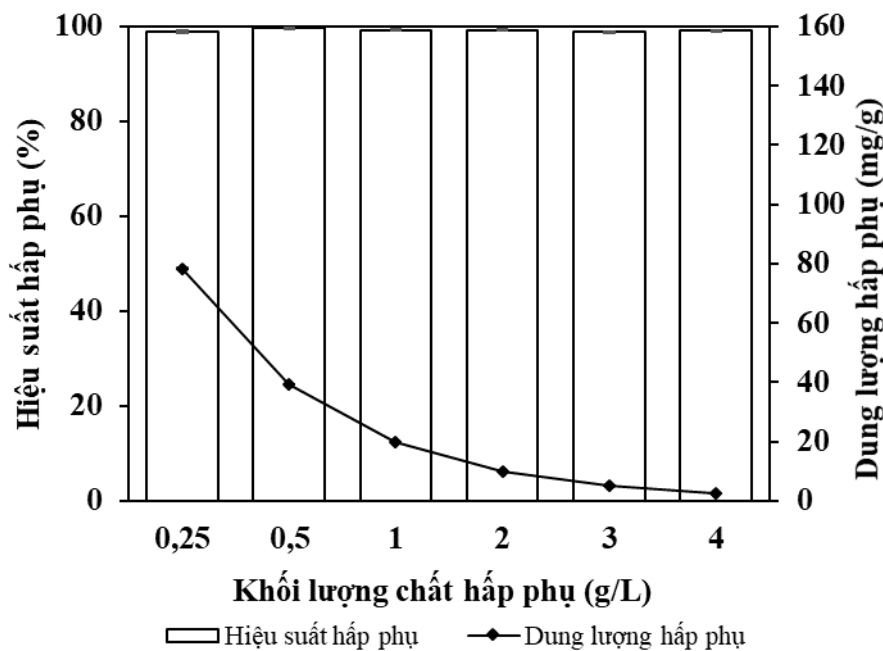


Hình 3-2 *Ảnh hưởng của pH đến khả năng hấp thụ  $\text{PO}_4^{3-}$  của  $\text{Fe}_3\text{O}_4/\text{NaP1}$*

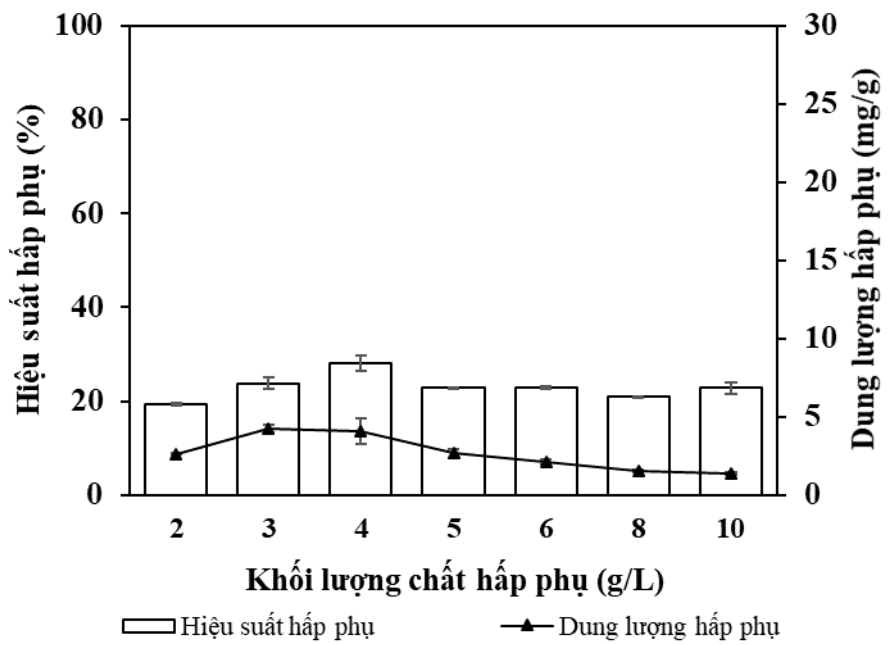
### Ảnh hưởng của khối lượng chất hấp phụ



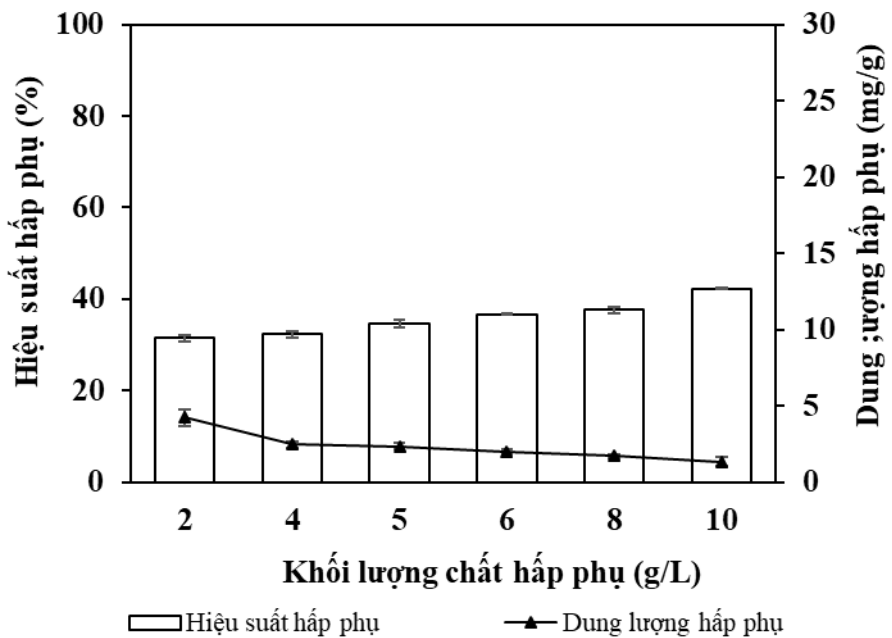
Hình 3-3 Ảnh hưởng của khối lượng chất hấp phụ đến khả năng hấp phụ  $\text{Cu}^{2+}$  của  $\text{Fe}_3\text{O}_4/\text{NaP1}$



Hình 3-4 Ảnh hưởng của khối lượng chất hấp phụ đến khả năng hấp phụ  $\text{Pb}^{2+}$  của  $\text{Fe}_3\text{O}_4/\text{NaP1}$

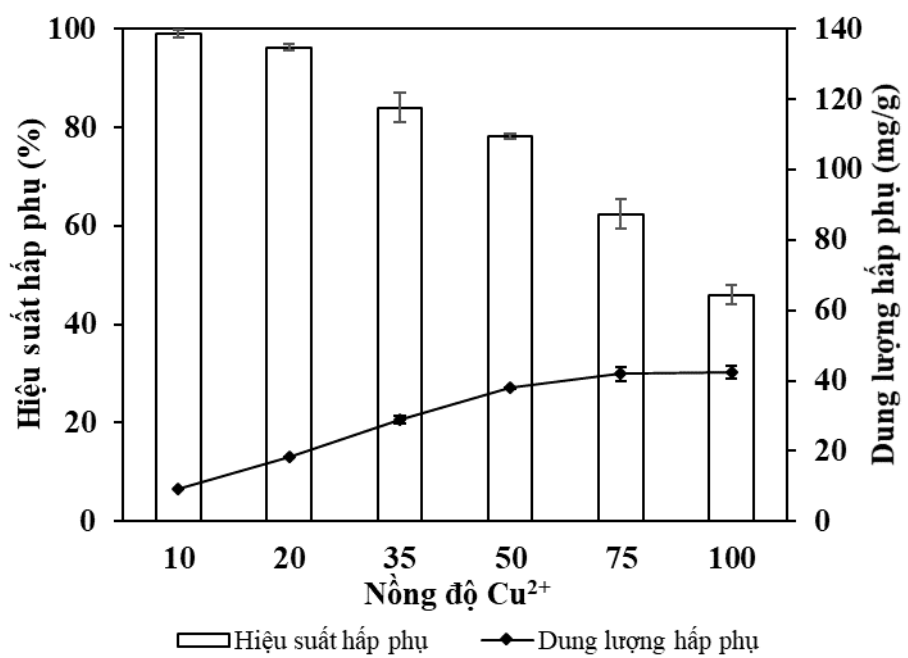


Hình 3-5 Ảnh hưởng của khối lượng chất hấp phụ đến khả năng hấp phụ  $\text{NO}_3^-$  của  $\text{Fe}_3\text{O}_4/\text{NaP1}$

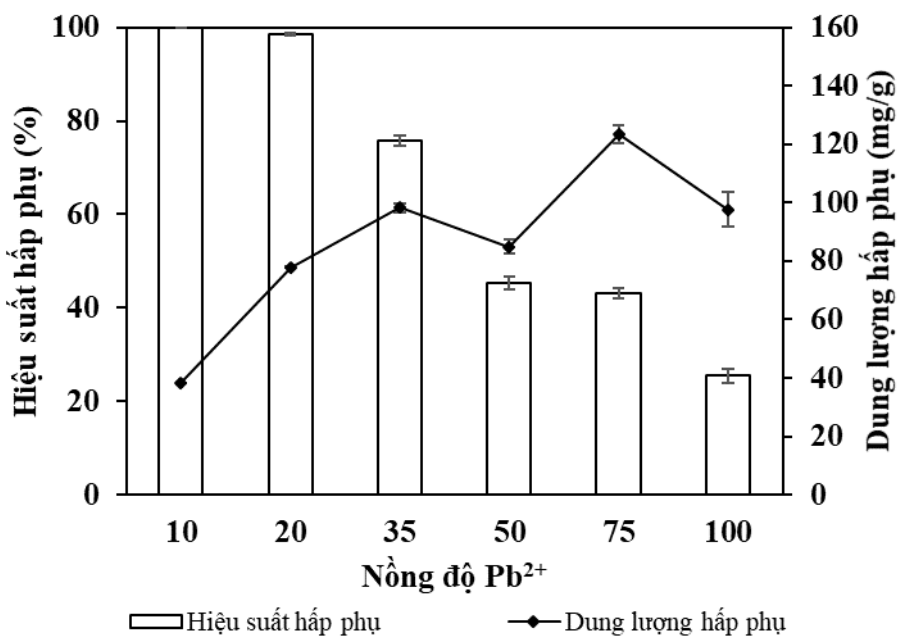


Hình 3-6 Ảnh hưởng của khối lượng chất hấp phụ đến khả năng hấp phụ  $\text{PO}_4^{3-}$  của  $\text{Fe}_3\text{O}_4/\text{NaP1}$

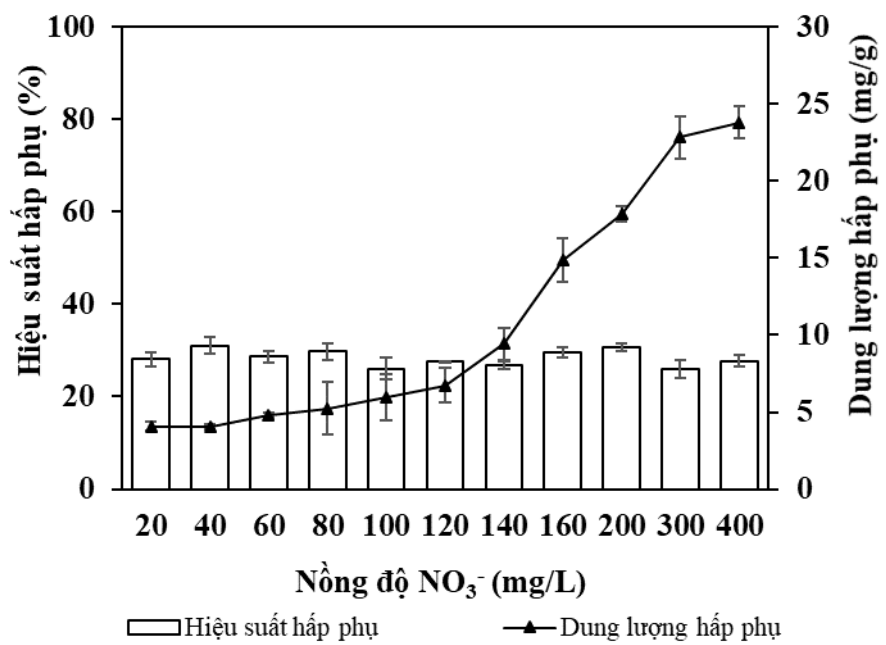
*Ảnh hưởng của nồng độ ion cần hấp phụ*



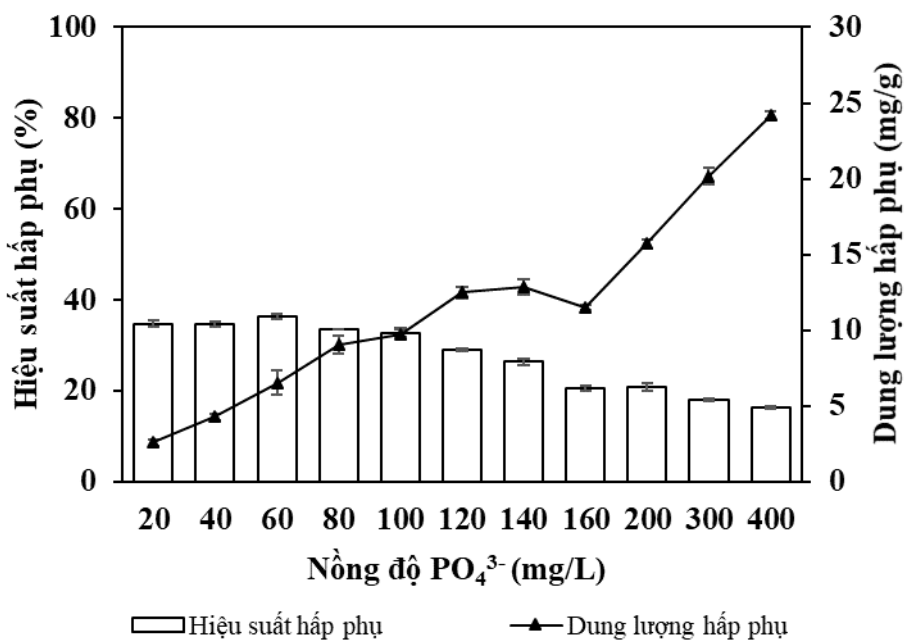
Hình 3-7 Ảnh hưởng của nồng độ  $\text{Cu}^{2+}$  đến khả năng hấp phụ  $\text{Cu}^{2+}$  của  $\text{Fe}_3\text{O}_4/\text{NaP1}$



Hình 3-8 Ảnh hưởng của nồng độ  $\text{Pb}^{2+}$  đến khả năng hấp phụ  $\text{Pb}^{2+}$  của  $\text{Fe}_3\text{O}_4/\text{NaP1}$

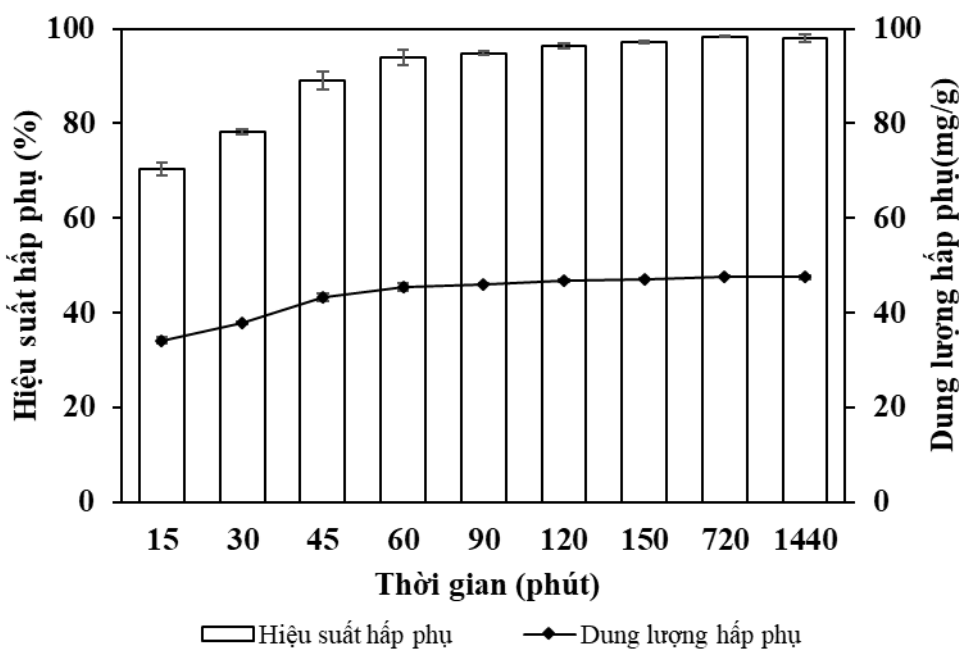


Hình 3-9 Ảnh hưởng của nồng độ  $\text{NO}_3^-$  đến khả năng hấp phụ  $\text{NO}_3^-$  của  $\text{Fe}_3\text{O}_4/\text{NaP1}$

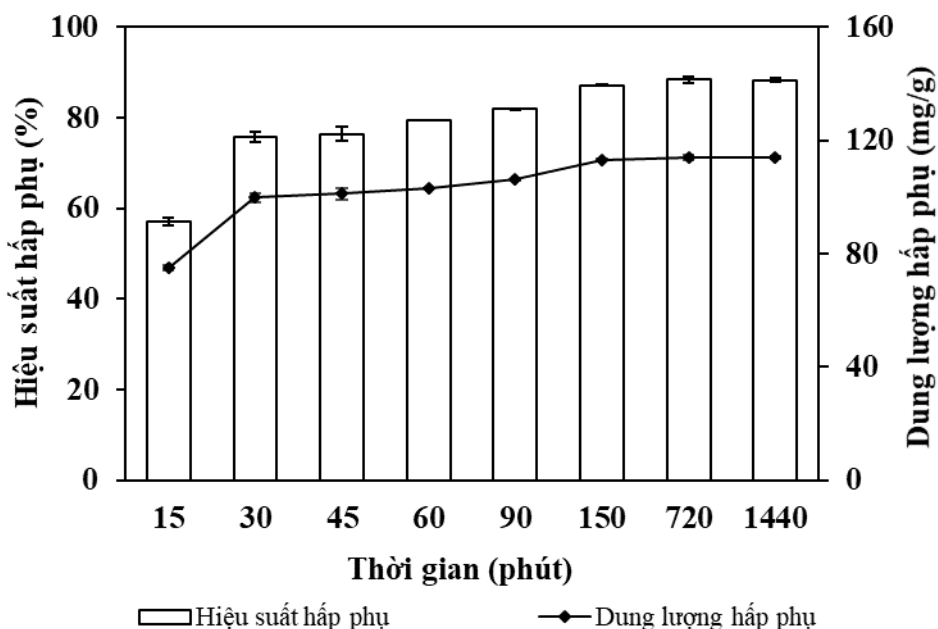


Hình 3-10 Ảnh hưởng của nồng độ  $\text{PO}_4^{3-}$  đến khả năng hấp phụ  $\text{PO}_4^{3-}$  của  $\text{Fe}_3\text{O}_4/\text{NaP1}$

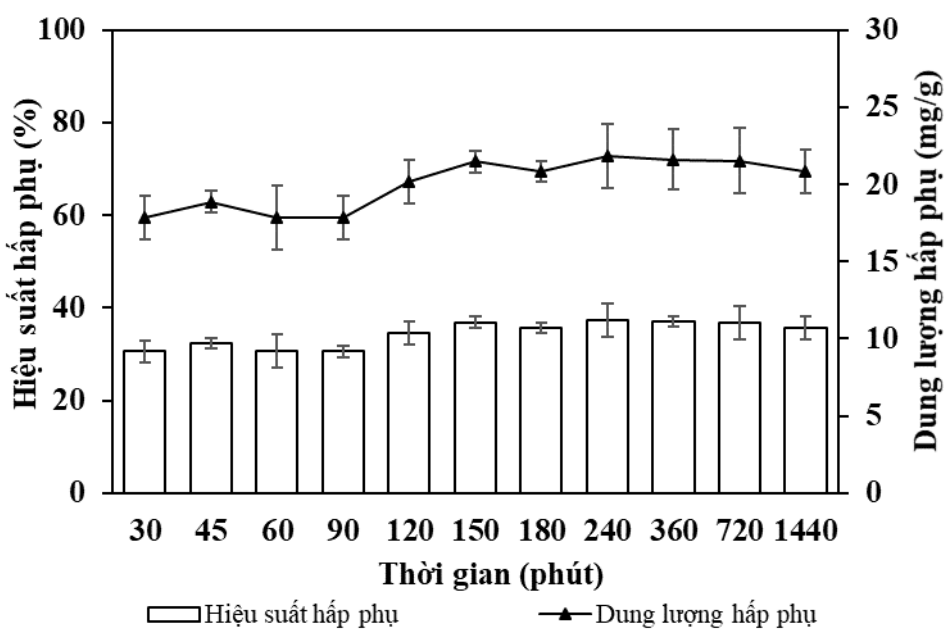
*Ảnh hưởng của thời gian hấp phụ*



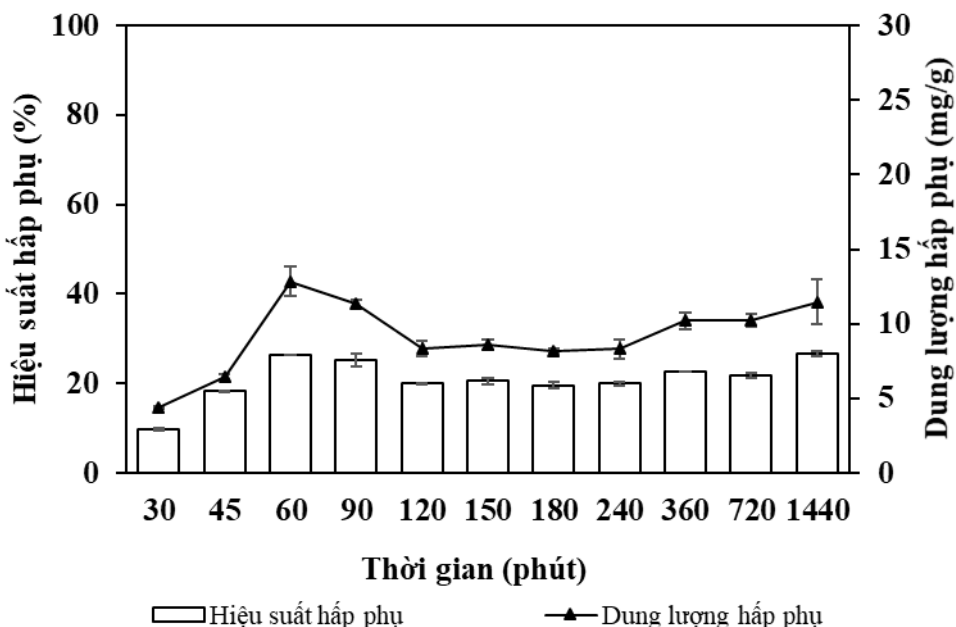
Hình 3-11 Ảnh hưởng của thời gian đến khả năng hấp thụ  $\text{Cu}^{2+}$  của  $\text{Fe}_3\text{O}_4/\text{NaP1}$



Hình 3-12 Ảnh hưởng của nồng độ  $\text{Pb}^{2+}$  đến khả năng hấp thụ  $\text{Pb}^{2+}$  của  $\text{Fe}_3\text{O}_4/\text{NaP1}$



Hình 3-13 Ảnh hưởng của thời gian đến khả năng hấp thụ NO<sub>3</sub><sup>-</sup> của Fe<sub>3</sub>O<sub>4</sub>/NaP1



Hình 3-14 Ảnh hưởng của thời gian đến khả năng hấp thụ PO<sub>4</sub><sup>3-</sup> của Fe<sub>3</sub>O<sub>4</sub>/NaP1

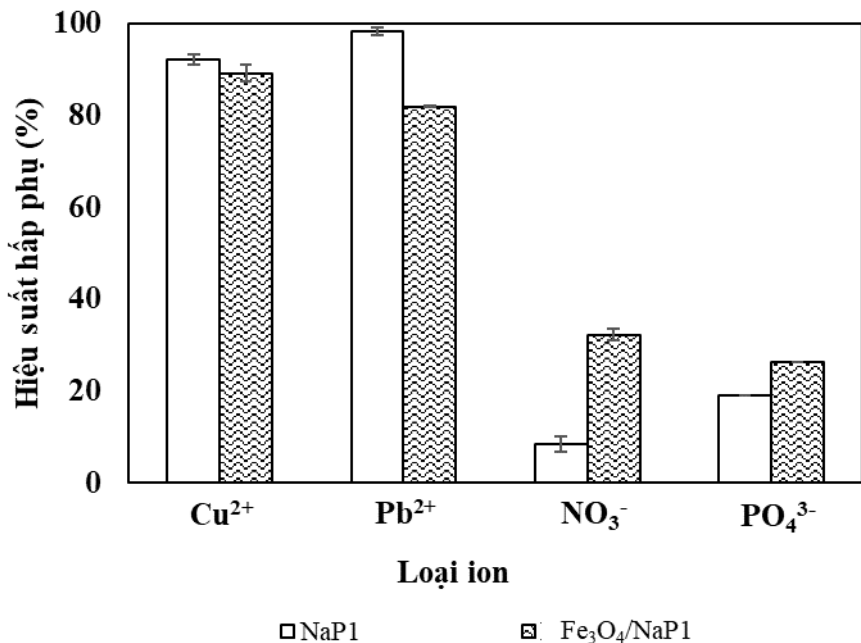
### So sánh khả năng hấp thụ các ion Cu<sup>2+</sup>, Pb<sup>2+</sup>, NO<sub>3</sub><sup>-</sup>, PO<sub>4</sub><sup>3-</sup> của NaP1 và Fe<sub>3</sub>O<sub>4</sub>/NaP1

Điều kiện hấp thụ Cu<sup>2+</sup>: pH 5, khối lượng chất hấp thụ 1.0 g/L, nồng độ Cu<sup>2+</sup> 50 mg/L, thời gian hấp thụ 45 phút.

Điều kiện hấp thụ Pb<sup>2+</sup>: pH 5, khối lượng chất hấp thụ 0,25 g/L, nồng độ Pb<sup>2+</sup> 35 mg/L, thời gian hấp thụ 30 phút.

Điều kiện hấp phụ  $\text{NO}_3^-$ : pH 6, khối lượng chất hấp phụ 4,00 g/L, nồng độ  $\text{NO}_3^-$  200 mg/L, thời gian hấp phụ 45 phút.

Điều kiện hấp phụ  $\text{PO}_4^{3-}$ : pH 6, khối lượng chất hấp phụ 5,00 g/L, nồng độ  $\text{PO}_4^{3-}$  140 mg/L, thời gian hấp phụ 60 phút.



Hình 3-15 So sánh khả năng hấp phụ các ion  $\text{Cu}^{2+}$ ,  $\text{Pb}^{2+}$ ,  $\text{NO}_3^-$ ,  $\text{PO}_4^{3-}$  của NaP1 và  $\text{Fe}_3\text{O}_4/\text{NaP1}$

### Mô hình hấp phụ đẳng nhiệt Langmuir and Freundlich

Mô hình hấp phụ đẳng nhiệt Langmuir và Freundlich được xây dựng dựa trên bộ số liệu khảo sát nồng độ ion đến quá trình hấp phụ của  $\text{Fe}_3\text{O}_4/\text{NaP1}$ .

Bảng 3-2 Các giá trị tham số của phương trình đẳng nhiệt Langmuir và Freundlich

Loại ion	Langmuir			Freundlich		
	$Q_{\max}$ (mg/g)	$K_L$ (L/mg)	$R^2$	$K_F$	n	$R^2$
$\text{Cu}^{2+}$	43,67	0,75	0,99	18,37	3,97	0,97
$\text{Pb}^{2+}$	101,01	12,38	0,98	70,86	9,18	0,79
$\text{NO}_3^-$	135,49	0,001	0,91	0,24	1,20	0,90
$\text{PO}_4^{3-}$	26,35	0,009	0,86	0,79	1,72	0,95

### 3.2.2. Khả năng hấp phụ của NaP1 và $\text{Fe}_3\text{O}_4/\text{NaP1}$ đối với nước ao nuôi tôm

**Bảng 3-3 Khả năng hấp phụ của NaP1 và Fe<sub>3</sub>O<sub>4</sub>/NaP1 đối với nước ao nuôi tôm**

Loại nước	Ion	NaP1		Fe <sub>3</sub> O <sub>4</sub> /NaP1	
		Hiệu suất hấp phụ (%)	Dung lượng hấp phụ (mg/g)	Hiệu suất hấp phụ (%)	Dung lượng hấp phụ (mg/g)
<sup>a</sup> MĐ 250 con/m <sup>3</sup>	NO <sub>3</sub> <sup>-</sup>	5,26 ± 0,72	0,62 ± 0,085	14,51 ± 2,29	1,70 ± 0,27
	PO <sub>4</sub> <sup>3-</sup>	47,15 ± 2,03	2,03 ± 0,21	48,33 ± 8,98	2,15 ± 0,69
<sup>a</sup> MĐ 300 con/m <sup>3</sup>	NO <sub>3</sub> <sup>-</sup>	2,18 ± 0,73	0,28 ± 0,094	18,67 ± 3,56	2,41 ± 0,46
	PO <sub>4</sub> <sup>3-</sup>	24,65 ± 1,79	1,42 ± 0,030	38,19 ± 3,71	2,23 ± 0,42
<sup>a</sup> MĐ 400 con/m <sup>3</sup>	NO <sub>3</sub> <sup>-</sup>	19,84 ± 2,56	1,88 ± 0,240	22,95 ± 2,95	2,16 ± 0,28
	PO <sub>4</sub> <sup>3-</sup>	25,76 ± 2,24	0,45 ± 0,030	75,71 ± 3,70	1,36 ± 0,27
<sup>b</sup> MĐ 250 con/m <sup>3</sup>	NO <sub>3</sub> <sup>-</sup>	15,27 ± 1,43	0,45 ± 0,043	32,11 ± 7,47	0,95 ± 0,22
	PO <sub>4</sub> <sup>3-</sup>	42,37 ± 1,69	4,08 ± 0,270	38,48 ± 8,41	3,81 ± 1,21

<sup>a</sup>MĐ Mật độ, <sup>a</sup> Đa loài, <sup>b</sup> Đơn loài

Càm Thơ, ngày 28 tháng 8 năm 2023

**Tổ chức chủ trì đề tài**

(Thủ trưởng đơn vị ký tên, đóng dấu)

**Chủ nhiệm đề tài**

(Họ tên, chữ ký)



  
Trần Nguyễn Thị Hường Lan